

**LITHIUM INTERCALATION
in preferentially oriented
submicron LiCoO_2 films**

Peter J. Bouwman

The work described in this thesis has been carried out at the MESA⁺ Research Institute of the University of Twente and at the Philips Research Laboratories in Eindhoven as a 'laboratorium-zonder-muren' project of the FOM foundation.

Cover: Sebo Uithol

Explanation of the cover:

The cover shows a computer circuit board containing a large 'inorganic lithium battery' for power backup to maintain time and BIOS settings (front side). These batteries can now be integrated within the chip itself (right side). The heart of this microbattery is the sub-micron Li_xCoO_2 film, which is capable of lithium intercalation (top side). The cube-like structure symbolises that the field of inorganic material science shares edges with electronic and computer science.

© P.J. Bouwman 2002

All rights reserved. No part of this publication may be reproduced, stored in a retrieval system, or transmitted, in any form or by any means, electronic, mechanical, photocopying, recording, or otherwise, without the prior written consent of the copyright owner.

Printing and binding: Febodruk, Enschede.

CIP-Gegevens Koninklijke Bibliotheek, Den Haag

Bouwman, Peter Jaime

Lithium Intercalation – in preferentially oriented submicron LiCoO_2 films

Proefschrift Universiteit Twente, Enschede, - Met lit. opg., -Met samenvatting in het Nederlands

ISBN 90-365-1728-1

Trefw.: Lithium Intercalation, LiCoO_2 , Thin Films, Preferential, Microbattery

LITHIUM INTERCALATION
in preferentially oriented
submicron LiCoO_2 films

PROEFSCHRIFT

ter verkrijging van
de graad van doctor aan de Universiteit Twente,
op gezag van de rector magnificus,
prof.dr. F.A. van Vught,
volgens besluit van het College voor Promoties
in het openbaar te verdedigen
op vrijdag 5 april 2002 te 16:45 uur.

door

Peter Jaime Bouwman
geboren op 22 juli 1974
te Cardenas (Mexico)

Dit proefschrift is goedgekeurd door de promotoren:

| | |
|----------------------------|---|
| Prof.dr.ir. D.N. Reinhoudt | Universiteit Twente |
| Prof.dr. P.H.L. Notten | Technische Universiteit Eindhoven Philips Research Laboratories, Eindhoven |

Samenstelling van de promotiecommissie:

| | |
|-------------------------|-------------------------------|
| Prof.dr. D. Feil | <i>voorzitter</i> |
| Dr. B.A. Boukamp | <i>assistent promotor</i> |
| Dr. H.J.M. Bouwmeester | <i>referent</i> |
| Prof.dr. P.J. Gellings | Universiteit Twente |
| Prof.dr.ir. B. Poelsema | Universiteit Twente |
| Prof.dr. J. Schoonman | Technische Universiteit Delft |

*“As for the answer to the Universe:
there is no Question
Only those we raise ourselves.”*

To my parents

Preface

The process of intercalation may appear distant, but is actually widespread as it is not just limited to lithium ions or even ionic species as a whole. The reversible character of this chemical mechanism allows repeated adsorption and desorption of the intercalate species within a host lattice. By obtaining control over the degree of intercalation, we can influence and exploit the changing material properties of the host. With electrochemical intercalation the stoichiometry is correlated to the flow of electrons, which makes the process compatible with electronic (measurement) devices.

Regarding the current trend of miniaturisation, there is a need for intercalation knowledge on a sub-micron scale, albeit for sensory applications or, as in this case, energy confinement. The study of the thin-film material properties and the electrochemical process requires advanced deposition and characterisation techniques. Their availability has contributed greatly to the success of this project.

The basis of this project is collaboration between the university and the Philips Research Laboratories, known as the: “laboratorium-zonder-muren project” of the FOM-foundation. The fresh researcher has the possibility to pursue and accomplish ambitious objectives, due to the vast amount of knowledge and experience at hand. This thesis is a compilation of the achievements realised in my period as a Ph-D student and hopefully it proves as entertaining for the reader as it has been for me.

| | | |
|-----------|--|-----------|
| 1. | General introduction | 1 |
| 1.1 | Rechargeable batteries | 2 |
| 1.2 | Definition of intercalation | 3 |
| 1.3 | Project motivation | 5 |
| 1.4 | Scope of this thesis | 6 |
| 1.5 | References | 6 |
| 2. | Literature review | 7 |
| 2.1 | Intercalation hosts | 8 |
| 2.1.1 | LiCoO ₂ | |
| 2.1.2 | LiMn ₂ O ₄ | |
| 2.2 | Current Research Topics | 15 |
| 2.2.1 | Preparation | |
| 2.2.2 | Thin film deposition | |
| 2.2.3 | Optimisation of LiCoO ₂ structure | |
| 2.2.4 | Charge control | |
| 2.2.5 | Computer simulations | |
| 2.3 | Electrolyte phase | 22 |
| 2.3.1 | Liquid electrolyte | |
| 2.3.2 | Solid electrolytes | |
| 2.4 | References | 25 |
| 3. | Structural characterisation of submicron films | 27 |
| 3.1 | Introduction | 28 |
| 3.2 | Experimental | 28 |
| 3.3 | Results and Discussion | 30 |
| 3.3.1 | Structural characterisation | |
| 3.3.2 | Influence of the annealing temperature | |
| 3.3.3 | Influence of annealing time | |
| 3.3.4 | Substrate influence | |
| 3.4 | Conclusions | 42 |
| 3.5 | References | 42 |
| 4. | Influence of diffusion plane orientation on intercalation | 43 |
| 4.1 | Introduction | 44 |
| 4.2 | Experimental | 45 |
| 4.3 | Results | 47 |
| 4.4 | Discussion | 59 |
| 4.4.1 | Leakage Current | |
| 4.4.2 | Lithium diffusion | |
| 4.4.3 | Phase Transformation | |
| 4.4.4 | An Equivalent Circuit | |
| 4.5 | Conclusions | 68 |
| 4.6 | References | 69 |

| | | |
|-----------|--|------------|
| 5. | Modelling of lithium intercalation | 71 |
| 5.1 | Introduction | 72 |
| 5.2 | Theory of lithium diffusion | 73 |
| 5.2.1 | Electro Motive Force | |
| 5.2.2 | The intercalation reaction | |
| 5.2.3 | Electrical potential distribution in the galvanic cell | |
| 5.2.4 | Lithium flux in the intercalation electrode | |
| 5.2.5 | Lithium concentration profile upon intercalation | |
| 5.2.6 | Chemical potential variation in a closed circuit | |
| 5.2.7 | Finite Space Warburg network model | |
| 5.2.8 | Simplified equivalent circuit | |
| 5.3 | Experimental | 87 |
| 5.4 | Results and Discussion | 88 |
| 5.4.1 | Exchange current density | |
| 5.4.2 | Diffusion Resistance | |
| 5.4.3 | Intercalation Capacity | |
| 5.4.4 | Electronic resistance | |
| 5.5 | Evaluation | 100 |
| 5.6 | References | 101 |
| 6. | Influence of film morphology | 103 |
| 6.1 | Introduction | 104 |
| 6.2 | Experimental | 105 |
| 6.3 | Results | 106 |
| 6.3.1 | RF-sputtered seed layer | |
| 6.3.2 | Deposition temperature | |
| 6.3.3 | LiCoO ₂ film patterning | |
| 6.3.4 | Stainless steel substrates | |
| 6.4 | Discussion | 115 |
| 6.4.1 | LiCoO ₂ crystal structure | |
| 6.4.2 | Rate of intercalation | |
| 6.4.3 | Metallic substrates | |
| 6.5 | Conclusions | 121 |
| 6.6 | References | 122 |
| 7. | Characterisation of Li_xCo_yMn_{1-y}O₂ powders and films | 123 |
| 7.1 | Introduction | 124 |
| 7.2 | Experimental | 125 |
| 7.3 | Results | 128 |
| 7.3.1 | Powder characterisation | |
| 7.3.2 | Composite electrode properties | |
| 7.3.3 | Structural analysis of thin films | |
| 7.3.4 | Electrochemical thin-film properties | |
| 7.3.5 | Spectral analysis | |

| | | |
|------------|---|------------|
| 7.4 | Discussion | 141 |
| 7.4.1 | Powder structure | |
| 7.4.2 | Composite electrode cycling | |
| 7.4.3 | Thin-film electrodes | |
| 7.4.4 | Spectroscopy | |
| 7.5 | Conclusions | 148 |
| 7.6 | References | 149 |
| 8. | Small Angle Neutron Scattering | 151 |
| 8.1 | Introduction | 152 |
| 8.2 | Experimental | 154 |
| 8.3 | Results and Discussion | 156 |
| 8.4 | References | 159 |
| 9. | μ-Battery development | 161 |
| 9.1 | Introduction | 162 |
| 9.1.1 | Material stack | |
| 9.2 | Experimental | 165 |
| 9.3 | Results | 167 |
| 9.3.1 | Structural analysis | |
| 9.3.2 | Electrochemical measurements | |
| 9.4 | Discussion | 174 |
| 9.5 | Conclusions | 176 |
| 9.6 | References | 177 |
| 10. | Evaluation & Recommendations | 179 |
| 10.1 | Tailoring the LiCoO ₂ film | 180 |
| 10.2 | Improving intercalation properties | 182 |
| 10.3 | Proposed research directions | 185 |
| 10.4 | References | 186 |
| | Summary | 187 |
| | Samenvatting | 188 |
| A | Ladder network impedance | 189 |
| B | Lithographic mask design | 192 |
| C | Temperature sensor circuitry | 193 |

List of symbols

| | | |
|-----------------|--|---|
| A | area | [cm ²] |
| a | hopping distance | [m] |
| a _j | activity of species <i>j</i> | [mol·dm ⁻³] |
| b _j | mobility of species <i>j</i> | [m ² ·s ⁻¹ ·V ⁻¹] |
| C | capacitance | [F] |
| C _j | concentration of species <i>j</i> | [at·dm ⁻³] |
| c _j | molar concentration of species <i>j</i> | [mol·dm ⁻³] |
| D | diffusion coefficient | [cm ² ·s ⁻¹] |
| d | bridge structure width | [mm] |
| E | electric potential field | [V·m ⁻¹] |
| E _a | activation energy | [J·mol ⁻¹] |
| F | Faraday's constant | [C·mol ⁻¹] |
| G | molar Gibbs free energy | [J·mol ⁻¹] |
| H | molar enthalpy | [J·mol ⁻¹] |
| i | current | [A] |
| J _j | flux of <i>j</i> | [mol·s ⁻¹] |
| k | Boltzmann constant | [J·K ⁻¹] |
| L | characteristic diffusion length | [m] |
| L _D | Debye's length | [m] |
| N | Avogadro's number | [mol ⁻¹] |
| Q | capacity | [C] |
| q _j | elementary charge of species <i>j</i> | [C] |
| R | Gas constant | [J·K ⁻¹ ·mol ⁻¹] |
| R _j | resistance | [Ω] |
| S | molar entropy | [J·mol ⁻¹ ·K ⁻¹] |
| T | Temperature | [K] |
| t | time | [s] |
| t _j | transport number of species <i>j</i> | - |
| u _j | electrical mobility of species <i>j</i> | [m ² ·C·s ⁻¹] |
| u ₀ | electrical mobility at T=0K | [m ² ·C·s ⁻¹] |
| w _j | thermodynamic enhancement factor of species <i>j</i> | - |
| X | arbitrary measured quantity | - |
| x | Lithium content | - |
| Z _j | impedance of species <i>j</i> | [Ω] |
| Z _{ei} | parallel electronic and ionic impedance | [Ω] |
| z | number of electrons | - |
| δ | film thickness | [m] |
| ε ₀ | vacuum permittivity | [J ⁻¹ ·C ² ·m ⁻¹] |
| ε _r | relative permittivity | - |
| φ | electrical potential | [J·C ⁻¹] |
| γ | activity coefficient | - |
| η | electrochemical potential | [J] |
| μ | chemical potential | [J] |
| ν | attempt frequency | [Hz] |
| ρ | density | [g·m ⁻³] |
| σ _j | partial conductivity of species <i>j</i> | [m ² ·mol·C·s ⁻¹] |
| τ | characteristic relaxation time | [s ⁻¹] |
| ω | radial frequency | [rad·s ⁻¹] |
| ∇ | derivative to place coordinate | |

1 General introduction

This Chapter gives a birds-eye view of the contents of this thesis. First some necessary technical background information is given on secondary lithium batteries in general. Next the basic principles behind their successful operation are briefly addressed. The objectives of this research project are stated against the major challenges in this field of science. The topics of the individual Chapters of this thesis are also described.

1.1 Rechargeable batteries

There are two types of electrochemical energy storage devices: primary and secondary batteries or, in other words, disposable and rechargeable batteries. In the first case the chemical energy cannot be restored once it has been converted to electrical energy, while in the second case the electrochemical process is reversible. To recharge it an external electrical energy source is required with a voltage higher than that of the secondary cell. Before the existence of electrical generators, primary batteries were used to charge the secondary ones.

This thesis focuses on rechargeable lithium batteries. Figure 1.1 shows how these compare with other commercially available, rechargeable cells. The lead-acid battery finds application in almost every vehicle for engine start-up due to its high current delivery capability (power), but normalised to its weight and volume the energy density is relatively low. For less power demanding electrical gadgets the nickel-cadmium batteries have proven most suitable, but are more and more replaced by the more environment friendly nickel-metal-hydride batteries. Both cell types exhibit a cell voltage of 1.2 V. The lithium cells exhibit a cell voltage of 3.5 to 4V. This means that the output voltage of only one battery is sufficient to replace three batteries of the Ni-Cd and Ni-MH type. Due to the high voltage and the low density of lithium ($0.5\text{g}\cdot\text{cm}^{-3}$), the amount of energy incorporated in this cell, scaled to its mass or volume, exceeds all other rechargeable battery types.

The lithium cell has been the best selling battery since 1996. The annual market growth rate is 9% and is expected to reach \$2.6 billion in 2006 in the US alone [1].

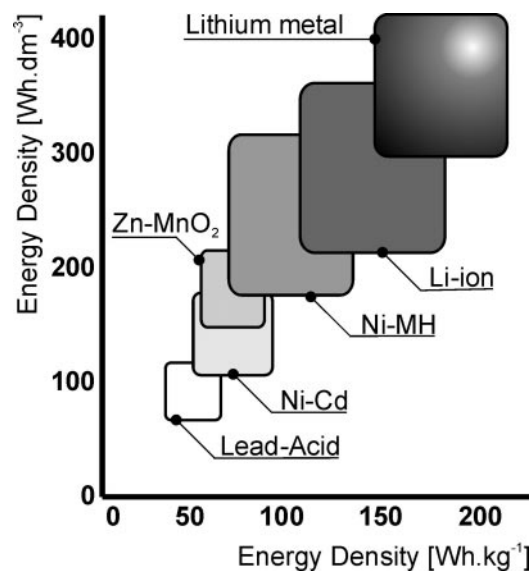


Figure 1.1: Energy density per unit of mass and volume plotted for several common secondary batteries.

1.2 Definition of intercalation

The energy involved with the lithium intercalation reaction in Li_xCoO_2 against metallic lithium is three times the equivalent of the (explosive) reaction between hydrogen and oxygen gas. More energy is required to enforce the reverse reaction during battery recharge and is only achieved without huge losses (heat production) thanks to the discovery of intercalation materials. These ‘hosts’ can temporarily accommodate lithium without undergoing major structural changes. Likewise, the dictionary [2] defines intercalation as:

“The insertion or introduction of something among other existing or original things.”

Generally, lithium is oxidised during the discharge of the cell and the released electrical energy is consumed in an external circuit. However, the formation of basic lithium oxide (Li_2O) cannot be reversed electrochemically without destroying the battery. Instead of direct oxidation, the lithium is ‘incorporated’ in the cobalt oxide intercalation host (CoO_2) of the positive electrode. The advantage of this process is its reversibility: during charging of the cell the lithium is

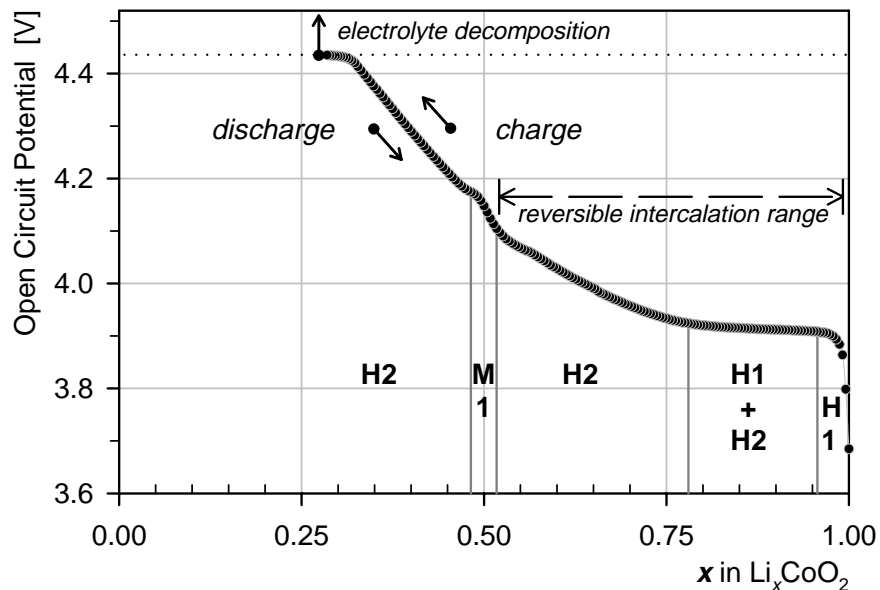


Figure 1.2: The Open Circuit Potential (OCP) of a commercial LiCoO_2 electrode recorded against metallic lithium as a function of the degree of lithium intercalation (25°C). The reported LiCoO_2 phase structures are indicated (H: hexagonal, M: monoclinic).

extracted from its host, while the basic CoO_2 lattice structure remains intact. Upon the following cell discharge, the lithium is again re-intercalated. The amount of lithium, which can be intercalated reversibly into the electrode determines the capacity of the battery (here: $\Delta x \approx 0.5$). The potential of Li_xCoO_2 (against metallic lithium) varies with the lithium concentration x , as shown in Figure 1.2.

The use of metallic lithium as a negative electrode in commercial batteries is regarded hazardous. For this reason, it has been replaced by another intercalation material, exhibiting an energy level close to that of metallic lithium, *i.e.* LiC_6 ($\sim 0.1\text{V}$ vs. Li) [3]. During cycling of the cell, lithium is transferred from the negative intercalation host to the positive host and *vice versa*. This cell type is also known as ‘rocking chair’ or ‘lithium-ion’ battery and illustrated in Figure 1.3.

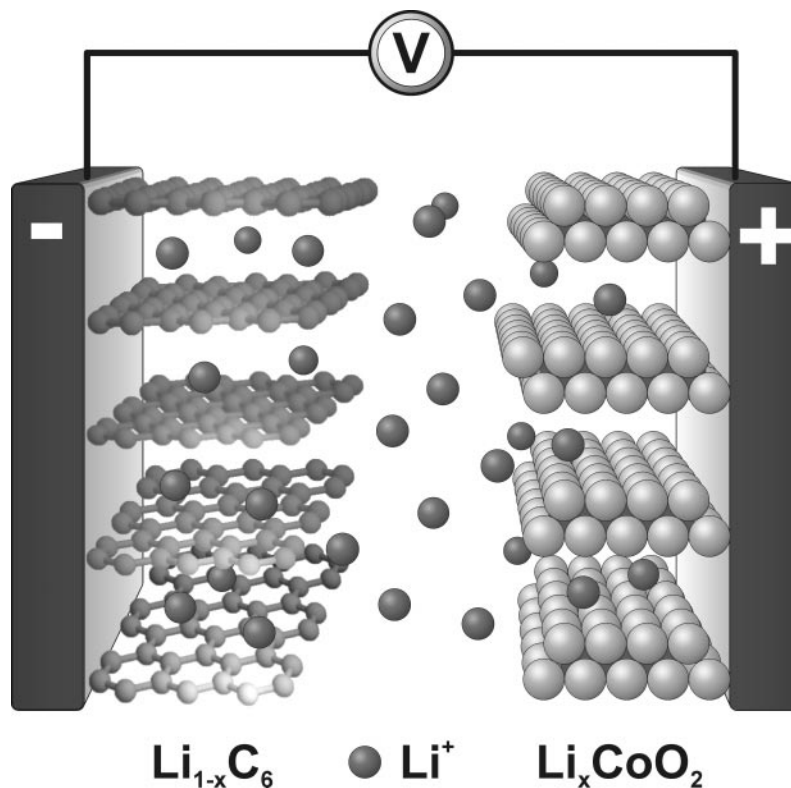


Figure 1.3: Schematic representation of the ‘rocking-chair’ or ‘lithium-ion’ battery in which the lithium is sequentially intercalated in the positive and negative electrode during discharge and charge of the cell, respectively.

1.3 Project motivation

The object of this “*Laboratorium-zonder-muren*” project is to perform fundamental research on the intercalation mechanism of the positive electrode. For this purpose the commercial electrodes cannot be used. Their performance has been optimised to achieve high intercalation rates by mixing the active powder material with additives, such as carbon black and polymer binder, to form a porous electrode. Due to many variables involved, it is difficult to interpret experimental data and unravel the process mechanism. Therefore, this study is carried out on thin-film electrodes, deposited on smooth substrates, which consist only of the active intercalation material.

LiCoO₂ has primarily been selected as host material, as it exhibits high cycling stability and has already proven its potential as intercalation electrode. Metallic lithium is used as a counter electrode. It provides a reliable reference potential and serves as lithium source. The risk of mishaps is limited, when only small quantities are handled in an inert helium atmosphere.

The intercalation performance of the thin-film LiCoO₂ samples is characterised in a self-constructed, electrochemical cell set-up using a liquid electrolyte. Although it is not a primary object of this investigation, the influence of the electrolyte phase cannot be disregarded, as the electrode|electrolyte interface is important for the intercalation process. Even the choice of the substrate material, which is the actual basis of the thin-film electrode, influences the final electrochemical properties.

In perspective of future applications, we have processed a prototype of a solid-state micro-battery, based on the thin-film intercalation electrode. Technically, it is possible to process the micro-battery together with an integrated circuit on one silicon substrate. However, the limited capacity of the thin-film intercalation electrode imposes practical limitations to the power delivery of the device.

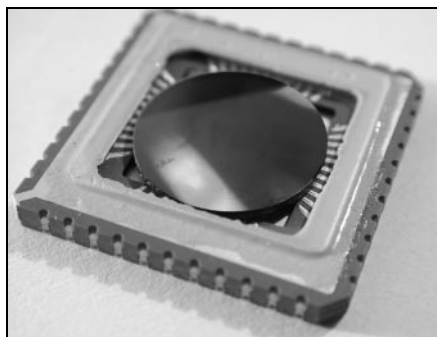


Figure 1.4: Artist impression of a micro-battery implemented in a ceramic chip package.

1.4 Scope of this thesis

In the second Chapter, the reported research on lithium batteries is reviewed with specific attention for subjects addressed in this project.

Chapter 3 focuses entirely on the preparation of the sub-micron LiCoO_2 films on silicon substrates and their structural characterisation. It appears that the preferential orientation of the 2-dimensional crystal structure depends strongly on the deposition method and process parameters. The electrochemical performance of these films as intercalation electrodes is presented in Chapter 4. The physical interpretation of the electrochemical results is presented in Chapter 5.

The substrate roughness can have indirect influence on the intercalation rate by determining the (non-)uniformity of the preferential orientation, as shown in Chapter 6. Lithographic patterning is applied to preferential films to investigate the dependency on the artificially controlled diffusion length.

Cobalt substitution of the manganese-based spinel $\text{LiCo}_y\text{Mn}_{1-y}\text{O}_2$ is studied in the range of $0 < y < 1$ to investigate possible synergetic effects, such as increased voltage and intercalation capacity and a three-dimensional lithium diffusion structure. Composite powder and thin-film electrodes of these compositions are characterised and compared in Chapter 7.

Neutron reflectometry is a novel analysis technique in development to study the ordering of lithium within the intercalation host as a function of potential. Chapter 8 describes the set-up and the preliminary results of this technique.

Chapter 9 focuses on the integration of sub-micron LiCoO_2 films in a solid-state device. An actual prototype of a microbattery has been constructed, which shows the feasibility of practical application.

An overview of the major results is given in Chapter 10 together with suggestions for continuation of this research project.

1.5 References

1. Business Communications Co., Inc., *Lithium batteries: market & materials* (2001).
2. "Webster's Comprehensive Dictionary", Trident Press International (1996).
3. "Electrochemical Systems", second edition, Prentice-Hall, New Jersey (1991).

2 Literature review

The current state of research of the intercalation electrode is reviewed. The factors relevant to achieve a high energy density and large capacity are briefly discussed. The different approaches to improve the electrode material properties are elucidated. The common lithium intercalation hosts LiCoO_2 and LiMn_2O_4 are considered in detail.

Progress is gained by improving the properties of the electrodes, but also through optimisation of the electrolyte material, battery design and charge procedure. These topics are mentioned to add perspective to the research presented in this thesis.

2.1 Intercalation hosts

The feasibility of high power-density lithium secondary batteries, based on intercalation technology, was first demonstrated with the Li_xTiS_2 cathode in 1976 [1]. Lithium can be reversibly extracted from a TiS_2 positive electrode over the compositional range $0 \leq x \leq 1$ at a cell voltage exceeding 2.0 V at current densities of 1 to 10 mA/cm^2 . Difficulties, among which the reversible deposition at the lithium negative electrode, have restricted the practical use of the $\text{Li}/\text{Li}_x\text{TiS}_2$ cell. In this case replacing the lithium anode by an intercalation host leads to unattractive low potentials. This stimulated the development of a cathode yielding higher cell voltages than Li_xTiS_2 , while retaining the wide intercalation range [2].

Electrical energy is proportional to voltage and charge. The energy stored in an intercalation electrode is determined by the intercalation *potential* and its *capacity*, normalised to the amount of ‘active’ material. Both aspects are briefly elaborated.

Potential - The operation voltage of the intercalation electrode is determined by the sum of (i) the effective electrostatic potential at the Li site, which corresponds to the energy required to remove a Li ion, and (ii) the energy of the highest occupied orbital, which is related to the energy required to remove an electron [3]. Some lithium intercalation compounds are plotted in Figure 2.1 on the energy scale vs. metallic lithium.

(i) The lithium site energy is influenced by the surrounding crystal lattice. The Madelung constant gives an indication of the magnitude of the crystalline field. The type of site and its relative occupation determines the energy

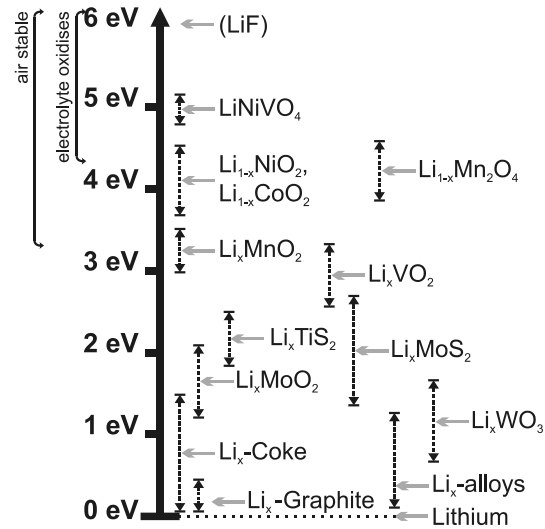


Figure 2.1: Intercalation energy range of some lithium compounds.

state of the intercalated lithium. For example, in case of $\text{Li}_{1+x}\text{Mn}_2\text{O}_4$ the transition of lithium from tetrahedral to octahedral sites results in a 0.8eV potential drop.

(ii) Primarily the redox couple determines the Fermi level* of the intercalation electrode. In General, the transition metal cation is reduced from M^{4+} to M^{3+} oxidation state during lithium intercalation. However, EXAFS measurements performed by Montoro *et al.* [4] have recently shown the Co remains in the M^{3+} state at all times. Upon de-intercalation, instead of direct cation oxidation, holes are formed in the valence band, which is largely of oxygen 2p origin. This indicates a significant influence of the anion on the redox potential.

The incorporation of anions with high electronegativity, leads to a decrease of the Fermi level and a subsequent increase of the cell potential against lithium. The Fermi level of oxides can be 2eV lower than that of chalcogenides, as the oxygen 2p band lies significantly below the corresponding sulfide 3p valence band. Substitution of oxygen anions with fluorine is expected to raise the intercalation potential of LiCoO_2 against lithium by another 2V, according to plane-wave pseudo-potential calculations of the band structure [3].

Capacity - The intercalation capacity of the cell is determined by the stability range of lithium non-stoichiometry. The conduction band serves as an accessible source and sink of electrons that readily compensates for the respective annihilation and formation of vacancies. Hence, non-stoichiometry is associated with the electronic delocalisation [5]. The transition metals cations are studied, as their multivalent character theoretically enables a large intercalation capacity. Note, that anion species can also contribute to charge compensation.

The crystal structure of the intercalation host also determines its capacity through the number of lattice vacancies. The transition metal oxide host materials can roughly be divided into rocksalt- and spinel-type structures. Both have cubic close

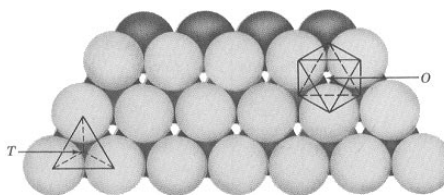


Figure 2.2: Illustration of a tetrahedral site (T) and an octahedral site (O) in a close-packed oxygen lattice.

* Note: the Fermi level is only defined at a temperature of 0K. What is referred to here is actually the chemical potential of the electrons.

packed oxygen planes. The rock-salt type structure consists of MO_2 sheets and accommodates lithium in the Vanderwaals gaps between the layers, while the spinel structure intercalates lithium in specific octahedral and tetrahedral lattice sites. The maximum intercalation capacity of the spinel-type structure is limited to the number of accessible sites.

The reversible intercalation capacity of a rocksalt-type structure is until recently believed to be restricted by the mechanical stability of the Vanderwaals gap, which may collapse upon excessive de-intercalation of lithium. However, it has been shown that only the highly charged oxide in contact with liquid electrolyte is subject to degradation [6]. Amatucci *et al.* [7] showed that a linear correlation exists between the intercalation capacity decrease and the loss of Co from the electrode, observed after 25 cycles to voltages ranging from 4.1 to 4.5V (indicated in Figure 2.3). The

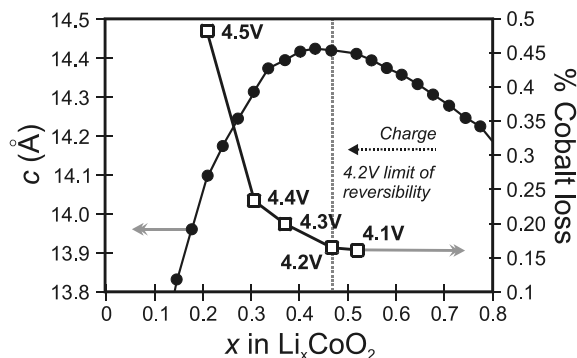


Figure 2.3: Graph showing the inverse relationship between the c -axis expansion and the relative Co loss observed with cut-off potentials above 4.1V as a function of composition [7].

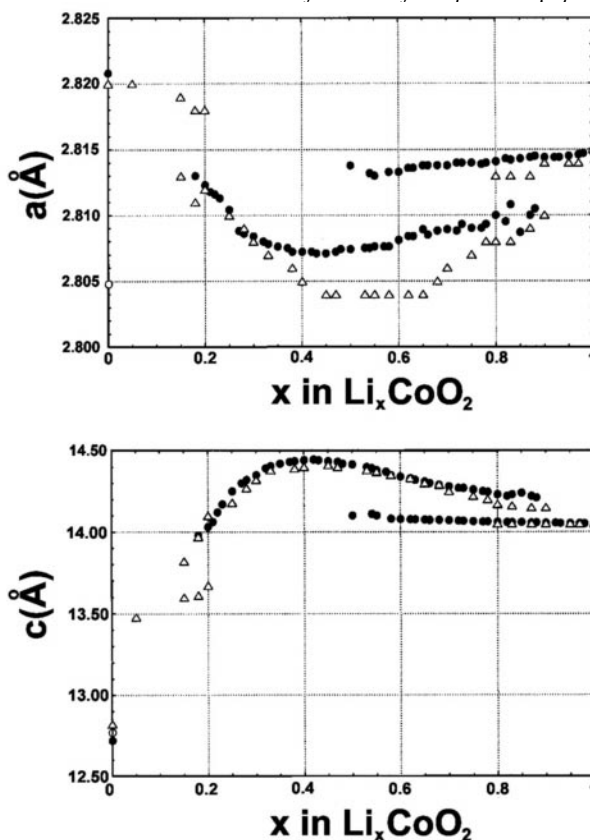


Figure 2.4: Lattice expansion measured by Levasseur *et al.* [8] (•) as a function of the degree of lithium intercalation (Δ : Amatucci *et al.* [21]).

exponential increase of the Co loss with extended de-intercalation range is ascribed to structural changes of the host.

The varying lithium composition in the intercalation host during lithium (de-)intercalation influences the dimensions of the lattice structure. The spinel-type structure shows isotropic expansion as function of the lithium concentration, while that of the rocksalt-type structure is strongly anisotropic (Figure 2.4). The volume gradually adjusts itself when the host forms a solid solution with the intercalating ions, but changes instantly with a phase transformation. Oxides, including LiCoO_2 , can only tolerate elastic strain of $\approx 0.1\%$ before fracture [7]. Repeated transformation, induced by repetitive cycling of the cell in this particular lithium composition range, can cause severe structural degradation of the electrode and consequential capacity loss. Limiting the intercalation range retains the initial capacity. Another option is doping the structure with ions that inhibit the phase transformation and thus improve the capacity retention. Some examples of beneficial additives are presented in paragraph 2.1.5, but first the basic intercalation host structures are elucidated.

2.1.1 LiCoO_2

Lattice structure - Two distinct phases of stoichiometric LiCoO_2 are known, which are commonly indexed by the temperature required for their synthesis: high temperature LiCoO_2 (HT- LiCoO_2) is rhombohedral (spacegroup $R\bar{3}m$), while low temperature LiCoO_2 (LT- LiCoO_2) has a cubic structure (spacegroup $Fd\bar{3}m$). The rhombohedral and cubic structures have the same oxygen sub-lattice and are distinguished by the spatial arrangement of cations. In HT- LiCoO_2 , Li and Co alternately occupy the layers of octahedral sites between the oxygen close-packed planes. In LT- LiCoO_2 , 6% of the Li exists in

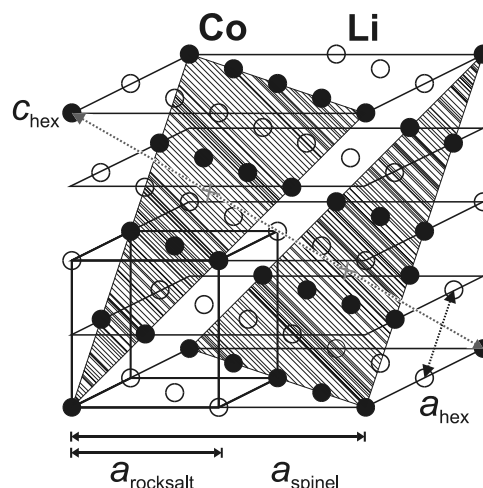


Figure 2.5: Cationic positions and unit cell constants indicated for the hexagonal, spinel and rocksalt lattice structure.

octahedral sites of the Co layer and *vice versa* resulting in cubic symmetry [9]. In case of random occupation of the cationic sites, the layers are indistinguishable and a rocksalt structure (isomorphic to NaCl) is obtained with approximately half the cell constant of the spinel structure.

The rhombohedral HT-LiCoO₂ structure would be identical to the spinel LT-LiCoO₂ structure, if the cell constant ratio c/a were fixed at 4.90. The presence of the hexagonal distortion leads to slight differences, most noticeable in the splitting of the spinel (222) diffraction peak into the hexagonal (006) and (012) peaks and also in the splitting of the cubic (440) peak into the hexagonal ((018) and the (110) peaks. In each case the sum of the hexagonal peak intensities in the HT-LiCoO₂ gives the same total intensity as the single cubic peak in LT-LiCoO₂. The spinel (111), (331), (511) and (442) diffraction peaks are reflections of the superlattice structure of the slightly disordered cation arrangement, with a 2×2×2 super structure (indicated in Figure 2.5). The spinel (222), (400), (440), (622) and (444) are independent of cationic ordering. Hence, solely the latter are observed for a rocksalt structure with random cationic occupation [10].

Lithium (de-)intercalation – The ordered HT-Li_xCoO₂ phase is most suitable for application in intercalation electrodes. Its reversible intercalation capacity is $0.95 < x < 0.45$ at a potential of 3.6V to 4.2V against lithium, respectively (see Figure 1.2). Within the composition range $0.9 < x < 1$ a single hexagonal phase *H1* exists, whereas within the range $0.78 < x < 0.9$, two hexagonal phases coexist giving rise to a potential plateau at 3.9V. Only the second phase *H2* exists in the region $0.51 < x < 0.78$. Upon further extraction of lithium a monoclinic distortion *M* of this second hexagonal phase is

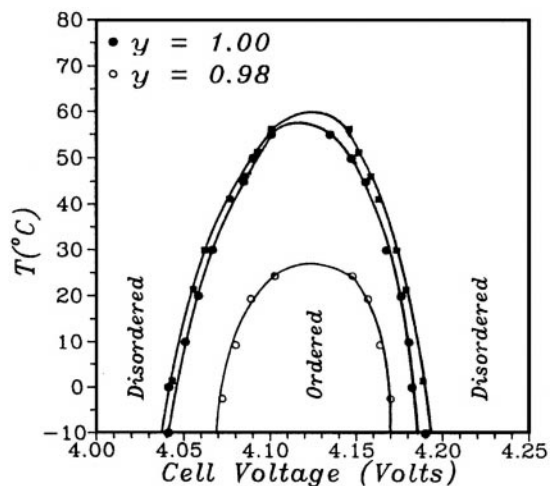


Figure 2.6: Electrochemically measured phase diagram of the order-disorder transition near $x=0.5$ of $\text{Li}_x\text{Co}_y\text{Ni}_{1-y}\text{O}_2$ [10].

observed in the narrow range of $0.45 < x < 0.51$, associated with ordering of lithium. The stability range of this phase can be reduced by substitution of Co with a small amount of Ni (Figure 2.6). Clearly the introduction of local lattice distortion breaks down the lithium super-lattice structure [10].

Electronic configuration - The oxide adopts a cubic close-packed arrangement with Co^{3+} and Li^+ alternately occupying the octahedral sites between adjacent oxide ion layers. Co^{3+} adopts a low spin configuration ($t_{2g}^6 e_g^0$) in an octahedral oxygen environment. The t_{2g} orbitals are energetically close to the oxygen 2p orbitals and the 2p orbitals of π symmetry will overlap strongly with the Co t_{2g} orbitals. Full occupancy of the $t_{2g}\pi^*$ orbitals, which are separated energetically from the $e_g\sigma^*$ orbitals, ensures semiconductor behaviour for LiCoO_2 . The extraction of lithium is associated with a contraction of the a-axis and subsequent shortening of the Co-Co distance, reduced from 2.83Å in the case of LiCoO_2 to 2.81Å for $\text{Li}_{0.9}\text{CoO}_2$. The critical distance for direct t_{2g} - t_{2g} Co-Co interaction across a shared octahedral edge is 2.82Å, which results in a narrow d-band. The change in the electronic configuration is consistent with the observed switch from insulator to metallic behaviour on extraction of a relatively small amount (10%) of lithium from LiCoO_2 [15].

2.1.2 LiMn_2O_4

Manganese is approximately 1% of the cost of cobalt and significantly more environment friendly. For these reasons the interest for this material from research point-of-view is large, but its application in commercial batteries is severely limited due to the large capacity decrease during constant cycling (usually expressed as relative capacity fade per cycle).

Lattice structure - LiMn_2O_4 is a three-dimensional host. The spinel structure (space group $\text{Fd}\bar{3}\text{-m}$) consists of cubic close-packed oxygen ions with Mn in one half of the octahedral sites and Li^+ in one eighth of the tetrahedral sites. The M_2O_4 structure is highly stable and possesses a series of intersecting tunnels, formed by the face-sharing of tetrahedral lithium (8a) sites and empty octahedral (16c) sites. This tunnel network enables 3-dimensional lithium diffusion and, unlike the layered rocksalt-type structure, is selective for lithium ions over solvent molecules (*i.e.* deleterious effects of solvent co-intercalation are avoided).

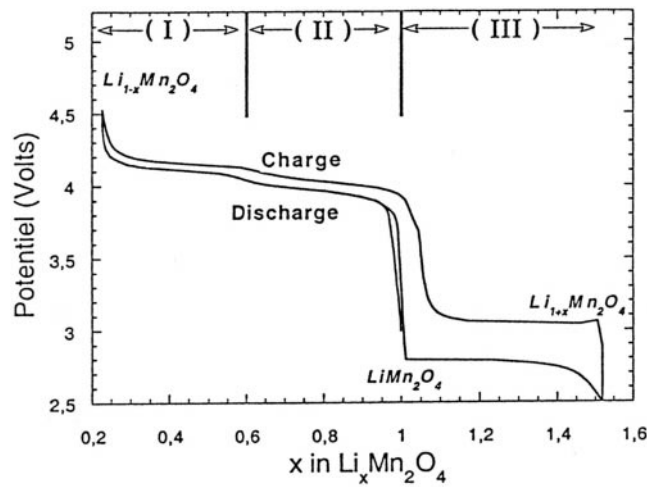


Figure 2.7: The potential of $\text{Li}_x\text{Mn}_2\text{O}_4$, measured against metallic lithium during constant current cycling, plotted as function of x [7].

During charging of LiMn_2O_4 -based cell, lithium is extracted from the tetrahedral sites. This extends over a continuous range of solid solutions in the range $0.55 < x < 1$ (region (II) in Fig. 2.7). It has been suggested that at $x \approx 0.5$ lithium ordering occurs at one half occupancy of the tetrahedral 8a sites. Below this composition two cubic spinel phases of approximate composition $x=0$ and $x=0.5$ coexist (region (I)). A small step of around 100mV between two essentially flat voltage profiles is observed.

LiMn_2O_4 can also adopt other (meta-stable) crystal structures, besides spinel [12]. When LiMn_2O_4 is synthesised exhibiting a layered crystal structure, the shape of the intercalation profile changes accordingly, as shown in Figure 2.8,

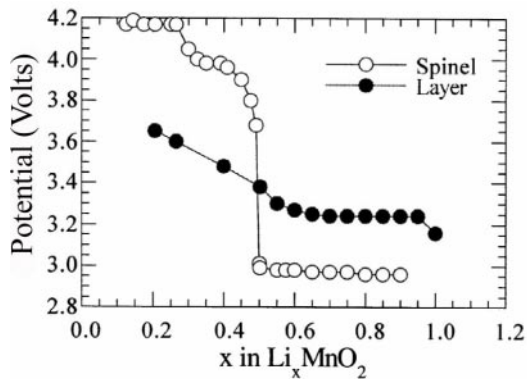


Figure 2.8: Cell voltages of the layered and spinel phases of manganese oxides [13].

resembling the layered Li_xCoO_2 intercalation profile. The higher potential of the spinel phase at low lithium content indicates a higher stability [13]. Cycling of the layered material shows strong capacity loss as a result of the gradual transformation towards spinel(-like) phases, due to Mn diffusion [14].

Surplus lithium may be intercalated into spinel-phase LiMn_2O_4 up to a maximum composition $\text{Li}_2\text{Mn}_2\text{O}_4$ (region (III) in Fig. 2.7)). In this composition range the additional lithium occupies the remaining octahedral sites. The cell potential against lithium is around 3.0V. At the composition $\text{Li}_{1.1}\text{Mn}_2\text{O}_4$ a phase transformation from cubic to tetragonal occurs and induces a volume change of 6.5%, which has a deleterious effect on the cycle stability. Several methods have been developed to maintain the average Mn oxidation state above 3.5 to avoid this Jahn-Teller distortion:

- Over-oxidation of Mn leading to a cation-deficient spinel: $\text{LiMn}_2\text{O}_{4+\delta}$.
- Excess lithium on Mn sites (similar to doping with divalent cations, but considered more effective and practical). This results in a shorter 4V plateau.

Another problem of the manganese intercalation electrode is the disproportionation reaction $2\text{Mn}^{3+} = \text{Mn}^{2+} + \text{Mn}^{4+}$, which results in dissolution of Mn^{2+} in the electrolyte and, hence, loss of active material. Overall, the performance of LiMn_2O_4 , in contrast to LiCoO_2 , is very sensitive to the preparative conditions.

Electronic configuration – Half of the octahedrally coordinated Mn cations are Mn^{3+} (high spin $3d^4, t_{2g}^3 e_g^1$) and half Mn^{4+} ($3d^3, t_{2g}^3$). The t_{2g} orbitals are too contracted to overlap directly across a shared octahedral edge and thus the d -electrons are localised. Half of the Mn sites are occupied by the Jahn-Teller active Mn^{3+} ions and this is insufficient to promote a cooperative Jahn-Teller distortion. The electronic transport occurs by thermally activated small polaron hopping of the e_g electron between neighbouring $\text{Mn}^{3+}/\text{Mn}^{4+}$ ions; the polaron is magnified by a dynamic Jahn-Teller distortion which must follow the electron.

2.2 Current Research Topics

Research on the intercalation hosts for secondary lithium batteries can roughly be divided into the categories: material preparation, optimisation, application and simulation. In the next paragraphs some hot topics in each field are addressed.

2.2.1 Preparation

Solid-state – The classic method for preparation of oxide powders is the mixture of nitrate or carbonate precursors and heating for long periods (>10h) at high temperatures (>800°C). Currently, this method has gained popularity for the synthesis of sodium-based oxides such as Na_xCoO_2 [16]. These oxides are subsequently ion-exchanged in hot lithium electrolyte solutions to obtain lithium-substituted oxides exhibiting meta-stable crystal structures.

Pyrolysis - The principle of the pyrolysis synthesis is the thermal decomposition of a stoichiometric salt solution, using organic complexing agents to enhance the solubility and fuel the combustion process. These methods have shown great potential in the preparation of homogeneous multi-component oxides with small particle size. In this project we have used a citrate method for the preparation of LiCoO_2 powders, similar to the one applied by Zhecheva *et al.* [17].

Sol Gel synthesis - The sol-gel process is suitable for powders and coatings [18]. The oxides are highly porous, which is very beneficial for the intercalation capacity: *e.g.* V_2O_5 xerogels can take up 3.3 $\text{Li}/\text{V}_2\text{O}_5$ instead of the usual 1.5 $\text{Li}/\text{V}_2\text{O}_5$, presumably due to the ‘open contact’ with the electrolyte solution. The sol-gel process does not require absolute stoichiometric quantities, as is the case with solid-state reactions. This makes this synthesis suitable for the preparation of transition metal oxides with cationic substitution. $\text{Li}_{1+x}\text{Mn}_{2-y}\text{M}_y\text{O}_4$ systems with $M=\text{Ni}, \text{Fe}$ and $0\leq y\leq 0.5$ have been synthesised successfully by Amine *et al.* [19] using sol-gel. Solid-state processing had produced NiO-phase impurities.

Hydrothermal proton exchange - In its most basic form, the oxides are dissolved in water and kept at temperatures between 100°C and 200°C for a few days [20]. This procedure is economically attractive compared with solid-state synthesis, as it requires low temperatures and can be executed in large industrial autoclaves.

Tarascon *et al.* [21] produced electrochemically active LiCoO_2 and LiNiO_2 by reaction of LiOH and H_xMO_2 phases for two days at 160°C (or even at 100°C) and a pressure of 60 bar. Longer reaction times produce powders with higher surface areas, which exhibit larger irreversible capacities upon cycling (*e.g.* shift $\Delta x_{\text{irr}}=0.07$ to 0.22 with surface increase from 0.3 to $8.2\text{m}^2\cdot\text{g}^{-1}$, respectively). Annealing temperatures around 250°C is sufficient for removing carbonate impurities and hydrolytic species and are necessary for improving the

electrochemical performance. Ball-milling of the hydro-thermally prepared LiCoO_2 powder is reported to be detrimental to the reversible intercalation capacity, as it would increase the polarisation significantly [21].

2.2.2 Thin film deposition

Pulsed Laser Deposition – This deposition method uses a 15ns laser pulse to induce a plasma plume of target material, which is collected on a (optionally heated) substrate in low-pressure atmosphere (<2mbar) [22]. Figure 2.9 shows the general set-up and a picture of the equipment in operation. The principle advantages of the laser ablation method are that the stoichiometry of the films is nominally the same as that of the target, the deposition can be carried out in oxidising environments and the ablated particles have excess energy, which enables epitaxial growth at reduced substrate temperatures [10]. Note that the deposition is only uniform in a circular area of 25mm \varnothing and thus the sample dimensions are limited.

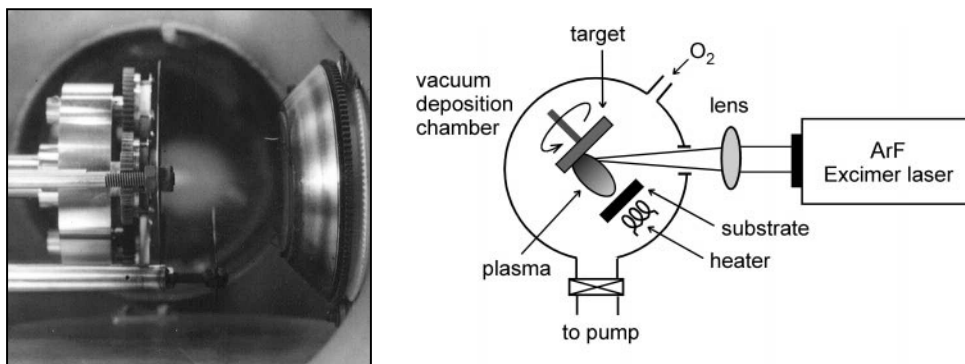


Figure 2.9: A schematic representation of the Pulsed Laser Deposition process. The picture shows the actual plasma plume invoked by the laser pulse.

Iriyama *et al.* [23] have reported the growth of *c*-axis oriented LiCoO_2 films on quartz substrates. With increasing film thickness a more random orientation is observed. Antaya *et al.* [10] have also observed a preferential *c*-axis orientation of their off-axis PLD deposited LiCoO_2 films on stainless steel substrates. Increasing substrate temperatures at constant O_2 partial pressure leads to an increase in grain size and improved cation ordering. The formation of the HT- LiCoO_2 phase is favoured at $p(\text{O}_2) < 2.5\text{mbar}$. Note that the columnar growth structure is directed

towards the plasma source and is here observed at a 45° angle with the substrate surface, due to the off-axis PLD set-up. There is no connection between the alignment of the columnar structure and the preferential orientation of the lattice.

J.D. Perkins *et al.* [24] have grown dense *c*-axis oriented LiCoO_2 and $\text{LiCo}_{0.5}\text{Al}_{0.5}\text{O}_2$ films from a stoichiometric target on SnO_2 -coated glass and fused silica substrates. For both materials the grain size increases substantially with increased substrate temperature in the range $400^\circ\text{-}700^\circ\text{C}$. Films grown at lower substrate temperatures and lower oxygen pressure than 0.2mbar tend to have reduced charge capacity.

RF sputtering - Bates *et al.* [25] have prepared thin-film LiCoO_2 electrodes with RF-sputtering from stoichiometric targets onto alumina and silicon substrates with Pt and Au current collectors (300nm). The applied RF-power ranged from 10 to $53\text{W}\cdot\text{cm}^{-2}$ for deposition rates of 10 to $100 \text{ \AA}\cdot\text{min}^{-1}$. This resulted in a columnar LiCoO_2 film consisting of 10nm nano-crystalline grains. After annealing at 700°C for 30 minutes, the film has cracked into clusters of sub-micrometer grains, which is attributed to shrinkage. Thin films (thickness $<500\text{nm}$) exhibit a (003) texture and with increasing film thickness a mixed (104) and (101) texture prevails, independent of the substrate material and uninfluenced by annealing treatment. Annealing treatment for longer periods of time (4h) does reveal an increase of the degree of (101) preferential orientation at the expense of the (104) orientation.

Here, it is assumed that texturing occurs to minimise the volume strain energy, caused by thermal expansion mismatch with the substrate, as well as the surface energy. Lattice model calculations have shown that the volume-strain energy



Figure 2.10: The white 6" target is engulfed in an Argon gas RF-plasma.

density u decreases in the order: $u(003) \ll u(104) < u(101) < u(110)$. Hence the latter orientations are preferred in case of thicker films, where the surface energy plays a minor role [26]. The fraction of (003) oriented grains is observed to increase with increasing substrate temperature during deposition ($>200^\circ\text{C}$), which is attributed to the increased surface mobility of atoms on the substrate.

Judging from the correlated lithium diffusion plane orientation, a decrease in the intercalation rate is expected for films with an increased fraction of (003) oriented grains. Pulsed charge/discharge experiments show that thicker films (0% (003)) are capable of higher discharge rates than thinner films (100% (003)). However, due to a dominating impedance of the charge-transfer process and electrolyte conductivity, it is not possible to distinguish a difference in diffusion/intercalation characteristics. A significant contribution of the ionic grain-boundary conductivity to the lithium transport process is suspected, as the films with coarser microstructure (large grains due to high substrate deposition temperature (300°C)) show a significant increase in resistance [25].

2.2.3 Optimisation of LiCoO₂ structure

Cation substitution - Jang *et al.* [27] have attempted to increase the structural stability of LiCoO₂ with partial substitution of Co by Al. The initial capacity of the LiCo_{1-x}Al_xO₂ decreased relative to undoped material. Cho *et al.* [28, 29] report coating of LiCoO₂ particles with a layer of SnO₂ and Al₂O₃. After heat treatment at 400°C the formation of a solid solution on the particle surface could be observed. The structural stability is increased significantly through inhibition of the hexagonal to monoclinic phase transformation and subsequently improves the capacity retention of the electrode upon cycling.

High-pressure oxygen treatment is observed to improve electrode intercalation capacity of LiCoO₂, as does the incorporation of a small amount of excess lithium (regardless of the oxygen treatment). Levasseur *et al.* [30] have reported that oxygen defects are generated in a lithium rich Li_xCoO₂ together with the occurrence of divalent Co²⁺. The solid solution limit of excess lithium is found around Li/Co = 1.15. The transformation from rhombohedral to monoclinic at $x=0.5$ does not appear in the material with a Li/Co ratio over 1.10 due to the deviation from the ideal structure. The lack of structural rearrangement is thought to be beneficial for the reversible capacity and the cycle life.

The application of mixed transition metal oxides to optimise the intercalation host is discussed in Chapter 7 of this thesis.

2.2.4 Charge control

A complementary development occurs in the charging circuitry of the portable equipment, which has evolved towards a battery management system [31]. Specific chips are designed to protect the battery against misuse by monitoring and controlling the charge and discharge cycle. For such a “fuel gauge” to give an accurate indication of the available charge, profound knowledge of the battery behaviour and deterioration characteristics is required. This information is currently being applied in “Smart Battery IC’s”.

Besides the problem of monitoring and controlling charge-discharge cycles for Li-ion batteries, there is the issue of voltage regulation and power consumption. The cell voltage depends on the state of charge and must be stepped up or down to the constant operating voltage of the device with a dc-dc conversion circuit, where adjusting the input pulse width controls the energy stored in a resonant LC circuit. Hence, in this perspective, the power of the lithium battery is of more importance than its cell potential. [32]

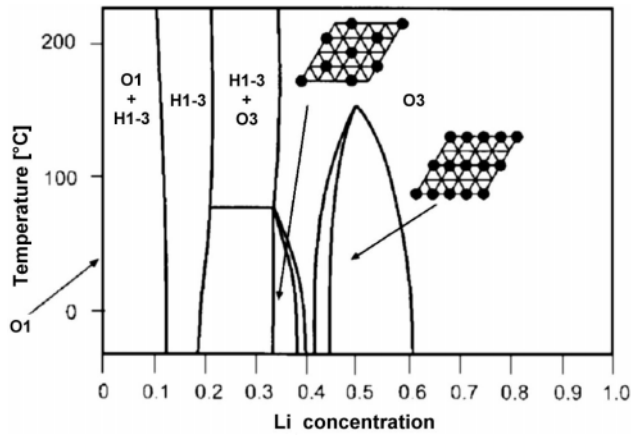


Figure 2.11: The calculated layered Li_xCoO_2 phase diagram. The insets show the predicted in-plane Li ordering [33].

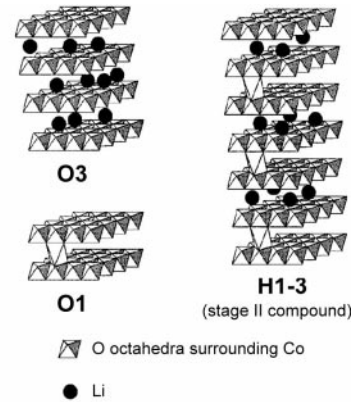


Figure 2.12: 3D drawing of the structures denoted in Figure 2.10 [33].

2.2.5 Computer simulations

Phase stability - First principle calculations can be of considerable value when studying novel or poorly characterised intercalation systems, as the phase diagram can be predicted without requiring experimental input besides some knowledge (or guess) of the host lattice. To determine the free energy of a host, first the energy is calculated of a set of ordered periodic structures, by solving the many body Schrödinger equation for the solid. Once a set of quantum mechanical energies has been resolved, they can be implemented in a least squares fit to obtain the effective cluster interaction parameters of a cluster expansion. The phase diagram illustrated in Figure 2.11 is obtained using this calculation procedure on the Li_xCoO_2 layered host structures shown in Figure 2.12.

The O3 structure is calculated to be the most stable phase from intermediate to high lithium concentration, with lithium ordering occurring at $x=0.33$ and $x=0.5$. One major disagreement is that the two-phase region between $x=0.75$ and $x=0.95$ is not predicted. This is due to the strong electron-electron correlation, which is difficult to implement in the first principles approximation.

Electronic transitions - Phase Transformations involving changes of the host can be caused by changes in the electronic properties of the host with Li concentration or temperature. The Jahn-Teller distortion, one of the best-known electronic transitions, can be seen as a special case of a band filling transition. The metal-insulator transition is another electronic phenomenon, which has been proposed to explain the large first order phase transition at high lithium concentration in Li_xCoO_2 .

Li_xCoO_2 is a semiconductor for $x>0.95$ and is metallic for $x<0.75$. Superimposed on this metal-insulator transition is a large two-phase region between a lithium concentration of $x=0.75$ to $x=0.95$. In the metallic phase, the holes of the valence bands are localised in space. Localised holes contribute to the free energy of the solid and to additional configurational entropy associated with the different ways of distributing the holes throughout the crystal. The entropy from delocalised electrons in narrow valence bands on the other hand, is an order of magnitude smaller.

The solid curve in Figure 2.13 is characteristic of complete solid solution of lithium in the intercalation host, considering only contributions to the free energy from the configurational degrees of freedom of the lithium ions and vacancies. When the intercalation compound undergoes a metal-insulator transition, (solid vertical line in Fig. 2.13) the additional configurational entropy arising from the localised holes in the insulating phase, lowers its free energy as is schematically illustrated by the dashed curve. If the free energy contributions of the localised holes on the insulating side are large enough to break the convexity of the initial free energy curve (solid line), a two phase region would arise with the phase boundaries determined by the common tangent [33].

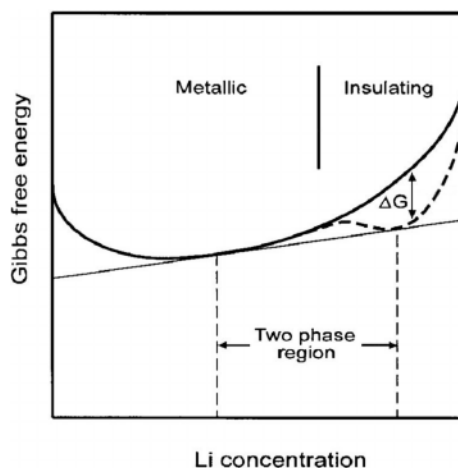


Figure 2.13: Diagram of the Gibbs free energy of a lithium-host solid solution as a function of lithium concentration (solid line) with the influence of a metal-insulator transition (dotted line) [33].

2.3 Electrolyte phase

The electrolyte separates both electrodes to prevent direct electrical contact, but allows mutual ionic exchange. The electrolyte phase can consist of a liquid salt solution, polymer gel or a glassy solid. Solid electrolytes have several advantages over liquid electrolytes, no accumulation of decomposition products on the interface, broad operating temperature range, excellent charge-discharge cyclic properties and low self-discharge. The liquid electrolyte, however, is more easily applied, shows a self-sustaining interface contact and exhibits higher conductivities.

Table 2.1: Physical constants of organic solvents [35].

| Solvent | Dielectric Constant | Density [g·cm ⁻³] | MP [°C] | BP [°C] | Viscosity [cP] |
|--------------------------|---------------------|-------------------------------|---------|---------|----------------|
| Ethylene Carbonate (EC) | 89.6 (40°C) | 1.3218 (39°C) | 39-40 | 248 | 1.85 (40°C) |
| Propylene Carbonate (PC) | 64.4 | 1.19 | 18.55 | 241 | 2.53 |
| Diethyl Carbonate (DEC) | 2.82 | 0.9693 | -43 | 127 | 0.748 |
| Dimethyl Carbonate (DMC) | 3.12 | - | 3 | 90 | 0.585 |

2.3.1 Liquid electrolyte

Table 2.1 shows the physical properties of common organic solvents used in non-aqueous electrolytes. PC is not used in lithium ion cells, as it causes exfoliation of the carbon-based electrode [34]. Ratnakumar *et al.* [35] investigated the solvent mixtures properties in intercalation cells for the binary mixtures of EC + DEC and EC + DMC and the ternary, equiportion mixture EC + DEC + DMC with 1M LiPF₆. At ambient temperatures the ionic electrolyte conductivity is highest for the EC + DEC mixture, as are the self-discharge and the irreversible capacity. The DMC-based electrolytes exhibit low irreversible capacity, capacity fade and self-discharge, due to the protective nature of the interfacial film formed on the carbon electrode. The properties of the ternary mixture excel at low temperatures (<0°C).

Table 2.2: Electrolyte conductivity of the carbonate-based solutions (1M at 25°C) [31].

| Electrolyte salt (1.0 M) | Solvent (1:1 by volume) conductivity ×10 ⁻³ [S.cm ⁻¹] | | |
|-----------------------------------|---|----------|----------|
| | EC + DMC | EC + DEC | PC + DMC |
| LiPF ₆ | 11.2 | 7.8 | 10.0 |
| LiClO ₄ | 10.1 | 6.4 | 6.8 |
| LiCF ₃ SO ₃ | 3.1 | 2.1 | 2.2 |

2.3.2 Solid electrolytes

Ion conducting glasses are generally made by conventional melt quenching and consist of three components: a network former, a network modifier and a doping salt. The absence of structural constraints allows easy modification of the relative contents to optimize electrical and electrochemical properties. Based on this theory, several solid electrolytes have been studied: $\text{Li}_2\text{S-P}_2\text{S}_5\text{-LiI}$ [37], $\text{Li}_2\text{S-B}_2\text{S}_3\text{-LiI}$ [38], $\text{LiS}_2\text{-SiS}_2\text{-LiI}$ [39], $\text{Li}_2\text{S-SiS}_2\text{-Li}_3\text{PO}_4$ [40, 41, 42, 43, 44], $\text{Li}_2\text{S-SiS}_2\text{-P}_2\text{S}_5$ [45], $\text{Li}_2\text{O-B}_2\text{O}_3\text{-LiI}$ [46], $\text{Li}_2\text{O-P}_2\text{O}_5\text{-Li}_2\text{SO}_4$ [47, 48], $\text{Li}_2\text{O-Al}_2\text{O}_3\text{-B}_2\text{O}_3$ [49], $\text{Li}_2\text{O-Al}_2\text{O}_3\text{-SiO}_2$ [50], $\text{Li}_2\text{O-SiO}_2\text{-B}_2\text{O}_3$ [51], $\text{Li}_2\text{O-Al}_2\text{O}_3\text{-TiO}_2\text{-P}_2\text{O}_5$ [52], $x\text{Li}_2\text{O-yP}_2\text{O}_5\text{-zPON}$ [53, 54]. The solid electrolytes based on LiS_2 show high ionic conductivity, but are unstable in air, while the Li_2O based electrolytes show high stability, but low conductivity. However, both materials decompose in direct contact with metallic lithium.

LiPON - The lithium phosphorous oxynitride (LiPON) developed by Bates *et al.* [53] is a solid electrolyte that is easy to handle in air, stable in contact with metallic lithium and has already been successfully incorporated in microbatteries. The conductivity is reported to be $2.3 \pm 0.7 \cdot 10^{-6} \text{S.cm}^{-1}$ with an activation energy of $0.55 \pm 0.22 \text{eV}$. The stability window is claimed to be 5.5V when sandwiched between Pt current collectors and 3.6V in contact with one metallic lithium electrode [54]. The nitrogen is incorporated into the amorphous structure of Li_3PO_4 during RF-sputtering in nitrogen gas atmosphere (2.0mbar) and contributes to the ionic conductivity. Consequently, the conductivity is improved by using low RF-power and a longer, inversely related, sputtering time for the thin-film deposition [55].

Choi *et al.* [56] have studied the composition of the LiPON_y film as a function of the RF-sputtering conditions and showed that the nitrogen is actually incorporated through reactive sputtering and not by the poisoning effect.

2.4 References

1. M.S. Whittingham, *Science*, **192** 1126 (1976).
2. A.K. Padhi, K.S. Nanjundaswamy, C. Masquelier, S. Okada, J.B. Goodenough, *J. Electrochem. Soc.*, **144**(5) 1609:13 (1997).
3. Y. Koyama, I. Tanaka, H. Adachi, *J. Electrochem. Soc.*, **147** (10) 3633-36 (2000).
4. L.A. Montoro, M. Abbate, J.M. Rosolen, *Electrochem. Solid State Letters*, **3** 410 (2000).
5. P.W. Atkins, "Physical Chemistry", 5th ed., Oxford University Press (1995).
6. M.G.S.R Thomas, P.G. Bruce, J.B. Goodenough, *J. Electrochem. Soc.*, **132** 1521 (1985).
7. G.G. Amatucci, J.M. Tarascon, L.C. Klein, *Solid State Ionics*, **83** 167-173 (1996).
8. S. Levasseur, M. Ménétrier, E. Suard and C. Delmas, *Solid State Ionics*, **128** [1-4] 11 (2000).
9. E. Rossen, J.N. Reimers, J.R. Dahn, *Solid State Ionics*, **62** 53-60 (1993).
10. M. Antaya, K. Cearns, J.S. Preston, J.N. Reimers, J.R. Dahn, *J. Appl. Phys.* **76** (5) 2799-2806 (1994).
11. J.N. Reimers, J.R. Dahn, U. von Sacken, *J. Electrochem. Soc.*, **140** [10] 2752-2754 (1993).
12. B. Ammundsen, J. Paulsen, *Adv. Mat.*, **13** [12-13] 943 (2001).
13. M.S. Whittingham, *Prog. Solid State Chem.*, **12** (1978) 41.
14. R. Chen, M.S. Whittingham, *J. Electrochem. Soc.*, **144** L64 (1997).
15. P.G. Bruce, *Chem. Comm.*, 1817 (1997).
16. D. Carlier *et al.*, *Solid State Ionics*, **144** 263-76 (2001).
17. E. Zhecheva, *et al.*, *Chem. Mater.*, **8** 1429-40 (1996).
18. I. Serebrennikova, V.I. Birss, *J. Electrochem. Soc.*, **144**(2) 566:572 (1997).
19. K. Amine, H. Tukamoto, H. Yasuda, Y. Fujita, *J. Electrochem. Soc.*, **143**(5) 1607:13 (1996).
20. M.S. Whittingham, R. Chen, T. Chirayil, P. Zavalij, *Solid State Ionics*, **94** 227-38 (1997).
21. G.C. Amatucci, J.M. Tarascon, D. Larcher, L.C. Klein, *Solid State Ionics*, **84** 169:80 (1996).
22. J.F.M. Cillessen, *Pulsed Laser Deposition of Oxidic Films*, JÉMÉ, Eindhoven, (1996).
23. Y. Iriyama, M. Inaba, T. Abe, Z. Ogumi, *J. Power Sources*, **94** 175-182 (2001).
24. J.D. Perkins, C.S. Bahn, J.M. McGraw, P.A. Parilla, D.S. Ginley, *J. Electrochem. Soc.*, **148**, A1302-12 (2001).
25. J.B. Bates, N.J. Dudney, B.J. Neudecker, F.X. Hart, H.P. Jun, S.A. Hackney, *J. Electrochem. Soc.*, **147** (1) 59-70 (2000).
26. F.X. Hart, J.B. Bates, *J. Appl. Phys.*, **83**, 7560 (1998)
27. Y.I. Jang, B. Huang, H. Wang, D.R. Sadoway, G. Ceder, Y.-M. Chiang, H. Liu, H. Tanamura, *J. Electrochem. Soc.*, **146**, 862 (1999).
28. J. Cho, Y.J. Kim, B. Park, *J. of Electrochem. Soc.*, **148** (10) A1110-A1115 (2001).
29. J. Cho, C.-S. Kim, S.-I. Yoo, *Electrochem. Solid-State Lett.*, **3**, 362 (2000).
30. N. Imanishi, M. Fujii, A. Hirano, Y. Takeda, *J. of Power Sources*, **97-98**, 287-89 (2001).
31. H.J. Bergveld, "Battery Management Systems; Design by modelling", 156, Thesis University of Twente, the Netherlands (2001).
32. S. Ohr, *Engineering times*, May edition (2001).
33. G.Ceder, A. Van der Ven, *Electrochimica Acta*, **45** 131-150 (1999).
34. D. Aurbach, "Nonaqueous Electrochemistry", Marcel Dekker Inc., New York (1999).
35. B.V. Ratnakumar, M.C. Smart, S. Surampudi, *J. Power Sources*, **97-98**, 137-39 (2001).
36. M. Morita, O. Yamada, M. Ishikawa, Y. Matsuda, *J. Appl. Electrochem.*, **28** 209:13 (1998).
37. R. Mercier, J.P. Malugani, B. Fahys, A. Saida, *Solid State Letters*, **5** 663 (1981).
38. H. Wada, M. Menetrier, A. Levasseur, P. Hagenmuller, *Mater. Res. Bull.*, **18**, 189 (1983).
39. J.H. Kennedy, Y. Yang, *J. Electrochem. Soc.*, **133**, 2437 (1986).
40. S. Kondo, K. Takada, Y. Yamamoto, *Solid State Ionics*, **53**, 1183 (1992).
41. N. Aotani, K. Iwamoto, K. Tanada, S. Kondo, *Solid State Ionics*, **68**, 35 (1994).
42. K. Tanada, N. Aotani, S. Kondo, *J. Power Sources*, **43-44**, 135 (1993).

43. N. Aotani, K. Iwamoto, K. Tanada, S. Kondo, *Solid State Ionics*, **68**, 35 (1994).
44. K. Tanada, N. Aotani, K. Iwamoto, S. Kondo, *Solid State Ionics*, **79**, 284 (1995).
45. R. Creus, J. Sarradin, M. Ribes, *Solid State Ionics*, **53-56**, 641 (1992).
46. A. Levasseur, J.C. Brethous, J.M. Reau, P. Hagenmuller, M. Couzi, *Solid State Ionics*, **1**, 177 (1980).
47. M. Ganguli, M. Harish Bhat, K.J. Rao, *Solid State Ionics*, **122**, 23 (1999).
48. M. Ganguli and K.J. Rao, *J. Non-Cryst. Solids*, **243**, 251 (1999).
49. M.D. Ingram, M.A. Machenzie, W. Muller, M. Torge, *Solid State Ionics*, **28-30**, 677 (1988).
50. K. Jackowska, A.R. West, *J. Mater. Sci.*, **18** 2380 (1983).
51. M. Tasumisago, K. Yoneda, N. Machida, T. Minami, *J. Non-Cryst. Solids*, **95-96**, 857 (1987).
52. I. Abrahams, E. Hadzifejzovic, *Solid State Ionics*, **134**, 249, (2000).
53. J.B. Bates, D. Lubben, N.J. Dudney, F.X. Hart, *J. Electrochem. Soc.*, **142**, L149 (1995).
54. J.B. Bates, G.R. Gruzalski, N.J. Dudney, C.F. Luck, X. Yu, *Solid State Ionics*, **70/71**, 619 (1994).
55. B.J. Neudecker, N.J. Dudney, J.B. Bates, *J. Electrochem. Soc.*, **147** (2) 517-23 (2000).
56. C.H. Choi, W.I. Cho, B.W. Cho, H.S. Kim, Y.S. Yoon, Y.S. Tak, *Electrochem. Solid State Letters*, **5** [1] A14 (2002).

3 Structural characterisation of submicron films

Sub-micron LiCoO₂ films were prepared with Pulsed Laser Deposition and RF sputtering using stoichiometric targets. The influences of both substrate material and annealing procedure on the polycrystalline microstructure of the LiCoO₂ films were investigated. XRD analysis revealed strong preferential orientation: annealed films deposited with Pulsed Laser Deposition had their (00 ℓ) planes parallel to the surface, while RF sputtered films had their (110) planes in this orientation. The RF-film also developed the (003) reflection typical of PLD-films, but only after prolonged annealing at 600°C. The degree of preferential orientation is influenced significantly by the annealing procedure and only little by the substrate material and the thickness of the deposited film. Pulsed Laser Deposition on an RF-sputtered seed layer revealed the PLD-film reflections. Extinction of the otherwise dominating (003) reflection indicated a random cationic distribution in LiCoO₂ with NaCl-type structure.

Published in: *J. Electrochem. Soc.*, **148** No.4 A311 (2000).

3.1 Introduction

The lithium intercalation ability of LiCoO_2 was discovered twenty years ago by J.B. Goodenough and has been exploited by Sony with the introduction of their rechargeable C/ LiCoO_2 battery in 1991. Presently, this technology finds large-scale commercial application as a power source for numerous hand-held devices. Extensive research is conducted to explore alternative materials, which are more cost effective and less toxic [1]. Up to now, lithium cobalt oxide based electrodes exhibit superior properties in terms of cycle stability and energy density, a favourable combination for a reliable power source [2, 3].

The common composite powder electrodes are unsuitable for microbattery application due to their porosity and the necessity of additives. The indistinct characteristics of powder-based electrodes also make modelling of the electrochemical intercalation behaviour difficult. The present paper describes preparation and properties of dense, submicron films of polycrystalline LiCoO_2 on a silicon wafer with Pulsed Laser Deposition and RF-sputtering. The well-defined composition, microstructure and dimensions of the deposited layers make these samples suitable for fundamental electrochemical studies of the lithium intercalation process. Eventually, these films could find application as positive electrodes in microbattery stacks. In this Chapter we provide a structural characterisation of the LiCoO_2 films in all stages of preparation.

3.2 Experimental

Thin film deposition - Submicron LiCoO_2 films were produced with Pulsed Laser Deposition and RF-sputtering using identical LiCoO_2 targets prepared by solid-state reaction. The composition was chemically analysed and proved to be stoichiometric.

In Pulsed Laser Deposition a 193nm ArF excimer laser was operated at 5Hz repetition rate and focussed to a beam intensity of $2\text{J}\cdot\text{cm}^{-2}$. Ablation was performed with a counter-rotating target and substrate, located at 6cm distance from each other. A background pressure of 0.2mbar pO_2 was maintained. At these

conditions the deposition rate was approximately $20\text{\AA}\cdot\text{min}^{-1}$. The substrate holder could be heated to temperatures as high as 700°C . The substrate temperature during deposition was 300°C . *In-situ* annealing was performed by increasing the temperature with $5^\circ\text{C}\cdot\text{min}^{-1}$ to 600°C and maintaining the level for 30min. After cooling to room temperature the samples were exposed to the ambient.

RF sputtering conditions were: substrate temperature 300°C , argon-oxygen background pressure of 0.1mbar in 3:1 ratio, RF power 50W and target to substrate distance 6 cm. At these conditions the growth rate of the oxide layer was of the order of $5\text{\AA}\cdot\text{min}^{-1}$. Annealing treatment of all RF sputtered samples was performed *ex-situ*. Samples were heated with $2^\circ\text{C}\cdot\text{min}^{-1}$ to 400° or 600°C in stagnant air or in a constant gas flow containing 90% O_2 / 10% N_2 with a flow of $60\text{ml}\cdot\text{min}^{-1}$ STP. Typical annealing times were 30 or 180 minutes and are referred to as short and prolonged annealing treatment, respectively.

Silicon wafers (6-inch diam., (100) orientation) served as substrate material for both deposition techniques. The polished surface was ion-implanted with antimony to obtain n-type electronic conductivity. The wafer was then laser cut into 15mm diameter discs. The backside and rim of these discs were covered with $0.15\mu\text{m}$ aluminium using RF sputtering. This metallic film served as electrical backside contact for electrochemical measurements, connecting the probe with the conducting silicon. In several cases an additional aluminium film ($0.15\mu\text{m}$) was sputtered as current collector together with an adhesion layer of 50\AA titanium prior to deposition of the LiCoO_2 film. Note that this substrate stack is subjected to the same temperature program as the LiCoO_2 film. The use of aluminium (as current collector) limits the upper annealing temperature to its melting point of 660.4°C . Even at temperatures below this value one must be aware of possible interdiffusion of soluble species in the individual stack layers. The time- and temperature window of the thin film annealing process is therefore limited.

Structural analysis - The crystal structure of the submicron film was analysed with X-ray diffraction using CuK_α at room temperature with a Philips PW 1800 diffractometer fitted with a spinning sample holder and automatic divergence slit. Visualisation of the film surface morphology was performed using a JEOL JSM 5800 Scanning Electron Microscope. A Philips CM30ST operated at 300kV, accommodated TEM analysis on cross-sections of RF-film prepared with Focussed Ion Beam thinning.

3.3 Results and Discussion

3.3.1 Structural characterisation

Generally, the LiCoO_2 host intercalation matrix is regarded to be derived from the NaCl structure. The structure is rhombohedral (space group $R\bar{3}m$) with atoms in the following positions: cobalt atoms in 3a sites (0, 0, 0), lithium atoms in 3b (0, 0, $\frac{1}{2}$), and oxygen in 6c sites $\pm(0, 0, z)$ with $z \cong 0.25$. Cobalt and lithium alternately occupy octahedral sites between adjacent close-packed planes of oxygen. The hexagonal cross section (110) is shown in Figure 3.1. This ordered structure is known as the High-Temperature (HT) phase of LiCoO_2 , since it develops during synthesis or annealing treatment at temperatures above 600°C . Once formed it remains stable at room temperature. The so-called Low-Temperature (LT) modification is produced with low temperature synthesis methods and is slightly disordered: it comprises 6% of the cobalt ions in lithium sites. LT- LiCoO_2 transforms into HT- LiCoO_2 upon annealing at temperatures around 600°C [4, 5].

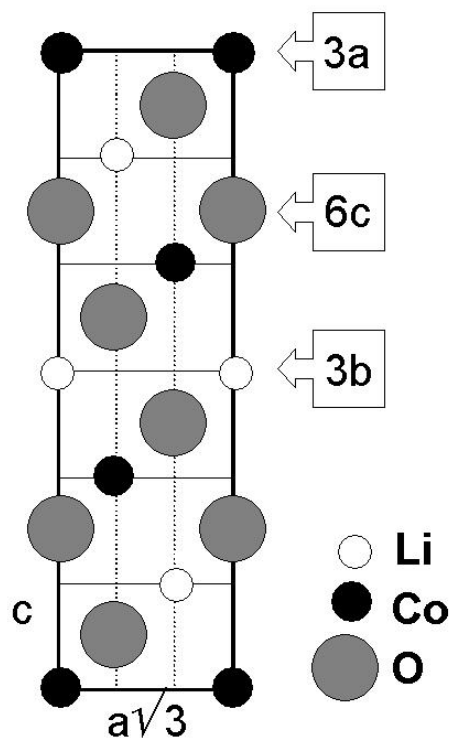


Figure 3.1: Cross-section of the LiCoO_2 unit cell along the hexagonal (110) plane. This representation visualises the octahedral co-ordination of the cobalt (3a sites) and the lithium (3b sites) cations by oxygen (6c sites). Note the threefold rotation symmetry of the axes in the c -direction.

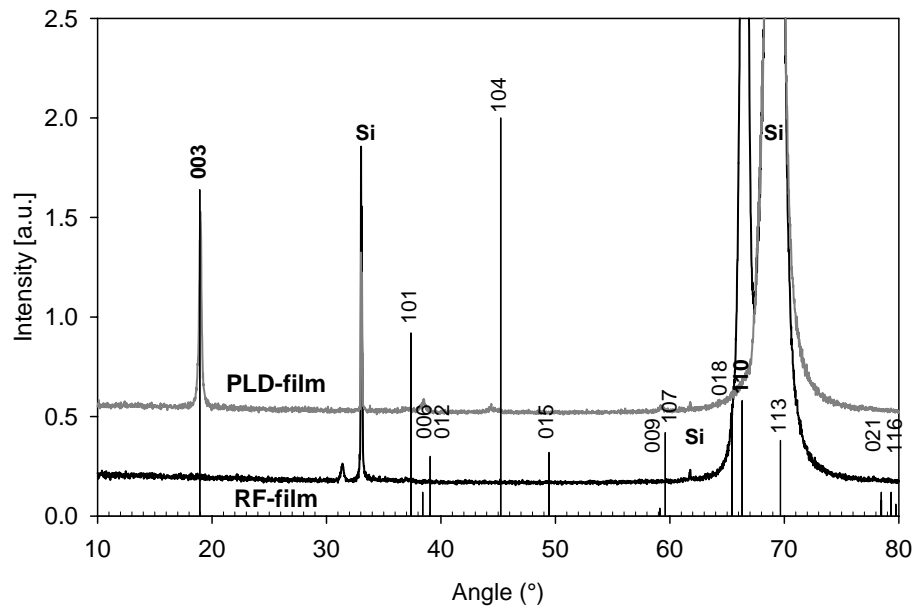


Figure 3.2: XRD patterns of typical submicron LiCoO_2 films deposited on silicon substrates with RF sputtering and Pulsed Laser Deposition and annealed at 600°C for 30 minutes.

In Figure 3.2 the reference X-ray diffraction pattern of the HT- LiCoO_2 powder is displayed. The bar labels indicate the associated lattice plane reflections. In the same graph two typical diffraction patterns are plotted of annealed LiCoO_2 films deposited with RF sputtering and PLD, respectively. The 2θ values of all reflections observed match those in the reference pattern to an accuracy of 0.04 degrees. The two strong diffraction maxima at $2\theta = 33^\circ$ and 69° can be ascribed to the single-crystal silicon substrate and have been indicated as such. The peak located at 31.3° in the RF-film pattern is probably Co_3O_4 (220).

Not all diffraction peaks, characteristic of LiCoO_2 , are detected and also different reflections are observed for RF-films and PLD-films. Due to the scanning geometry of the XRD equipment only the diffraction of the lattice planes oriented parallel to the substrate surface is observed (the detection angle is kept equal to the X-ray angle of incidence). A random unit cell orientation, as is common for powders, will result in a typical XRD powder pattern. The absence of specific diffraction intensities revealed that both samples exhibited strong preferential

orientation. In the case of the RF-film however, the (110) lattice plane reflection showed the highest intensity, while in case of the PLD-film the (003) reflection was the major diffraction peak. Virtually no other LiCoO_2 diffraction maxima were detected. This indicates that the RF-films have their (110) planes parallel to the substrate surface (c-axis of the unit cell in plane of film). This orientation is perpendicular to that of the PLD-films, which have their (00 ℓ) planes parallel to the substrate surface (c-axis of the unit cell normal to film surface).

The alignment of the unit cell towards the substrate is visualised in Figure 3.3 for the PLD-film and RF-film, respectively. The reflecting lattice planes are indicated. Changing deposition conditions and film thickness only influenced the degree of crystal orientation. This is discussed in the following paragraphs.

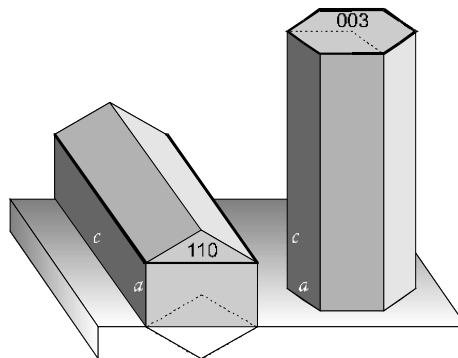


Figure 3.3: Schematic drawing showing the LiCoO_2 unit cell orientation when deposited with RF-sputtering (left) and with PLD (right).

3.3.2 Influence of the annealing temperature

Figure 3.4 shows the XRD patterns of $0.5\mu\text{m}$ RF-films recorded after deposition and after annealing treatment at 400° and 600°C for 3h (prolonged annealing). Small crystallites have already been formed during deposition, as revealed by the broad, low intensity reflections at 2θ angles 36.5° and 65° . The XRD pattern of the as-deposited PLD-film (not shown here) exhibits similar broad diffraction peaks, but located around the positions of the (00 ℓ) plane diffraction. Additional broad reflections appear with annealing treatment of the RF-film at 400°C for 3h. These are ascribed to (00 ℓ) and (104) planes. Strong peak sharpening is observed after annealing at 600°C for 3h. The (110) peak still retains the highest intensity, followed by the (003) peak. A small amount of Co_3O_4 is evident from the Co_3O_4 (220) peak at 31.3° and the (400) peak at 44.8° , which appears as a shoulder on the LiCoO_2 (104) peak.

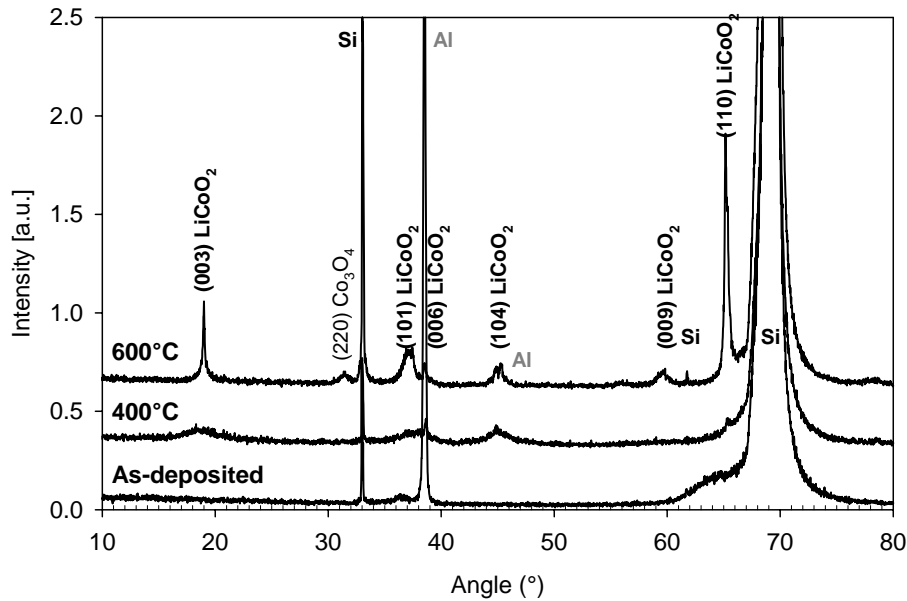


Figure 3.4: XRD patterns of three $0.5\mu\text{m}$ RF-films at different stages of preparation: As-deposited at 300°C and after annealing for 3h in air at 400°C and 600°C , respectively (patterns vertically displaced for clarity).

As stated in Chapter two, in case of a randomly oriented powder sample the question of whether the HT-LiCoO₂ intercalation phase is present, can be answered by the distinct separation of the (110) and (018) plane diffraction [6]. The difference in peak location is determined by the c/a ratio of the unit cell. Cubic LT-LiCoO₂ exhibits a c/a ratio of $2\sqrt{6} = 4.899$ and exhibits overlapping (110) and (018) peaks (classified as the (440) reflection in Fd3m symmetry). The layered hexagonal structure of HT-LiCoO₂ is reported to have a c/a ratio of $(14.05/2.815) = 4.991$ [7], which results in a peak separation of 1 degree. The preferential RF-films show only the (110) peak, while the annealed PLD-films show neither the (110) nor the (018) diffraction. It is difficult to discern, whether peak splitting has not yet occurred or the (018) diffraction is out of the detection plane due to preferred orientation. Annealing at 900°C does not generate the expected separation. However, the RF-films annealed at 600°C for 3h show both the (003) and the (110) diffraction peaks and allows the c/a ratio to be deduced. The value is calculated to be 4.894, which suggests cubic symmetry and that peak splitting is not to be expected.

A X-ray texture analysis was performed to visualise the 3D orientation of the (110) planes on a $0.75\mu\text{m}$ RF film annealed only a short time at 600°C . The pole plot, shown in Figure 3.5, indicates a fibre texture with a fixed (110) plane alignment. The major intensity is recorded at $\varphi=0^\circ$ (sample tilting angle) and corresponds with the original diffraction peak observed in the XRD pattern (Figure 3.2). The omega scan of this peak reveals a FWHM (=Full Width Half Maximum) value of 6.25° , indicating a sharp orientation distribution. Also at $\varphi=60^\circ$ diffraction intensity is recorded at all rotation angles originating from the other two orientations of the (110) plane within the hexagonal unit cell. Likewise, the (104) planes show sharp diffraction intensity at $\varphi=45^\circ$. Even though the (003) peak diffraction, located at $\varphi=90^\circ$, is technically undetectable, some intensity increase is observed at $\varphi=85^\circ$.

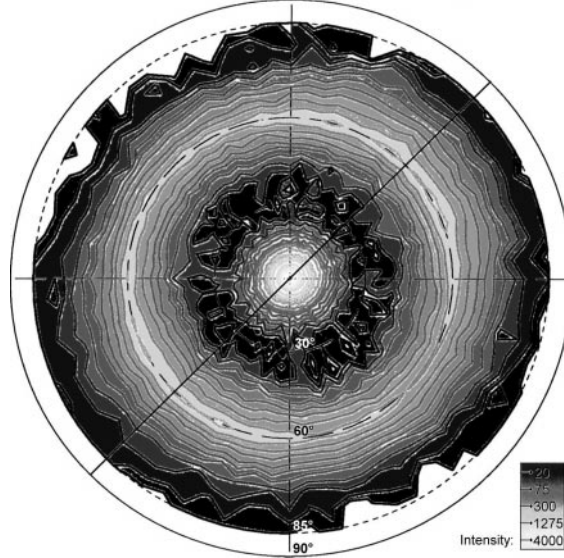


Figure 3.5: XRD texture analysis of the (110) diffraction of a $0.75\mu\text{m}$ RF-film (annealed at 600°C , 30min) visualised in a Wulff projection. Light shades of grey represent high intensity.

The required (018) reflection of the RF-film is expected at $\varphi=60^\circ$ and in this particular crystal alignment the peak is indeed detected at $2\theta=65.31^\circ$, well separated from the (110) reflection at $2\theta=66.33^\circ$. The (018) intensity is slightly less than that of the (110) planes ($\text{FWHM}_{(018)/(110)}$ ratio=0.80). According to the recorded 2θ values of the (018) and (110) diffraction, the c/a ratio equals $(14.085/2.816)=5.002$, which is in agreement with the c/a ratio of $(14.079/2.818)=4.996$ calculated from the (110) and (104) diffraction angles measured during preceding texture analysis ($2\theta_{(104)}=45.18^\circ$, recorded at $\varphi=45^\circ$). This c/a ratio is too large for an ideal cubic-close-packed lattice and coincides

with literature values of HT-LiCoO₂. Hence, this confirms that in these thin films full cationic ordering and subsequent formation of the HT-LiCoO₂ phase is achieved during short annealing treatment at 600°C.

The oxygen background pressure during film deposition has little influence on the post-anneal XRD pattern. Tested pO₂ values range between 1·10⁻⁷ - 5·10⁻⁷ mbar for RF sputtering and between 2·10⁻³ - 2·10⁻¹ mbar for PLD. Some formation of Co₃O₄ occurs during annealing at 600°C. At elevated temperatures volatile Li₂O is released and as a result LiCoO₂ is transformed. The process appears to be accelerated by increased oxygen gas flow during annealing treatment. The Co₃O₄ diffraction intensity increases at the expense of LiCoO₂ peak intensity. Hence, annealing times should be kept as short as possible to prevent loss of active material. In other studies surplus Li₂O is often incorporated in the target material to compensate this high temperature degradation [8].

3.3.3 Influence of annealing time

The annealing time has a significant influence on the extent of the crystallisation and the degree of preferential orientation of the LiCoO₂ film. The RF-films annealed at 600°C for only 30 minutes, show virtually only (110) diffraction (Figure 3.2). The intensity and width of the reflections indicate that the annealing time is sufficient to achieve complete crystallisation. Samples, which have been annealed for extended periods of time, develop a (003) diffraction peak. Simultaneously, the (101) and the (104) diffraction intensity increases slightly, while the initial (110) peak intensity decreases. Intensification of the (003) peak is also reported by Wang *et al.* [8] for LiCoO₂ thin films after annealing in air at 700°C for 2h.

Short exposure to the high annealing temperature appears critical to maintain the preferential orientation of the polycrystalline film. In order to reduce the annealing time to a minimum, Rapid Thermal Annealing (RTA) experiments have been conducted in nitrogen ambient as described by van de Leest *et al.* [9]. Two 0.25µm RF-films have been annealed at 550° and 600°C for only one minute (ramp 10°C·s⁻¹). At 550°C the LiCoO₂ film remains intact, while at 600°C the film is severely cracked. The XRD patterns of both RF-films show no (00ℓ) diffraction peaks intensity after this short annealing treatment. However, the

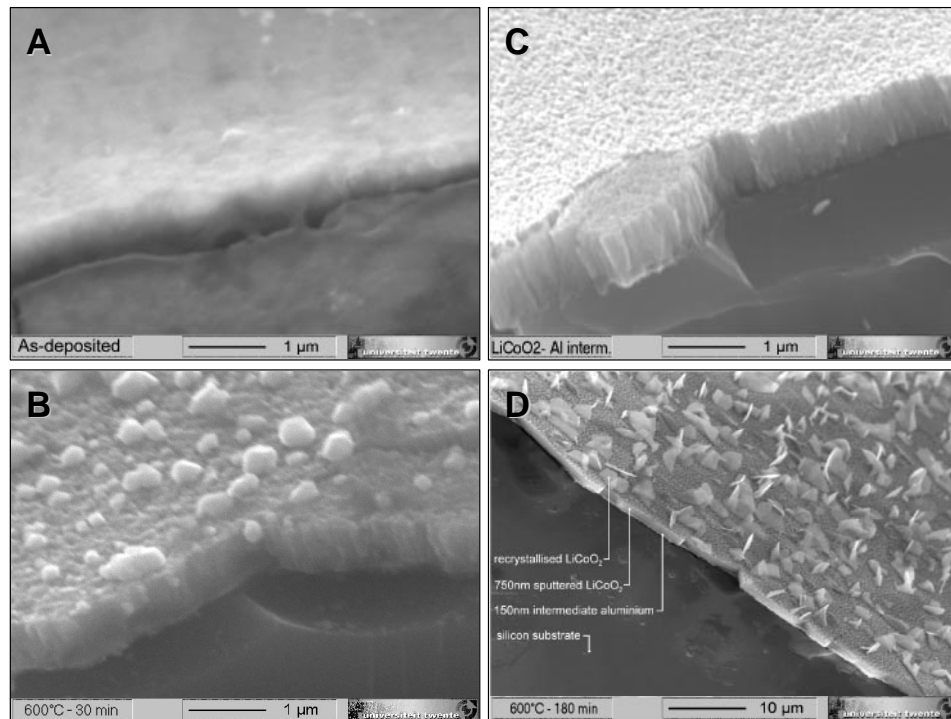


Figure 3.6: SEM micrographs showing the cross-sections of RF films (60° tilt): $0.5\mu\text{m LiCoO}_2$ on $0.15\mu\text{m Al}$, as-deposited with RF sputtering (A) and after annealing at 600°C for 30min (B); $0.75\mu\text{m LiCoO}_2$ on $0.15\mu\text{m Al}$ after annealing at 600°C in air for 30min (C) and 3h, respectively (D).

initial (110) preferential orientation is destroyed and large amounts of Co_3O_4 are observed for the sample annealed at 600°C . Under the present conditions, RTA is no suitable alternative for the standard annealing procedure at 600°C for 30min.

The cross-section of an as-deposited RF-film is shown in Figure 3.6A. The morphology appears amorphous. A columnar polycrystalline structure develops with annealing treatment at 600°C . This is visible on the micrographs of the RF-film cross section in Figure 3.6B and 3.6C, which also reveals the silicon substrate and aluminium current collector. Bates *et al.* [9] have recently observed similar LiCoO_2 film morphologies, but with a preferential (101) lattice orientation. No structural differences were observed between the RF-films of 0.25, 0.50 and $0.75\mu\text{m}$ thickness.

Thin, hexagonal crystals are observed on the surface of the RF-films subjected to prolonged annealing treatment (Figure 3.6D). Visualisation using the Backscattered Electron mode of the SEM shows very low contrast between the bulk and the surface crystallites, which strongly suggests identical chemical composition. Apparently, the exposure to high temperatures for a prolonged time leads to the outgrowth of crystals from the LiCoO_2 film. In contrast to the bulk, the latter crystals exhibit a more or less random orientation. This observation coincides with the previously discussed intensity increase of the (003) lattice plane diffraction. Therefore, the first c/a ratio calculation based on this $2\theta_{(003)}$ value is unreliable, as this peak is not related to the lattice structure of the film itself.

The TEM cross-section of the $0.75\mu\text{m}$ LiCoO_2 RF-film in Figure 3.7A shows the columnar structure in detail. The dark area at the bottom is the silicon substrate and is covered with the intermediate aluminium layer and adhesive Ti coating. In Figure 3.7B the corresponding electron diffraction pattern of the LiCoO_2 film is shown, which is assumed to be a statistically correct representation of the film

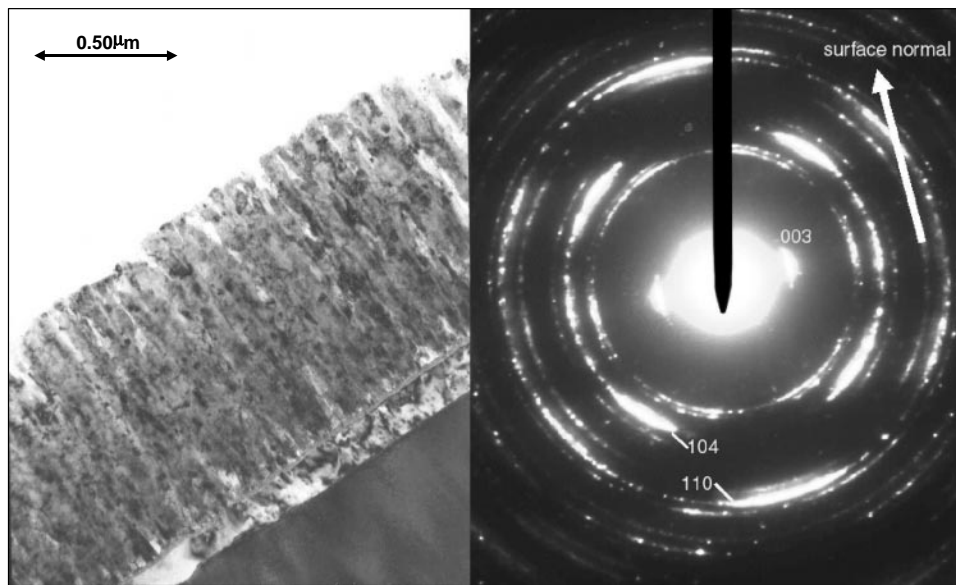


Figure 3.7: TEM photograph of the cross section of an RF-film annealed at 600°C for 30min. Visible are the silicon substrate, the intermediate aluminium current collector ($0.15\mu\text{m}$), Ti adhesive layer and the LiCoO_2 film ($0.75\mu\text{m}$). The electron diffraction pattern of the LiCoO_2 layer is shown on the right.

texture, due to the relatively large spot size of the electron beam. The reflections of the (003), (104) and (110) lattice planes are labelled. The two intense (003) maxima indicate perpendicular orientation of the (00 ℓ) planes toward the substrate surface. This was also derived from XRD patterns of RF-films.

With conventional XRD only the lattice plane reflections are observed, which have their electron diffraction maximum on the imaginary line across the centre of the pattern and parallel to the line of the substrate normal. This clearly illustrates why only the (110) lattice planes show up with XRD analysis. Polycrystalline films with fully random orientation would exhibit circular electron diffraction patterns and thus powder-like XRD patterns.

3.3.4 Substrate influence

The substrate has been reported to play an important role in determining the microstructure and surface morphology of the LiCoO₂ films [11]. To investigate this influence, RF-films of 0.25, 0.50 and 0.75 μm thickness have been deposited on untreated silicon, on HF-etched silicon and on silicon with an intermediate aluminium film (0.15 μm). The complete batch of nine samples was annealed *ex-situ* at 600°C for 30min.

In Figure 3.8 three XRD patterns are shown of annealed 0.75 μm RF-films, deposited on the three different substrates mentioned above. The LiCoO₂ film, grown on the HF-etched silicon surface, exhibited strong preferential (110) orientation. The application of the intermediate aluminium layer introduced some degree of misalignment, which is reflected by the weak diffraction of the (101) and the (104) planes. These peaks have increased intensity for the RF-film on untreated silicon, indicating a more random crystal orientation. Clearly, there is some influence of the substrate and its pre-treatment on the degree of texture. Note that the adhesion of the LiCoO₂ film to the aluminium layer is superior to the adhesion to plain silicon: The cross-sectional SEM micrographs show no sign of peeling from the aluminium layer on the fracture line, in contrast to the other samples where at the edge crumbling of the LiCoO₂ film has left the bare silicon exposed.

The XRD pattern in Figure 3.4 shows evidence of strong interaction between the LiCoO_2 film and the aluminium film on silicon. The (111) diffraction of the aluminium (38.5°) diminishes and the (220) reflection (located at 65.1°) increases during annealing treatment, indicating a switch of the preferential (111) orientation of the Al crystallites to the (220) alignment. This orientation change is not observed in absence of the LiCoO_2 film. Connected to this observation is the solubility limit of 0.5%Al in silicon at room temperature, which increases drastically above 572°C . During annealing treatment the Al dissolves into the silicon substrate, but is segregated at the interface during cooling. The presence of LiCoO_2 apparently determines the lattice orientation of the re-crystallised aluminium film. The boundary between the aluminium and the transition metal oxide appears sharp and unaffected. The partial dissolution of the current collector does establish good ohmic contact with the doped silicon substrate.

To examine the consistency of the preferred lattice orientation of the PLD and RF-films towards each other, a PLD-film is grown on an RF-sputtered seed layer of $0.1\mu\text{m}$ LiCoO_2 (annealed at 600°C , 30min). As a reference, the PLD-film is

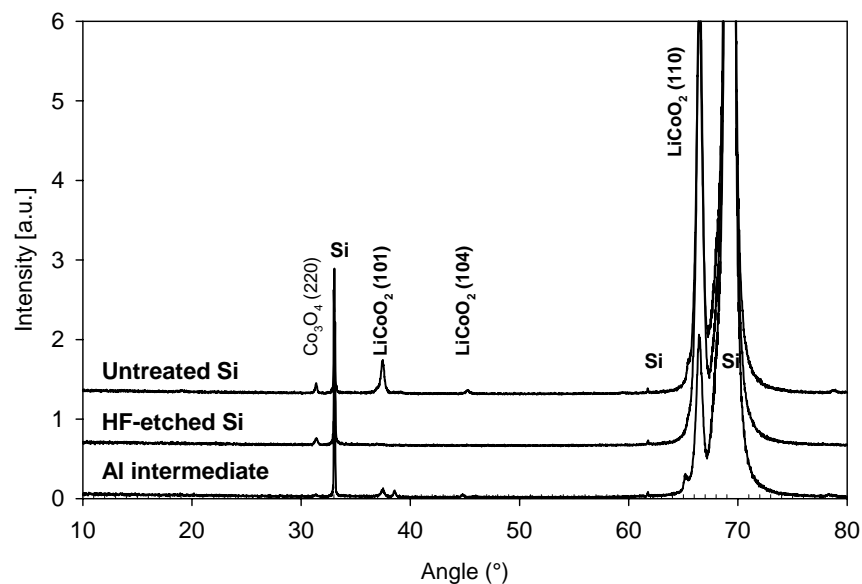


Figure 3.8: XRD patterns of $0.75\mu\text{m}$ LiCoO_2 films deposited on different substrates (annealed at 600°C , 30min): untreated silicon, HF-etched silicon and HF-etched silicon with $0.15\mu\text{m}$ Al intermediate layer.

simultaneously grown on a second, blank silicon substrate. The reference sample exhibits the typical PLD-film diffraction pattern, indicating (00ℓ) lattice plane orientation. The PLD-film deposited on the seed layer, which revealed only the (110) reflection before PLD, now shows distinct (006) and (0012) reflections, but the (003) and (009) reflections were completely absent (see Figure 6.1). This result indicates that the film structure is not entirely determined by the deposition technique. The distinctive diffraction pattern can be explained by assuming complete cationic disorder [12]. A random distribution of the lithium and cobalt atoms would lead to a structure similar to that of NaCl. Hence, the (003) and (009) reflections disappear.

AFM - Figure 3.9 shows the three-dimensional representation of the surface of the RF-film and the PLD-film. Both samples consist of films of equal thickness and a comparable history (annealed at 600°C for 30min). The RF-film exhibits coarser grains and increased surface roughness compared with the PLD-film. The LiCoO_2 lattice growth during deposition and annealing treatment is not isotropic. Apparently the growth rate of both the (110) oriented RF-film, whose c -axis is parallel to the film surface and the (003) oriented PLD-film with its c -axis normal

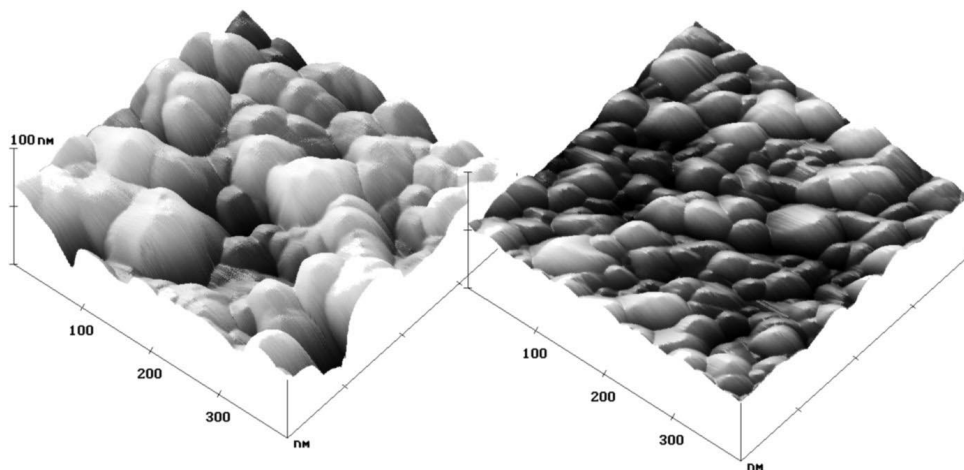


Figure 3.9: Three-dimensional AFM representation of the surface of the RF-film (left) and the PLD-film (right) after annealing at 600°C for 30min.

to the film surface, is largest along the a-axis. This is in agreement with the observed outgrowth of crystals on the surface of RF-films during prolonged annealing at elevated temperatures.

Rutherford Backscattering Spectroscopy - The RBS spectrum recorded in the centre of the RF-film, annealed at 600°C for 30min, is shown in Figure 3.10. The oxygen cobalt ratio is determined to be a few percent above two. Measurements at multiple locations confirm a constant composition profile and constant film thickness across the full sample width. The small oscillations in the Co recoil spectrum do suggest that the oxygen content is higher near the surface of the film. This could be explained by the presence of some Li_2O or adsorbed water.

The recoil intensity on the low energy side of the Co spectrum decreases gradually, indicating a surface roughness of the substrate or a reaction zone of approximately $0.13\mu\text{m}$ thickness. Some interlayer diffusion of cobalt ions may have occurred at 600°C. However, the TEM photographs revealed that the substrate- LiCoO_2 interface remains distinct upon annealing and judging by the AFM results, surface roughness is most likely to be the major cause of the fading recoil spectrum.

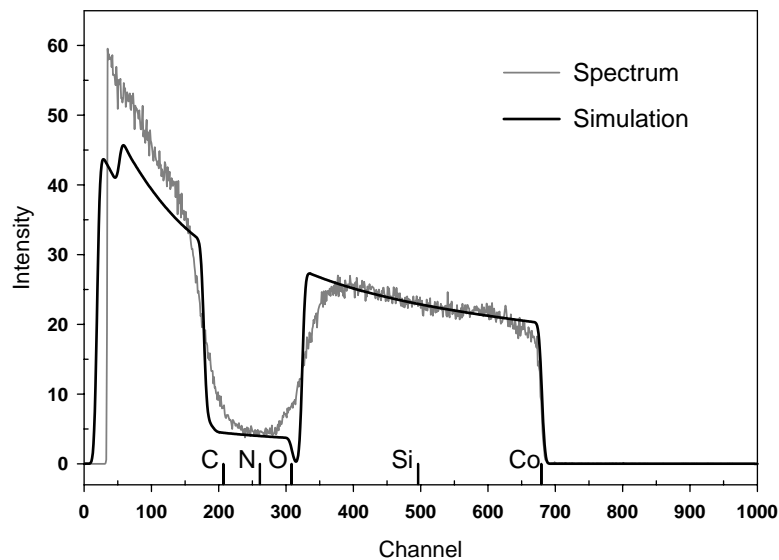


Figure 3.10: RBS spectrum of $0.75\mu\text{m}$ RF-sputtered LiCoO_2 film on silicon substrate annealed at 600°C for 30min.

3.4 Conclusions

The preparation of preferentially oriented, sub-micron LiCoO₂ films has been achieved. The deposition technique largely determines the LiCoO₂ unit cell alignment with the substrate and, thus, the preferential orientation of the film. RF and PLD-films exhibit (110) and (003) lattice planes parallel to the substrate surface, respectively. Deposition at 300°C on pre-etched silicon substrates and subsequent short annealing treatment at 600°C provides uniform film texture. Prolonged annealing treatment results in loss of LiCoO₂ and degradation of the preferential orientation.

This research has shown that LiCoO₂ films with well-defined geometry and structure can be prepared using materials common to the IC industry. A material interaction at the interfaces between the layers of the stack is observed, but is considered beneficial since it contributed to the adhesion strength of the LiCoO₂ film to the substrate. Thus, these films are suitable for fundamental research on electrochemical lithium intercalation and have a prospect for application in microbatteries. The favourable outward orientation of the lithium diffusion plane, which is only the case for the (110) oriented RF films, and the high surface area of these films could lead to excellent intercalation electrode characteristics. The electrochemical properties of these films are presented in Chapter 4.

3.5 References

1. M.M. Tackeray, J.O. Thomas M.S. Whittingham, *MRS Bulletin March 2000*, 39 (2000).
2. Y. Gao, J.R. Dahn, *J. Electrochem. Soc.*, **143**, 1783 (1996).
3. P. Fragnaud, T. Brousse, D.M. Sleich, *J. Power Sources*, **63**, 187 (1996).
4. R. Alcántara, P. Lavela, J.L. Tirado, E. Zhecheva, R. Stoyanova, *J. Solid State Electrochem.*, **3**, 121 (1999).
5. R.J. Gummow, D.C. Liles, M.M. Tackeray, *Mat. Res. Bull.*, **28**, 235 (1993).
6. G.G. Amatucci, J.M. Tarascon, D. Larcher, L.C. Klein, *Solid State Ionics*, **84**, 169 (1997).
7. M. Antaya, J.R. Dahn, J.S. Preston, E. Rossen, J.N. Reimers, *J. Electrochem. Soc.*, **140** [3] 575-78 (1993).
8. B. Wang, J.B. Bates, F.X. Hart, B.C. Sales, R.A. Zuhr, J.D. Robertson, *J. Electrochem. Soc.*, **143**, 3203 (1996).
9. R.E. van de Leest, F. Roozeboom, *Mat. Res. Soc. Symp. Proc.*, **525**, 351 (1998).
10. J.B. Bates, N.J. Dudney, B.J. Neudecker, F.X. Hart, H.P. Jun, S.A. Hackney, *J. Electrochem. Soc.*, **147**, 59 (2000).
11. J.K. Lee, S.J. Lee, H.K. Baik, H.Y. Lee, S.W. Jang, S.M. Lee, *Electrochem. Solid State Letters*, **2**, 512 (1999).
12. H.W. Wang, Y.I. Jang, B. Huang, D.R. Sadoway, Y.M. Chiang, *J. Electrochem. Soc.*, **146**, 473 (1999).

4 Influence of diffusion plane orientation on intercalation

Sub-micron LiCoO₂ films have been prepared on silicon substrates with RF-sputtering and Pulsed Laser Deposition. The electrochemical activity of both types of thin film electrode is compared using Scanning Cyclic Voltammetry, Galvanostatic and Potentiostatic Intermittent Titration and Electrochemical Impedance Spectroscopy. The RF-films exhibit a-axis orientation and have an accessible diffusion plane alignment, unlike the c-axis oriented PLD-films. The preferential orientation of the host crystal lattice towards the electrolyte solution is critical for the intercalation rate and cycling efficiency. The RF-films show superior electrochemical performance and faster relaxation characteristics than the PLD-films. Based on the analysis of the time- and frequency domain measurements a model for the electrode response is proposed. Apparently, the intercalation rate of the RF-films is not diffusion-limited, but hindered by the large charge transfer resistance, the phase boundary movement and the hindrance by the Solid Electrolyte Interface (SEI).

Accepted for publication in: J. Electrochem. Soc.(2002).

4.1 Introduction

The key to the rechargeable lithium battery is the reversible lithium intercalation mechanism. In the lithium ion cell it exists in both the anode and cathode. The positive electrode of such a 'rocking chair' cell consists of a transition metal oxide, the negative electrode usually has a carbide composition. The power of the cell depends on the rate capability of the electrodes and, hence, the kinetics of the lithium intercalation. The exchange current densities of typical commercial LiC_6 and LiCoO_2 composite electrodes differ approximately two orders of magnitude [1]. The positive LiCoO_2 electrode is expected to be rate limiting during intercalation. The solid-state diffusion of lithium within the host intercalation structure is regarded as one of the slower processes involved.

The transition oxide materials can roughly be divided into rock-salt related and spinel structures, *e.g.* LiCoO_2 and LiMn_2O_4 , respectively. The first type is layered with lithium in octahedral sites between O-Co-O sheets. Hence, it exhibits two-dimensional pathways for lithium diffusion via neighbouring vacancies [2]. The second type has a three-dimensional lithium network and allows stable lithium occupation of octahedral as well as tetrahedral sites, thus enabling 3D diffusion. In commercial composite powder electrodes the intercalation host grains are embedded in a porous carbon/binder mixture to allow maximum exposure towards the electrolyte solution. The characteristic diffusion length L is determined by the particle size distribution. For a randomly oriented polycrystalline thin film electrode a virtual 3D diffusion is obtained. Hence, the characteristic length, L , is of the order of the film thickness.

Two types of submicron LiCoO_2 film with contrasting preferential orientations have been prepared [3]. The films deposited with RF-sputtering (RF-films) have a preferential (110) plane orientation, indicating that the diffusion planes are aligned vertically to the substrate surface, toward the electrolyte solution. Due to this favourable orientation a high intercalation rate is expected [4]. The films prepared with Pulsed Laser Deposition (PLD-films) have a preferential (00 ℓ) (c-axis) orientation and have the diffusion planes parallel to the substrate surface. As a result of this adverse alignment the diffusion length L is large and the transport of lithium is expected to be slow [5].

The electrode interface area and the exposure of the host lattice diffusion planes to the electrolyte solution are influenced by the film morphology. Using substrates with a large surface roughness results in non-uniform films containing irregularities, which are not necessarily detrimental for the intercalation process. Particularly PLD-film properties have been observed to improve with the application of polished stainless steel [6,7,8] and aluminium sheet substrates [9], due to significant surface inhomogeneity. To demonstrate the influence of the host lattice orientation on the intercalation behaviour without interference of substrate morphology, only silicon wafer substrates are used for the RF- and PLD-films in this publication.

4.2 Experimental

Silicon wafers (110 orientation, n-type) served as substrate material for film deposition with Pulsed Laser Deposition (PLD) and RF sputtering. The wafer was laser-cut into 15mm \varnothing discs. The rear and sides of these discs were covered with 200nm aluminium using RF sputtering. This metallic film served as backside contact for electrochemical measurements connecting the probe with the conducting silicon. Prior to the deposition of the LiCoO_2 an additional aluminium film (200nm) was sputtered as current collector (optional) together with an adhesion layer of 50Å titanium applied between the aluminium and the LiCoO_2 film. The LiCoO_2 films are grown on heated substrates (300°C) under low oxygen background pressure (0.02 to 0.2mbar). For the exact deposition parameters for PLD-films as well as RF-films we refer to Chapter 3. All films discussed in this paper have been annealed at 550°C for 30 minutes and are polycrystalline.

The electrochemical analysis was performed using a PGstat20 Autolab Potentiostat (ECO-Chemie) with integrated Frequency Response Analyser. The electrochemical cell shown in Figure 4.1 is constructed from Kel-F, a polymer, which is highly resistant against organic electrolytes. The working electrode sample is glued to a rotating disc electrode (RDE) and positioned above the lithium counter electrode. Commercial battery grade liquid electrolyte (1M LiClO_4 , EC:DEC 1:1, Merck) is used. In a three-electrode configuration a Luggin capillary containing a strip of metallic lithium, is used as reference electrode. The counter electrode is a piece of 2x2 cm lithium foil (thickness 1mm) pressed onto the grooved surface of the nickel-plated copper (bottom) plate. This plate also

seals the bottom of the electrolyte compartment. The top of the electrolyte compartment is closed off by a slipring enveloping the RDE tip. This construction minimises evaporation of the volatile organic solvents and thus reduces crystallisation of the salt at the circumference. The cell is operated inside a helium glove box.

The copper bottom plate of the electrochemical cell also conducts heat produced or extracted by the two underlying 36W Peltier elements. These devices allow accurate temperature control of the electrochemical cell. The temperature is recorded automatically with an AD590 linear temperature sensor (details in Appendix C), which is in contact with the electrolyte solution and connected to the data acquisition computer.

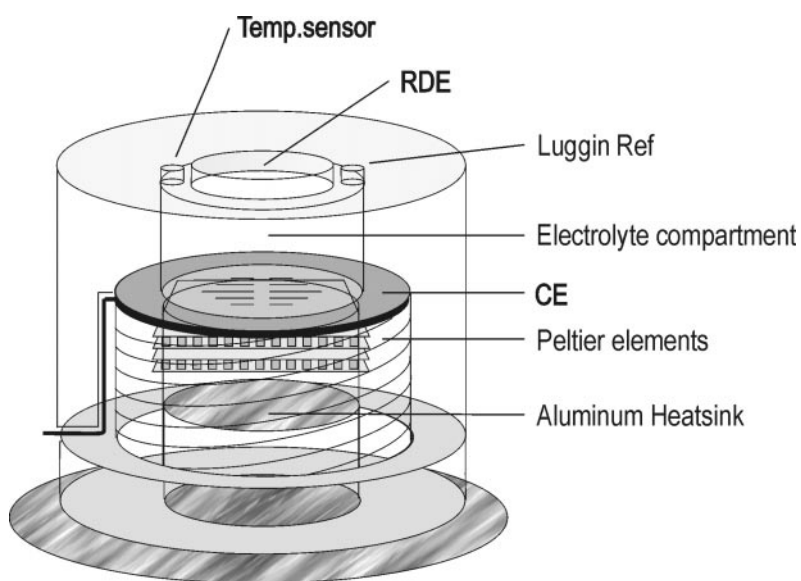


Figure 4.1: Design of the temperature controlled, electrochemical cell set-up.

4.3 Results

Liquid electrolyte is chosen to guarantee good ionic contact between the electrodes and to enable the use of a Rotating Disc Electrode (RDE) to study interface-related phenomena. No clear dependency of the electrochemical behaviour of the thin film LiCoO_2 electrode on the rotation velocity is observed. Hence, in order to reduce noise the measurements have been performed with a stationary RDE.

Upon cell assembly the Open Circuit Potential (OCP) vs. lithium varies with time between 3.0 and 3.5V. After passing a small amount of charge (de-intercalation) a stable OCP is obtained. Using Slow Scanning Cyclic Voltammetry (SSCV) the current is monitored, while the potential is increased with a rate of 0.1mV/sec to the first vertex potential of 4.2V and subsequently decreased down to the second vertex potential of 3.3V (3.5V for the RF-films). In figure 4.2 the first and second scan of an RF- and a PLD- LiCoO_2 electrode are shown. The first scan is irreproducible. In subsequent scans the electrochemical capacity and Faradaic yield of the RF-film are close to their theoretical values. The cathodic peak potential of the RF-film is located at 3.72V in the first scan and decreases slightly in the second scan. No distinct anodic peak is observed, even when the scan range was temporarily increased to 4.4V. The PLD-electrode exhibits low capacity and poor Faradaic yield. At this scan rate only low currents are observed with no specific anodic or cathodic peaks, except for the small cathodic peak at 3.72V in the first scan.

Figure 4.3 shows the actual potential response of a $0.75\mu\text{m}$ RF-film to multiple 200s current pulses of $50\mu\text{A}$ on the left and of a $0.2\mu\text{m}$ PLD-film to 400s pulses of $2.5\mu\text{A}$ on the right. Each current pulse is followed by a period of zero-current relaxation to allow the system to reach equilibrium before the next pulse is applied. The PLD-film is charged with smaller current pulses to avoid excessive overpotentials and consequential electrolyte decomposition. Note, that during the first charging pulses of the RF-film the voltage drops as a result of a large decrease in overpotential with progressing lithium de-intercalation.

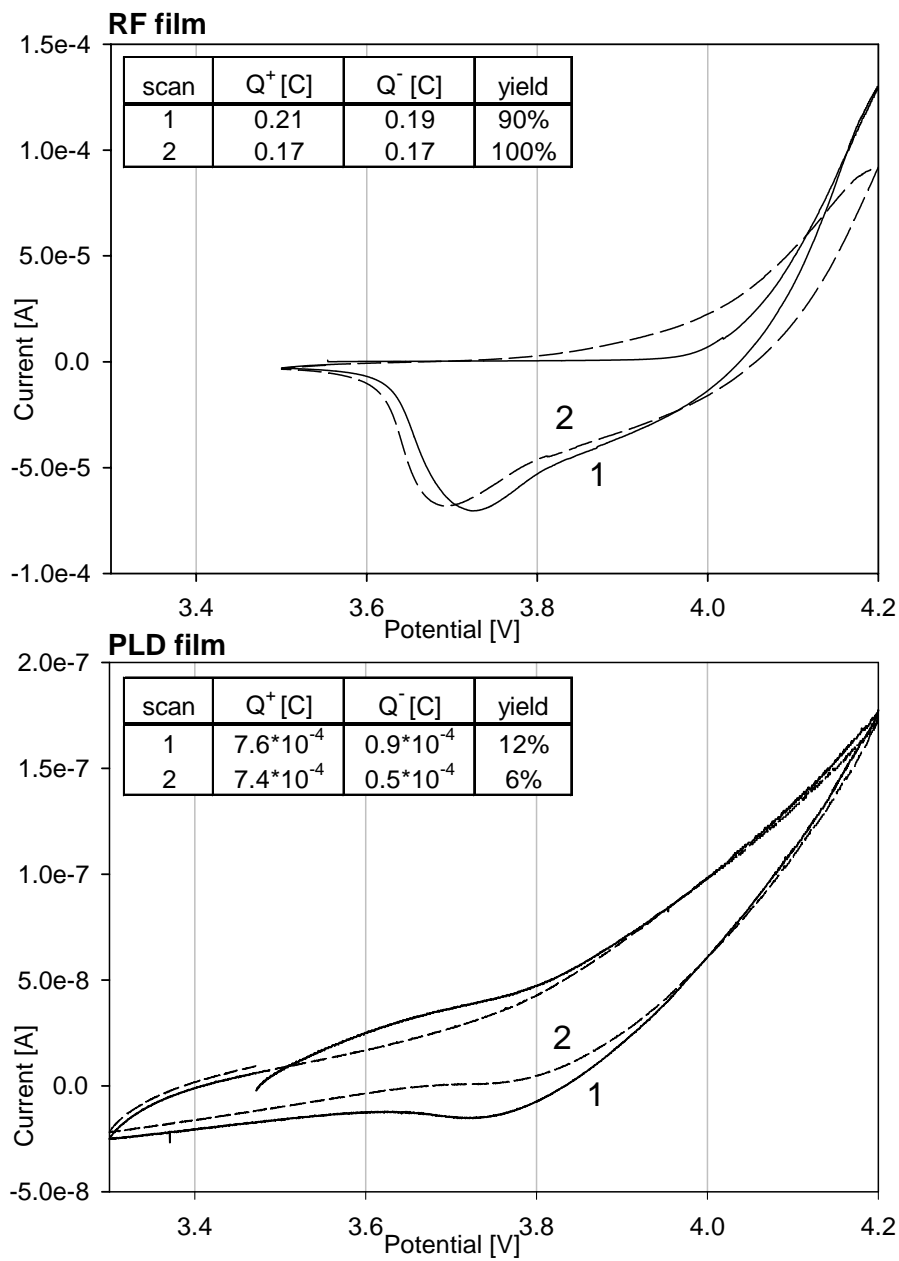


Figure 4.2: Cyclic Voltammogram of a $0.75\mu\text{m}$ RF-film and a $0.2\mu\text{m}$ PLD-film recorded at 0.1mV/s scan rate against metallic lithium plotted on different vertical scales. The charge introduced during oxidation (Q^+), extracted during reduction (Q^-) and the efficiency (%) of the first and second scan are noted in the inset table.

The extent of potential relaxation of the RF-film upon current termination is orders of magnitude smaller than that of the PLD film. The voltage at the end of the relaxation period (1h and 3h for the RF- and PLD-film, respectively) is assumed to represent the Open Circuit Potential (OCP), although the potential of the PLD-film still shows a gradual decay. These values are plotted in Figure 4.4 for both types of films: the RF-film OCP (\blacklozenge) as function of x in Li_xCoO_2 on the bottom x -axis and the PLD-film OCP (\blacksquare) as function of absolute capacity on the top axis. Note, that the scale of the top axis is interrupted and stretched to show a similarity between both curve trends (Capacity=0.75C corresponds to a fully de-intercalated PLD-film ($x=0$)).

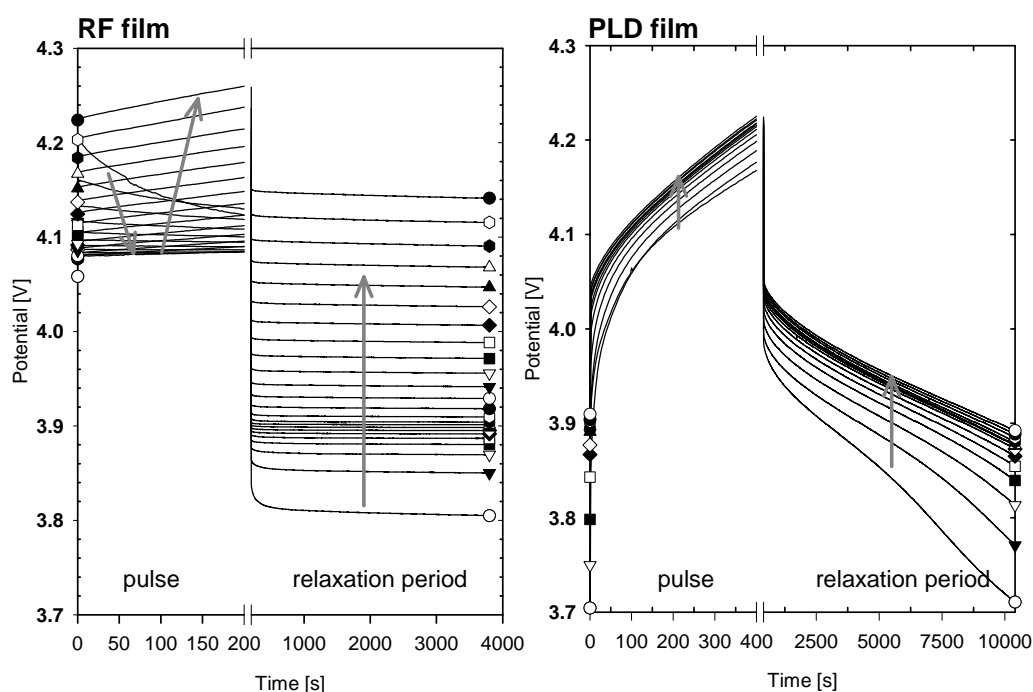


Figure 4.3: Potential response of the RF-film (a) and the PLD-film (b) to a positive current pulse of 10mA/200s and 1mA/400s, respectively. Both the pulse width and the subsequent zero-current relaxation period are shown. The markers indicate the beginning and end of each curve and the arrows indicate their sequence.

As the assumed ‘OCP’ of the PLD-film depends strongly on the chosen equilibration time, mutual comparison of the OCP curves is not realistic, unless mathematical correction is applied. The potential relaxation of both films can be described accurately with an empirical, double exponential function.

$$E(t) = E^{eq} + a \cdot \exp\left(-\frac{t}{\tau_a}\right) + b \cdot \exp\left(-\frac{t}{\tau_b}\right) - \dot{E}^{decay} \cdot t \quad (4.1)$$

where E_{eq} is the new OCP potential, a and b the pre-exponential factors of the two inverse exponential functions with time constants τ_a and τ_b , respectively, and $\dot{E}^{decay} \cdot t$ the product of potential decay (assumed constant) and time. This last term represents the continuous self-discharge of the cell, while the other parameters characterise the potential relaxation process, stabilising at E^{eq} . Typical sets of fit-parameters are listed in table 4.1. The calculated E^{eq} values represent the true OCP(x), corrected for self discharge. These values have also been plotted in Figure 4.4 for the RF-(\diamond) and the PLD-film (\square). For the RF-film the correction is insignificant, while for the PLD-film the discrepancy between the experimental and the corrected OCP is quite large.

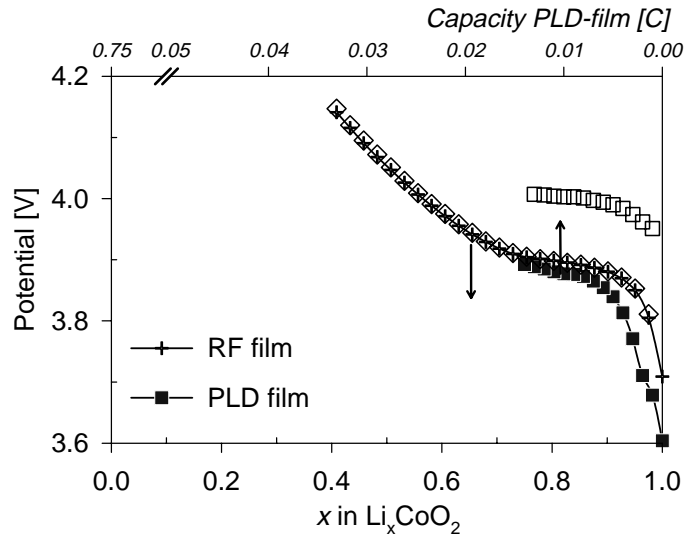


Figure 4.4: Open Circuit Potential (OCP) of the RF-film (+) and the PLD-film (■) as function of the degree of lithium intercalation. The open markers (\diamond and \square , respectively) indicate the calculated E^{eq} for both films. The top axis, scaling the PLD-film capacity, is stretched to match the potential curve of the RF-film (see text).

Figure 4.5a shows the fit of an RF- and PLD-film potential relaxation curve to equation (4.1) and the relative deviation from the experimental data ($dV < 0.01\%$). The accuracy of the fit is limited by the bit-noise of the measurement equipment.

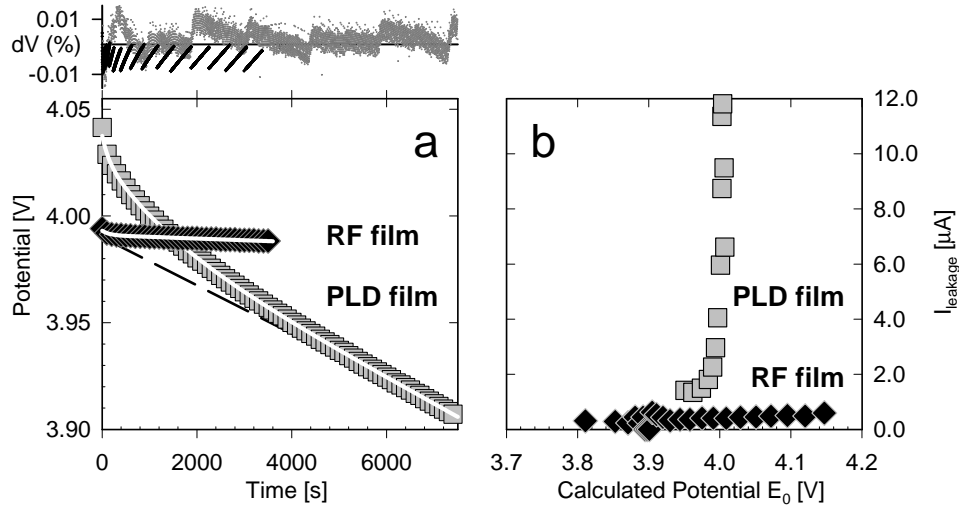


Figure 4.5: Figure a shows the potential relaxation of both film types according to equation (4.1). The top inset graph shows the relative deviation between the raw data and the fit. In figure b the apparent leakage current $i_{leakage}$ is plotted for the RF-film (\blacklozenge) and the PLD-film (\blacksquare) as a function of potential.

Both curves exhibit $E^{eq} = 3.99V$. Here, the ratio between time constants τ_a and τ_b is commonly a factor of 10. Both τ -values are slightly lower for the RF-film. The dissimilarity in relaxation behaviour of both films is mainly reflected by the ten-fold difference in the pre-exponential factors. Note, that the parameters enable mutual comparison, but have not yet been given physical interpretation.

The parameter \dot{E}^{decay} is in fact $(d(OCP)/dt)$ in units $[V \cdot s^{-1}]$ (for an open cell). This value can be translated into an apparent leakage current defined in amperes by correcting for the voltage intercalation profile using the calculated parameter E^{eq} .

Table 4.1: Parameters of empirical equation (4.1) and (4.2) describing the potential relaxation of the RF- and PLD-film electrodes during pulsed current charging. The data sets are listed according to the amount of intercalated charge.

| | Capacity [C] | E^{eq} [V] | a [V] | τ_a [s ⁻¹] | b [V] | τ_b [s ⁻¹] | i_{leak} [A] |
|----------|-----------------|-----------------|------------|--------------------------------|------------|--------------------------------|-------------------|
| RF-film | 0,01 | 3,811 | 9,2E-03 | 50 | 1,7E-02 | 334 | 3,1E-07 |
| | 0,06 | 3,892 | 1,6E-03 | 50 | 9,5E-04 | 632 | 4,5E-07 |
| | 0,12 | 3,920 | 8,9E-04 | 60 | 1,8E-03 | 554 | 4,4E-07 |
| | 0,18 | 4,009 | 2,1E-03 | 53 | 9,6E-04 | 1057 | 4,1E-07 |
| | 0,24 | 4,147 | 2,0E-03 | 48 | 1,8E-03 | 767 | 6,0E-07 |
| PLD-film | 0,001 | 3,951 | 8,7E-03 | 63 | 2,6E-02 | 577 | 1,4E-06 |
| | 0,006 | 3,994 | 1,0E-02 | 143 | 3,0E-02 | 1388 | 3,0E-06 |
| | 0,012 | 4,006 | 9,8E-03 | 150 | 3,3E-02 | 1640 | 9,5E-06 |

$$\frac{d(OCP)}{dt} = \frac{d(OCP)}{dQ} \cdot \frac{dQ}{dt} \equiv \frac{d(E^{eq})}{dQ} \cdot i_{leakage} = \dot{E}^{decay} \quad (4.2)$$

where Q stands for the stored charge in Coulomb. The apparent leakage current $i_{leakage}$ is plotted in Figure 4.5b for the RF- and PLD-film. In case of the RF-film the current is approximately 0.04 μ A up to 4 volts and then shows a linear increase to 0.06 μ A at 4.15V. Since little charge is lost during relaxation, the x value of the RF-film data in Figure 4.3 needs no correction. The apparent leakage current of the PLD-film shows a dramatic increase towards 10 μ A above 4V. At some point the leakage current fully consumes the intercalated charge during the open-circuit relaxation period and no higher OCP can be attained using pulsed charging with this specific pulse width/relaxation time ratio. Note, that the intercalation capacity values of the PLD-film data in Figure 4.4 have not been corrected. Estimation of the lithium content x would be highly unreliable.

In Figure 4.6 the cell potential is plotted as a function of the relative extracted capacity (also called “State of Charge”, or abbreviated SoC) during galvanostatic cycling of the RF and PLD-films versus lithium using different current loads. The lower cut-off voltage is set at 3.0V for both films. The upper cut-off voltage is set at 4.3V for the RF-film and 4.5V for the PLD-film, as this film shows significantly higher overpotentials at the same current density. At equal current

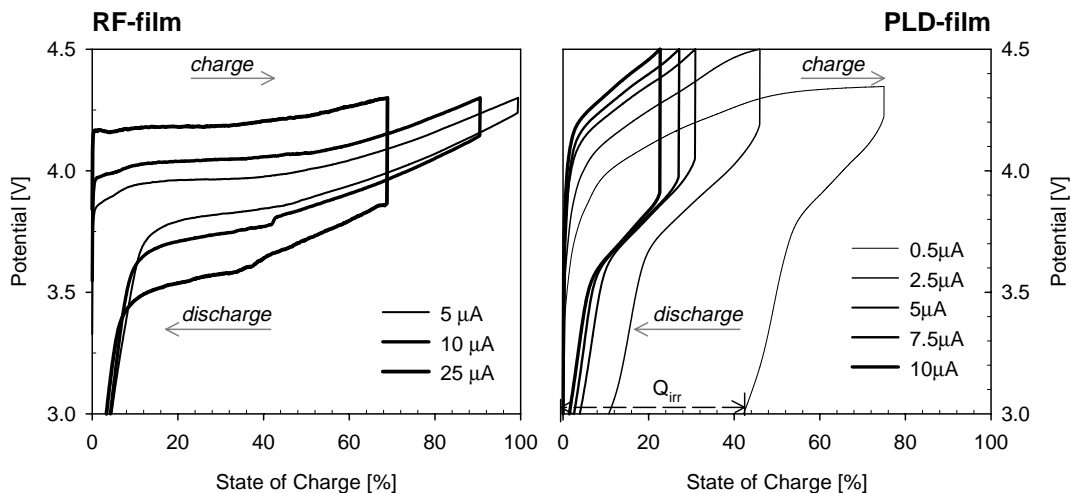


Figure 4.6: Constant current charge and discharge of the RF-film (left) and the PLD-film (right) plotted as function of State of Charge (SoC). Note that the charging currents of the RF-film are larger than those applied to the PLD-film.

densities, related to the macroscopic surface area, the RF-films are able to supply a larger percentage of their theoretical capacity than the PLD-films do between the limits of their cut-off voltage specifications. The capacity retention of the RF-films is even maintained under larger loads. Due to the competitive effect of the apparent leakage current, very low charge and discharge currents do not enhance the reversible capacity of PLD-films. The irreversible capacity, Q_{irr} , is indicated for the $0.5\mu\text{A}$ curve at the bottom of the PLD-film graph.

To obtain complementary data on the underlying intercalation mechanism, potential steps have also been applied to change the equilibrium composition of the electrode. The subsequent electric current may be analysed according to the Potentiostatic Intermittent Titration Technique to evaluate a chemical diffusion coefficient [10]. The potential of the cell is increased in steps of 50mV from 3.80 to 4.20V, while the current is measured with a sampling rate of 100Hz for the first second, 10Hz for the next 10 seconds and at 1Hz for the next hour. Both films show an extremely fast current decay in the first 0.05s (10^{-3} - 10^{-5} A). This part is disregarded in the graph as well as in the discussion, as it is assumed to be a capacitive artefact induced by the measurement equipment. The subsequent part

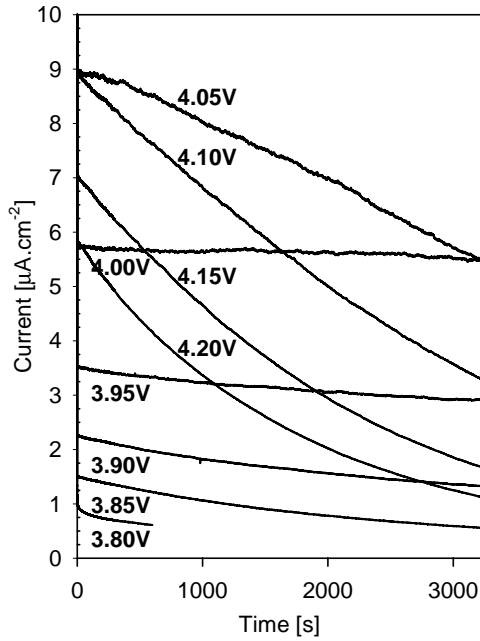


Figure 4.7: Current response of a $0.75\mu\text{m}$ RF-film to sequential 50mV potential steps from 3.80V to 4.20V as function of time.

of the current response is generally an order of magnitude larger for the RF-film than for the PLD-film (approximately $1\text{-}9\mu\text{A}\cdot\text{cm}^{-2}$ vs. $0.1\text{-}0.3\mu\text{A}\cdot\text{cm}^{-2}$, respectively), although the residual current at the end of the relaxation period is generally larger for the PLD-film. Figure 4.7 shows the current relaxation of the $0.75\mu\text{m}$ RF-film in a two-electrode set-up. It is remarkable that after stepping the potential to 4.00V the resulting current remains constant for almost an hour. In the plateau region of the OCP profile the intercalation process appears rate-limited by a kinetic process other than single-phase diffusion. The next potential step to 4.05V shows an increase in current density and with the following steps the trend of exponential-like current

decay is regained.

The PLD-film shows exponential current decay at all potential steps.

Figure 4.8 shows the impedance plot of an RF-film recorded at several States of Charge (SoC) in the frequency range $10^5\text{-}10^{-2}$ Hz. The impedance of the lithium counter electrode proved insignificant in a lithium-lithium test configuration. Hence, it is assumed that the lithium electrode does not contribute to the overall impedance. The initial spectrum recorded directly after cell construction (open circles) is transformed with cycling of the cell. The impedance spectrum of the cycled RF-film resembles the cycled PLD-film spectrum, although in the latter case the absolute values for Z' and Z'' are an order of magnitude larger. Both spectra show a decrease in the impedance with charging of the cell (deintercalation of lithium). In the discussion one model is proposed, describing both

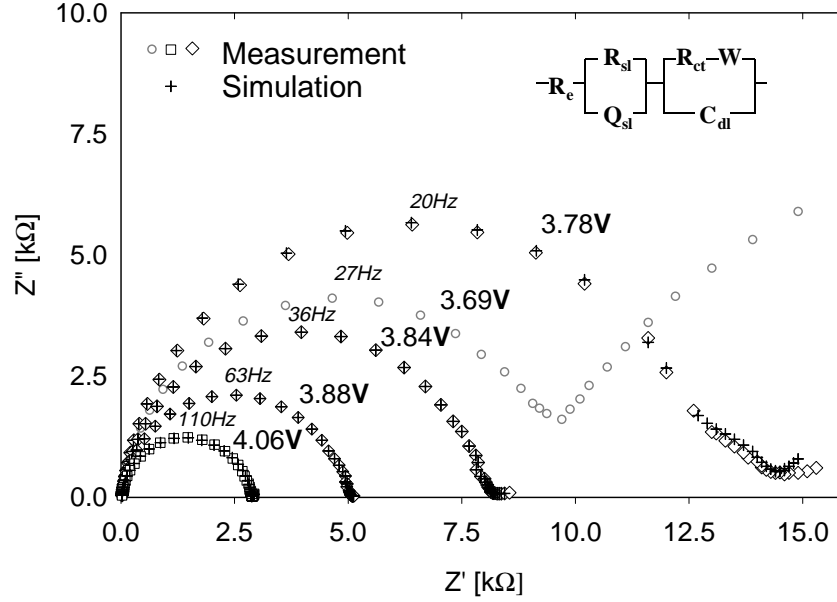


Figure 4.8: Impedance spectra of an RF-film electrode directly after cell construction (\circ), in charged state (\square) and at intermediate SoC (\diamond). Simulated responses, according to the inset equivalent circuit, are presented by (+). The OCP of the measurement and the summit frequency of the semi-circles are indicated.

types of electrodes. In Figure 4.14 the parameters of this equivalent circuit are plotted as function of OCP for a $0.50\mu\text{m}$ the RF-film.

Phase transformations are known to occur for Li_xCoO_2 powders in the range $1 < x < 0.45$ [11]. To investigate structural changes in these thin films, the temperature of the electrochemical cell is controlled accurately between 10° and 40°C at a specific SoC. It is assumed that the moderate temperature cycling itself does not induce phase transformation nor inflicts damage to the cell. The measured OCP(x) is plotted in Figure 4.9a as function of absolute temperature. It is related to the Gibbs free energy $G(x)$ as follows:

$$\Delta_r G(x, T) = -nF \cdot \text{OCP}(x, T) \quad (4.3)$$

$$dG(x, T) = \sum_i \mu_i dx_i = \left(\mu_{\text{Li}}^{\text{Li}} - \mu_{\text{Li}}^{\text{Li}_x\text{CoO}_2} \right) \cdot dx = -nF \cdot d\text{OCP}(x, T)$$

The chemical potential of lithium (μ_{Li}) in either electrode is defined by its partial molar entropy (s_{Li}) and partial molar enthalpy (h_{Li}). Both contributions are derived from the temperature dependence of the open cell potential using the modified Gibbs-Helmholtz equation:

$$\text{with: } \mu_{Li} = h_{Li} - Ts_{Li}$$

$$s_{Li}^{Li_xCoO_2} - s_{Li}^{Li} = \left(\frac{\partial S}{\partial x} \right)_T = - \left(\frac{\partial G}{\partial T} \right)_x = - \frac{1}{zF} \cdot \left(\frac{\partial OCP}{\partial T} \right)_x \quad (4.4)$$

$$h_{Li}^{Li} - h_{Li}^{Li_xCoO_2} = \left(\frac{\partial H}{\partial x} \right)_T = \left(\frac{\partial \left(\frac{G(x)}{T} \right)}{\partial \left(\frac{1}{T} \right)} \right)_x = \frac{1}{zF} \cdot \left(\frac{\partial \left(\frac{OCP(x)}{T} \right)}{\partial \left(\frac{1}{T} \right)} \right)_x$$

The results for the RF-film are plotted in Figure 4.9b, where the partial molar enthalpy (grey squares) is plotted on the left and the partial molar entropy (open circles) is plotted on the right. The slope of both curves changes simultaneously, suggesting that a phase transformation occurs at those specific compositions (vertical dotted lines drawn as guide to the eye). The inset reveals a phase diagram reported by Dahn *et al.* [12]. No discrepancy is observed between experiments performed with increasing or decreasing SoC. This indicates a lack of hysteresis and a good reproducibility of the measurements.

After electrochemical characterisation the electrode is disconnected and analysed with AFM and XRD to assess cycling-induced changes. Figure 4.10 shows the XRD pattern of an RF-film in discharged state ($x \approx 1$), recorded before and after extensive electrochemical cycling. For this analysis the sample has been tilted a few degrees to suppress the monocrystalline silicon diffraction peaks. The baseline intensity of the ‘before’ situation has been vertically displaced for clarity. Besides the increase of the baseline noise, a slight increase of the Co_3O_4 content is observed. The preferential orientation of the rhombohedral host lattice is preserved.

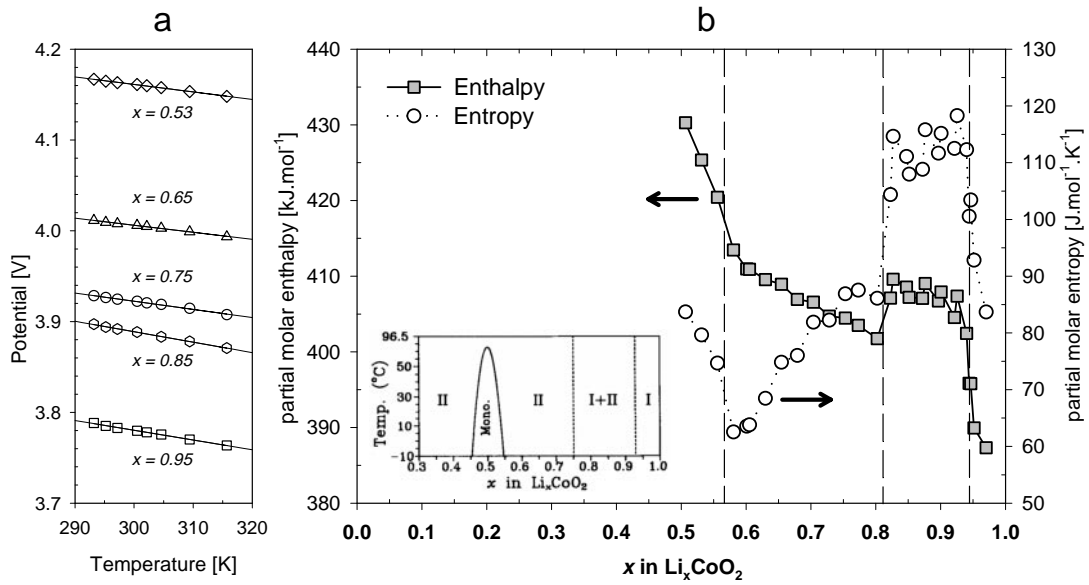


Figure 4.9: Figure (a) shows the measured OCP of a $0.75\mu\text{m}$ RF-film as a function of temperature at the specified SoC and (b) shows the calculated partial molar enthalpy (■) and entropy (○) as function of the lithium composition. Both curves change at similar lithium concentrations corresponding to the inset phase diagram reported by Reimers et al. [12].

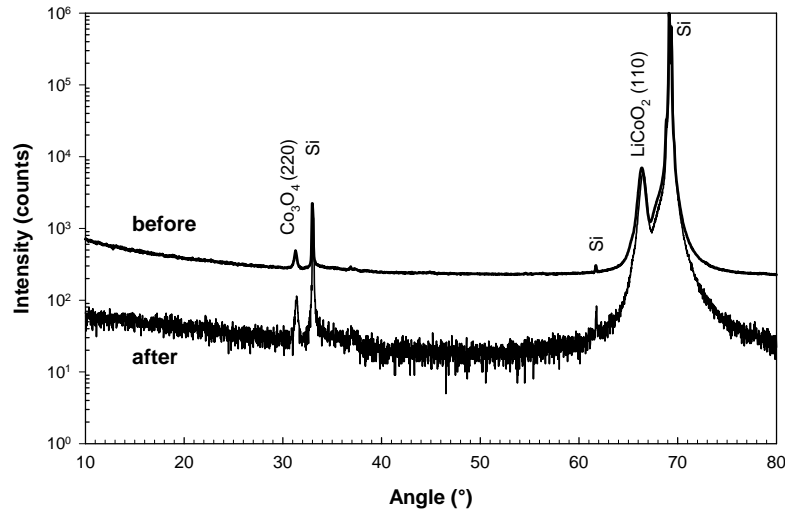


Figure 4.10: XRD patterns of the $0.75\mu\text{m}$ RF-film recorded before and after electrochemical analysis. The reflections of the silicon substrate are marked with Si.

The surface of the RF-film is visualised in Figure 4.11 using AFM tapping mode. The left AFM image (a) shows the electrode surface before electrochemical cycling, and the right image (b) shows the situation afterwards. In order to clearly show the surface structure and roughness, the shading is greatly exaggerated. The impression is given that during electrochemical cycling an additional surface layer cover the original microstructure. Image analysis reveals that the actual surface area of the RF-film decreases from 152% before cycling to 122% after cycling, relative to the geometric surface area of $0.16\mu\text{m}^2$. The PLD films show a decrease from 119% to 108%. The difference is directly related to the surface roughness of the samples, which is largest for the RF-films. Further specifications are listed in Table 4.2.

Table 4.2: Image analysis results calculated from AFM surface scans of RF- and PLD-film before and after electrochemical cycling in liquid electrolyte (EC:DEC 1:1, 1M LiClO₄).

| | | RF-film | | PLD-film | |
|-------------------------------|---------------------|---------|-------|----------|-------|
| | | before | after | before | after |
| Z-range | [nm] | 114.62 | 64.87 | 31.56 | 25.81 |
| RMS roughness | [nm] | 17.36 | 10.66 | 5.63 | 4.35 |
| Image surface area | [μm^2] | 0.243 | 0.196 | 0.190 | 0.173 |
| Image surface area difference | | 51.8% | 22.3% | 18.7% | 7.9% |

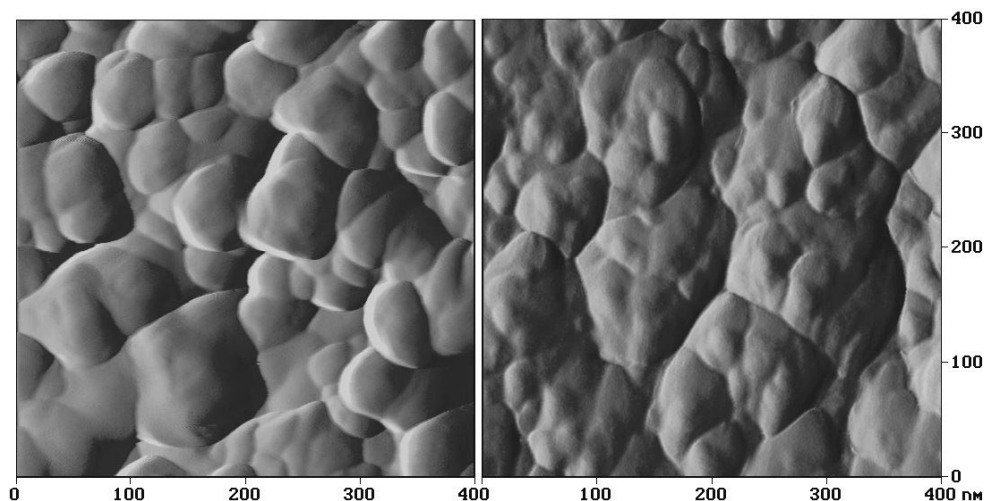


Figure 4.11: AFM amplitude plot of the $0.75\mu\text{m}$ RF-film obtained in tapping mode before exposure to electrolyte solution (left) and after extensive electrochemical cycling (right). Note: the colours do not represent absolute height.

4.4 Discussion

Both LiCoO_2 films show electrochemical lithium de-intercalation activity as positive electrode in a lithium|EC:DEC - $\text{LiClO}_4(1\text{M})|\text{LiCoO}_2$ cell. The thin film performance depends heavily on the preferential orientation of the intercalation host structure. For example, almost the full theoretical capacity can be extracted from the RF-film with 100% Faradaic yield using cyclic voltammetry at a scan rate of $0.1\text{mV}\cdot\text{s}^{-1}$, while at this rate the PLD film releases merely 0.1% of its theoretical capacity with a yield of only 6%. The strong dependence on the host lattice orientation is caused by the exposure of the lithium diffusion planes toward the electrolyte solution. Theoretically, the RF-film is fully ‘open’ for intercalation (Fig 4.12a). Hence, the entire film is directly involved in the intercalation process and due to the fast inward diffusion of lithium equilibration is quickly achieved. The diffusion planes in the PLD-film are closed off and accessible only through ‘openings’ provided by film irregularities and surface roughness (Fig. 4.12b).

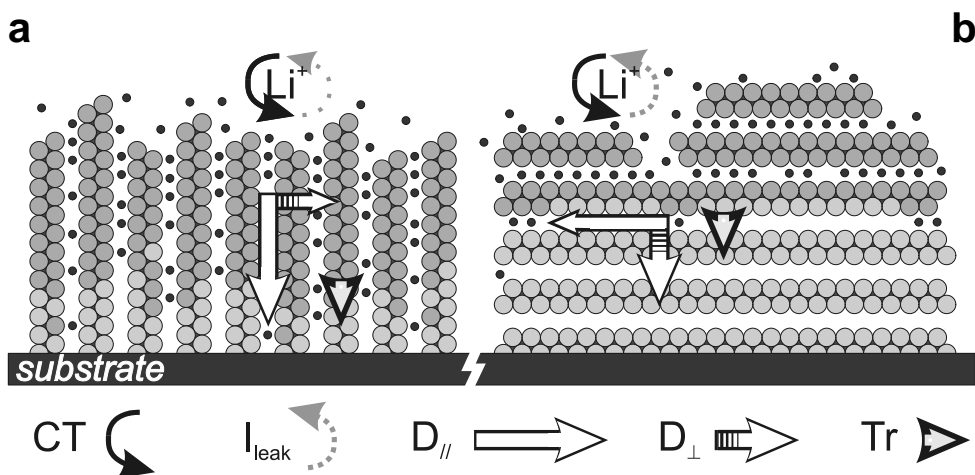


Figure 4.12: Schematic model representing the host structure of the RF-film (a) and the PLD-film (b). The arrows represent the direction of the processes involved in lithium intercalation: Charge Transfer (CT), Current leakage (I_{leakage}), lithium diffusion parallel (D_{\parallel}) and perpendicular (D_{\perp}) to the diffusion planes and Phase boundary movement (Tr).

As has been reported also by Iriyama *et al.* [5] only material in close proximity of these defects can contribute to the intercalation process. The intercalation rate and capacity of our PLD-films have indeed been observed to improve with the etching of a gauze-like pattern into the existing PLD-film or the application of stainless steel substrates [6].

Figure 4.12 shows a schematic representation of the intercalation process in Li_xCoO_2 in the case of RF- (left) and PLD-films (right), where CT stands for Charge Transfer, I_{leakage} the leakage current due to electrolyte decomposition, $D_{//}$ the in-plane lithium diffusion, D_{\perp} the slow cross-plane lithium diffusion and Tr indicates the direction of host phase transformation. These elements are addressed and correlated with the observed phenomena in the following discussion.

4.4.1 Leakage Current

As the intercalation into the PLD-film is restricted to the surface region of the LiCoO_2 , relatively little charge can induce a potential far from the equilibrium value of the electrode. Evidence are the high overpotentials and the low (reversible) capacity observed with galvanostatic cycling. A high surface potential of the intercalation electrode also accelerates the oxidation of the electrolyte (and simultaneous electrode reduction), causing increased self-discharge and irreversible capacity loss. The apparent leakage current, estimated from pulsed current charging (GITT), is indeed particularly large above 4V (Fig. 4.5b).

The mechanism of the electrolyte decomposition is expected to be similar for RF- and PLD films. As the RF-film also exhibits the largest surface area, the large difference in the apparent leakage current is unexpected. The residual currents measured with PITT can be interpreted as the actual leakage current and show a similar trend as the apparent leakage current shown in Figure 4.5b. The actual leakage current increases from $0.05\mu\text{A}$ at 3.9V to $0.18\mu\text{A}$ at 4.20V for the PLD-film and exceed the residual current values of the RF-film by a factor 2, which is more plausible. Comparable currents are recorded with cyclic voltammetry to maintain a steady cell potential. The difference between the apparent and actual leakage current of the PLD-film indicates that the linear part of the potential decay under open circuit conditions cannot be contributed solely to electrolyte decomposition.

4.4.2 Lithium diffusion

The intercalated charge at the surface of the electrode is equilibrated through inward diffusion of the lithium. If this intercalation process is diffusion-limited we can assume semi-infinite conditions for short times ($t \ll L^2/\tilde{D}$) and define an effective diffusion coefficient from the pulsed current charging experiment according to the Galvanostatic Intermittent Titration Technique [10]:

$$\frac{dE}{dt^{1/2}} = V_m \cdot \frac{dE}{dx} \cdot \frac{2I}{zFS(\pi\tilde{D})^{1/2}} \quad (4.5)$$

where V_m is the molar volume, I is the pulse current, z the number of electrons ($z=1$), F the Faradaic constant, S the surface area and \tilde{D} the chemical diffusion coefficient. This equation does not provide a convincing fit for the experimental RF- and PLD-film data over extended time periods. Confining our data to the first 50 seconds yields an effective chemical diffusion coefficient of approximately 10^{-4} [$\text{cm}^2 \cdot \text{s}^{-1}$] and 10^{-14} [$\text{cm}^2 \cdot \text{s}^{-1}$], respectively (plotted in Figure 4.13). The first value is orders of magnitude above chemical diffusion coefficients reported even for composite electrodes [13]. Based on this chemical diffusion coefficient the maximum measurement time would be $5 \cdot 10^{-5}$ s, which is an order of magnitude smaller than the 50s used for the calculation. This discrepancy indicates, that the observed potential relaxation is not related to a true diffusion process and the diffusion coefficient calculated with this (or any other) semi-infinite diffusion model must be regarded as an effective one. The PLD-film does reveal an effective chemical diffusion coefficient of the expected order of magnitude. Even though the derived quantities are indicative, the absolute difference is remarkable and agrees with the strongly anisotropic lithium diffusion.

A diffusion coefficient can also be deduced from the current relaxation following a potential step according to the Potentiostatic Intermittent Titration Technique [10]. The current response of the PLD-film confirms the low diffusion coefficient value found previously with GITT, while the RF-film response does not match this model: the current becomes virtually constant after stepping to 4.0V (Figure 4.7), suggesting a kinetically limited intercalation reaction. This potential lies just above the OCP(x) voltage plateau and corresponds to the end of the two-phase intercalation region. With this particular 50mV-step a large amount of lithium is

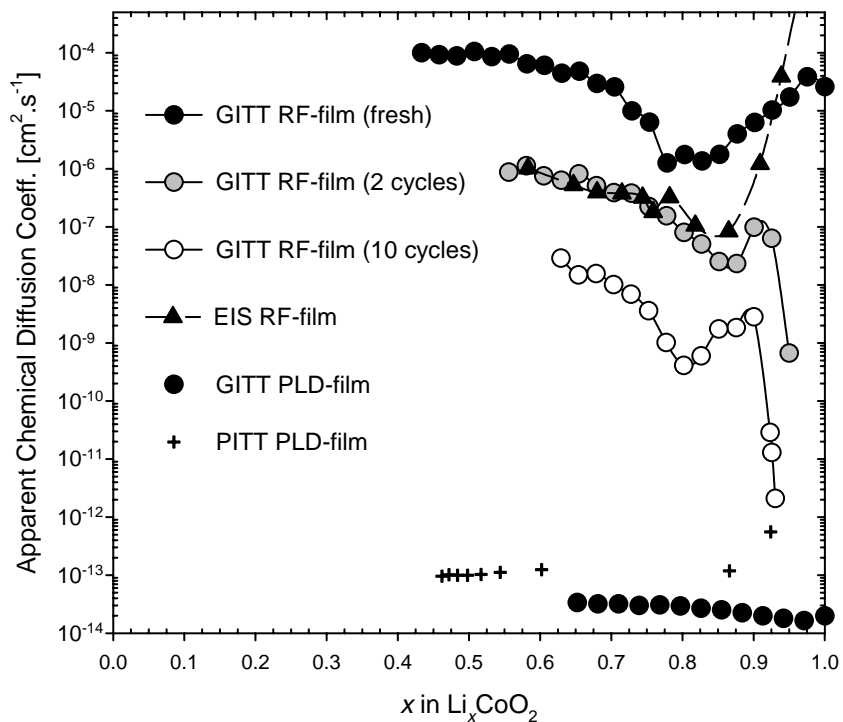


Figure 4.13: The apparent chemical diffusion coefficient calculated with GITT, PITT and EIS for the RF- and PLD-film electrodes plotted as a function of x .

de-intercalated, which induces a phase transformation. Here the phase boundary movement is expected to be the rate determining process, as the next potential step shows a further increase in the initial current response and subsequent decay.

4.4.3 Phase Transformation

Phase transformation of the RF-films is revealed by resolving the OCP(T) at a specific SoC into a the temperature-dependent component (partial molar entropy difference) and temperature independent component (partial molar enthalpy difference) which both are plotted in Figure 4.9b. The potential of the lithium counter electrode is assumed constant and thus all features are attributed to the working electrode (in other words: $s_{\text{Li}}^{\text{Li}}$ and $h_{\text{Li}}^{\text{Li}}$ assumed constant).

The changes in the partial molar entropy and enthalpy as function of lithium concentration correspond well with the inset phase diagram in Figure 4.9b. The absolute values of x could be slightly overestimated due to the slowly receding intercalation capacity (e.g. $x=0.55$ is in fact $x=0.50$). Phase I and II denote two rhombohedral structures with different lithium concentrations and both exist in the two-phase region in the range $0.75 < x < 0.93$. The left region specified as Mono indicates the monoclinic $\text{Li}_{0.5}\text{CoO}_2$ stability range and corresponds with composition $x < 0.57$. In the two-phase region the applied GITT and PITT diffusion equations are not applicable and thus only an effective diffusion coefficient, correlated to the phase boundary diffusion, is calculated in the range 3.87-3.93V versus lithium.

For LiCoO_2 powders the phase transformation from phase I to II is accompanied with a c -axis increase (14.09Å to 14.26Å) and a small a -axis decrease (2.816Å to 2.812Å) of the unit cell, resulting in a volume expansion of approximately 1% [12]. In case of the RF-films the c -axis lies parallel to the surface and might suffer constraint due to the substrate confinement. However, no cracking or peeling of the 0.75µm film is observed with cycling of the cell. During this process the preferential orientation of the host lattice is also maintained. Apparently, the phase transformation occurs, unhindered by the bonding to the substrate.

The partial molar entropy shows a strong increase upon lithium de-intercalation from LiCoO_2 , due to the introduction of lithium vacancies and electronic charge carriers. In the two-phase region the partial molar entropy and enthalpy are approximately constant, as the Gibbs Free Energy (sum of h_{Li} and $T \cdot s_{\text{Li}}$) designates the plateau potential. Upon further lithium extraction the Li_xCoO_2 enters the single-phase region II and the partial molar enthalpy increases with the charging of the electrode, while the partial molar entropy decreases due to clustering of vacancies to the point where a long-range ordered structure remains [14]. Lithium de-intercalation from this monoclinic phase leads to a strong increase in both partial molar enthalpy and entropy. No further de-intercalation was attempted.

Phase transformation is also expected to occur in the PLD-film, but it could not be analysed as function of temperature due to the unstable OCP. However, the estimated equilibrium potential E^{eq} obtained from pulsed charging, predicts that the PLD-film electrode has initially a potential around 4V, which coincides with

the phase II region of the RF-film. It is possible that with each charge pulse, phase transformation is induced at the surface of the PLD-film electrode. Lattice expansion upon lithium de-intercalation is unhindered by bonding to the substrate due to the *c*-axis orientation. Lithium extraction from the exposed diffusion planes is expected to be as fast as observed for the RF-films and results in a layer-by-layer de-intercalation plus transformation of the host structure. The simultaneous phase boundary movement would restrain the (de-)intercalation process [13].

4.4.4 An Equivalent Circuit

Analysis of the intercalation process in the frequency domain is suitable for providing a physical interpretation of the electrochemical behaviour. The empirical equation (4.1) describing the time-dependent potential relaxation can be converted to the frequency domain using a Laplace transformation. However, the high frequency end (>1Hz) of the Li-transformed data is rather inaccurate due to the sampling rate limitation. There are some analogies with the impedance spectra data: the similarity in the relaxation time constants of the RF- and PLD-films is reflected by the mutual resemblance of the impedance spectra and the ratio of the pre-exponential factors corresponds to the tenfold higher impedance of the PLD-films.

The model that describes the frequency-dependent behaviour of both types of electrodes successfully is drawn as equivalent circuit in the inset in Figure 4.8. This basic model has been applied successfully for numerous intercalation materials [15]. R_e stands for the electrolyte resistance, R_{sl} and Q_{sl} represent the interface with a surface layer (signifies the SEI layer). The charge transfer resistance, double layer capacity and diffusion are described with a Randles circuit using the elements R_{CT} , C_{dl} and W , respectively. The equivalent circuit is fitted to the impedance spectra using Equivalent Circuit [16]. The pseudo χ^{2*} value ranges from 10^{-4} to 10^{-6} indicating acceptable fits. Figure 4.14 shows the values of the equivalent circuit parameters for a $0.5\mu\text{m}$ RF-film as a function of potential versus lithium in 10mV steps. The electrolyte resistance is not presented, since it remains constant at 17Ω .

♣ The modulus weighted mean variance between experimental data and fit

The dominant semicircle in the Impedance plot of the RF- (Fig. 4.8) and the PLD-film scales inversely with increasing SoC and is associated with the $R_{CT}C_{dl}$ network. The summit frequency changes from 20Hz to 110Hz for RF-films and from 0.5Hz to 0.8Hz for PLD-films. The double layer capacity, assumed equal to the constant phase element Q_{dl} as n_{dl} approximates one, appears to be almost equal for the RF-film and the PLD-film ($0.9 \cdot 10^{-6}F$ and $1.4 \cdot 10^{-6}F$, respectively) indicating a similar contact with the electrolyte. The Q_{dl} for the PLD-film remains constant at all SoC, but the RF-film value shows a decrease at 3.72V and 3.88V suggesting a correlation with the phase transformation $I \rightarrow I + II \rightarrow II$. The small variations in the n-value of the constant phase element show a similar, but inverse trend.

The Charge Transfer resistance R_{CT} is related to the exchange current density, i_0 , by the equation:

$$i_0 = \frac{RT}{zFR_{CT}} \quad (4.6)$$

In the discharged state the charge transfer resistance is high, but it decreases rapidly and becomes constant above 3.90V. Levi *et al.* [17] reported similar behaviour for porous $LiCoO_2$ electrodes. The calculated exchange current density of the $0.50\mu m$ RF-film is initially $10^{-5}A \cdot cm^{-2}$ and increases to $3 \cdot 10^{-5}A \cdot cm^{-2}$. Again the trend seems to follow the phase transformations, as observed above with Q_{dl} . In case of the PLD-film the exchange current density shows a slight increase from $10^{-7}A \cdot cm^{-2}$ to $1.7 \cdot 10^{-7}A \cdot cm^{-2}$ at 4.14V. Although the PLD-film kinetics are clearly inferior, the charge transfer resistance of both films is high compared with that of composite electrodes and is responsible for the high overpotentials.

After subtraction of the charge transfer related semicircle from the impedance plot, a 'smaller' semicircle with lower summit frequency remains, which can be described by the surface layer network consisting of a parallel resistance R_{sl} and the constant phase element Q_{sl} . The impedance of these elements also appears to be dependent on the cell potential and increases gradually with ageing of the sample. Lithium de-intercalation from stoichiometric $LiCoO_2$ causes an immediate decrease of R_{sl} and a simultaneous response of Q_{sl} ; both stabilising beyond 3.75V. This behaviour suggests a correlation with the increase in

electronic conductivity as the LiCoO_2 changes from semi-conducting to conducting. According to this model the physical SEI layer is affected by the electrode properties. In case of the PLD-film the impedance characteristics of the surface film are small compared with the large influence of R_{sl} and could not be resolved accurately.

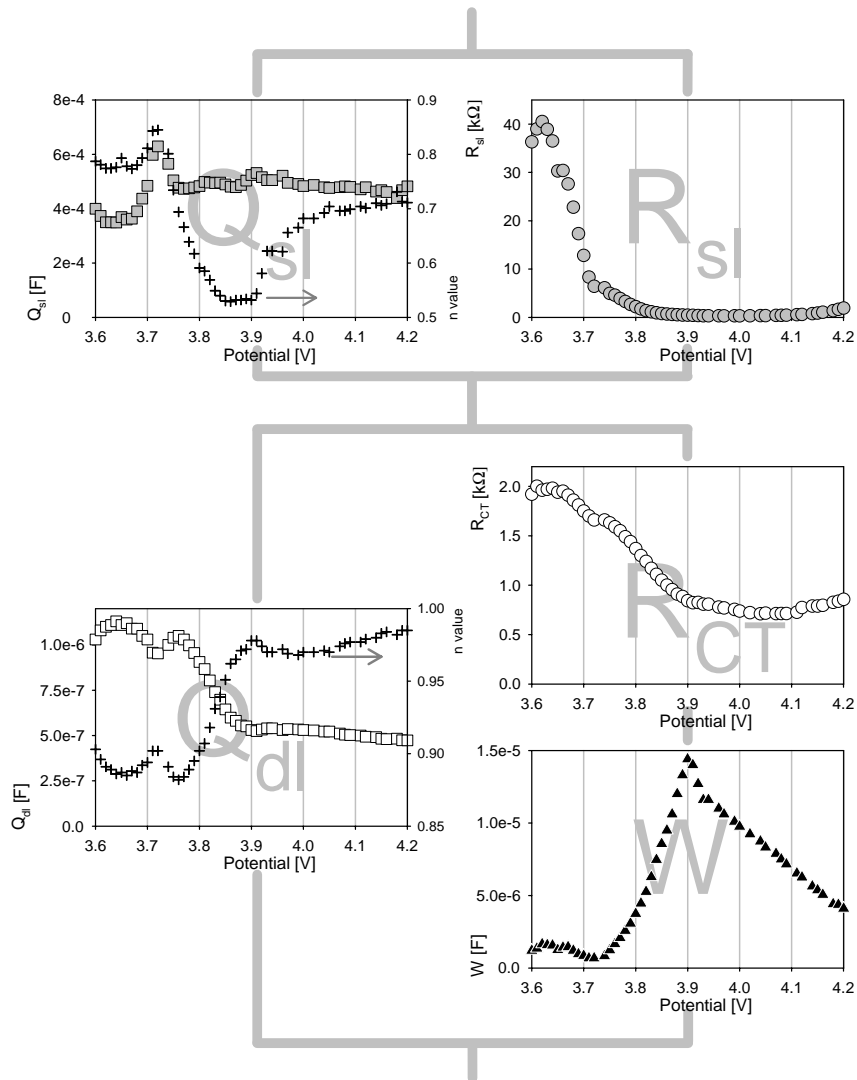


Figure 4.14: The values of the equivalent circuit parameters used to fit the impedance spectra of a $0.50\mu\text{m}$ RF-film plotted as function of potential.

The Warburg coefficient in Figure 4.14 also shows a strong phase-dependency. It remains stable at low potential and shows a steady increase towards the maximum obtained at the plateau potential at 3.9V. This peak corresponds with a minimum in the chemical diffusion coefficient (see equation 4.7), which is expected in a two-phase region and confirmed by the measurements in time-domain. The linear decrease in the Warburg coefficient upon further charging suggests that the diffusion rate increases with increasing lithium deficiency in the single phase II region.

Assuming semi-infinite conditions, the chemical diffusion coefficient of the RF-film can be estimated from the Warburg impedance Z_W [10]:

$$Z_W = \frac{V_M}{\sqrt{2}zFA\tilde{D}_{Li}^{1/2}} \frac{dE}{dx} (1-j)\omega^{-1/2} = \sigma(1-j)\omega^{-1/2} \quad (4.7)$$

where σ is the Warburg coefficient, V_M the molar volume of the host structure, dE/dx the slope of the OCP(x) plot and z the number of the electrons involved in the charge transfer ($z=1$). The chemical diffusion coefficient calculated for the 0.75 μm RF-film is plotted together with the other corresponding semi-infinite diffusion coefficient estimates in Figure 4.13. The Warburg impedance indicates high chemical diffusion coefficients. These shows good similarity to the values calculated from the second GITT experiment, which was performed just before the impedance measurement. The upward deviation, observed as x approaches unity, is the result of fitting inaccuracy in the low frequency domain. As there is no evidence of a transition of semi-infinite to finite space diffusion at a specific frequency, the value calculated with equation (4.7) from the Warburg impedance must also be regarded as an effective chemical diffusion coefficient for the lithium (de-) intercalation process.

The outstanding performance of the RF-film is subject to deterioration. The GITT estimate of the chemical diffusion coefficient after 10 cycles clearly shows a decrease in intercalation rate and capacity, but the shape of the curve remains the same. This suggests that the host material itself does not degrade upon cycling, but merely less material is involved in the intercalation process. Due to the continuous increase of the surface film impedance, the ageing effect is mainly attributed to the growth of a SEI layer on the electrode surface caused by electrolyte decomposition [18]. Avoiding contact with liquid electrolyte by

applying a (thin) solid-state electrolyte layer could be the key to control the SEI and thus minimise the capacity fade. Providing a passivation film with constant low charge transfer resistance could possibly even enhance the current rate capability.

4.5 Conclusions

Thin film electrodes of LiCoO_2 have been prepared using RF-sputtering and Pulsed Laser Deposition and exhibit a perpendicular (hence accessible) and a parallel (thus inaccessible) alignment of the lithium diffusion plane towards the electrolyte solution, respectively. In the first case the full film capacity is involved, while in the second case only the surface of the electrode contributes to the electro-chemical intercalation process and low capacities are observed. The favourable orientation of the RF-films enables fast inward diffusion and thus quick response to current pulses. The lithium intercalation process in PLD-films is difficult and the potential relaxation slow. The apparent chemical diffusion coefficient estimated for the RF-films is many orders of magnitude larger than that of the PLD-film. Solid-state diffusion is not necessarily the rate-limiting process.

Phase transformation of the LiCoO_2 thin film electrode is observed at specific lithium concentrations and appears to be unhindered by the bonding to the substrate. These structural transformations affect the electrochemical characteristics of the intercalation electrode. The intercalation process is generally restrained by the large Charge Transfer resistance and in some cases by phase boundary movement. Cycling does not lead to reorientation or permanent transformation of the host structure. The observed deterioration of intercalation rate and capacity is attributed to the growth of a SEI layer, which decreases the electrode surface area and poses an additional barrier for lithium intercalation.

For two-dimensional intercalation materials the accessible alignment of the lithium diffusion planes is essential for optimal electrode performance.

4.6 References

1. H.J. Bergveld, "Battery Management Systems; Design by modelling", 156, Thesis University of Twente, the Netherlands (2001).
2. A. van der Ven, G. Ceder, *Electrochemical and Solid-State Letters*, **3** [7] 301 (2000).
3. P.J. Bouwman, B.A. Boukamp, H.J.M. Bouwmeester, H.J. Wondergem, P.H.L. Notten, *J. Electrochem. Soc.*, **148** [4] A311 (2001).
4. J.B. Bates, N.J. Dudney, B.J. Neudecker, F.X. Hart, H.P. Jun, S.A. Hackney, *J. Electrochem. Soc.*, **147** [1] 59 (2000).
5. Y. Iriyama, M. Inaba, T. Abe, Z. Ogumi, *J. Power Sources*, **94** 175 (2001).
6. P.J. Bouwman, B.A. Boukamp, H.J.M. Bouwmeester, P.H.L. Notten, *Solid State Ionics*, Conference proceedings (2001).
7. K.A. Striebel, C.Z. Deng, S.J. Wen, E.J. Cairns, *J. Electrochem. Soc.*, **143** 1821 (1996).
8. M. Antaya, J. R. Dahn, J. S. Preston, E. Rossen, J. N. Reimers, *J. Electrochem. Soc.*, **140** 575 (1993).
9. P. Fragnaud, T. Brousse, D.M. Sleich, *J. Power Sources*, **63** 187 (1996).
10. H.J.M. Bouwmeester, A.J. Burggraaf, "Principles of Main Experimental Methods", in: *CRC Handbook of Solid State Electrochemistry*, ed. P.J. Gellings and H.J.M. Bouwmeester, CRC Press, Boca Raton 1997.
11. X.Q. Yang, X. Sun, J. McBreen, *Electrochemistry Communications*, **2**, 100 (2000).
12. J.N. Reimers, J. Dahn, *J. Electrochem. Soc.*, **139** [8] 2091 (1992).
13. Y. Jang, B.J. Neudecker, N.J. Dudney, *Electrochem. and Solid State Letters*, **4** [6] A74 (2001).
14. G. Ceder, A. Van der Ven, *Electrochimica Acta*, **45** 131 (1999).
15. M. Mohamedi, D. Takahashi, T. Uchiyama, T. Itoh, M. Nishizawa, I. Uchida, *J. Power Sources*, **93**, 93 (2001).
16. B.A. Boukamp, Equivalent Circuit Program (2000).
17. M.D. Levi, G. Salitra, B. Markovsky, H. Teller, D. Aurbach, U. Heider, L. Heider, *J. Electrochem. Soc.*, **146** [4] 1279 (1999).
18. D. Aurbach, *J. Power Sources*, **81-82** 95 (1999).

S Modelling of lithium intercalation

The intercalation behaviour in a LiCoO₂ RF-film has been studied with the Potentiostatic Intermittent Titration Technique (PITT) and Electrochemical Impedance Spectroscopy measurements (EIS). The Fourier transformed PITT-results and the EIS-spectra are complementary in the frequency domain, covering different frequency ranges. The equivalent circuit reported by Jamnik et al.[1] is used as a tool to interpret the experimental data. The electrochemical impedance attributed to charge-transfer processes is observed to increase with increasing degree of lithium intercalation. The diffusion related impedance is relatively constant as a function of cell potential. The derived chemical diffusion coefficient is estimated approximately at $10^{-11} \text{cm}^2 \cdot \text{s}^{-1}$ based on the transformed PITT results, while the EIS results predict a value around $10^{-6} \text{cm}^2 \cdot \text{s}^{-1}$. This difference is explained with a dragging influence of phase boundary movement on lithium diffusion.

5.1 Introduction

Basically, the charge and discharge process of the lithium cell is equivalent to the displacement of lithium from one electrode to the other, which increases or decreases the mutual energy difference, respectively. In this chapter the driving force behind the lithium transport in the cell is discussed and subsequently related to the Gibbs free energy of the reactions occurring at the electrodes.

The driving force induces a lithium flux in the intercalation electrode, which is related to the conductivity of the individual charge carriers. In addition to the previous chapters, the possibility of a significant influence of the electronic charge carriers on the flux is considered, as the fully intercalated LiCoO_2 is known to exhibit semiconducting behaviour. The electro-neutrality condition imposes an equal flux of positive and negative charges and, hence, an ambipolar diffusion model is derived. In this case a limited electronic conductivity could increase the 'drag' on the ionic diffusion and thus restrain the total lithium transport rate.

The time-dependent diffusion equations for the electronic and ionic charge carriers become complicated, if simultaneous lithium intercalation and electrical charge accumulation are considered. Jamnik *et al.* [1] have proposed a transition line model to describe the electrochemical behaviour of an intercalation electrode. We have used their approximating equivalent circuit to model our measurement data. Thus we have obtained a good indication of the separate processes contributing to the observed intercalation impedance.

In this work, EIS measurements are used to characterise the intercalation impedance as a function of the cell potential. Unfortunately, the low frequency measurements are limited by external noise to about 10mHz in our set-up. Time domain voltage step measurements (PITT) can give accurate current response for long times. Fourier Transformation yields an impedance spectrum well down to the micro hertz range. However, the initial and final states are different for this voltage step method.

Additional electrical conductivity measurements are performed in order to distinguish the partial contributions of the electronic and ionic charge carriers to the total conductivity.

5.2 Theory of lithium diffusion

5.2.1 Electro Motive Force

The standard electrochemical cell comprises two electrodes in contact with each other through a purely ion-conducting medium, *i.e.* electrolyte phase, and an external circuit for electron transport. The potential of the cell is called the Electro Motive Force ($=EMF$) and can be measured with a voltmeter connected between the current collectors of both electrodes (CC_{CE}) and (CC_{WE}). Figure 5.1 shows the lithium cell configuration and explains the abbreviations used.

$$EMF = \phi(CC_{WE}) - \phi(CC_{CE}) \quad (5.1)$$

The origin of the observed cell voltage is derived in this section. The electrical potential ϕ is related to the electrochemical potential $\bar{\mu}$ of electrons

$$\bar{\mu}_e = \mu_e + q_e \cdot \phi \quad (5.2)$$

where μ_e is the chemical potential of the electrons and q_e is the electron charge. As both leads consist of the same metal, the chemical potential μ_e of the electrons in both current collectors is equal:

$$\mu_e(CC_{CE}) = \mu_e(CC_{WE}) \quad (5.3)$$

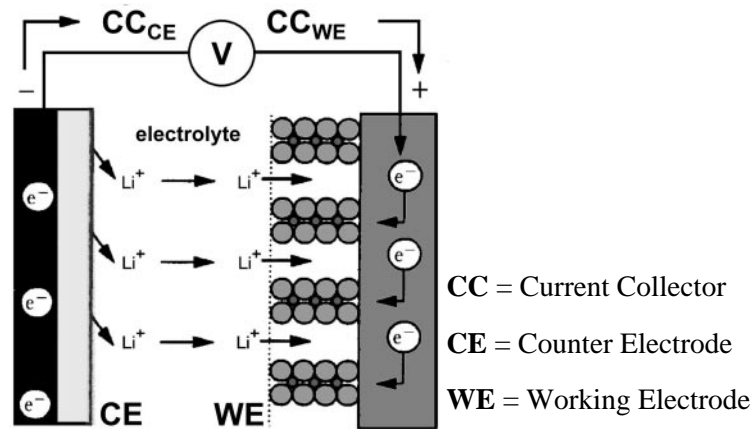


Figure 5.1: Schematic representation of the lithium cell during discharge; the electrons pass through an external circuit, while the lithium ions diffuse/migrate through the electrolyte solution.

Contact of dissimilar materials results in a so-called electrical contact potential in order to equilibrate the chemical potential of electrons. Incorporating the electrochemical potential $\bar{\mu}_e$ in equation (5.1) leads to:

$$q_e \cdot EMF = \bar{\mu}_e(CC_{CE}) - \bar{\mu}_e(CC_{WE}) \quad (5.4)$$

Equation (5.4) implies that the measured EMF relates to the difference in electrochemical potential of the electrons between the current collectors. In an open circuit situation (infinite impedance of the voltmeter), local equilibrium exists between the current collectors and the electrodes. As these components are regarded to be electronic conductors, their electrochemical potential of electrons on either side of the interface is assumed to be equal

$$\begin{aligned} \bar{\mu}_e(CC_{CE}) &= \bar{\mu}_e(CE) \\ \bar{\mu}_e(CC_{WE}) &= \bar{\mu}_e(WE) \end{aligned} \quad (5.5)$$

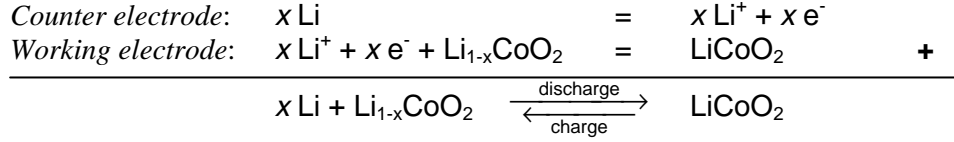
Expression (5.4) can be rewritten using the statements above

$$q_e \cdot EMF = \bar{\mu}_e(CE) - \bar{\mu}_e(WE) \quad (5.6)$$

Thus, the measured EMF directly relates to the electrochemical potential difference of the electrons between both electrodes, indifferent of the electrode reactions. Contact potentials at the interface $(CC_{CE})|(CE)$ and $(WE)|(CC_{WE})$ compensate each other as long as the temperature is constant. The type of metal chosen for the current leads should not influence the measurement.

5.2.2 The intercalation reaction

The half-cell reactions occurring at the electrodes are formulated below. The individual lithium ion and electron cancel out after addition. However, for the description of the (dynamic) chemical potential of the intercalation electrode itself, it is sufficient to consider only the separate activity of the lithium ions and electrons. The chemical potential of the oxide host is fixed by these two independent quantities, as can be shown using the Gibbs-Duhem relation.



The CE serves as lithium source. Upon discharging, equivalent amounts of lithium ions are released into the electrolyte solution as there are intercalated into the WE. The lithium concentration in the electrolyte solution does not change, due to the electro-neutrality condition. Upon charging the direction of charge carrier transport is reversed.

Now the electrochemical potential of the lithium ions in the galvanic cell is considered, as done for the electrons in the previous section. In the electrolyte phase there is no electrochemical potential gradient for lithium ions, due to the high ionic conductivity

$$\bar{\mu}_i(\text{electrolyte}) = \text{constant} \quad (5.7)$$

The lithium ions in the electrolyte phase are in local equilibrium with those in both electrodes; hence their electrochemical potential is equal

$$\bar{\mu}_i(CE) = \bar{\mu}_i(WE) \quad (5.8)$$

Equation (5.6) can be rewritten using the combined expressions for the electrochemical potential of electrons and lithium ions

$$q_e \cdot EMF = (\bar{\mu}_i(CE) + \bar{\mu}_e(CE)) - (\bar{\mu}_i(WE) + \bar{\mu}_e(WE)) \quad (5.9)$$

The collective electrochemical potential of the lithium ions and electrons is equal to that of a neutral lithium particle. As the electrical potential does not affect neutral species, only the chemical potential needs to be considered

$$\begin{aligned}
 q_e \cdot EMF &= \bar{\mu}_{Li}(CE) - \bar{\mu}_{Li}(WE) \\
 &= \mu_{Li}(CE) - \mu_{Li}(WE)
 \end{aligned} \quad (5.10)$$

$$EMF = \frac{1}{F} (\Delta G_{Li}^0(CE) - \Delta G_{Li}(WE))$$

The difference in lithium ‘energy state’ between the electrodes determines the

EMF of the cell. The CE consists of bulk lithium and thus its energy level is equal to the standard Gibbs free energy, when normalised for one mole of lithium. The Gibbs free energy of lithium in the WE depends on the degree of lithium intercalation and is increased with discharging (intercalation) or decreased with charging (de-intercalation).

5.2.3 Electrical potential distribution in the galvanic cell

An electrical potential gradient in the form of an ionic adsorption- or electrical double layer compensates a chemical potential difference between two adjacent elements of the galvanic cell, provided equal electrochemical potentials exist due to local equilibrium (see Eq. 5.2). As the secondary lithium cell generates high voltages, it is valuable to predict the location of the electrical potential jumps.

The galvanic cell depicted in Figure 5.1 is considered, assuming a zero-current situation and absence of lithium transport across the internal interfaces (*i.e.* no leakage current). Figure 5.2 schematically shows the electrochemical potential of the electrons and lithium ions as well as the separate contributions of the chemical and the electrical potential for the entire cell. The development of the electrical potential distribution is elucidated in the following paragraphs.

The CE consists of metallic lithium and exhibits a fixed chemical potential. The contact potential with the current collector is constant and of no influence to the *EMF*, as it is compensated by the contact potential of the WE|CC interface. The electrical potential difference between the CE and the electrolyte is also constant and depends on the electrolyte material and its lithium ion activity.

The chemical potential of lithium in the WE is determined by the degree of intercalation and consists of a contribution of the lithium ions and the electrons (Eq.5.9). It is, however, necessary to gain further information on the defect chemistry of the intercalation electrode before further statements concerning the electrical potential distribution can be made [2]. As an example, it is now assumed that the chemical potential of the lithium ions in the intercalation electrode varies with the activity of the lithium and that the chemical potential of electrons in this electrode is constant due to a high density of states. As the electrochemical potential of ions across the electrolyte|WE interface is constant, the electrical potential gradient follows the variation in lithium activity in the

electrode. A large electrical potential gradient at this particular interface could lead to electrolyte decomposition.

The electrical potential jump at the WE|CC_{WE} interface is fixed, as the chemical potential of electrons is assumed constant. An example of the opposite situation is Ag_{2-x}S. Here the electrical potential gradient at the WE|CC_{WE} interface varies as a function of the degree of intercalation due to the influence of the chemical potential of electrons, while the silver ion activity is virtually constant [2].

The difference of the electrochemical potential of the electrons between the CE and WE, interpreted as the *EMF*, also induces an electrochemical potential gradient of electrons, and consequently a chemical potential gradient of electrons, across the electrolyte phase. This is the driving force behind internal lithium diffusion and in case of significant electron mobility causes self-discharge.

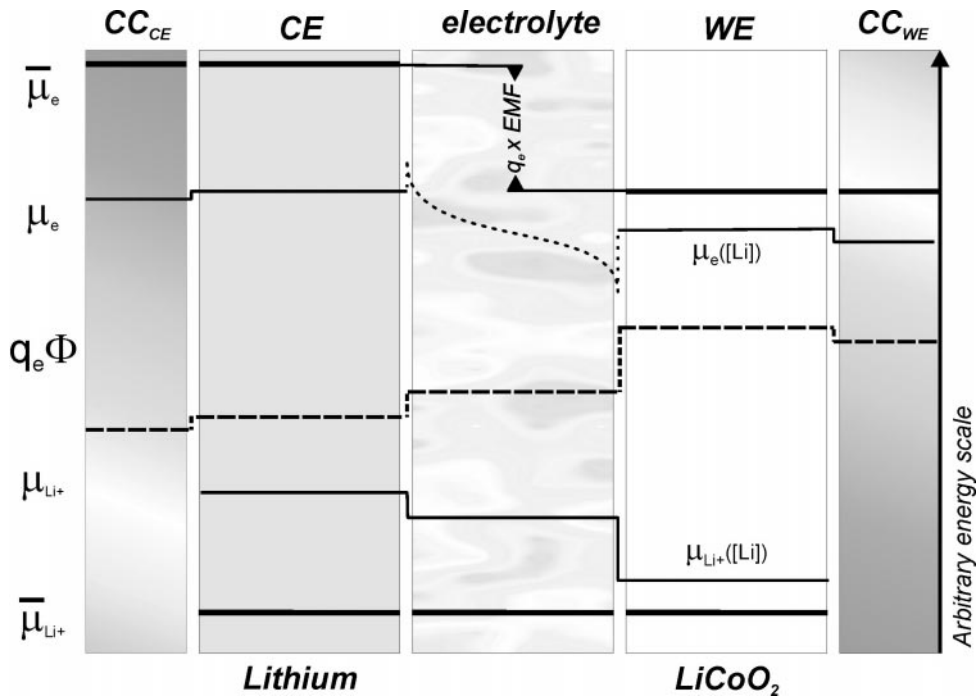


Figure 5.2: Representation of the electrochemical potential distribution of lithium ions and electrons in the elements of a galvanic cell. The separate contributions of the chemical potential of the electrons and ions are also specified together with the electrical potential. The chemical potential gradient of electrons in the electrolyte is arbitrarily drawn. The product $q_e \times EMF$ is indicated according to equation (5.6).

5.2.4 Lithium flux in the intercalation electrode

In this section the lithium transport within the intercalation electrode is considered. Expressions are first formulated for the steady-state situation, which also serve as boundary conditions for solving the time-dependent differential equations.

The lithium flux is related to the product of its electrochemical potential gradient and the effective lithium conductivity σ_{Li} [3]

$$J_{Li} = -\frac{\sigma_{Li}}{z^2 q_e^2} \nabla \bar{\mu}_{Li} \quad (5.11)$$

The fluxes of the ionic and electronic charge carriers are directed in the same way, so that the electrical potential gradient has no influence on the neutral lithium transport [4]. Therefore:

$$J_{Li} = -\frac{\sigma_{Li}}{z^2 q_e^2} \nabla \mu_{Li} \quad (5.12)$$

Although the ionic and electronic charge carrier fluxes are coupled through the electro-neutrality condition, the individual conductivity could be different. The effective lithium conductivity can be interpreted using the ambipolar diffusion model

$$\begin{aligned} \frac{1}{\sigma_{Li}} &= \left(\frac{1}{\sigma_i} + \frac{1}{\sigma_e} \right) \\ J_{Li} &= -\frac{1}{z^2 q_e^2} \left(\frac{1}{\sigma_i} + \frac{1}{\sigma_e} \right)^{-1} \nabla \mu_{Li} \end{aligned} \quad (5.13)$$

The conductivity of a charged species j is proportional to the product of its concentration and the electrical mobility u_j . This latter parameter is related through the species charge $z_j q_j$ (here $z=1$) to the mechanical mobility b_j , which can be correlated with the component diffusion coefficient D_j using the Nernst-Einstein relation

$$\sigma_j = z_j q_j u_j C_j = z_j^2 q_j^2 b_m C_j \equiv z_j^2 q_j^2 \frac{D_j}{kT} C_j \quad (5.14)$$

The flux expression in (5.13) can now be rewritten in terms of the charge carrier component diffusion coefficients D and concentrations C

$$J_{Li} = -\frac{1}{kT} \left(\frac{1}{C_i D_i} + \frac{1}{C_e D_e} \right)^{-1} \nabla \mu_{Li} \quad (5.15)$$

Equation (5.12) is rewritten as a function of the concentration gradient by substituting an expression for the chemical potential gradient of lithium

$$\nabla \mu_{Li} = \left(\frac{\partial \mu_{Li}}{\partial C_{Li}} \right) \nabla C_{Li} \quad (5.16)$$

The term $(\partial \mu_{Li} / \partial C_{Li})$ describes the activity of the lithium and is reflected by the experimental Open Circuit Potential (=OCP) profile as a function of the degree of lithium intercalation

$$\left(\frac{\partial \mu_{Li}}{\partial C_{Li}} \right) = \frac{z q_e}{kT} \cdot \left(\frac{dE}{dx} \right) \quad (5.17)$$

Substitution of (5.16) in equation (5.15) leads to

$$J_{Li} = -\frac{1}{kT} \left(\frac{1}{C_i D_i} + \frac{1}{C_e D_e} \right)^{-1} \cdot \left(\frac{\partial \mu_{Li}}{\partial C_{Li}} \right) \nabla C_{Li} \quad (5.18)$$

which is a different form of Fick's first law of diffusion

$$J_{Li} \equiv -\tilde{D} \nabla C_{Li} \quad : \quad \text{Fick's first law} \quad (5.19)$$

The chemical diffusion coefficient \tilde{D} incorporates the mobility and the activity of lithium. The term $(\partial \mu_{Li} / \partial C_{Li})$ can be evaluated further using $\mu_j = kT \ln(a_j)$ and neglecting any mutual influence of the charge carriers

$$\begin{aligned} \left(\frac{\partial \mu_{Li}}{\partial C_{Li}} \right) &= \left(\frac{\partial \mu_{Li}}{\partial \ln(C_{Li})} \right) \left(\frac{\partial \ln(C_{Li})}{\partial C_{Li}} \right) = kT \left(\frac{1}{C_i} \left(\frac{\partial \ln(a_i)}{\partial \ln(C_i)} \right) + \frac{1}{C_e} \left(\frac{\partial \ln(a_e)}{\partial \ln(C_e)} \right) \right) \\ &= kT \left(\frac{w_i}{C_i} + \frac{w_e}{C_e} \right) \end{aligned} \quad (5.20)$$

where w_i and w_e are the thermodynamic enhancement factors of lithium ions and electrons, respectively. Their values approach unity for dilute defects. Hence, for the indicated limiting situations, equation (5.18) can be simplified to the four expressions listed in Table 5.1.

Table 5.3: A list of simplified expressions derived from equation (5.18) for four limiting situations

| Situation | Example | Result |
|-------------------------------------|----------------------|---|
| $C_e D_e \gg C_i D_i$ $C_e \gg C_i$ | electronic conductor | $J_{Li} = -D_i \nabla C_{Li}$ |
| $C_e D_e \gg C_i D_i$ $C_e \ll C_i$ | mixed conductor | $J_{Li} = -D_i \frac{C_i}{C_e} \nabla C_{Li}$ |
| $C_e D_e \ll C_i D_i$ $C_e \gg C_i$ | mixed conductor | $J_{Li} = -D_e \frac{C_e}{C_i} \nabla C_{Li}$ |
| $C_e D_e \ll C_i D_i$ $C_e \ll C_i$ | ionic conductor | $J_{Li} = -D_e \nabla C_{Li}$ |

One should be careful in drawing conclusions from these simplified formulas. For example, the second situation gives the impression that decreasing the electron concentration enhances the lithium flux. This seems illogical. For correct statements one should re-observe the initial equations, where only few substitutions have been made. For clarity transport numbers t_j are used to view the electronic and ionic conductivity separately:

$$t_j = \frac{\sigma_j}{\sum_n \sigma_n} \quad (5.21)$$

$$t_i + t_e = \frac{\sigma_i}{\sigma_i + \sigma_e} + \frac{\sigma_e}{\sigma_i + \sigma_e} = 1$$

$$J_{Li} = -\frac{1}{q^2} \left(\frac{1}{\sigma_i} + \frac{1}{\sigma_e} \right)^{-1} \nabla \mu_{Li} = -\frac{1}{q^2} \sigma_{Li} t_e t_i \nabla \mu_{Li}$$

Substitution of t_i leads to

$$J_{Li} = -\frac{1}{q^2} \sigma_{tot} t_e (1 - t_e) \nabla \mu_{Li} \quad (5.22)$$

Expression (5.22) states correctly that the flux of neutral lithium particles is maximum at $t_e=0.5$ (equal ionic and electronic conductivity). In general, any increase in concentration of charge carriers contributes to the total conductivity and thus enhances lithium transport.

5.2.5 Lithium concentration profile upon intercalation

In the previous section the lithium transport was discussed, considering the lithium ions and the electrons to be the only charge carriers. The electro-neutrality condition directs an equal concentration of both carriers and couples their fluxes. However upon lithium intercalation, the lithium ions enter the WE at the electrolyte interface, while the electrons are injected from the current collector. The lithium concentration profile is determined by the (local) conductivity of the individual charge carriers.

Two limiting situations can be discerned, if the difference between the conductivity of the two charge carriers is large.

A Limiting ionic conductivity or: $t_i \ll t_e$

B Limiting electronic conductivity or: $t_i \gg t_e$

The expected lithium concentration profiles upon intercalation are drawn in Figure 5.3 for both cases. The activity of the lithium ions in the electrolyte and the activity of the electrons in the current collector are assumed constant. In situation A the lithium ions have the lowest diffusion rate. The influence of the electrons is virtually imperceptible (first case in Table 5.3) and lithium intercalation proceeds from the interface with the electrolyte solution. In situation B the diffusion of electrons is rate-limiting and the intercalation appears to proceed from the interface with the current collector (final case in table 5.3). When local equilibrium is regained, the concentration profiles of the charge carriers in the intercalation electrode level off at a new concentration.

Note that the lithium chemical potential gradient can differ from the concentration profile, as it is influenced by the local activity and mobility of the individual charge carriers in a current-drawing situation. This problem is considered in the next section.

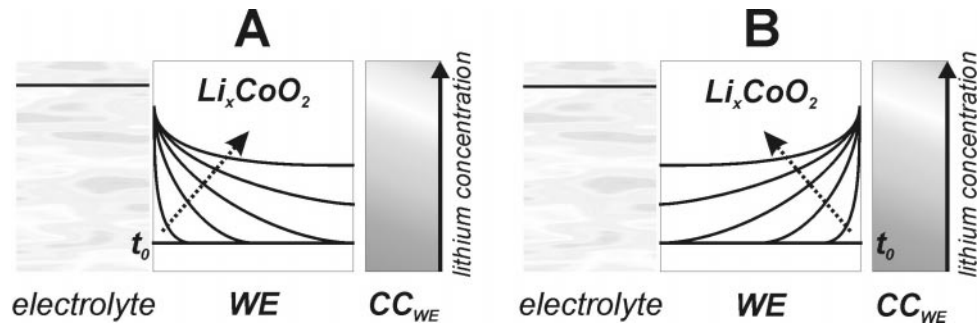


Figure 5.3: The progressing lithium concentration profile in the WE upon intercalation is drawn for two limiting cases A and B (see text). The lithium ion concentration in the electrolyte phase is assumed constant.

5.2.6 Chemical potential variation in a closed circuit

The intercalation of lithium into the LiCoO_2 electrode can be described with a lithium mass balance and subsequently the time-dependent concentration profile resolved using the derived steady-state flux expressions as boundary condition. However, the electrochemical system is non-ideal and too many processes are simultaneously involved in the intercalation process to solve the differential equations analytically.

An alternative approach to a complete description of the galvanic cell behaviour is the construction of a finite element model where the differential equations, which correspond to the involved processes, are solved numerically for all node points [6]. Bergveld *et al.* [7] has reported elaborate models for the Ni-Cd battery system and the lithium ion battery.

Usually, the charge carrier fluxes are translated to electrical currents, as the experiments are also based on electrical measurements [8]

$$i = F \sum_n z_j J_j \quad (5.23)$$

Jamnik *et al.* [1] have modelled the chemical potential change of neutral lithium as function of an *ac*-current perturbation, considering separate diffusion of electronic and ionic charge carriers. Different ratios of the electronic/ionic conductivity are simulated for the intercalation electrode. Figure 5.4 shows two limiting situations. In case of a large ionic resistance the chemical potential of

lithium changes mainly against the interface with the electrolyte solution. However, in case of limited electronic conductivity the chemical potential variation occurs mainly against the interface with the current collector.

A similarity exists with the location of the chemical potential gradients discussed in the previous paragraph. In the zero-current situation, the charge carrier exhibiting the largest activity variation as a function of lithium intercalation, induces the major chemical potential gradient and corresponding electrical potential jump. Here, in a dynamic situation, the major $\Delta\mu_{Li}$ is observed at the ‘source’ interface for the charge carrier with the lowest mobility (highest resistance). The lithium chemical potential change is attributed to this particular species, which apparently exhibits high activity variation. As a result of the dynamic chemical potential of the rate-limiting charge carrier, a large electrical potential variation is introduced as well.

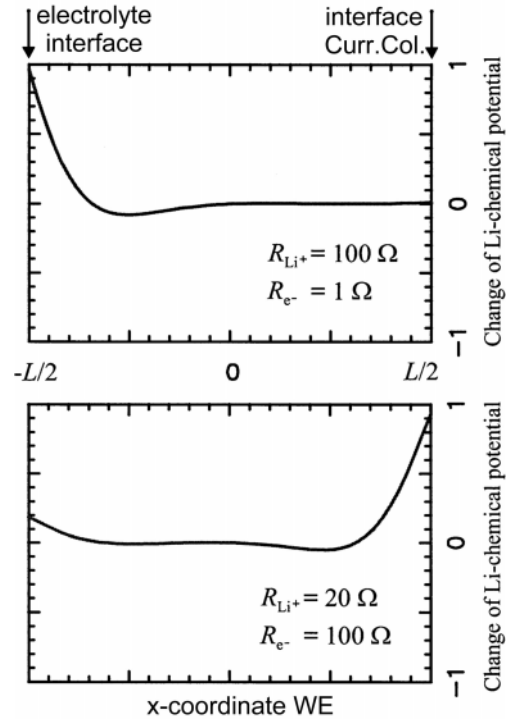


Figure 5.4: The change of chemical potential of lithium caused by the ac-signal perturbation, plotted as function of spatial coordinate of the intercalation electrode for two different ratios of electrical and ionic conductivity [1].

5.2.7 Finite Space Warburg network model

An equivalent circuit is used to describe the observed impedance characteristics with a network of separate electrical elements, which exhibits the same frequency dispersion as the electrochemical system under study. The schematic network model for a Finite Space Warburg shown in Figure 5.5, represents a boundary value solution to Fick’s second law of diffusion [9].

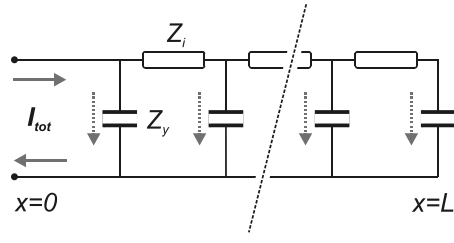


Figure 5.5: Ladder network representing the Finite Space Warburg element.

A more appropriate network model for the intercalation electrode is shown in appendix A, where both the combined ionic and electronic charge transport as well as the capacitive coupling between both current fluxes is simultaneously evaluated [10]. The model shown in Figure A.1 can be simplified to describe finite ionic diffusion, by ignoring the

impedance of the electronic rail. In the limit $R_e \rightarrow 0$, equation (A.9) transforms into:

$$Z_{tot}(\omega) = Z_0(\omega) \coth(LQ(\omega))$$

$$\text{with : } Z_0(\omega) = \sqrt{\frac{Z_i}{Y_y}} = \sqrt{Z_i Z_y}, \quad Q(\omega) = \sqrt{Z_i Y_y} \quad (5.24)$$

The remaining expression is typical of a Finite Space Warburg element (FSW). The total ionic resistance is determined by the charge carrier concentration and mobility and the film thickness L . The argument $Q(\omega)$ is defined as a function of the chemical diffusion coefficient and the quantity Z_0 changes accordingly

$$Q(\omega) \equiv \sqrt{\frac{j\omega}{\tilde{D}_i}}$$

$$\text{with : } Z_0 = \frac{RT}{z^2 F^2 A C_i^0} \left(\frac{d \ln a_{Li}}{d \ln c_{Li}} \right) \quad (5.25)$$

$$Z_{tot}(\omega) = \frac{Z_0}{\sqrt{j\omega \tilde{D}_i}} \coth \left(L \sqrt{\frac{j\omega}{\tilde{D}_i}} \right)$$

For two limiting cases the formula simplifies [11]

$$\begin{aligned} \frac{\omega L}{\tilde{D}_i} \gg 10 &\Rightarrow Z_{tot}(\omega) = \frac{RT}{(zF)^2} \left(\frac{L}{c_{Li} \tilde{D}_i} \right) \cdot \left(\frac{j\omega}{\tilde{D}_i} \right)^{-1/2} = \frac{RT}{(zF)^2} (c_{Li}^2 \tilde{D}_i)^{-1/2} \cdot (j\omega)^{-1/2} \\ \frac{\omega L}{\tilde{D}_i} \ll 0.1 &\Rightarrow Z_{tot}(\omega) = \frac{RT}{(zF)^2} \left(\frac{L}{c_{Li} \tilde{D}_i} \right) \cdot \left(3 - j \frac{\tilde{D}_i}{\omega L^2} \right) = 3Z_0 - \frac{j}{\omega C} \end{aligned} \quad (5.26)$$

In the first case, the perturbation frequency is high and thus the wave period small compared with the characteristic diffusion length. Semi-infinite Warburg impedance is observed, showing a 45° line in the impedance plot. This is the equivalent of semi-infinite diffusion in the time domain, where the diffusion coefficient is small compared with the characteristic diffusion length $\omega \gg (L^2/\tilde{D})$.

In the second case the diffusion process encounters the geometric boundaries of the sample. Hence, the intercalation profile becomes ‘flat’ and capacitive behaviour is observed at low frequency. Note, that in intercalation electrodes a considerable portion of the capacitive behaviour can be attributed to the chemical intercalation of the electrode itself. In literature equivalent circuits are presented, which describe the diffusion behaviour and the intercalation capacity with a semi-infinite Warburg and a capacitance in series [12]. This is physically incorrect.

5.2.8 Simplified equivalent circuit

Jamnik *et al.* [1,13] have modelled the intercalation behaviour of a LiMn_2O_4 film by discretisation of the electrode and numerically solving the differential equations separately for the ionic and the electronic rail at all loci. This transmission line model is simplified to an equivalent circuit shown in Figure 5.6 according to the following assumptions:

- The transport and accumulation of neutral lithium can be described by a finite length (O) and a finite space diffusion element (T)*, respectively, connected in series to the total real impedance of the parallel ionic and electronic rails. Note: in case the electronic resistance becomes insignificant compared with the ionic resistance, the pre-factors of the *coth* and the *tanh* terms in the original impedance equation become equal and substitution with one diffusion term is allowed according to $\tanh(x) + \coth(x) = 2 \coth(2x)$. This coincides with the first situation in Table 5.1, which describes single particle diffusion. However, this does not follow from the equivalent circuit representation in Figure 5.6.

* Symbols applied as defined by Boukamp [11].

- In the electrode bulk all the elements are spatially invariant as no equilibrium space charges are present. Local electro-neutrality is assumed. Hence, the electrical bulk capacitance can be replaced by a single capacitance C_{dl} . This double layer capacitance is the geometric mean of the sample dielectric and chemical capacitances. Since these are arranged in a transmission line the term “diffuse layer capacitance” is very meaningful*

$$C_{dl} = \sqrt{C_i^{chem} C_i^{dielec}} = \epsilon \epsilon_0 A \sqrt{\frac{z^2 q^2 c}{\epsilon \epsilon_0 k T}} = \epsilon \epsilon_0 \frac{A}{L_D} \quad (5.27)$$

$$\text{with } L_D = \sqrt{\frac{\epsilon \epsilon_0 k T}{z^2 q^2 c}}$$

- The carrier density in the interfacial region of the electrode in contact with electrolyte solution is different from the bulk, since the underlying structure differs from the regular structure in the bulk. The complicated capacitive network is approximated by two parallel elements ($R_{CT}Q_{CT}$) reflecting the diffuse layer capacitance. This layer is supposed to be involved in the charge transfer to the lithium ions in the electrolyte solution.

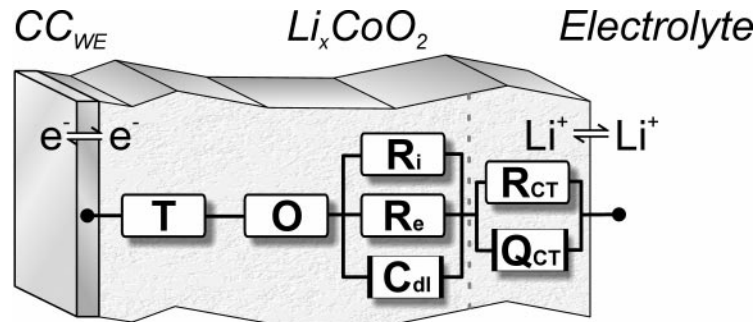


Figure 5.6: The equivalent circuit proposed by Jamnik et al.[1] to describe the behaviour of the intercalation electrode. The individual elements are explained in the text.

* Note, that the interfacial capacitance does not refer to the parameter C_{dl} defined in equation (5.31). Under selective blocking conditions the interfacial capacitance is determined by the blocked (not necessarily majority) carrier and thus by the Debye length L_D referring to the one (blocked) carrier.

5.3 Experimental

Electrochemical experiment - Sequential Potentiostatic Intermittent Titration Technique (PITT) and Electrochemical Impedance Spectroscopy (EIS) measurements were conducted on a 0.5 μ m RF-film of LiCoO₂ on silicon (deposition conditions in Chapter 3). The potential was increased from 3.60V to 4.20V in 10mV steps. At each step the current decay was measured (sample rate: 0-10s:100Hz, 10-300s:10Hz, 300-3000s:1Hz) and subsequently an impedance plot was recorded (10kHz-10mHz, ~8 steps /decade; 10mV) before proceeding to the following step.

Frequency transformation - The Fourier transform of the time domain measurement can serve as extension to lower frequencies for the EIS measurement. Comparison of both datasets was done in the frequency domain. Therefore, the PITT data points were converted using Fourier transformation (referred to as: TtF-PITT data). As the emphasis is placed on the very low frequency response (down to 100 μ Hz) a rather simple discrete Fourier transformation was used. For the finite time span, $t_0 - t_N$, the following expression was used:

$$\bar{X}(\omega) = \int_0^{t_N} X(t) \cdot e^{-j\omega t} dt \approx \sum_{k=1}^N \frac{X(t_k) - X(t_{k-1})}{t_k - t_{k-1}} (\cos \omega t - j \sin \omega t) \quad (5.28)$$

where $X(t)$ is the measured variable. At $t = t_N$ the signal has not yet reached a stable value, hence it is important to extrapolate the data to $t \rightarrow \infty$. This is accomplished using a simple exponential decay:

$$X(t) = X_0 + X_1 e^{-t/\tau} \quad (5.29)$$

where X_0 represents the dc term. This is in effect the leakage current and is subtracted from the entire signal before the Fourier transformation. The exponential decay function is fitted to the last 10% of the data

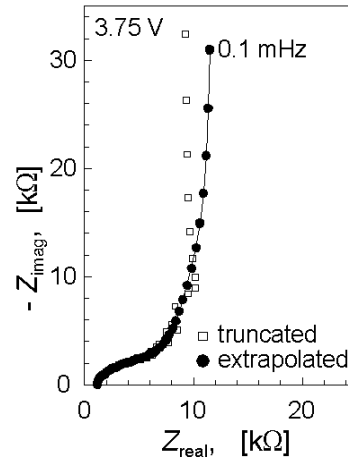


Figure 5.7: Comparison between Fourier transformed impedance, using truncated time set (□) or extrapolated time set (●).

set. It was observed, that this extrapolation especially improved the mid-frequency section of the transformed impedance spectra (noise reduction).

It can be argued that this exponential decay modelling for $t > t_N$ implicitly introduces pure capacitive behaviour at very low frequencies. But this capacitive behaviour was already observable in the impedance spectra when the transformation was truncated at $t = t_N$. The capacitive behaviour also follows from the theoretical considerations of the overall electrode impedance.

Electronic conductivity measurement - The electronic conductivity was measured on a LiCoO₂ thin film, RF-sputtered with a 6" LiCoO₂ target on an undoped 4" silicon wafer using the Nordico Model NM-2000 set at 500W RF-power and a background gas pressure of 2.5mbar, Ar:O₂ ratio of 3:1. The thickness was measured on a Dectac 8 profilometer. Test structures were patterned lithographically and wet-etched rapidly using 50% HF. Silver paint was applied to establish electrical contact with the bonding pads. A *dc*-current (0.1-2.5μm) was applied with an Autolab potentiostat through the outer pads, while the potential gradient was recorded with a Keithley Voltmeter between two intermediate pads. The temperature of the wafer was controlled between 15° and 40°C with two underlying peltier elements and an accurate AD590 temperature sensor (details in Appendix C).

5.4 Results and Discussion

In this section the experimental EIS data and the Frequency Transformed GITT data are both described using the simplified equivalent circuit proposed by Jamnik *et al.* [1]. This equivalent circuit is preferred over the modified Randles circuit used in Figure 4.8, as it has a profound physical basis and shows a more accurate fit to the data. Moreover, the Randles circuit was developed for metal deposition on a blocking electrode with a diffusion layer in the electrolyte solution.

The impedance plot in Figure 5.8 shows both the EIS-data and the transformed TtF-PITT data recorded at a cell potential of 3.80V against lithium. The two measurement techniques cover a different frequency range of the impedance spectrum, but the results are expected to be complementary. Indeed the overlapping mid-frequency range shows good similarity. The EIS-data and the TtF-PITT data could both be fitted to the simplified equivalent circuit discussed

in the previous paragraph with an accuracy of χ^2 of $9.8 \cdot 10^{-6}$ and $5.4 \cdot 10^{-4}$, respectively. The relative errors between the data and the fit of $\Delta Z'$ and $\Delta Z''$ are plotted in the inset of Figure 5.8 as a function of frequency.

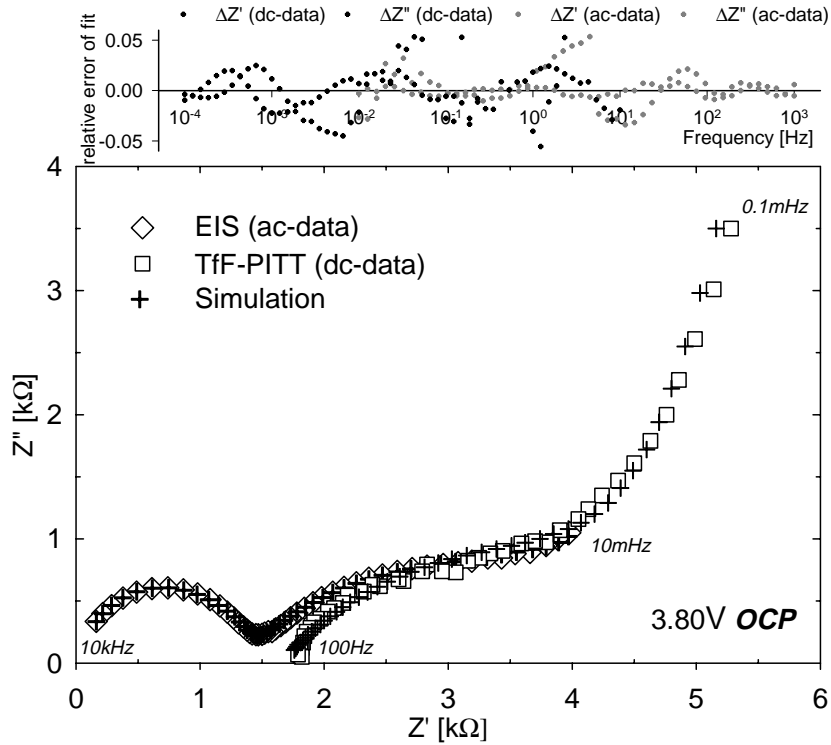


Figure 5.8: The impedance plot of the LiCoO_2 intercalation electrode showing the EIS-data and the TfF-PITT data measured at 3.80V against lithium. The simulation is based on the equivalent circuit shown in Fig. 5.6 and the relative errors of both fits are plotted in the inset graph for the $\Delta Z'$ and the $\Delta Z''$ as a function of frequency. Note the different frequency range of both measurement results.

For all cell potentials 3.60V, 3.61V ... 4.20V against lithium both impedance data sets have been fitted to the proposed model. The values of the equivalent circuit parameters of the EIS-data have been plotted as function of cell potential in Figure 5.9 and are discussed separately.

R_e As expected $R_{\text{electrolyte}}$ (EIS) shows a constant value of approximately 20Ω independent of the cell potential. It is therefore not plotted.

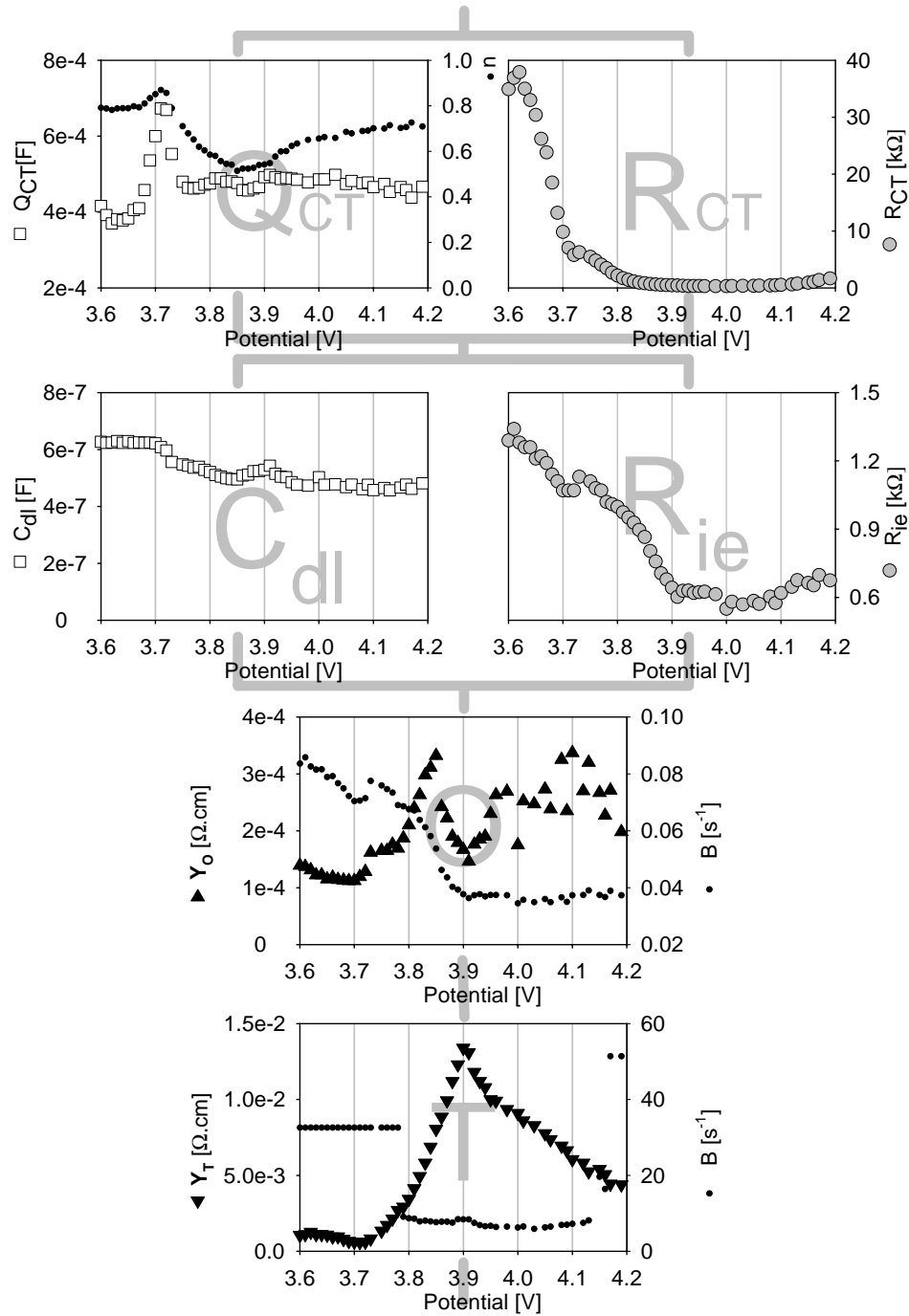


Figure 5.9: Values of the equivalent circuit elements describing the electrochemical intercalation impedance measured with EIS as function of the cell potential.

- R_{CT}Q_{CT}** The parallel elements (R_{CT}Q_{CT}) describe the interface of the intercalation host with the electrolyte solution. The impedance of this feature appears dominating at low cell potential (high degree of intercalation). The n -value of the constant phase element indicates a distributed capacitance, which can be expected as the element replaces a complicated ladder network. Above 3.72V the elements appear constant.
- R_{ie}C_{dl}** The (R_{ie}C_{dl}) circuit should be interpreted as (R_iR_eC_{dl}), which is the parallel impedance of the ionic conduction path, the electronic conduction path and the series capacitance of the displacement line, respectively. As expected, the value of C_{dl} is fairly independent of the cell potential. R_{ei} decreases with increasing potential up to 3.9V and appears to be affected by the phase transformation. In the impedance plot the semi-circle attributed to this RC-circuit has a characteristic frequency in the mHz range and is of minor importance.
- O** The hyperbolic cotangent produces a real impedance value at low frequency, which is an estimate for the diffusion resistance of the charge carriers. The parameters Y_0 and the argument B are fitted. According to the model based on Jamnik [1] the argument of the *coth* and the *tanh* should be identical.

$$Z_O = \frac{\tanh(B\sqrt{j\omega})}{Y_0(\sqrt{j\omega})} \quad (5.30)$$

- T** The hyperbolic tangent describes exhibits capacitive behaviour at low frequency and represents the chemical intercalation capacity. The Y_0 impedance trend appears similar to the Warburg value in Figure 4.14.

$$Z_T = \frac{\coth(B\sqrt{j\omega})}{Y_0(\sqrt{j\omega})} \quad (5.31)$$

The TtF-PITT impedance results can be described with the same equivalent circuit, only with lower accuracy in the high frequency range. The effective frequency range is 10Hz-0.1mHz. Therefore, the equivalent circuit is slightly modified: R_{sum}(Q_{CT}R_{CT})OT. As a result of this simplification the values of the parameters R_{sum} and Q_{CT} appear to comprise the neglected (Q_{dl}R_{ie}) impedance. The parameter R_{CT}(TtF-PITT) is similar to the R_{CT}(EIS) shown in Figure 5.9.

5.4.1 Exchange current density

The exchange current density i_0 can be derived from the charge transfer resistance element R_{CT} according to equation (4.6) and is plotted in Figure 5.10 as a function of potential. Mohamedi *et al.* [12] have observed the maximum of the exchange current density at the location of the current peak in the cyclic voltammogram. Here the current density curve can be fitted to a parabolic curve and with the maximum current around 3.99V. The symmetric nature suggests a physical origin of the exchange current characteristics as derived by Notten *et al.* [14], rather than an intrinsic material property.

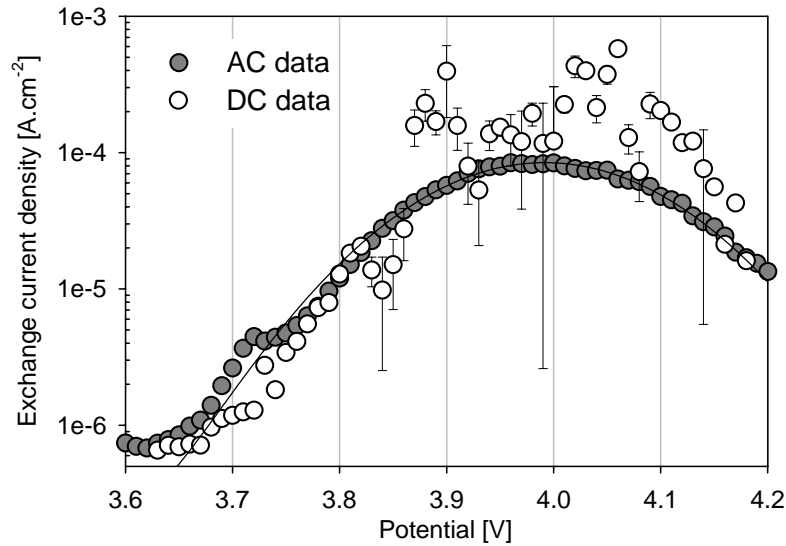


Figure 5.10: Exchange current density estimated from the R_{CT} element, as measured with Impedance spectroscopy (AC data) and the potential step technique (DC data).

5.4.2 Diffusion Resistance

Chemical Diffusion Coefficient - The factor B in the argument of the elements O and T , is related to the chemical diffusion coefficient \tilde{D} and the characteristic diffusion length L

$$B = \frac{L}{\sqrt{\tilde{D}}} \quad (5.32)$$

The chemical diffusion coefficient of lithium in the host structure is deduced from the factor B of the FLW element O and is plotted in Figure 5.11 as a function of potential against lithium for both data sets on separate axis. Since the polycrystalline film exhibits a columnar structure, the characteristic diffusion length is supposed to be equal to the film thickness ($0.5\mu\text{m}$). Under these conditions the chemical diffusion coefficient is of the order of $10^{-6}\text{cm}^2\cdot\text{s}^{-1}$ based on the EIS data and of the order of $10^{-12}\text{cm}^2\cdot\text{s}^{-1}$ based on the TtF-data. If the calculation were based on the argument of the FSW element T the diffusion quantity would be 10^{-12} - $10^{-10}\text{cm}^2\cdot\text{s}^{-1}$ and 10^{-11} - $10^{-9}\text{cm}^2\cdot\text{s}^{-1}$, respectively.

The argument factors B_O and B_T predict different diffusion coefficients. The values of the B_O factor are regarded more reliable than the B_T factor values, as the latter exhibit erratic jumps over orders of magnitude, suggesting possible fitting artefacts. Moreover, the ' B_O ' chemical diffusion coefficient calculated from the EIS data shows a trend as function of potential, which corresponds to that of the other circuit elements and the characteristics of the apparent diffusion coefficient shown in Figure 4.13. The fact that the TtF-PITT data predict a low and featureless diffusion coefficient could be related to another rate-limiting process, possibly phase-boundary movement.

The fitting parameter Y_0 expressed in equations (5.30) and (5.31) depends on the diffusion constant, the charge carrier concentration as well as the physical dimension of the system under study [12]. The real value of the diffusion resistance is calculated from equation (5.30) in the limiting situation $\omega \rightarrow 0$. Likewise, the real diffusion capacitance is calculated from equation (5.31). The equations reduce to

$$\begin{aligned} \lim_{\omega \downarrow 0} Z_O &= \frac{B_O}{Y_0} \equiv R_{diffusion} \\ \lim_{\omega \downarrow 0} Z_T &= B_T Y_0 \equiv C_{diffusion} \end{aligned} \quad (5.33)$$

The calculated values of $R_{diffusion}$ are plotted in Figure 5.12 for both data sets as function of cell potential. Note, that the value of $R_{diffusion}$ (EIS), plotted on the left axis, is greater by a factor 50 than $R_{diffusion}$ (TtF-PITT), due to the difference in the B factors. In both cases the resistance shows an increase at lower cell potentials.

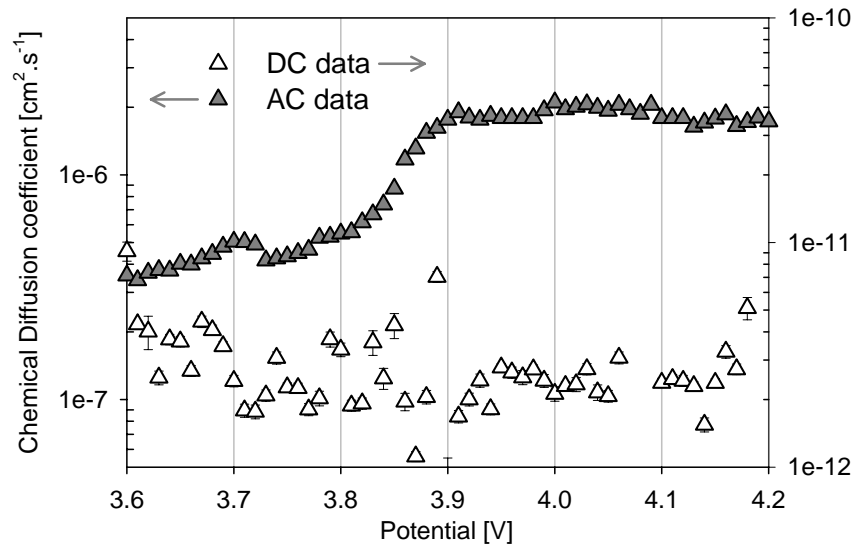


Figure 5.11: The chemical diffusion coefficient estimated with equation (5.32) from the data measured with Impedance spectroscopy (\blacktriangle AC data, plotted on left axis) and the potential step technique (\triangle DC data, plotted on right axis).

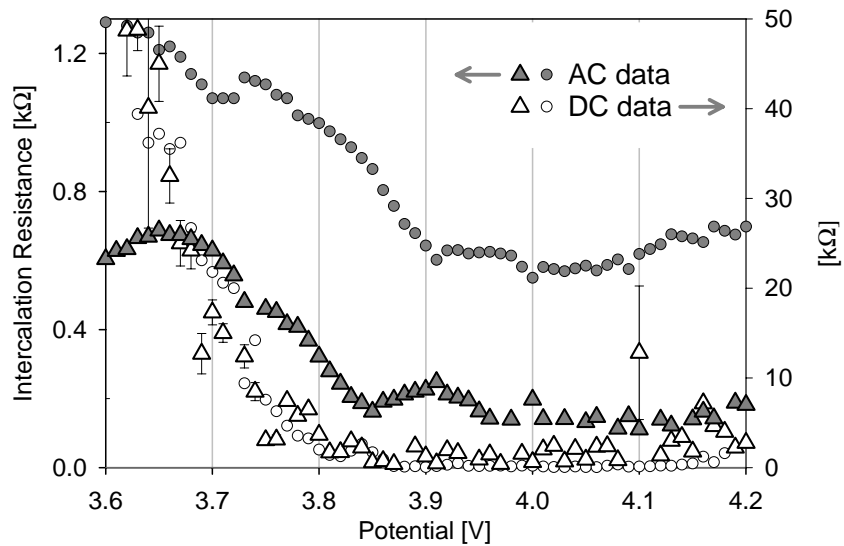


Figure 5.12: Diffusion resistance $R_{diffusion}$ calculated with equation (5.33) from the EIS- (\blacktriangle AC data, left axis) and the PITT results (\triangle DC data, right axis), compared with the values of their R_{ei} (\bullet) and $R_{CT\&ie}$ (\circ) elements, respectively, as function of potential.

The close correspondence of the calculated $R_{diffusion}$ (EIS) with the value of the R_{ie} element (EIS) and the $R_{diffusion}$ (PITT) to the R_{CT} element (PITT) is remarkable and suggests a large influence of the diffusion process on the impedance of the ionic and electronic charge carrier transport. Note, that in case of the TtF-PITT measurement the R_{ie} and the R_{CT} are combined, as these could not be distinguished, due to the limited high-frequency range of the measurement. This also explains the different characteristics of the curve.

5.4.3 Intercalation Capacity

The lithium intercalation capacity is related to the diffusion capacitance $C_{diffusion}$ (calculated according to equation (5.33)) and is plotted in Figure 5.13. A maximum is observed at 3.9V for both the EIS and the TtF-PITT data sets, which coincides with the OCP plateau potential of the intercalation profile (see Figure 4.4). The curves show a similar trend as function of potential, although the latter does exhibit a larger uncertainty. Note, that the peak in the Warburg element in Figure 4.14 is attributed to an apparent diffusion coefficient, while here it is interpreted as chemical storage capacity.

In Figure 5.14 the cumulative intercalation capacities derived from the $C_{diffusion}$ (EIS) and the $C_{diffusion}$ (TtF-PITT) quantities, are plotted as function of potential against lithium. The OCP intercalation profile of this particular sample is shown twice in the background, stretched along the x-axis to match both curves. Although the predicted capacity deviates from the actual intercalation capacity, the trend of the predicted potential profile is remarkably similar. The TtF-GITT data appear to provide a better fit in the supposed single-phase intercalation region above the plateau potential (3.9V), while the results based on the EIS data better describe the supposed two-phase region around the plateau potential of the intercalation profile. This distinction is to be expected, as the PITT measurement experiences interference by phase boundary movement (see Figure 4.7) as the initial and final state are different, while the EIS measurement is very sensitive to other parallel decomposition processes occurring at high cell potentials.

The voltage profile can also be calculated from the FLW element O , assuming the chemical diffusion coefficient is given by its argument. Using the predicted $\tilde{D} \approx 10^{-6} \text{cm}^2 \text{s}^{-1}$, the Y_O (EIS) data describes the OCP profile well and gives a realistic estimate of the actual intercalation capacity (not shown).

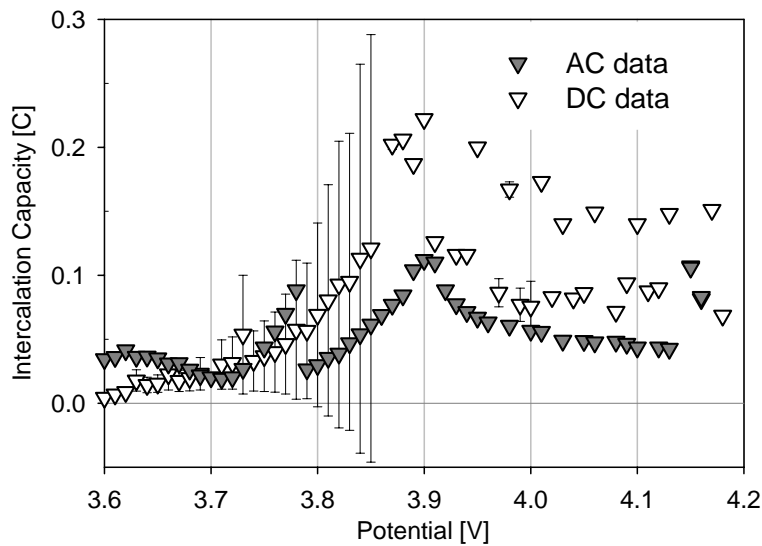


Figure 5.13: The calculated intercalation capacity of the LiCoO_2 electrode estimated from the data measured with Impedance spectroscopy (\blacktriangledown AC data) and the potential step technique (∇ DC data).

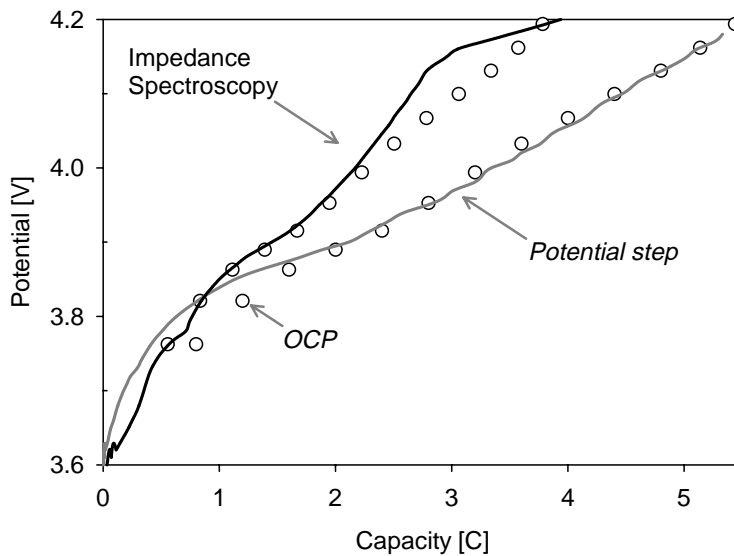


Figure 5.14: Cumulative intercalation capacity calculated from the TtF-PITT and EIS data plotted as a function of potential. The intercalation profile (\circ) is plotted twice in the background and stretched horizontally to match the predicted capacity.

5.4.4 Electronic resistance

The intercalation process encounters the major resistance at low potentials as depicted by the elements R_{CT} and R_{ei} , which describe the real impedance of the charge transfer region of the electrode and the combined real impedance of the electronic and ionic rail, respectively.

The electronic conductivity is determined in a separate experiment in order to distinguish the contribution of the electron mobility from that of the ionic transport to the observed impedance. *Dc*-current measurements on a stoichiometric LiCoO_2 thin-film structure (silicon substrate) show resistance-like behaviour. The results are plotted in Figure 5.15 for different temperatures. The film with thickness $\delta=285\text{nm}$ has a resistance of $2.7\Omega\cdot\text{cm}^{-1}$, averaged over the structures with bridge widths $d=1,2,5\text{mm}$. The resistance of the structure with $d=1\text{mm}$ is higher than expected. This is attributed to the relatively larger influence of under-etch of the LiCoO_2 film.

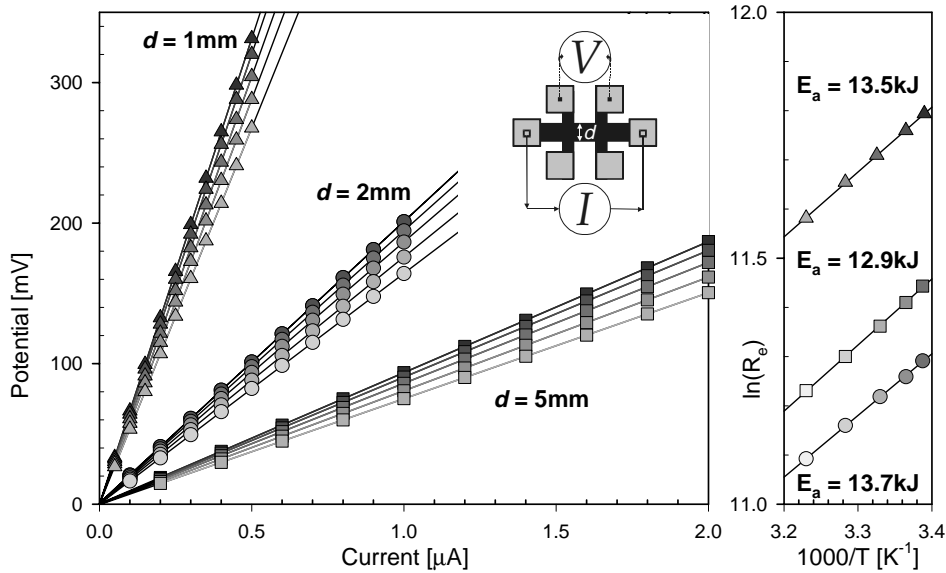


Figure 5.15: Electrical conductivity of LiCoO_2 on silicon wafer annealed at 600°C for 30min, measured as function of temperature (22.2°C , 24.2°C , 27.3°C , 31.6°C and 36.6°C , respectively; darker colours indicate higher temperature). The test structure is shown in the inset picture in which d represents the characteristic line width in mm.

Assuming the electronic conductivity occurs through small polaron hopping, the mobility can be described as [15]:

$$u_e = \left[(1 - c_e) q_e a^2 \frac{v_0}{kT} \right] \exp\left(-\frac{E_a}{kT}\right) = u_0 \cdot \frac{1}{T} \exp\left(-\frac{E_a}{kT}\right) \quad (5.34)$$

where E_a is the hopping activation energy, $(1 - c_e)$ is the fraction of sites not already occupied by mobile electrons, a the hopping distance and v_0 the attempt frequency. The estimated E_a and u_0 are listed in Table 5.2. The value of u_0 is common for small polarons. Due to the high activation energy, the electronic charge carriers exhibit low mobility at room temperature within the fully intercalated host. The impedance attributed to electronic charge carriers in this fully intercalated host is considerable.

Table 5.4: The dc-resistance and the calculated mobility and the hopping activation energy of the thin film structures according to equation (5.38).

| Width d [mm] | R_{dc} [k Ω ·cm $^{-1}$] | u_0 [cm 2 ·V $^{-1}$ ·s $^{-1}$] | E_a [kJ] | E_a [eV] |
|-------------------|---------------------------------------|---|-----------------|-------------------|
| 1 | 3.47 | 0.019 \pm 0.001 | 13.5 \pm 0.10 | 0.140 \pm 0.001 |
| 2 | 2.12 | 0.025 \pm 0.001 | 12.9 \pm 0.13 | 0.134 \pm 0.001 |
| 5 | 2.45 | 0.030 \pm 0.001 | 13.7 \pm 0.12 | 0.142 \pm 0.001 |

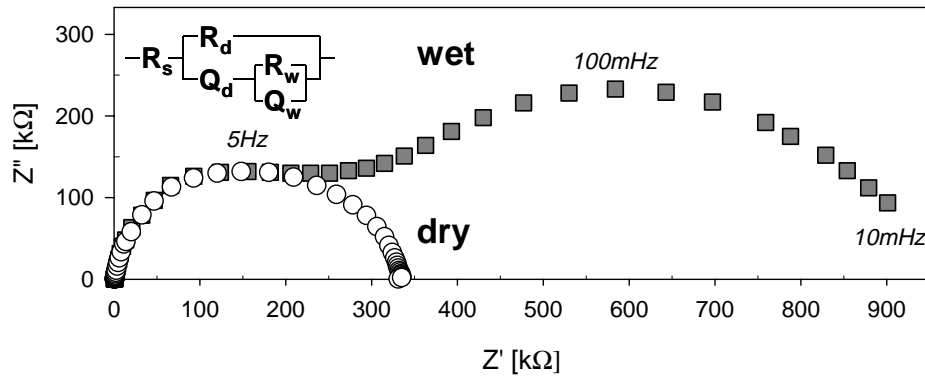


Figure 5.16: Electrical conductivity of the LiCoO_2 film structure shown in Fig 5.15 ($d=2\text{mm}$) now measured with Impedance spectroscopy before and in contact with the electrolyte solution (dry and wet condition, respectively). The equivalent circuit shown in the inset can simulate both results.

The ac-impedance characteristics of the LiCoO_2 test structure ($d=2\text{mm}$) are shown in Figure 5.16. The impedance plot shows a depressed semi-circle, due to parallel connection of the electronic dc-resistance, corresponding to the real impedance at low frequency (equal to dc-resistance), and the geometric capacitance caused by the underlying silicon substrate. After wetting the centre bridge part of the test structure with electrolyte solution (EC:DEC, 1:1; 1M LiClO_4), an additional semicircle appeared. With the addition of a parallel ionic conductivity path, the increase of the real impedance value can only be explained by the development of an additional (charge transfer) process. The (mixed) conductivity within the thin-film structure remains unaltered. The equivalent circuit describing both situations is shown in the inset. The parallel $R_d Q_d$ elements correspond to the impedance of the dry film, while the parallel $R_w Q_w$ elements reflect the depressed semicircle introduced with the electrolyte wetting.

As the electrolyte appears to have little influence on the electronic conductivity, the dc-resistance listed in Table 5.2 may be used for the estimation of the electronic impedance contribution. As the cross-sectional area of the sample film is $1 \cdot 10^5$ times larger than that of the measurement structure and the diffusion length is another factor 5 times smaller, the value of R_e is estimated to be $1 \cdot 10^{-6} \Omega$. This is insignificant compared with the total observed resistance R_{ei} . Levasseur *et al.* [16] reported a slightly higher electronic conductivity for pressed LiCoO_2 powder samples, but similar hopping activation energies (see Figure 5.17). Apparently, the plain electron conductivity, as quantified with this set-up, does not significantly contribute to the lithium intercalation resistance in LiCoO_2 .

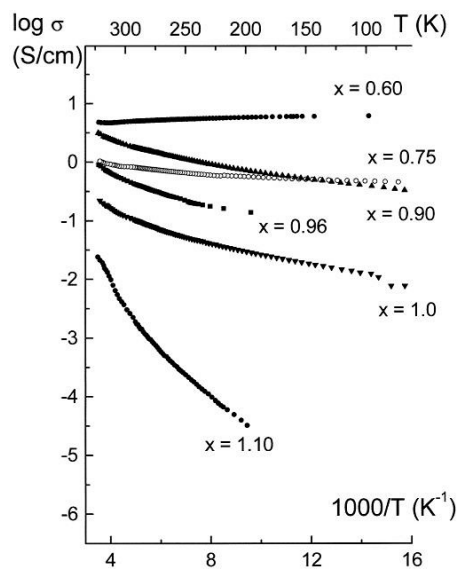


Figure 5.17: Variation of the log of electronic conductivity vs. reciprocal temperature of pressed LiCoO_2 ($x=1.10$) and de-intercalated samples [16].

5.5 Evaluation

It has been shown that in a zero-current situation the *EMF* of an electrochemical cell equals the difference in the chemical potential of lithium between both electrodes and is the driving force behind the internal lithium transport.

In the closed circuit situation, the gradient in the chemical potential of lithium within the intercalation electrode is determined by local charge carrier mobility and concentration. The lithium intercalation process can be described with an elaborate transition line model or, as in this case, with an approximate equivalent circuit.

The EIS data and the TtF-PITT results give similar impedance spectra as a function of the cell potential, which indicates that the techniques are complementary. All spectra could be fitted to an acceptable degree of accuracy and showed coherent values and ‘independent’ trends for the separate elements, which validates this equivalent circuit. The potential dependent behaviour suggests significant influence of the phase structure of LiCoO_2 on the observed impedance spectra.

A weakness of the current model is the observation of dissimilar arguments for the two diffusion elements O and T , which lead to different estimates of the chemical diffusion coefficient and intercalation capacity. The current EIS data predict a phase-dependent $\tilde{D} \approx 10^{-6} \text{cm}^2 \text{s}^{-1}$, while the TtF-PITT data suggest a constant $\tilde{D} \approx 10^{-11} \text{cm}^2 \text{s}^{-1}$. Possibly, a different rate-limiting process, such as phase boundary movement, hinders the potential step experiment.

The charge transfer resistance R_{CT} and electronic/ionic rail resistance R_{ei} increase sharply with a high degree of lithium intercalation. This cannot be attributed solely to limiting electron conductivity. However, a concentration decrease of available electron charge-carriers could have a large impact on the ambipolar diffusion and the interface processes.

For comprehensive characterisation of the lithium intercalation process in LiCoO_2 more samples have to be analysed with various thickness of the thin-film electrodes. However, the applied equivalent circuit is a useful tool to gain insight in the measured or transformed impedance spectra.

5.6 References

1. J. Jamnik, *Solid State Ionics*, to be published (2002).
2. H. Rickert, "Electrochemistry of Solids, an introduction", Springer-Verlag, New York (1982).
3. J. Maier, *J. Am. Ceram. Soc.*, **76** [5] 1212 (1993).
4. J.S. Newman, "Electrochemical Systems", second edition, Prentice-Hall, New Jersey (1991).
5. M.H.R. Lankhorst, H.J.M. Bouwmeester, H. Verweij, *J. Am. Ceram. Soc.*, **80** [9] 2175 (1997).
6. J.-P. Diard, B. Le Gorrec, C. Montella, *J. Electroanal. Chem.*, **499** 67 (2001).
7. H.J. Bergveld, "Battery Management Systems; Design by modelling", 156, Thesis University of Twente, the Netherlands (2001).
8. J.R. Macdonald, "Impedance Spectroscopy", John Wiley & Sons, New York, (1987).
9. B.A. Boukamp, G.A. Wiegers, *Solid State Ionics*, **9&10** 1193 (1983).
10. B. de Boer, "SOFC Anode, Hydrogen oxidation at porous nickel and nickel/yttria-stabilised zirconia cermet electrodes", Thesis University of Twente, The Netherlands, (1998).
11. B.A. Boukamp, *Solid State Ionics*, **20** 31 (1986).
12. M. Mohamedi, D. Takahashi, T. Uchiyama, T. Itoh, M. Nishizawa, I. Uchida, *J. Power sources*, **93** 93-103 (2001).
13. J. Jamnik, J. Maier, *Phys. Chem. Chem. Phys.*, **3** 1668-78 (2001).
14. P.H.L. Notten, W.S. Kruijt, H.J. Bergveld, *J. Electrochem. Soc.*, **145** [11] 3774 (1998).
15. J.O.M. Bockris, A.K.N. Reddy, "Modern electrochemistry; Ionics" second edition, Plenum Press, New York (1998).
16. S. Levasseur, M. Ménétrier, E. Suard, C. Delmas, *Solid State Ionics*, **128** 11-24 (2001).



Influence of film morphology

*Submicron LiCoO_2 films have been deposited on silicon and stainless steel substrates using RF sputtering and Pulsed Laser Deposition (PLD). In Chapter 4 it was shown, that the intercalation rate is strongly influenced by the orientation of the lithium diffusion plane toward the electrolyte solution. In this chapter the influence of the polycrystalline film morphology on the intercalation properties is studied. Electrochemical measurements indicate that the *c*-axis orientated LiCoO_2 films show improved electrode performance, when deposited on stainless steel substrates instead of on silicon. The *a*-axis oriented films showed no gain from a change of substrate. In case of the *c*-axis oriented film, the concealed host lattice can be significantly exposed with the introduction of defects of sub-micron dimension.*

6.1 Introduction

Oriented sub-micron LiCoO_2 films have previously been deposited on conducting silicon substrates. The preferential orientation of the polycrystalline films depends on the growth conditions [1]. The (00ℓ) orientation is obtained using the Pulsed Laser Deposition technique, while the (110) orientation is achieved with RF-sputtering. Typical XRD patterns of both films with the different alignment relative to the substrate are shown in Figure 3.2. The same deposition methods are applied as to produce both types of preferential LiCoO_2 films.

It has been shown, that the orientation of the lithium diffusion plane has large influence on the intercalation rate of polycrystalline LiCoO_2 films on silicon substrates. A decrease of the degree of uniformity and preferential orientation is expected, if these films are deposited on microscopically rough substrates, such as polished metal sheets. In our case, the PLD-films could benefit from a more random crystal structure. Note that LiCoO_2 films, which show preferential c -axis orientation, are reported to exhibit reasonable intercalation behaviour when deposited on metallic substrates [2,3,4].

In this chapter the LiCoO_2 films are deposited with RF-sputtering and PLD on silicon as well as stainless steel substrates at different substrate temperatures. The influence of the substrate material and the substrate temperature (during film deposition) on the film morphology is investigated. These thin-film electrodes are also studied electrochemically. The influence of the preferential host lattice orientation on the intercalation rate is expected to decrease with an increase of the surface roughness of the substrate.

The RF- and PLF-films on silicon substrates are subjected to lithographic patterning techniques and subsequent etching to create artificial pinholes in the LiCoO_2 film. A sequence of lithographic patterns of different mesh dimensions is used in order to observe a trend in the electrochemical properties. If charge transfer at the electrode interface restricts the lithium intercalation process, the kinetics should scale with the total created surface area, while if diffusion appears limiting the intercalation rate should correlate with the effective lithium diffusion length of the thin-film electrode.

6.2 Experimental

Thin-film deposition - Submicron LiCoO₂ films were prepared on stainless steel and silicon substrates with Pulsed Laser Deposition and RF-sputtering using stoichiometric LiCoO₂ targets. The metal substrate discs (15mm Ø) were stamped from sheet metal and polished with diamond paste (1µm). The silicon substrates (15mm Ø) were doped with phosphor to obtain n-type electrical conductivity. For the deposition parameters used with RF sputtering and Pulsed Laser Deposition we refer to previously published work [1]. Annealing was either performed *in-situ* in the vacuum chamber (pO₂=0.2mbar) by increasing the substrate temperature or *ex-situ* in a constant gas flow of 30ml·min⁻¹ STP containing 90% O₂ / 10% N₂. The typical annealing process was 30min at 600°C using a ramp rate of 5°C·min⁻¹ (*in-situ*) or 2°C·min⁻¹ (*ex-situ*).

Structural analysis - The crystal structure of the submicron films was analysed with X-ray diffraction using CuK_α at room temperature with a Philips PW 1800 diffractometer fitted with a rotating sample holder and an automatic divergence slit. Visualisation of the film surface morphology was performed using a JEOL JSM 5800 Scanning Electron Microscope.

Electrochemical analysis – Electrochemical experiments were conducted on a PGstat20 Autolab Potentiostat (ECO-Chemie) with integrated Frequency Response Analyser using a two-electrode set-up. The metallic lithium counter electrode was separated from the LiCoO₂ working electrode by a polymer sheet, which was soaked with commercial battery grade liquid electrolyte (1M LiClO₄, EC:DEC 1:1, Merck). The cells were operated inside a helium glove box.

Lithographic patterning – In some PLD-films square islands of 0.1mm were patterned at 0.1mm spacing using standard lithographic techniques. These squares were etched with 5% HF solution until a clear gauze-like pattern appeared in the LiCoO₂ film. One quarter of the active material was removed. These etched samples are referred to as ‘wet-patterned’ films. A second lithographic mask was designed for dry-etching of finer patterns using an argon plasma. The lay-out of this mask is shown in Appendix B.

6.3 Results

6.3.1 RF-sputtered seed layer

In a separate experiment a PLD-film was simultaneously grown on a blank silicon substrate and on a silicon substrate covered previously with an RF-sputtered seed layer of $0.1\mu\text{m}$ LiCoO_2 (annealed at 600°C , 30min) at 300°C substrate temperature. Figure 6.1 shows the XRD patterns of both samples after *in-situ* annealing at 600°C for 30min. The reference sample reveals the typical PLD-film diffraction pattern, indicating (00ℓ) lattice plane orientation. The PLD-film deposited on the seed layer, which before the deposition experiment showed only the (110) reflection, now shows distinct (006) and (0012) reflections. The (00ℓ) orientation is maintained, but the (003) and (009) reflections are completely absent.

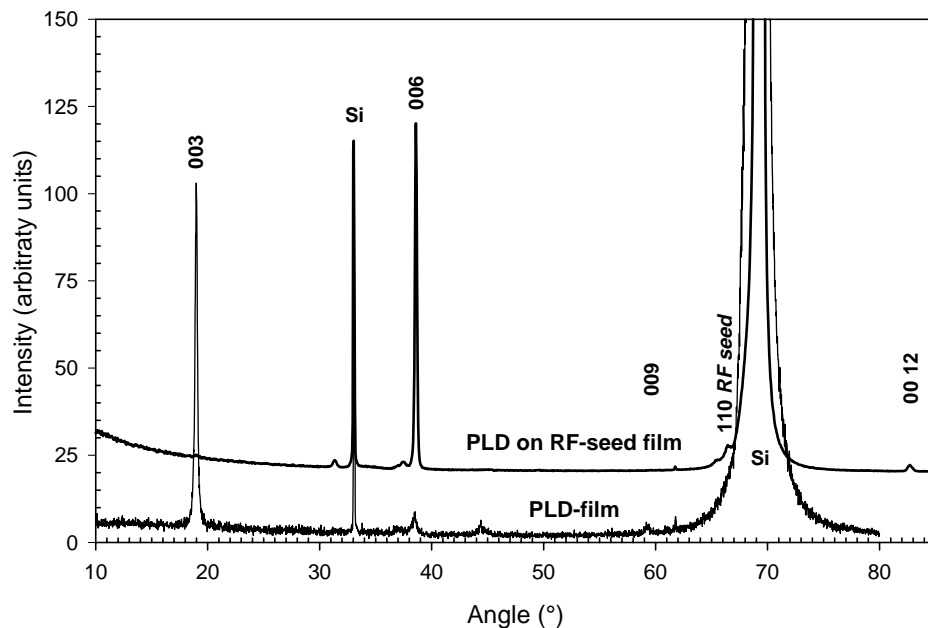


Figure 6.1: XRD patterns of two, *in-situ* annealed PLD-films deposited simultaneously on a $0.1\mu\text{m}$ RF-seed layer on silicon and on a blank silicon substrate, respectively.

Figure 6.2 shows a TEM photo of the cross-section of the sample. The columnar structure of the RF-sputtered seed layer is not continued in the PLD-film. The LiCoO_2 film is too thin to distinguish the transition of crystal structure by electron diffraction. Due to the polycrystalline nature of the film the boundary is expected to be inter-granular. The Pt film on top of the LiCoO_2 is merely convenient for TEM sample preparation.

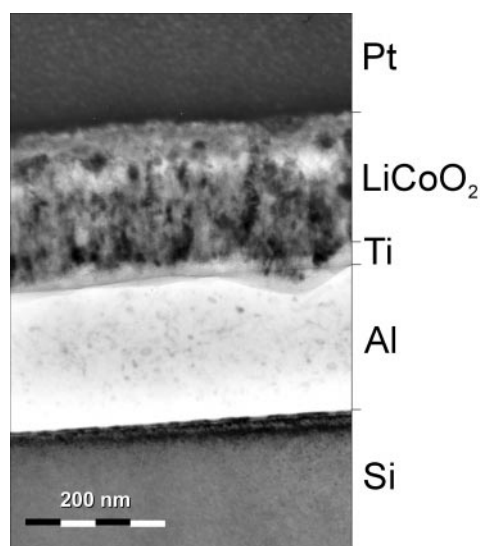


Figure 6.2: TEM cross-section of the LiCoO_2 film deposited with PLD on an RF-sputtered seed layer (100nm).

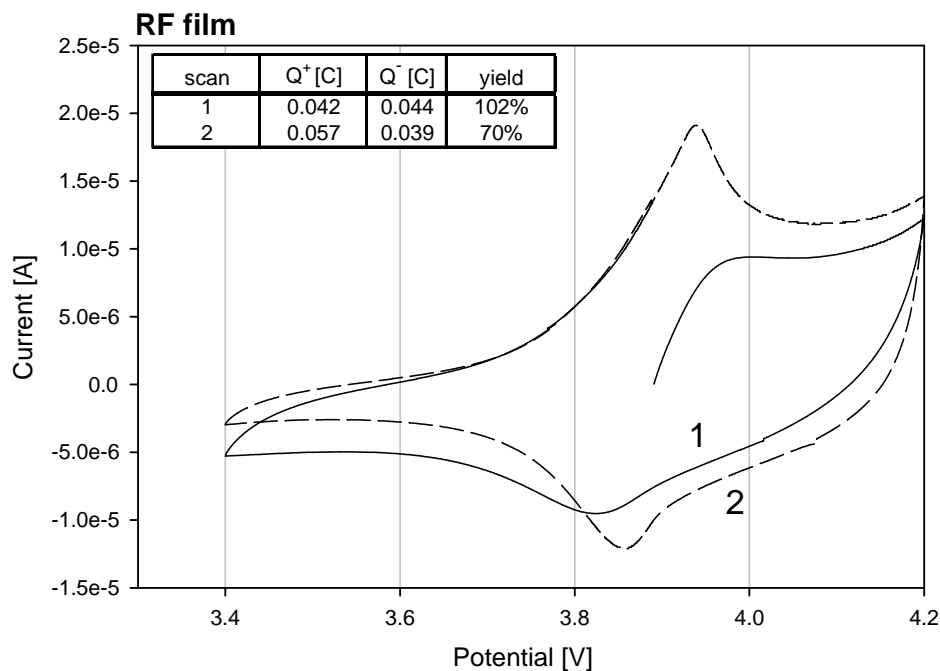


Figure 6.3: Cyclic voltammogram of a $0.1\mu\text{m}$ RF-film recorded at 0.1mV/s scan rate against metallic lithium. The capacity and Faradaic yield of the first and second scan are noted in the inset table.

A 0.1 μm RF-film on silicon, similar to the seed layer used for the PLD-experiment, is electrochemically active. The cyclic voltammogram is shown in Figure 6.3 (scan rate = 0.1 $\text{mV}\cdot\text{s}^{-1}$). Upon the second cycle the oxidation and reduction peak become well defined at 3.94V and 3.86V, respectively. The 84mV peak separation is close to the 69mV predicted by the Nernst equation, which is indicative of a good reversibility of the intercalation reaction. The intercalation capacity regained on discharge is close to the theoretical value of 48mC (0.1 μm , 1.76 cm^2). The Faradaic yield decreases with subsequent cycles.

The PLD-films deposited on silicon exhibit a Faradaic yield of 5 to 10% and employ only 3% of their theoretical capacity, when measured with cyclic voltammetry at this scan rate. The PLD-film with the NaCl type structure (exhibiting full cationic disorder; see Chapter 3) shows similar intercalation properties, inferior to those of the underlying RF-deposited seed layer.

6.3.2 Deposition temperature

Figure 6.4 shows the XRD patterns of two PLD-films on silicon produced with an identical number of laser pulses. The first is deposited at 300°C and subsequently annealed at 600°C (*in-situ*) and the second grown directly at 600°C. The intensity is plotted logarithmically to bring out the smaller diffraction peaks. Both samples exhibit a similar (00 l) orientation of the LiCoO₂. The sample grown at high substrate temperature generally shows increased Co₃O₄ diffraction intensity (only the peak at 31.2° remains similar).

The SEM pictures in Figure 6.5 display the film topography of the samples discussed in the previous section. Assuming that the substrate temperature has no significant influence on the deposition rate, the quantity of LiCoO₂ deposited is equal for both PLD-films. The PLD-film deposited at 300°C (Figure 6.5a) shows a polycrystalline structure with grains in the range of 10...100nm after annealing treatment. The film grown directly at 600°C (Figure 6.5b) exhibits larger and non-uniform grains in the range of 100...500nm. The excessive grain growth on the latter sample appears to have depleted the LiCoO₂ material in some locations and exposed the silicon substrate.

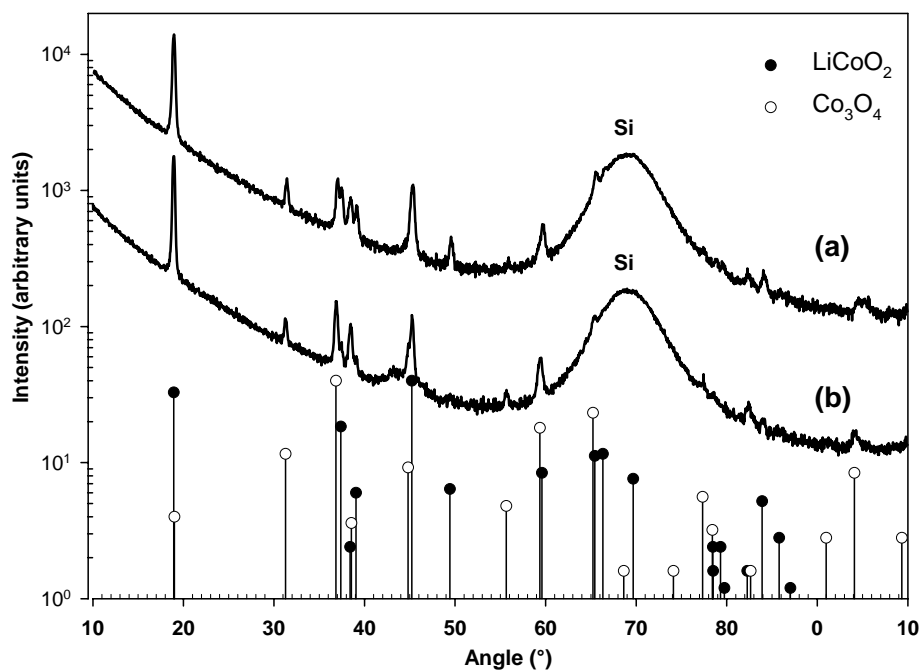


Figure 6.4: XRD patterns of two PLD-films on silicon: (a) deposited at 300°C and annealed in-situ at 600°C and (b) grown directly at 600°C on silicon. The reference patterns of LiCoO_2 and Co_3O_4 are plotted as bars with closed and open circles, respectively. The intensity is plotted logarithmically.

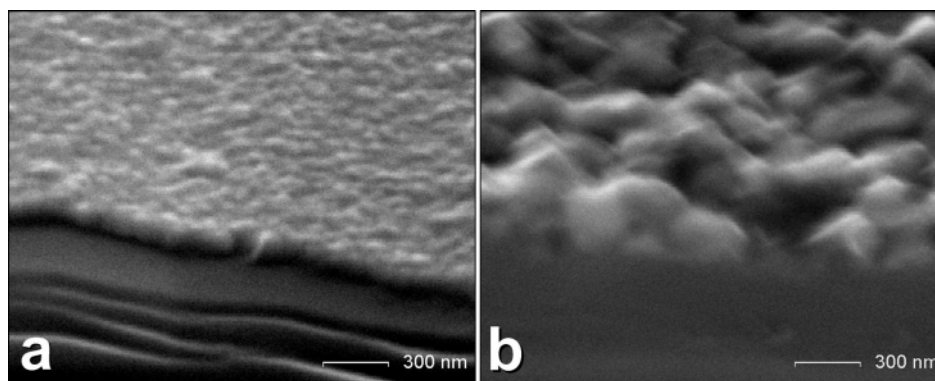


Figure 6.5: Cross-section micrographs of PLD-films on silicon substrates: (a) deposited at 300°C and annealed in-situ at 600°C; (b) deposited directly at annealing temperature (600°C). The corresponding XRD patterns are shown in Figure 6.4.

6.3.3 LiCoO₂ film patterning

Wet-chemical etched patterns - Figure 6.6 shows the constant current charge and discharge behaviour of a patterned PLD-film as a function of charge. Theoretically, the observed capacity accounts for approximately 15% of the deposited Li_xCoO₂ (with 0.5 < x < 1). This is an improvement on the unpatterned PLD-films. The increased capacity, obtained upon wet-chemical etching of a mesh-like pattern, is a direct result of an overpotential decrease. With constant current cycling, a low overpotential allows more charge to be extracted within the limits of the cut-off voltages and enables the use of higher currents, e.g. 10 μA·cm⁻² or even 25 μA·cm⁻². The maximum reversible capacity is observed with a cycling current of 1 μA·cm⁻². The reversible capacity decreases with lower current densities, due to the parasitic effect of the leakage current.

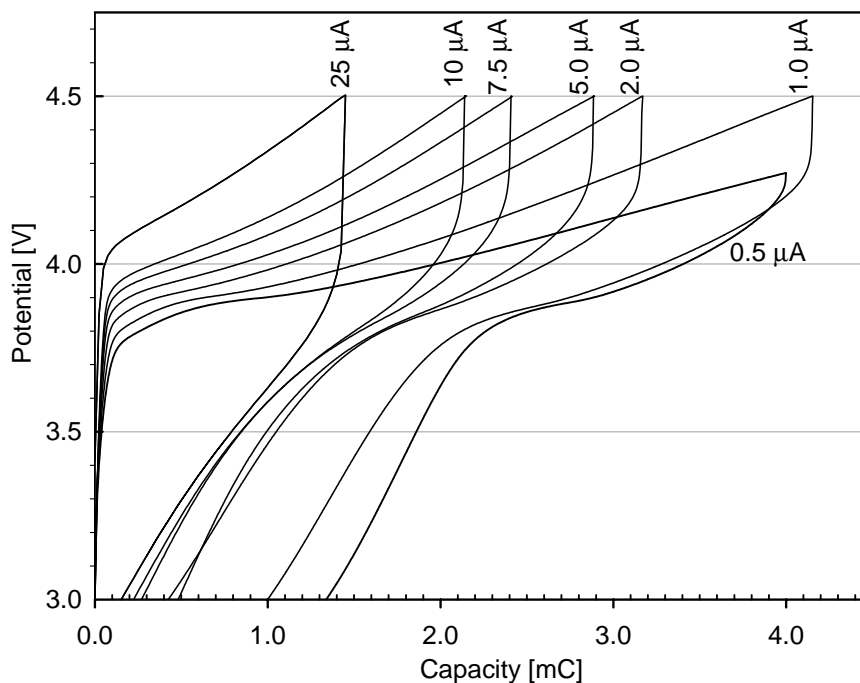


Figure 6.6: Constant current charge-discharge diagrams showing the cycling behaviour of a patterned PLD-film at various currents between the cut-off voltages of 3.0V and 4.5V.

The impedance of the patterned PLD-film remains approximately one order of magnitude above that of the RF-films. However, compared with the unpatterned PLD-films, it is easier to attain a specific state of charge. The impedance model, derived in Chapter 5 to analyse the RF-film behaviour, could also describe the observed spectra of this patterned PLD-film. The impedance spectra recorded as a function of state of charge (plotted in Figure 6.7) matched the Laplace frequency-transformed PITT results. The trends of the separate element values, as a function of the cell potential, resemble those of the RF-film displayed in Figure 5.9.

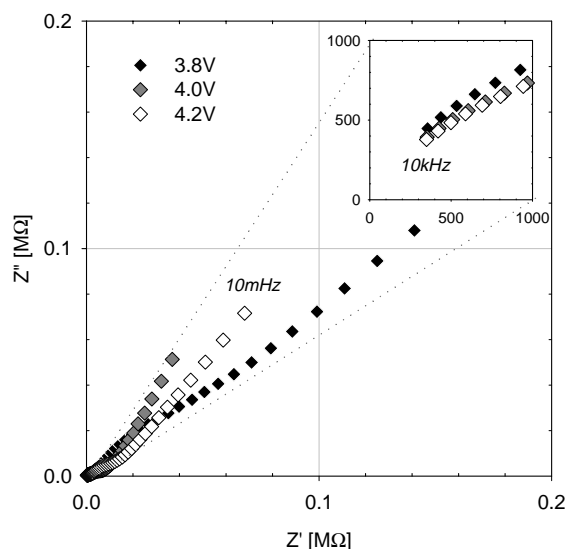


Figure 6.7: Three of the patterned PLD-film impedance plots recorded at the indicated OCP against lithium.

Dry-etched patterns – In order to investigate the influence of the etch-pattern dimensions, a sequence of mesh- and line-type patterns are applied on one single LiCoO_2 film. Due to the required dimension of this film, RF-sputtering was used to grow $0.2\mu\text{m}$ of LiCoO_2 on a conducting, 4" silicon wafer, with preferential *c*-axis orientation. After *ex-situ* annealing treatment and lithographic patterning, dry etching is performed over the centre 3" area and finally the wafer is broken into 1cm^2 pieces containing one particular pattern. An unpatterned reference sample is taken from outside the etching area. XRD analysis has shown, that the LiCoO_2 film exhibits a preferential *c*-axis orientation, but with full cationic disorder.

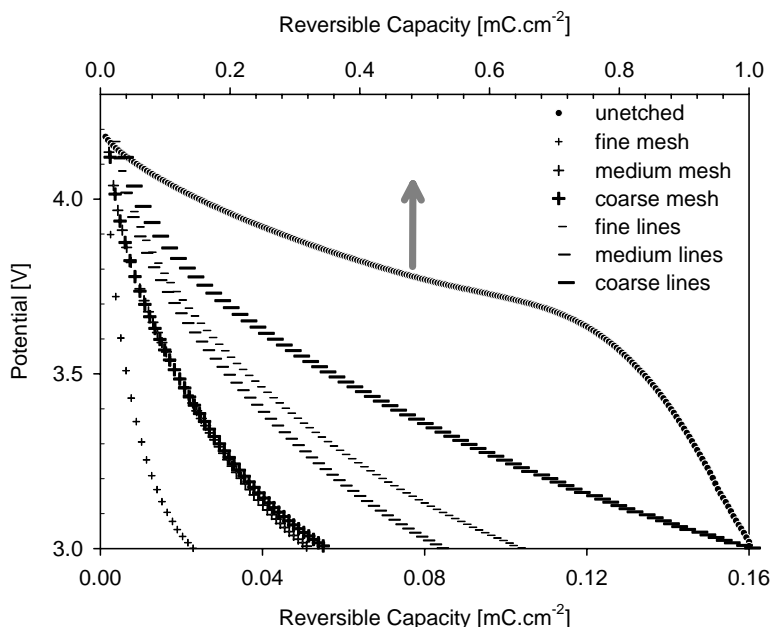


Figure 6.8: Voltage profile of patterned LiCoO_2 (dry-etched) samples during discharge with $1\mu\text{A}\cdot\text{cm}^{-2}$ from 4.3V and 3.0V against lithium.

The electrochemical properties are measured with galvanostatic cycling ($1\mu\text{A}\cdot\text{cm}^{-2}$) between 3.0V and 4.3V and impedance spectroscopy at 3.60V against lithium. In Figure 6.8 the cell potential is plotted against lithium during galvanostatic discharge of the patterned samples (scaled on bottom axis) and one unpatterned reference sample (scaled on top axis). The voltage profile of the reference sample during cycling corresponds to that of LiCoO_2 . However, the observed reversible capacity (Fig. 6.8) is only 5% of the lithium de-intercalated with the preceding charge.

The voltage profiles of the patterned samples during discharge appear featureless. The injected and regained charges indicate, that only 0.1% of the active film is involved in the lithium re-intercalation, while up to 25% contributes to the lithium intercalation during charge. Strong capacity fade is observed with cycling. Similar (featureless) behaviour is measured for unpatterned films cut from within the 3" dry-etch area. Apparently, LiCoO_2 film degradation occurs during dry-etching in spite of the presence of resist.

6.3.4 Stainless steel substrates

Cyclic voltammetry – Figure 6.9 shows the cyclic voltammogram of a 300nm LiCoO_2 PLD-film on a stainless steel substrate, measured after annealing treatment (600°C , 30min) against metallic lithium (electrolyte: EC:DEC 1:1, 1,0M LiClO_4). The electrochemical properties are much better than those of the PLD-film deposited on silicon, as shown in Figure 4.2. The anodic and cathodic peak current are both well resolved when measured at $1\text{mV}\cdot\text{s}^{-1}$ and become broader with increasing scan rate, but do not show any sharpening with lower scan rates. The peak separation is close to the 59mV predicted by Nernst equation for a reversible, one-electron reaction [7] and suggests that intercalation occurs under quasi-equilibrium conditions. The peak separation increases with increasing scan rate and also with ageing of the sample, but cathodic current peak remains around 4.0V.

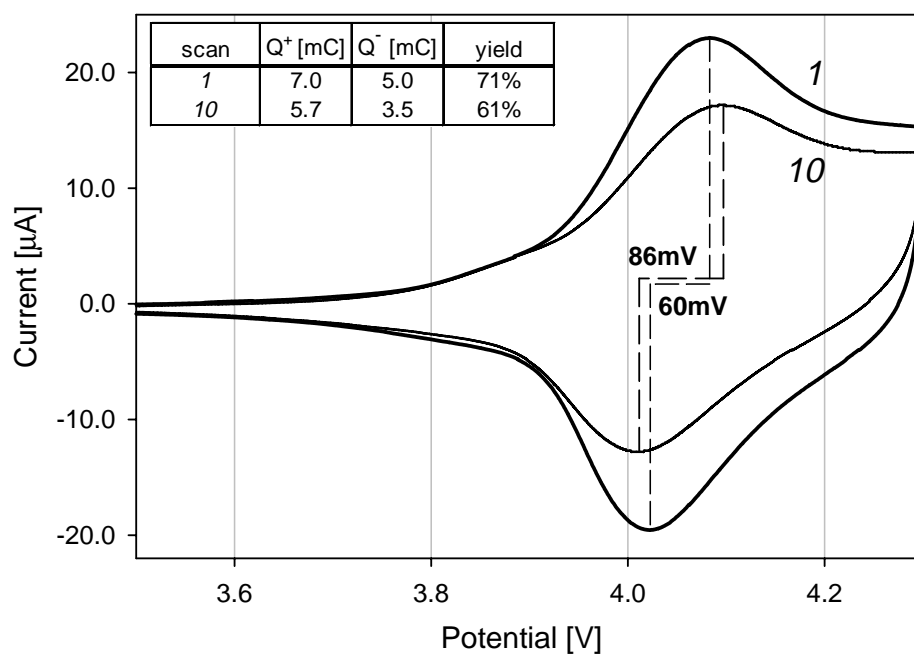


Figure 6.9: Cyclic voltammogram of a PLD-film on a stainless steel substrate after annealing treatment (600°C , 30min). The first and tenth scan at $1\text{mV}\cdot\text{s}^{-1}$ are indicated and the corresponding charge and Faradaic yield are listed in the inset table.

Pulsed current charging - The potential response of a similar PLD-film, deposited on a stainless steel substrate, to pulsed charging is compared with that of an RF-film on silicon and the patterned PLD-film on silicon (wet-etched). In Figure 6.10 the potential is plotted as a function of time during the current pulse as well as the zero-current relaxation period. It was not possible to use a similar pulse for all three samples, due to the unequal rate capabilities. The observed potential relaxation, subsequent to a current pulse, appears immediate for the RF-film, while the silicon PLD-film potential relaxation progresses into a linear decay. The voltage of the PLD-film deposited on stainless steel, also shows the gradual relaxation behaviour typical of PLD-films, but after some time shows stabilisation at a new equilibrium potential, as observed for the RF-film. The electrochemical behaviour of the PLD-film on stainless steel substrate appears intermediate between the RF-film and the patterned PLD-film on silicon.

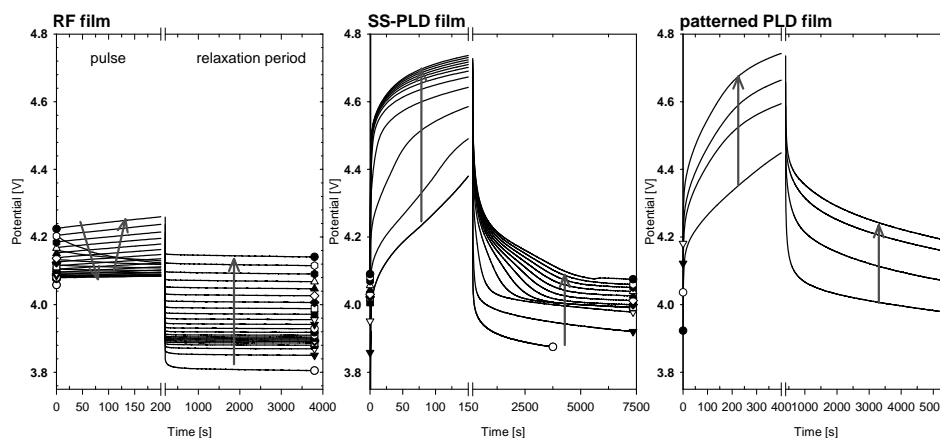


Figure 6.10: Potential response to pulsed galvanostatic charging of an RF-film, a PLD-film on stainless steel substrate and a patterned PLD-film on silicon as a function of time. The RF-film is charged with a 50mA pulse of duration 200s, the stainless steel PLD-film is charged with 10mA pulses of 150s and the patterned silicon PLD-film subjected to 2.5mA pulses of 400s. The current pulse is followed by a period of zero-current relaxation before the next pulse is applied (arrows indicate pulse sequence).

6.4 Discussion

6.4.1 LiCoO₂ crystal structure

The close-packed (00 ℓ) planes of LiCoO₂ have the highest density and low surface energy. This is frequently regarded as the main cause for this preferential orientation. However, the c-axis alignment is only observed for films, which have been deposited with a (momentary) high growth rate and is no longer stable with increasing film thickness (>0.2 μ m). The preferential orientation of the PLD-films is indeed observed to fade gradually until a random orientation of the crystal structure remains. This transformation occurs for both PLD-films on silicon and stainless steel substrates (although best observed on silicon substrates).

The RF-films are grown in continuous plasma at low power, which results in an 'a-axis' oriented LiCoO₂ film, even at low thickness. Judging by the typical flat hexagonal crystals of annealed LiCoO₂ powder, crystal growth occurs fastest in the *a*-axis direction. During (slow) deposition, the RF-film shows an outward expansion of the lattice normal to the substrate surface, which coincides with the observed columnar grain growth. The (110) alignment appears thermodynamically stable, since it is possible to grow thick RF-films (>0.75 μ m) without loss of preferential orientation. Recently, it has been observed that with a strong increase of the RF-power the unfavourable (00 ℓ) orientation reappears [7].

When LiCoO₂ is deposited by means of PLD on an annealed RF seed layer, the existing (110) orientation is not continued, but overgrown with a preferential (00 ℓ) alignment. However, the film structure differs from that grown on a blank silicon substrate, as not all (00 ℓ) reflections are observed. The distinctive diffraction pattern can be explained by assuming complete cationic disorder [1]. A random distribution of the lithium and cobalt ions leads to a structure similar to that of NaCl, which explains why the (003) and the (009) reflections become extinct. The present results clearly demonstrate, that the substrate can influence the lattice structure of the LiCoO₂ film, although the preferential orientation appears primarily related to the rate of deposition.

6.4.2 Rate of intercalation

The orientation of the layered intercalation host toward the electrolyte solution is still primarily responsible for the observed electrochemical behaviour. Lithium intercalation appears unhindered in the RF-film on silicon as well as on stainless steel substrates. In case of the PLD-film the overall direction of lithium transport is normal to the diffusion planes. Therefore the lithium intercalation in the PLD-film is severely limited and thus highly dependent on other means of inward lithium diffusion (*e.g.* grain boundaries, defects, cracks).

Hot deposition – An increase of substrate temperature during deposition does not alter the preferential orientation, but has large influence on the grain size of the polycrystalline film. Excessive grain growth is observed for LiCoO₂ films deposited directly at the annealing temperature (600°C), probably due to a higher surface mobility. This leads to an irregular morphology of the film, but also to a smaller number of grains and grain boundaries. Normalised to a specific amount of material, fewer but larger grains also exhibit a lower surface area. ‘Hot-deposited’ LiCoO₂ films are generally observed to have an increased intercalation resistance compared with their ‘cold-deposited’ and shortly annealed counterparts. Iriyama *et al.* [9] have attributed this difference to the total grain boundary length, which is assumed to assist lithium transport.

A detrimental effect of maintaining a LiCoO₂ film at elevated temperatures (>600°C) for long periods of time (>30min) is the evaporation of volatile Li₂O, which results in Co₃O₄ formation (estimated ~5% in Figure 6.4). Since the growth rate of the film is low, more time is spent at high temperature during deposition, than is gained by the redundancy additional annealing treatment. Thus, film deposition at high substrate temperatures is not useful, unless the development of a large-grained structure is required.

Lithographic patterning - Patterning of the LiCoO₂ film is directed to increase the effective surface area towards the electrolyte solution, or in other words, to increase the exposure of the lithium diffusion planes. Obviously, due to the *c*-axis orientation, the PLD-films benefit most from the introduction of defects. The wet-chemical etch pattern is coarse compared with the thickness and the grain size of the polycrystalline film. Therefore, it is suspected that not just the 0.1mm square holes are responsible for the observed improvement of the intercalation rate and

capacity, but that the HF-solution has also introduced pinholes over the entire surface of the PLD-film. SEM observation of the sample surface shows a slightly corroded shape of the patterned squares, which indicates a low selectivity for the wet-etching treatment. Another method should be used to create smaller defects and hence to increase the ‘accessibility’ of the host structure.

The dry etching of the lithographically patterned LiCoO_2 film on 4” silicon wafer is highly accurate, but appears ineffective and even detrimental for the electrochemical performance. The observed reversible capacity is low, due to the structural cationic disorder and thus the absence of distinct lithium diffusion planes. However, the characteristic voltage profile disappears for all samples exposed to the argon plasma, despite a covering resist layer. Apparently, the (patterned) boundaries of the ordered host structure are distorted or damaged by the ion bombardment and thus lose their effectiveness as interface for lithium intercalation.

Figure 6.11 shows a photograph taken with an optical microscope of a 200nm thick LiCoO_2 film after dry-etching a gauzelike pattern ($100\mu\text{m}$ holes). Its step-

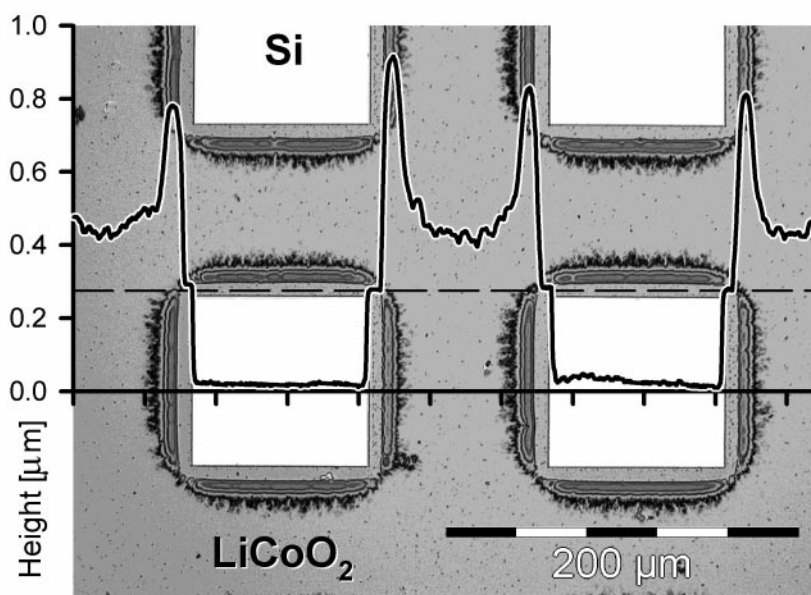


Figure 6.11: Photograph taken with an optical microscope of the dry-etched $100\times 100\mu\text{m}$ mesh pattern. The height profile measured across the square holes is superimposed.

height profile is superimposed. The horizontal dashed line indicates the original surface of the silicon substrate. The hillocks on the edges of the hole are the result of re-deposition of material against the walls of the initial resist layer. SEM analysis using backscattered electrons indeed verifies, that the composition of the hillocks is identical to that of the LiCoO_2 film. It is plausible, that the intercalation into the ordered host structure is hindered by the presence of an amorphous layer of re-deposited LiCoO_2 .

The capacity of the dry-etched samples, measured during constant current charge and discharge, reveals no direct correlation to the mesh dimensions of the etched pattern. However, a linear relation is observed between the geometric surface area (introduced through patterning) and the geometric capacity C_{dl} , calculated by fitting the impedance spectra (recorded at 3.60V) to the model described in Chapter 5. Figure 6.12 shows that fine patterning increases the double layer capacity.

The values for the *charge-transfer* and *electronic-ionic* resistance circuit elements (R_{CT} and R_{ei}) showed an inverse linear and exponential correlation with the reversible intercalation capacity, respectively, as plotted in Figure 6.13.

As the value of these resistive elements is proportional to the overpotential

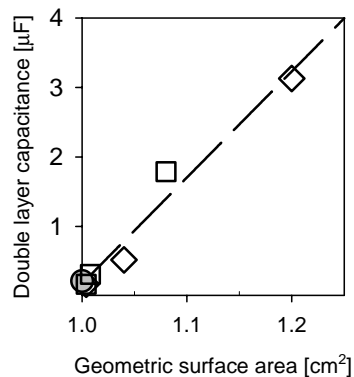


Figure 6.12: The modelled double layer capacitance plotted as a function of the calculated geometric surface area at 3.6V. (\circ : no pattern, \diamond : line pattern, \square : mesh pattern). The dashed line indicates the linear relationship.

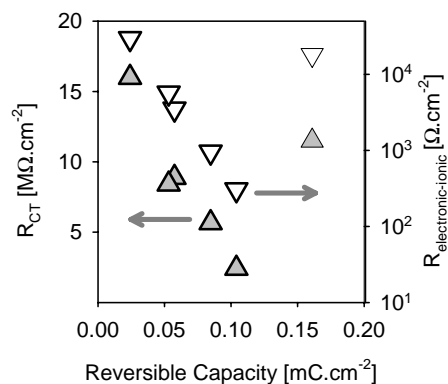


Figure 6.13: Correlation between the reversible capacities observed with galvanostatic discharge and the resistances R_{CT} and R_{ei} measured with impedance spectroscopy.

encountered during in a current-drawing situation, *i.e.* galvanostatic discharge (see Figure 6.8), more charge can be extracted from the low impedance films within the limits set by the cut-off potentials. The impedance data obtained at the cell potential of 3.60V, are sufficient to make this correlation, because the bulk of the host material will still be expected to be in this fully-intercalated state due to the severely limited intercalation rate and the relatively high current density.

Although the internal resistance of the film can explain the observed intercalation capacity of the dry-etched films, the corresponding intercalation properties cannot be controlled by patterning of the film in this case. Further experiments could be more successful in absence of the cationic disorder and when dry-etching is performed prior to the annealing treatment, so that the lattice has an opportunity to restore the structural ordering at the edges of the pattern.

The wet-etched PLD-film shows reasonable intercalation properties. From the impedance spectra a geometric capacitance value $C_{dl} = 0.7 \pm 0.1 \mu\text{F}$ is calculated (independent of cell potential), which, according to the trend line in Figure 6.12, agrees with the applied coarse patterning. The trend of the other calculated elements of the impedance model coincides with those of an unpatterned RF-film displayed in Figure 5.5. Apparently, the intercalation mechanisms in RF- and PLD films are in fact identical. Only the characteristics of the latter are usually distorted, due to severe diffusion limitation.

6.4.3 Metallic substrates

At first, we used polished aluminium substrates instead of stainless steel, as commercial LiCoO_2 electrodes are based on aluminium foil and the thin aluminium films on silicon substrates proved suitable current collectors. However, at temperatures above 400°C the interface is unstable and the bulk aluminium consumes the LiCoO_2 film. Stainless steel substrates appear more inert during annealing treatment or high temperature deposition.

The intercalation capacity of the PLD-film observed with cyclic voltammetry (Fig. 6.9) is approximately 10% of the theoretical reversible capacity (81mC). The decrease in absolute capacity with ageing is mainly attributed to evaporation of the electrolyte and a subsequent decrease of the exposed electrode area.

However, the remaining capacity is available at high scan rates and exhibits very low overpotentials. With increasing scan rate the reversible capacity decreases and the peak separation is observed to increase. However, the capacity does not increase with decreasing scan rate, which indicates that either a significant leakage current exists or that the remaining capacity, expected from this amount of active material, is inaccessible and thus not involved in the intercalation process.

The current pulse response of the stainless steel PLD-film appears intermediate between the behaviour of the RF-film and the patterned PLD-film on silicon substrates (see Figure 6.10). The high overpotential encountered during the current pulse and the slow potential relaxation afterwards is typical for PLD-films and attributed to a low diffusion rate. The subsequent OCP stabilisation after a specific relaxation period is typical for the RF-films.

Clearly, the lithium intercalation rate and capacity of PLD-films are improved, when deposited on stainless steel. This improvement is attributed to the surface irregularity of the metal substrate on the (sub-) micron scale, as it directly causes spread of the preferential *c*-axis orientation (always parallel to substrate). The misaligned lithium diffusion planes can contribute to the inward diffusion. Further, the lithium transport could be assisted by inter-granular micro-cracks and pinholes, possibly introduced due the increased mismatch. Film defects could also be the result of mechanical stress relief, built up during annealing treatment, due to a difference in thermal expansion ($\alpha_{\text{Fe}} \approx 4 \times \alpha_{\text{Si}}$).

The artificial pinholes increase the diffusion plane exposure of the LiCoO_2 film on a sub-micron scale and subsequently decrease the lithium diffusion distance within the intercalation host. This allows a limited amount of lithium to be (de-)intercalated in a short period of time. The artificial introduction of defects on this scale cannot be achieved with the current lithographic method.

6.5 Conclusions

The electrochemical intercalation properties of the LiCoO_2 films are mainly determined by the preferential host lattice orientation towards the electrolyte solution, which depends on the deposition rate. Film growth at the annealing temperature (600°C) results in excessive grain growth and loss of volatile Li_2O thus transforming LiCoO_2 into electrochemically inactive Co_3O_4 . The substrate material has no influence on the alignment of the close-packed oxygen planes, but deposition on a LiCoO_2 seed-layer has been observed to induce cationic disorder. The absence of distinct lithium diffusion planes, due to random octahedral site occupation of Co and Li, is detrimental for the reversible intercalation capacity.

Dry-etching of defects in an annealed, *c*-axis oriented film is effective for increasing the geometric surface area, but does not improve the intercalation performance as degradation of the host structure is observed at the pattern edges. Wet-chemical etching is unselective and believed to affect the entire film integrity, as the increase in intercalation rate and capacity of the wet-etched PLD-film on silicon is out of proportion with the applied coarse pattern.

LiCoO_2 deposition on substrates with increased surface roughness, *e.g.* polished stainless steel, results in a polycrystalline film with lower degree of preferential orientation. The superior performance of *c*-axis films on stainless steel compared with those on silicon substrates, is attributed to the presence of defects on a sub-micron scale, referred to as pinholes, which further increase the host lattice exposure and decrease the effective diffusion length.

6.6 References

1. Chapter 3 of this thesis.
2. P. Fragnaud, T. Brousse, D.M. Schleich, *J. Power Sources*, **63**, 187 (1996).
3. K.A. Striebel, C.Z. Deng, S.J. Wen, E.J. Cairns, *J. Electrochem. Soc.*, **143** [6] 1821 (1996).
4. Y. Iriyama, M. Inaba, T. Abe, Z. Ogumi, *J. Power Sources*, **94** 175 (2001).
5. K. Nishioka, N. Mizutani, H. Komiyama, *J. Electrochem. Soc.*, **147** [4] 1440 (2000).
6. H.W. Wang, Y.I. Jang, B. Huang, D.R. Sadoway, Y.M. Chiang, *J. Electrochem. Soc.*, **146**, 473 (1999).
7. D.K. Gossner, "Cyclic Voltammetry – simulation and analysis of reaction mechanisms", VCH Publishers Inc. New York, (1993).
8. Chapter 9 of this thesis.
9. Y. Iriyama, M. Inaba, T. Abe, Z. Ogumi, *J. Power Sources*, **94** 175 (2001).



Characterisation of $\text{Li}_x\text{Co}_y\text{Mn}_{1-y}\text{O}_2$ powders and films

Mixed transition metal oxide powders of the composition $\text{Li}_x\text{Co}_y\text{Mn}_{1-y}\text{O}_2$ ($0 < y < 1$) have been prepared with EDTA synthesis. Purification of the pyrolysed product is achieved through calcination at 600°C and full crystallisation is observed with sintering treatment at 900°C . For $0 < y < 0.5$ a solid solution is formed and the cubic unit cell dimensions decrease gradually with increasing Co concentration.

Electrochemical activity of the powders is observed only after annealing at 600°C . The intercalation performance of the composite electrodes is improved with increasing Co concentration. Thin-film electrodes have been prepared from the $\text{Li}_x\text{Co}_y\text{Mn}_{1-y}\text{O}_2$ ($0 < y < 1$) powders using Pulsed Laser Deposition. The as-deposited LiCoO_2 films showed stable cycling behaviour, the as-deposited $\text{Li}_x\text{Mn}_2\text{O}_4$ films showed rapid degradation. Generally, the films with a higher Co concentration exhibited stronger IR lattice vibrations indicating good structural integrity.

No significant synergistic effect of the mixed transition metal oxide on the electrode potential is observed.

7.1 Introduction

Transition metal oxide compounds are popular materials for lithium intercalation electrodes, as these maintain structural stability over a large lithium concentration range. The combination of transition metals in one host lattice can benefit the electrode properties in several ways.

Recently, $\text{Li}_x\text{Co}_y\text{Mn}_{1-y}\text{O}_2$ with $0 < y < 1$ has received attention as a positive electrode material. Manganese-based material is available at low cost and has the advantage of being non-toxic. Cobalt-based structures exhibit good cycling stability, but lack the previous benefits. Both transition metal ions are suitable for lithium intercalation at a high cell potential versus lithium, due to their accessible $\text{M}^{3+/4+}$ oxidation states.

The LiMn_2O_4 spinel structure is stabilised by Co substitution. It prevents the Jahn Teller distortion by raising the average oxidation state above the critical point of $\text{Mn}^{3.5+}$. The addition of trivalent Co^{3+} ions induces the transition of an equivalent amount of Mn^{3+} to Mn^{4+} . The decreased amount of Mn^{3+} ions also reduces the possibility of disproportionation reactions. The beneficial effect is already noticeable with a few percent of Co doping [1].

Half of the lithium ions can be removed from the layered LiCoO_2 structure, before lattice instability leads to capacity decreases. The rigid spinel structure of LiMn_2O_4 enables virtually all lithium to be extracted and replaced reversibly. The capacity of LiCoO_2 could be increased, if Mn doping would induce a spinel crystal structure and make the tetrahedral sites available to lithium occupation. First principle calculations have predicted the LiCoO_2 to be most stable in the spinel structure, but its synthesis has not been achieved yet. Spontaneous transformation to spinel during cycling has not been observed.

The accessibility of tetrahedral sites also enables three-dimensional lithium diffusion. Although the diffusion in a spinel structure has been reported to be slower than in a layered hexagonal structure, the large influence of the preferential orientation of the crystal structure on the intercalation rate would disappear [2].

For LiCoMnO_4 an unexpected oxidation and reduction peak has been reported at 4.5V, attributed to defects in the internal structure of the $\text{Li}[\text{Mn}^{4+}\text{Co}^{3+}]\text{O}_4$ spinel

structure. The Mn^{4+} ions are unable to contribute to further lithium de-intercalation. Apparently, the $\text{Co}^{3+/4+}$ redox potential can increase from 3.9V (in LiCoO_2) to 4.5V, if stabilised in an Mn-rich spinel structure [3].

In this chapter the structural transition of $\text{LiCo}_y\text{Mn}_{1-y}\text{O}_2$ from spinel to layered-hexagonal is investigated with the increasing Co doping concentration. The electrochemical properties of the materials are to be studied for synergistic effects of Co and Mn combination on their lithium de-intercalation potentials and capacities.

7.2 Experimental

Powder synthesis - Mixed transition metal oxides with the stoichiometric formula $\text{Li}_x\text{Co}_y\text{Mn}_{1-y}\text{O}_2$ were prepared in six compositions ($y=0, 0.10, 0.25, 0.50, 0.90,$ and 1.0) with the EDTA synthesis [4]. This violent process is very suitable for producing multi-component powders with an average grain size below $0.1\mu\text{m}$. Stoichiometric quantities were weighed and dissolved in concentrated HNO_3 and subsequently neutralised with ammonium hydroxide. EDTA was added as combustion fuel. Care was taken not to invoke any precipitation during evaporation. Decomposition of the precursor batch occurred in an oven designed for this purpose, set at 240°C .

The powder is dry-milled for 8 hours, followed by calcination at 600°C to remove residual organic compounds. The agglomerates were then re-dispersed during wet milling using zirconia balls for another 8 hours. Part of this powder was used directly in composite electrodes. The other part was sealed in quartz glass tubes and calcined at 900°C for 120 hours to allow complete homogenisation through solid-state diffusion. These powders were tape-cast on aluminium foil in a mixture consisting of 85% active material, 10% Carbon black and 5% teflon powder as binder. These composite electrodes were cut to 15mm circles and installed in coin cells, together with a metallic lithium counter electrode and 1.0M LiPF_6 electrolyte with EC:DEC ratio 1:1.

Thin film preparation - PLD-targets were prepared from the low-temperature (600°C) calcined and subsequently wet-milled powders. After isostatic pressing the pellets ($25\text{mm } \varnothing$) were sintered at 900°C for three hours. Thin film electrodes have been deposited on silicon wafer using RF-sputtering and Pulsed Laser

Deposition (PLD). 15mm \varnothing discs, punched from stainless steel and aluminium sheets, were polished to a roughness $<0.1\mu\text{m}$ and served as substrate. The sub-micron films are grown on heated substrates (300°C) under low oxygen background pressure. The detailed deposition parameters are described in Chapter 3.

Electrochemical Analysis - The electrochemical analysis was performed using a PGstat20 Autolab potentiostat (ECO-Chemie) with integrated Frequency response analyser. The composite electrodes were measured in sealed coin cells in ambient using a two-electrode configuration. The thin-film electrodes were measured in a re-usable electrochemical cell in the He glove box using a three-electrode configuration. A metallic lithium strip in a Luggin capillary positioned directly under the working electrode, was used as reference electrode. Commercial battery grade liquid electrolyte (1M LiPF₆, EC:DEC 1:1, Merck) was used.

Table 7.1: *The composition of the $\text{Li}_x\text{Co}_y\text{Mn}_{1-y}\text{O}_2$ powders as measured by AAS at various stages of synthesis. The lithium molar ratio (x) is normalised to the total transition metal content. The value for y is listed in the Co column.*

| Sample | Calcination at | Li:(Co+Mn) | Co | Mn |
|--|----------------|------------|------|------|
| LiCoO ₂ | 600°C | 1.27 | 1 | 0 |
| | 900°C | 0.65 | 1 | 0 |
| LiCo _{0.9} Mn _{0.1} O ₂ | 600°C | 1.21 | 0.89 | 0.11 |
| | 900°C | 0.71 | 0.91 | 0.09 |
| LiCo _{0.5} Mn _{0.5} O ₂ | 600°C | 1.19 | 0.52 | 0.48 |
| | 900°C | 0.88 | 0.53 | 0.47 |
| Li _{0.5} Co _{0.25} Mn _{0.75} O ₂ | 600°C | 0.68 | 0.25 | 0.75 |
| | 900°C | 0.49 | 0.28 | 0.72 |
| Li _{0.5} Co _{0.1} Mn _{0.9} O ₂ | 600°C | 1.86 | 0.16 | 0.84 |
| | 900°C | 0.46 | 0.11 | 0.89 |
| Li _{0.5} MnO ₂ | 600°C | 1.12 | 0 | 1 |
| | 900°C | 0.29 | 0 | 1 |

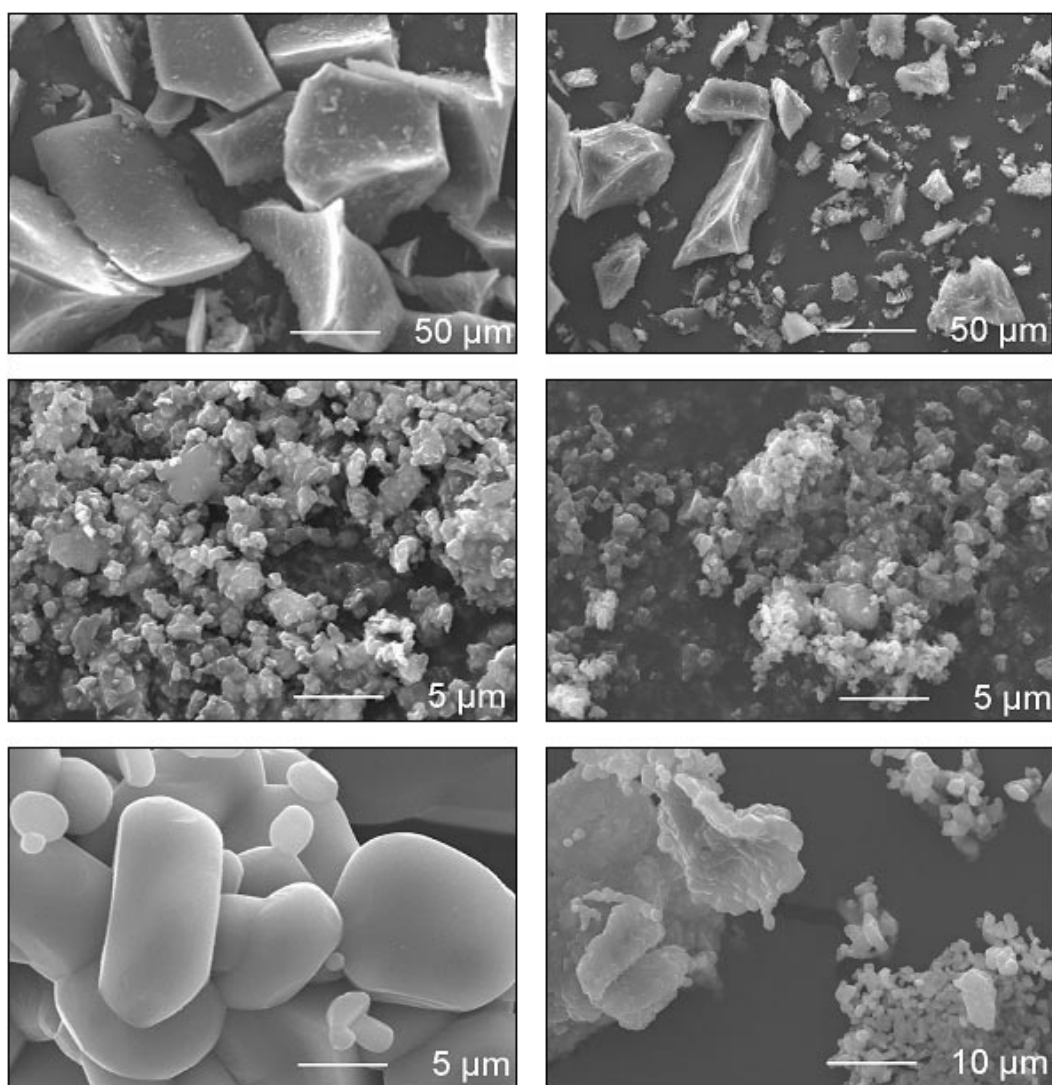


Figure 7.1: SEM micrographs showing the LiCoO_2 powder on the left and the LiMn_2O_4 powder on the right at various stages of synthesis. The pyrolysed precursor is displayed at the top, the calcined and wet-milled powder in the middle and the sintered product at the bottom (900°C , 120h).

7.3 Results

7.3.1 Powder characterisation

Table 7.1 shows the results of the Atomic Absorption Spectroscopy composition analysis of the mixed transition metal oxide powders at various stages of the synthesis. The pyrolysed (not shown) and the calcined powder show excess lithium, due to the 10% surplus added to the precursor solution to compensate for any loss during sintering. The pyrolysed products contain roughly 42% of carbon, 20% of nitrogen and 3.5% of hydrogen, which are all removed upon calcination at 600°C (1% of C remains). It is unclear whether the observed lithium is present in the transition metal oxide structure or as Li_2O . The crystalline Li_2O phase could not be detected with XRD.

The SEM micrographs of the powders at the three stages of the synthesis are shown in Figure 7.1: after pyrolysis, after calcination at 600°C (LT) and wet-milling and after final calcination at 900°C (HT). The particle size of the LT-calcined powders appears to be larger with increasing cobalt content.

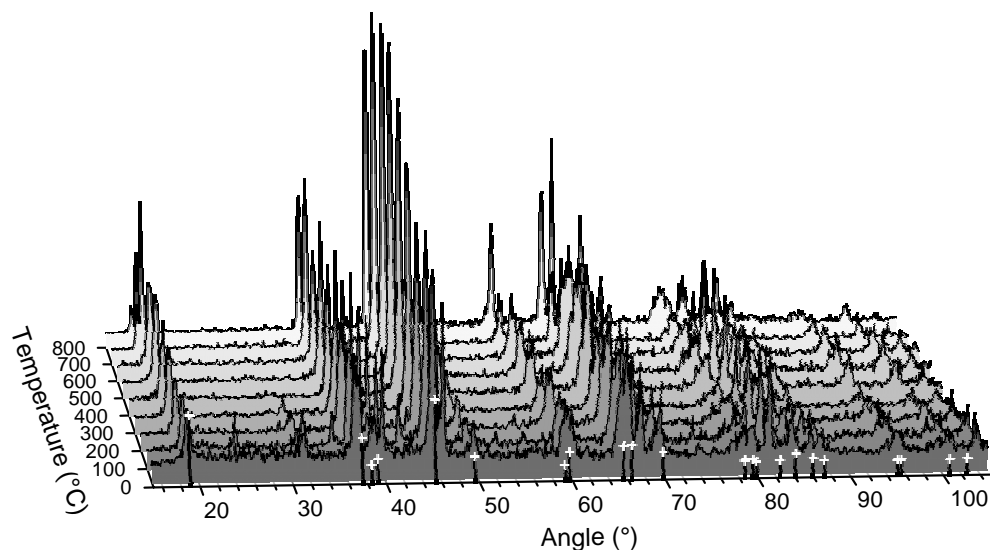


Figure 7.2: XRD patterns of pyrolysed LiCoO_2 powder measured in-situ as function of substrate temperature. The reference spectrum is plotted in front of the patterns as open circles with dotted drop lines.

Particularly the LiCoO_2 powder shows excessive grain growth during HT-calcination.

Figure 7.2 shows the High Temperature XRD patterns of LiCoO_2 during annealing treatment at increasing temperature (steps of 100°C). Only at 800°C does the expected (018) and the (110) peak splitting at 65° occur. This indicates the formation of an ordered rhombohedral LiCoO_2 structure (also referred to as the High Temperature LiCoO_2 phase). Note, that all reflections shift to a lower angle with increasing temperature due to the lattice expansion. The patterns could not be re-measured upon cooling, but the room-temperature measurement revealed the typical HT- LiCoO_2 diffraction pattern.

The XRD patterns of all $\text{Li}_x\text{Co}_y\text{Mn}_{1-y}\text{O}_2$ powders after HT-calcination are shown in Figure 7.3. Not all compositions are completely single phase: the samples with $y=0.1$ and $y=0.5$ show additional MnO_2 reflections in the 20° to 35° range. Si contamination from the quartz container is insignificant, as the amount observed with XRF is below the detection limit.

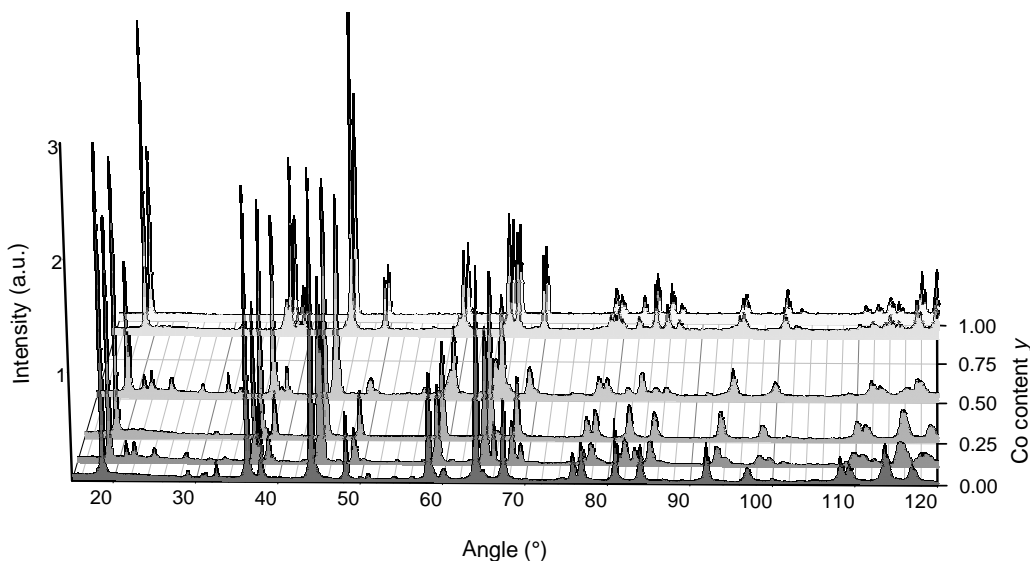


Figure 7.3: XRD patterns of the $\text{Li}_x\text{Co}_y\text{Mn}_{1-y}\text{O}_2$ powders plotted as a function of Co content y after HT-calcination at 900°C for 120h in quartz tubes.

The unit cell dimensions of the cubic spinel phase exhibit a gradual decrease with increasing Co content. Hexagonal symmetry is observed at $y > 0.5$. The A -axis of the cubic unit cell is plotted in Figure 7.4 as a function of y . The last two values for $y = 0.9$ and $y = 1$ have been calculated from the rhombohedral (110) plane diffraction. The unit cell dimensions of the quenched and slow-cooled powders reported by Zhecheva *et al.* [5] show that the thermal history has a large influence on the lattice dimensions. The rhombohedral a -axis has been estimated for all compositions and is a measure for the in-plane O-O distance.

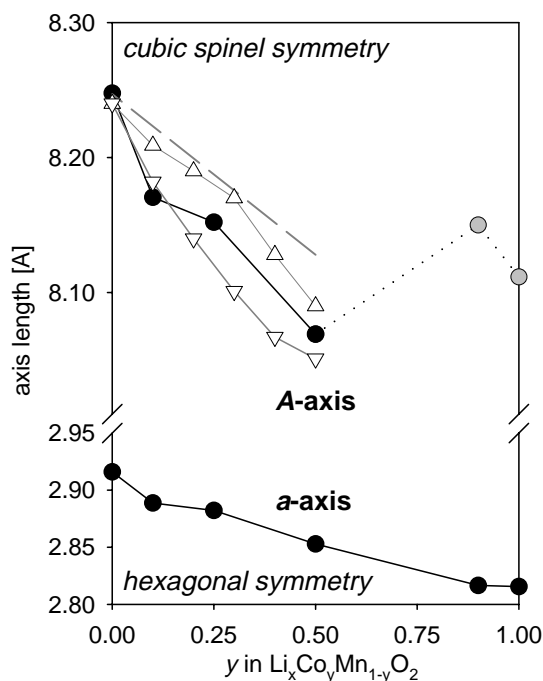


Figure 7.4: The closed circles indicate the unit cell dimension of the $\text{Li}_x\text{Co}_y\text{Mn}_{1-y}\text{O}_2$ powders plotted as function of y . The a -axis is related to a hexagonal unit cell, the A -axis to a cubic cell. The triangles represent the A -axis values of quenched (Δ) and slow-cooled (∇) powders as reported by Zhecheva [5,6]. The dashed, grey line indicates the unit cell contraction solely due to the increase of Mn oxidation state in $\text{Li}_x\text{Mn}_2\text{O}_z$ thin-films as reported by Morcrette [1].

7.3.2 Composite electrode properties

The cyclic voltammogram of a coin cell consisting of HT-calcined LiCoO_2 is shown in Figure 7.5 (scan rate $0.5\text{mV}\cdot\text{s}^{-1}$). The first scan exhibits large irreversible capacity, which is observed for all composite electrodes. The yield is only 45%, but increases to 79% in the second cycle. Three specific reduction peaks are observed at 3.81V, 4.01V and 4.14V, which have a mutual charge ratio of 7:2:1, respectively. These could not be reproduced in the second cycle, but do re-appear at a lower scan rate of $0.01\text{mV}\cdot\text{s}^{-1}$. Under these conditions the surface area of the peaks approximates the theoretical capacity deduced from the amount of active material. This suggests, that current leakage has little effect on this particular electrode.

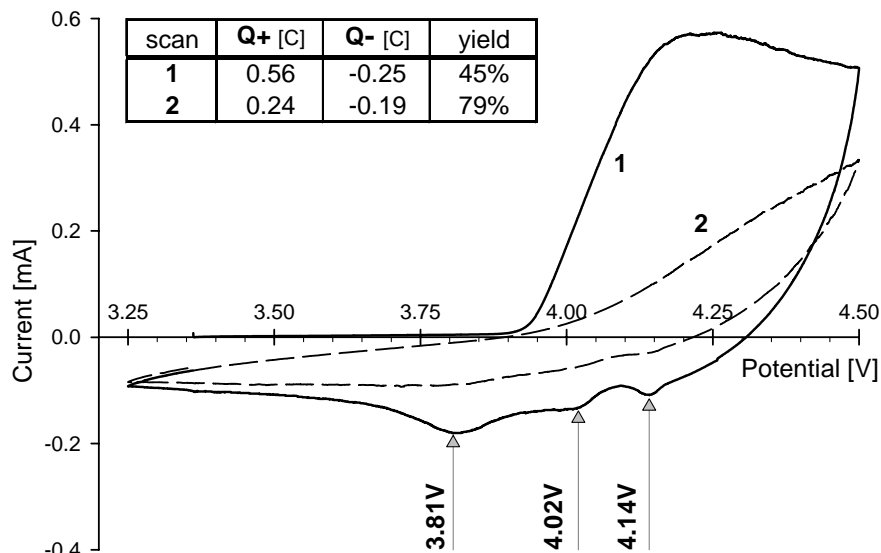


Figure 7.5: Cyclic voltammogram of the LiCoO_2 powder embedded in a composite electrode against metallic lithium recorded with a scan rate of $0.5\text{mV}\cdot\text{s}^{-1}$. The charge involved in the anodic ($Q+$) and cathodic part ($Q-$) of the first and second scan (marked 1 and 2, respectively) have been listed in the inset table, together with the Faradaic yield.

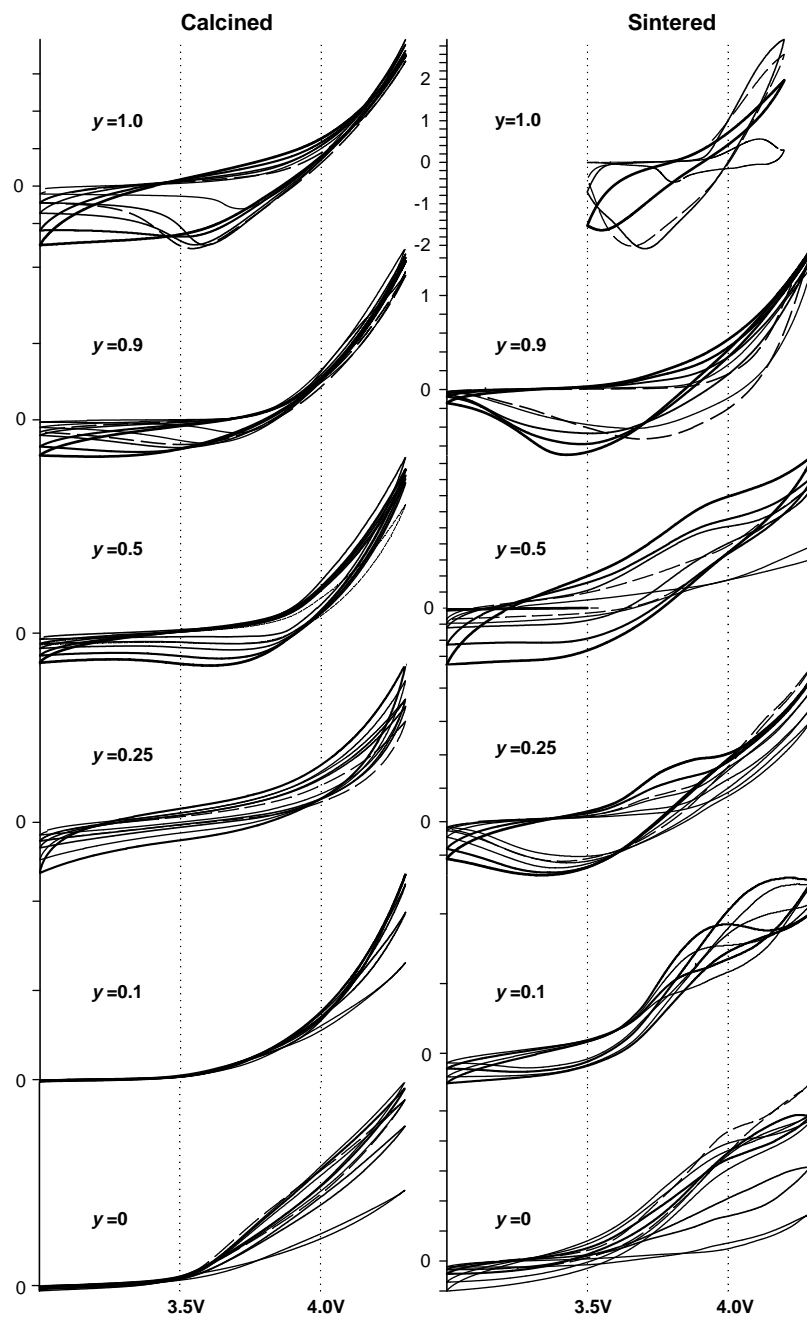


Figure 7.6: Cyclic Voltammograms of the LT- and HT-calcined $\text{Li}_x\text{Co}_y\text{Mn}_{1-y}\text{O}_2$ powders embedded in composite electrodes and cycled against metallic lithium with incrementing scan rate: 0.5, 1, 2, 5, and $10\text{mV}\cdot\text{s}^{-1}$ between 3.0 and 4.3V. A thicker line denotes a higher scan rate; the dotted line represents the concluding $1\text{mV}\cdot\text{s}^{-1}$ scan. Y-axis ticks indicate 0.1mA, 1mA steps are numbered.

The cyclic voltammograms of all composite electrode compositions are plotted in Figure 7.6. The LT-calcined powders are shown on the left, the HT-calcined powders on the right. The potential scan ranges from 3V to 4.3V and has been recorded with incrementing scan rate: 0.5, 1.0, 2.0, 5.0 and 10.0mV/s. At each step two cycles are completed of which only the second scan is displayed. The thickness of the lines in Figure 6 indicates the applied scan rate. At the end of this sequence, the 1mV/s cycle is re-measured to reveal any changes in the electrode behaviour (dashed curve). To enable comparison of typical features, all graphs are plotted on the same size and use the same type indications for the current scale: the major ticks represent a current of 0.1mA and the 1mA steps are numbered. Hence, a large amount of ticks implies a large current response. The charges associated with the anodic current (Q+) and the cathodic current (Q-) of the first and concluding 1mV·s⁻¹ scans are listed in Table 7.2.

Table 7.2: The anodic (Q-) and cathodic (Q+) capacity of the $\text{Li}_x\text{Co}_y\text{Mn}_{1-y}\text{O}_2$ powders at various stages of synthesis as recorded with cyclic voltammetry at 1mV·s⁻¹ in the second and the concluding scan. The Faradaic yield is calculated as percentage for both scans.

| Sample | | second scan | | | final scan | | |
|--|-----------|---------------|---------------|--------------|---------------|---------------|--------------|
| | | Q+ [mAh/g] | Q- [mAh/g] | yield [%] | Q+ [mAh/g] | Q- [mAh/g] | yield [%] |
| LiCoO ₂ | pyrolysed | 0.14 | -0.03 | 21% | 0.13 | -0.03 | 22% |
| | calcined | 2.66 | -1.24 | 47% | 2.30 | -1.43 | 62% |
| | annealed | 101.14 | -93.74 | 93% | 94.42 | -91.97 | 96% |
| LiCo _{0.9} Mn _{0.1} O ₂ | calcined | 1.95 | -0.39 | 20% | 2.89 | -1.79 | 62% |
| | annealed | 17.81 | -9.97 | 56% | 28.81 | -8.47 | 29% |
| LiCo _{0.5} Mn _{0.5} O ₂ | calcined | 0.54 | -0.09 | 17% | 0.44 | -0.10 | 22% |
| | annealed | 14.72 | -1.69 | 12% | 17.75 | -1.06 | 6% |
| Li _{0.5} Co _{0.25} Mn _{0.75} O ₂ | calcined | 0.19 | -0.02 | 13% | 0.16 | -0.02 | 16% |
| | annealed | 5.71 | -2.33 | 41% | 8.64 | -2.16 | 25% |
| Li _{0.5} Co _{0.1} Mn _{0.9} O ₂ | calcined | 2.21 | 0 | 0% | | | |
| | annealed | 8.64 | -2.16 | 25% | | | |
| Li _{0.5} MnO ₂ | pyrolysed | 0.57 | -0.19 | 34% | 0.48 | -0.17 | 35% |
| | calcined | 1.14 | 0 | 0% | 1.39 | 0 | 0% |
| | annealed | 8.28 | -0.39 | 5% | 16.66 | -0.40 | 2% |

The pyrolysed $\text{Li}_x\text{Mn}_2\text{O}_4$ and LiCoO_2 powders exhibit some intercalation capacity, but the featureless voltammograms are not shown. Overall, the HT-calcined powders show improved performance compared with the LT-calcined powders of the same composition. Specifically the cathodic part of the current response, corresponding to lithium de-intercalation, decreases with a decreasing value of y . As a result, the Faradaic yield decreases with decreasing Co content. Above 4.0V a strong (linear) increase of the anodic current is observed with increasing potential for all voltammograms, which is related to electrolyte decomposition. The sintered, Mn-rich powders show an additional broad current maximum around 4V. The origin of this anodic peak is yet unclear.

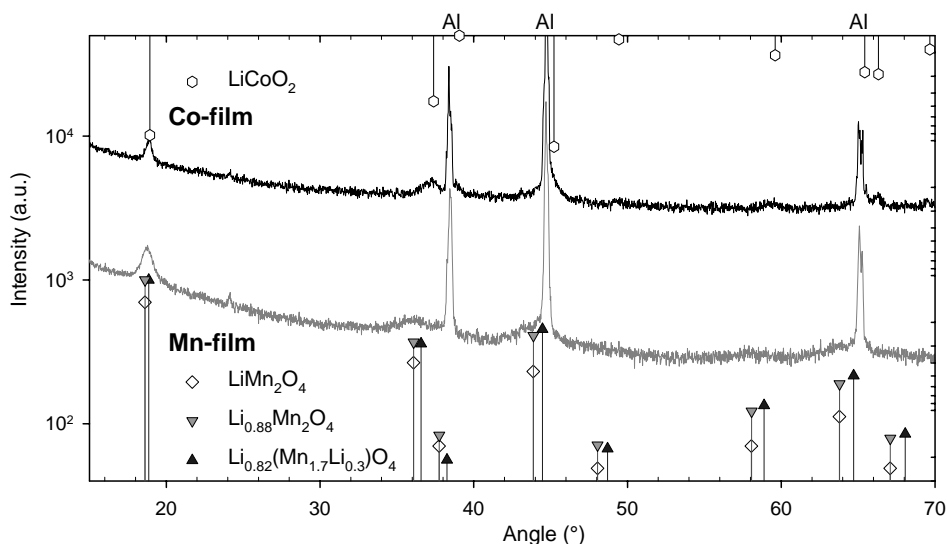


Figure 7.7: XRD patterns of the as-deposited LiCoO_2 and the $\text{Li}_x\text{Mn}_2\text{O}_4$ thin-films on aluminium substrates plotted together with the possible reference patterns.

7.3.3 Structural analysis of thin films

Upon deposition at 300°C substrate temperature the deposited films already exhibit some crystal structure. Figure 7.7 shows the XRD patterns of the as-deposited, thin-film LiCoO_2 and $\text{Li}_x\text{Mn}_2\text{O}_4$ electrodes on aluminium substrates. The substrate reflections are indicated with *Al* and all reference patterns are plotted as bars. The LiCoO_2 PLD-films exhibit a strict *c*-axis orientation on a silicon substrate, but here a more random orientation is observed. The peaks of

the $\text{Li}_x\text{Mn}_2\text{O}_4$ film do not completely match the reference spectrum, but are shifted slightly towards that of $\text{Li}_{0.82}(\text{Mn}_{1.7}\text{Li}_{0.3})\text{O}_4$. This suggests that the lithium site occupation is not uniform. Evidence for lithium deficiency cannot be derived from this diffractogram, as it does not cause peak shifting.

XRF is used to make a semi-quantitative estimate of the elements in the as-deposited $\text{Li}_x\text{Mn}_2\text{O}_4$ and LiCoO_2 films. The results are listed in Table 7.3. The mutual ratio of Li:Co:O coincides with the stoichiometric formula. The Li quantity in the Mn-film cannot be measured and the Mn:O ratio already shows discrepancy with the $\text{Li}_x\text{Mn}_2\text{O}_4$ formula. Some carbon has also been detected in the films.

Table 7.3: *The semi-quantitative estimate obtained from XRF analysis of the as-deposited LiCoO_2 and $\text{Li}_x\text{Mn}_2\text{O}_4$ films on aluminium substrate.*

| Element | Mn-film [conc.%] | Co-film [conc.%] |
|---------|---------------------|---------------------|
| Mn | 38.53 | |
| Co | | 21.98 |
| O | 43.02 | 43.69 |
| Li | | 11.00 |

7.3.4 Electrochemical thin-film properties

The as-deposited LiMn_2O_4 and LiCoO_2 thin-film electrodes have been cycled against lithium with a constant current of $2\mu\text{A}\cdot\text{cm}^{-2}$. The first three cycles are shown in Figure 7.8. For the LiCoO_2 film the typical charge-discharge curve is observed (compare Figure 4.6). The reversible capacity stabilises at $4.21\mu\text{Ah}$, which is 8% of its theoretical capacity. The $\text{Li}_x\text{Mn}_2\text{O}_4$ film exhibits a rather steep charge-discharge curve and a continuous capacity fade.

After heat treatment at 500°C for 15h, the intercalation activity is virtually reduced to zero. At these elevated temperatures the aluminium substrate appears to react with the film and oxides are formed.

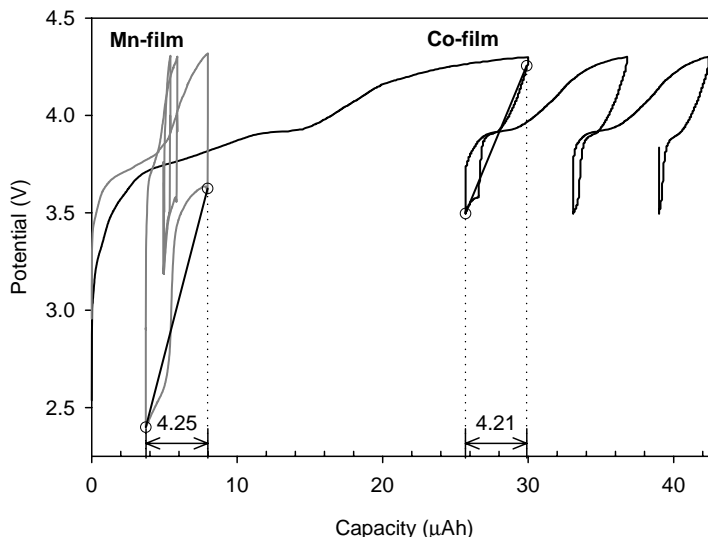


Figure 7.8: The constant current cycling of as-deposited LiCoO_2 and $\text{Li}_x\text{Mn}_2\text{O}_4$ films on aluminium substrates against metallic lithium using $2\mu\text{A}\cdot\text{cm}^{-2}$. The first discharge capacity is indicated.

7.3.5 Spectral analysis

Raman spectroscopy - Raman spectra of the LiCoO_2 films depend on the thermal and electrochemical history of the sample, as shown in Figure 7.9a. The top curve is recorded from a cycled LiCoO_2 RF-film; the next curve is from an as-deposited PLD-film on a silicon substrate. The peak located at 521cm^{-1} is attributed to the Raman mode of the silicon substrate. LiCoO_2 exhibits two Raman bands at 486cm^{-1} (E_g mode) and 596cm^{-1} (A_{1g} mode) with an intensity ratio of 1:2. The peak at 694cm^{-1} is attributed to the presence of Co_3O_4 [5].

Deposition on aluminium substrates changes the ratio of both LiCoO_2 bands and introduces three peaks at 199cm^{-1} , 530cm^{-1} and 628cm^{-1} . The latter bands increase in intensity with annealing treatment, while the A_{1g} mode disappears completely. As the Co_3O_4 peak increases as well, it is assumed that LiCoO_2 degrades through loss of volatile Li_2O . The laser light intensity has not been observed to induce degradation of the transition metal oxide films.

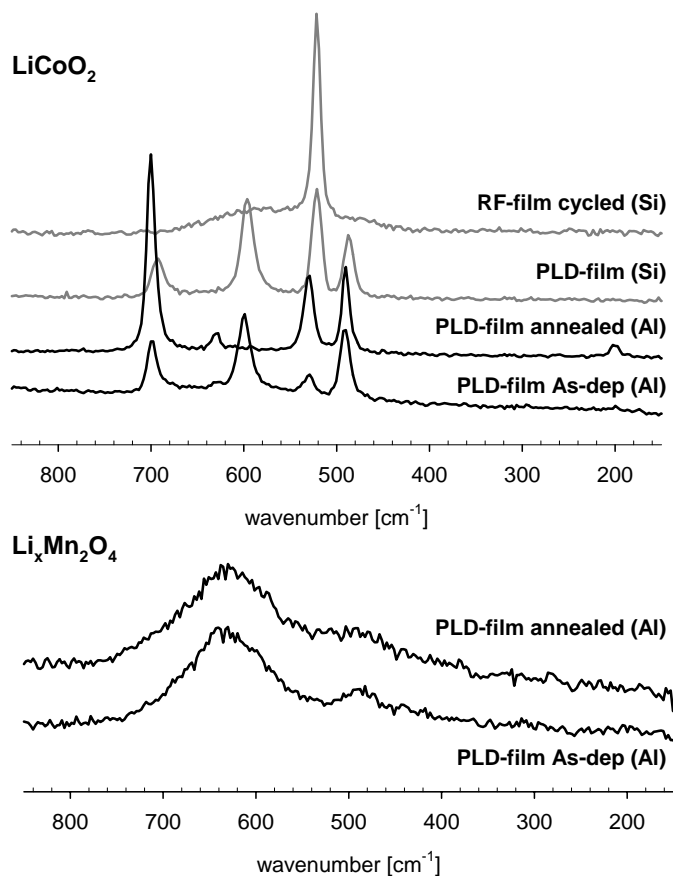


Figure 7.9: RAMAN spectra between 100cm^{-1} and 1000cm^{-1} of as-deposited LiCoO_2 films on silicon and aluminium substrate are shown on the top, together with the spectrum of an annealed LiCoO_2 film. The RAMAN spectra of the as-deposited and annealed $\text{Li}_x\text{Mn}_2\text{O}_4$ films on aluminium are shown on the bottom.

The $\text{Li}_x\text{Mn}_2\text{O}_4$ films on aluminium remain unaltered during annealing treatment. According to the theoretical factor-group analysis, five modes are active in the Raman spectrum of the spinel crystal: a band at 622cm^{-1} (A_{1g} mode), at 437cm^{-1} (E_g mode) and three modes at 374cm^{-1} , 499cm^{-1} and 573cm^{-1} (F_{2g} modes). The mode located at 374cm^{-1} corresponds to a vibration of the LiO_4 tetrahedra [2]. The A_{1g} and the E_g modes are located within the broad peaks shown in Figure 7.9b, but cannot be identified separately. The bands observed at 640cm^{-1} could indicate Mn sub-oxides, such as Mn_3O_4 and Mn_2O_3 .

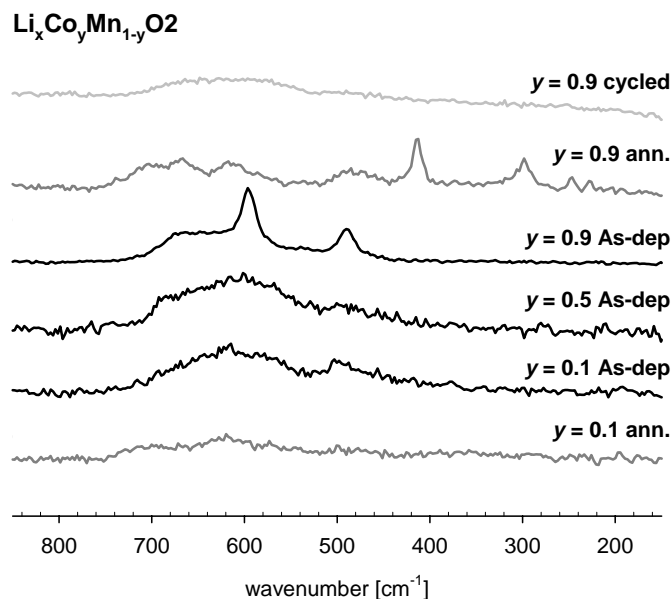


Figure 7.10: RAMAN spectra of the as-deposited and annealed $\text{Li}_x\text{Co}_y\text{Mn}_{1-y}\text{O}_2$ films on stainless steel substrates, plotted for $y=0.1$, $y=0.5$ and $y=0.9$. The curves have been vertically shifted for clarity.

The Raman spectra of the as-deposited and annealed (30min, 600°C) $\text{Li}_x\text{Co}_y\text{Mn}_{1-y}\text{O}_2$ films on stainless steel substrates are compared in Figure 7.10. The Co-rich film with $y=0.9$ shows a clear A_{1g} band at 595 cm^{-1} and E_g band at 488 cm^{-1} similar to the LiCoO_2 spectrum on silicon. However, other undefined peaks appear in the range 627 cm^{-1} to 676 cm^{-1} .

As the Co content decreases to $y=0.5$, the broad, Mn-like bands overwhelm the sharp Co features, which suggests a different crystal structure exists. The former E_g band appears shifted to 492 cm^{-1} . At $y=0.1$, this band located at 498 cm^{-1} , can also be attributed to the F_{2g} modes of the spinel. Other spinel bands can also be identified, such as the 374 cm^{-1} and the 573 cm^{-1} bands and the A_{1g} mode at 620 cm^{-1} . Also a Co_3O_4 like band exists at 678 cm^{-1} . These results suggest a gradual structural transition with decreasing Co content.

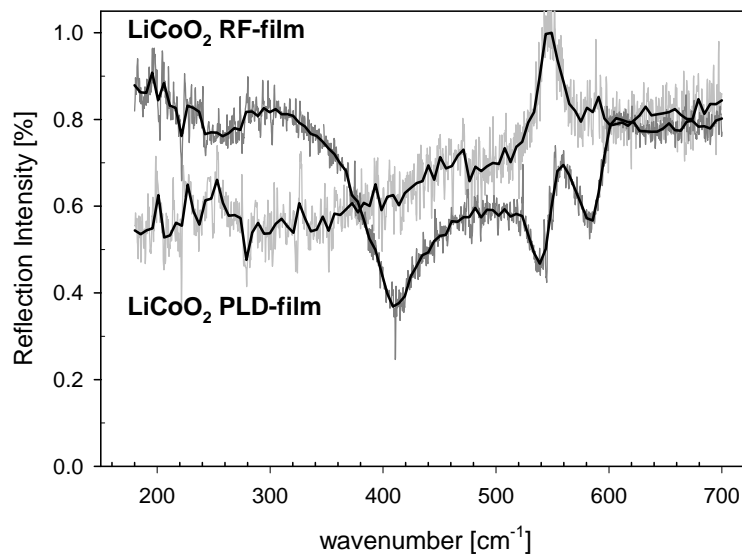


Figure 7.11: FTIR spectra of an as-deposited, LiCoO_2 RF-film and PLD-film on silicon substrates (recorded in reflection mode).

FTIR - Fourier Transform Infra Red experiments are conducted under ambient conditions using the reflection mode. For most thin-film electrodes the IR-spectrum is determined entirely by the substrate material: *n* and *p*-type silicon could be discerned and the thermal history of the stainless steel substrates is recognized. However, the as-deposited LiCoO_2 films on silicon substrates showed some typical features (see Figure 7.11). The RF-film exhibits minimum reflection intensity at 242cm^{-1} , 408cm^{-1} , 539cm^{-1} and 586cm^{-1} . Alcántara *et al.* [7] reported strong bands at 535cm^{-1} and 598cm^{-1} and weaker bands at 554cm^{-1} and 598cm^{-1} . The PLD-film shows total reflection at 549cm^{-1} .

XPS - Figure 7.12 shows the X-ray Photon Spectroscopy spectra of the $\text{LiCo}_y\text{Mn}_{1-y}\text{O}_2$ films on stainless steel substrates for the specific binding energy ranges of Co 2p, Mn 2p, O 1s and Li 1s electron orbitals.

The Co 2p_{3/2} peak at 780eV and the minor peak at 790eV are typical for Co-oxides in a M³⁺ oxidation state. Sub-oxides such as CoO and Co₃O₄ exhibit the Co 2p_{3/2} band at 780.8eV and 780.3eV, respectively. The LiCo_yMn_{1-y}O₄ films exhibit the 780.0eV peak that shifts to lower binding energies with an increasing value of y. The as-deposited LiCoO₂ film shows similar downward shift of the Co 2p_{3/2} band with the annealing treatment, together with an intensity increase. This annealed LiCoO₂ film spectrum (dashed) has been reduced by a factor of 6 to allow comparison of the peak positions.

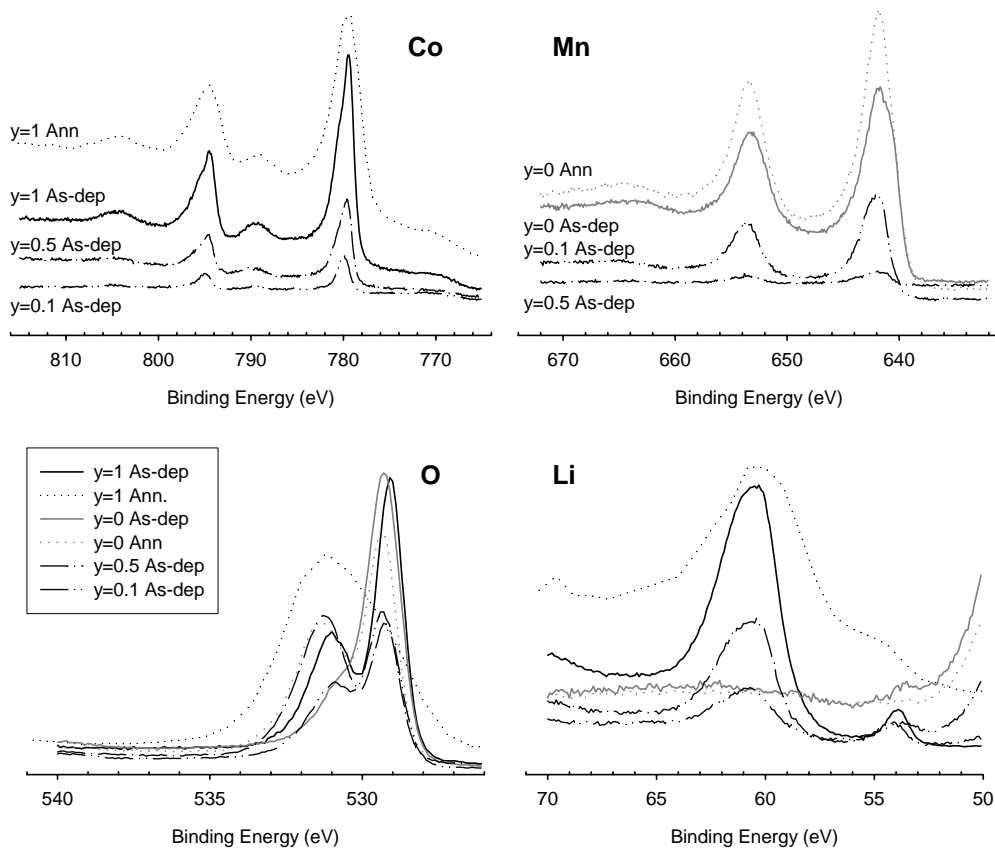


Figure 7.12: XPS spectra of the as-deposited and annealed LiCoO₂ and Li_xMn₂O₄ films on aluminium substrates and the as-deposited Li_xCo_yMn_{1-y}O₂ films on stainless steel substrates. Only the ranges of the Co2p, Mn2p, O1s and Li1s binding energies are shown. The intensity of the dotted line has been reduced by a factor of 6 for means of comparison.

The Mn spectra show two major peaks at 641.8eV and 653.4eV. The peak location remains unaltered, while the intensity decreases linearly with increasing Co content. Annealing treatment induces band sharpening.

The binding energy of the O-2p electrons is split up into two separate maxima: the peak at 529.5eV is assigned to oxygen incorporated in the film structure, while the second peak at 531.4eV is attributed to oxygen adsorbed on the sample surface [8]. The peak ratio indicates, that the as-deposited films have oxygen species involved mainly in the bulk film structure, while the annealed films exhibit more surface-related oxides, possibly as a result of degradation. The lattice-oxygen binding energy of the as-deposited Mn-rich samples is slightly higher than for the Co-rich samples: 529.8 and 529.1eV for $y=0$ and $y=1$, respectively. The peak intensity is comparable.

The Li-1s could not be observed within scan range for the $\text{Li}_x\text{Mn}_2\text{O}_4$ films, but could be shifted to around 50eV, as the intensity is observed to incline toward the edge. The Co-rich films exhibit a large peak at 61eV and a smaller one at 54eV. The latter could be related to the presence of Li_2O .

7.4 Discussion

7.4.1 Powder structure

The pyrolysis synthesis method is suitable for preparing homogeneous mixed transition metal oxides, while maintaining the small grain size. The SEM micrographs reveal amorphous, glass-like pyrolysed products for all compositions. Upon annealing at 600°C the nitrogen, hydrogen and carbon compounds are removed and uniform grains of roughly 0.5 μm remain. The LiCoO_2 powder diffractogram in Figure 7.2 indicates that additional calcination at high temperatures is necessary to obtain a fully ordered crystal structure. The classical synthesis of $\text{Li}_x\text{Mn}_2\text{O}_4$ also involves heating to 800°C in air [9].

All powder compositions have undergone identical heat treatment of 120h at 900°C. The Co-rich powders show excessive grain growth during the heat treatment, while the Mn-rich powders tend to show agglomeration of the

individual grains. This suggests that Co enhances the material transport during sintering.

Loss of lithium is observed (Table 7.1), due to the long period of time at elevated temperature. The 10% surplus lithium incorporated in the synthesis procedure proved insufficient. A scavenging effect of the quartz tube containers could be responsible for the unexpected lithium deficiency.

Unit cell dimensions - The cubic unit cell dimensions decrease with increasing Co doping from $y=0$ to $y=0.5$. This composition range is reported to form a solid solution. The powders with $y=0.9$ and $y=1.0$ fit in another solid solution range with hexagonal symmetry.

In the spinel structure, the lattice parameters are linearly related to the average M-O bond length, as only the octahedral sites of an undistorted cubic lattice are occupied [3]. With increasing Co substitution, a decrease of A is consistent with the smaller size of Co^{3+} compared with Mn^{3+} . However, the bond length also depends on the valence state of the Mn [1]. As indicated by the dashed line in Figure 7.4, the major part of the lattice contraction is attributed to the increasing Mn oxidation state from M^{3+} to M^{4+} . The higher electronegativity of Co compared with Mn could cause further reduction of the unit cell. The slightly parabolic behaviour of the lattice contraction suggests that a non-random distribution of the Mn and Co exists in the intercalation structure [5].

7.4.2 Composite electrode cycling

All powders and films show a large irreversible capacity upon the first cycle. Most characteristic features, such as oxidation and reduction peaks, fade on subsequent cycles and re-appear only at decreased cycling rate. This suggests lithium (de-)intercalation is detrimental to the structural integrity of the host.

The cyclic voltammograms reveal superior intercalation behaviour of the HT-calcined LiCoO_2 composite electrode. Increasing Co substitution in $\text{Li}_x\text{Co}_y\text{Mn}_{1-y}\text{O}_2$ composite electrode also improves their cycling properties. The reduction current in the cathodic curve appears correlated with the Co content. In case of pure LiCoO_2 this current peak, located at 3.8V, delivers the full theoretical capacity at low scan rate ($0.01\text{mV}\cdot\text{s}^{-1}$). With increasing scan rate, the peak

separation between the reduction peak and the corresponding oxidation peak increases and the associated capacity decreases.

Most curves in Figure 7.6 show similar distortion, which suggests that the scan rate is too fast to maintain quasi-equilibrium intercalation conditions. The low reversible capacities listed in Table 7.2 also suggest that the intercalation process cannot follow a scan rate of $1\text{mV}\cdot\text{s}^{-1}$ or even $0.5\text{mV}\cdot\text{s}^{-1}$. Due to significant electrolyte decomposition, it is not useful to apply extremely low scan rates. The decomposition reaction rate increases with the cell potential and causes a linear anodic current, which leads to the low Faradaic yield. The increment of this current depends on the scan rate and has been observed to increase with time.

Especially the Mn-rich samples show characteristics of electrolyte degradation and exhibit low Faradaic yields. This cannot be attributed to a disproportionation reaction, as it is unlikely to occur in the case of $y=0.5$, when all Mn ions are in the M^{4+} state. Apparently, the Mn-based intercalation hosts are not in their stable form and thus incapable of lithium (de-)intercalation. Hence, the injected charge is not used to change the lithium stoichiometry, but lost to electrolyte decomposition. No intercalation capacity has been observed in the 3V range against lithium, corresponding to the surplus lithium intercalation in the spinel structure.

The HT-calcination treatment does improve the reversible intercalation capacity to some extent, probably through equilibration of the structure. The presence of Co could accelerate this rearrangement process by enhancing the cationic mobility. Excessive grain growth has been observed for Co-rich powders on the micrographs in Figure 7.1. The presence of additional phases observed in XRD for the $y=0.1$ and the $y=0.5$ powders is regarded of minor influence.

7.4.3 Thin-film electrodes

The LiCoO_2 and $\text{Li}_x\text{Mn}_2\text{O}_4$ films show the same crystal symmetry as the bulk powders. Some preferential orientation is observed, but due to the surface roughness of the aluminium substrates it is not as strong as observed on silicon. The planes with highest density are parallel to the substrate surface, being (003) and (111) for the hexagonal and spinel structure, respectively. The presence of some Co and Mn sub-oxides is observed.

Deposition of the LiCoO_2 films at lower oxygen background pressure has little influence on the crystal structure. However, in case of $\text{Li}_x\text{Mn}_2\text{O}_4$ films the deposition at $p\text{O}_2=0.02\text{mbar}$ (instead of $p\text{O}_2=0.2\text{mbar}$) leads to unknown symmetries, which cannot be identified from their diffraction peaks (generally around $2\theta = 35^\circ\text{-}45^\circ$). The substrate temperature has some effect on the appearance of these unrecognisable XRD reflections. The current as-deposited $\text{Li}_x\text{Mn}_2\text{O}_4$ films also do not show the expected composition (Table 7.3). This suggests that the manganese spinel structure is very sensitive to the preparation conditions and that the required LiMn_2O_4 phase is only stable within a small process window. Morcrette *et al.* [1] have reported the $p\text{O}_2$ sensitivity during

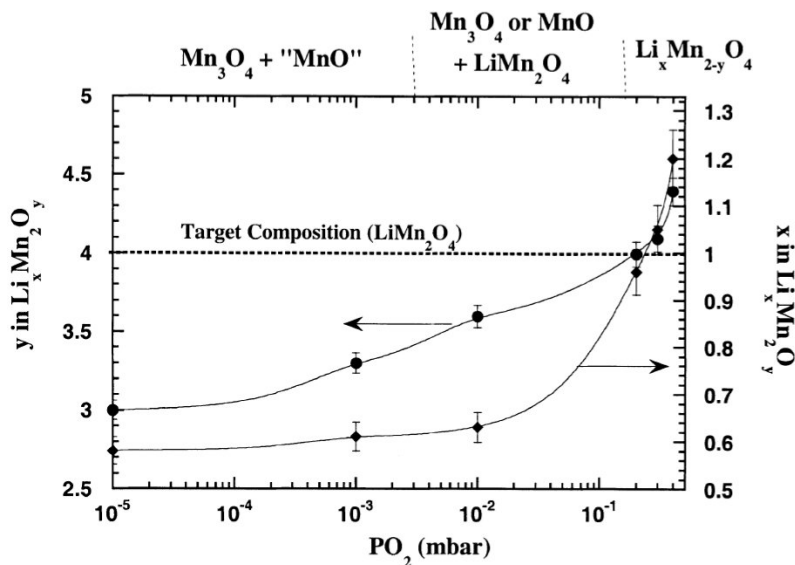


Figure 7.13: Oxygen and lithium content as a function of the oxygen pressure during deposition at 500°C determined by nuclear reaction analysis [1].

Pulsed Laser Deposition (see Figure 7.13). Lithium and oxygen deficiency could well account for the structural disorder and subsequent inferior electrochemical performance of the manganese films.

The as-deposited LiCoO_2 film exhibits only its theoretical capacity on the first galvanostatic charge cycle. A limited amount of material remains active in subsequent cycles. The LiMn_2O_4 suffers a continuous capacity loss, which appears to be caused by loss of active material. The $\text{Li}_x\text{Co}_y\text{Mn}_{1-y}\text{O}_2$ thin-films also show fast disintegration of the host structure for low values of y . The structural integrity of the films is further investigated with spectroscopy.

7.4.4 Spectroscopy

The $R\bar{3}m$ structure of the LiCoO_2 displays two gerade modes A_{1g} and E_g which are Raman active and two ungerade modes $2A_{2u}$ and $2E_u$, which are Infra Red active. The Raman active modes are attributed to the vibration of the oxygen atoms. Line broadening indicates a disorder in the oxygen sublattice, which could be caused by an amorphous structure of the material, distortion in the oxygen coordination of cations (*e.g.*, Mn, Co) or by the random site occupation by lithium.

LiCoO₂ - The LiCoO_2 films reveal sharp Raman bands and thus exhibit a well-defined structure upon deposition. Annealing treatment does not improve the Full Width Half Maximum (=FWHM) of the peaks, but leads only to the formation of additional sub-oxides. The sharp peak at 699cm^{-1} can be attributed to Co_3O_4 and indeed gains intensity upon annealing. Note, that the A_{1g} band of the LiCoO_2 film on the aluminium substrate is lost during 15h annealing at 500°C and new bands are introduced at 628cm^{-1} and 530cm^{-1} for which we do not have an interpretation. Short annealing treatment (600°C , 30min) does not have such a detrimental influence.

After electrochemical cycling, the LiCoO_2 films do no longer exhibit the distinct hexagonal vibration bands. Electrochemical de-intercalation of lithium is reported to generate a second hexagonal phase with less Raman intensity, exhibiting the A_{1g} and E_g modes at 586cm^{-1} and 480cm^{-1} , respectively, due to the c -axis expansion [10]. However, all films have been measured in the intercalated state and none of the complementary bands were observed. Apparently, repeated

lithium intercalation disrupts the symmetry of the local crystal structure. This ‘amorphisation’ is also observed for the as-deposited $\text{Li}_x\text{Co}_{0.9}\text{Mn}_{0.1}\text{O}_4$ film on stainless steel substrate (see Fig. 7.9), but not detectable for compounds with lower value of y .

$\text{Li}_x\text{Mn}_2\text{O}_4$ - The $\text{Li}_x\text{Mn}_2\text{O}_4$ films reveal broad bands upon deposition and show a small decrease of the FWHM upon annealing. The spinel lattice appears to be unstructured. Julien *et al.* [2] have reported that the Raman spectra of $\text{Li}_x\text{Mn}_2\text{O}_4$ PLD-films, deposited from targets containing less than 10% surplus Li_2O , are less resolved and the 622cm^{-1} peak is broadened towards the higher wavenumber. These observations agree with our results and suggest lithium deficiency is a problem. This could also contribute to the formation of sub-oxides, which exhibit broad bands in the region 640cm^{-1} to 700cm^{-1} .

$\text{Li}_x\text{Co}_y\text{Mn}_{1-y}\text{O}_2$ - In the Raman spectra of the mixed transition metal oxide films the sharp Co features are easily recognised between the broad Mn-related bands. The octahedral coordination of the Co appears more rigid than that of Mn and this suggests that the site occupation and oxidation state of Co are also more consistent. With decreasing Co content the E_g band attributed to CoO_6 octahedra decreases in intensity and shifts to higher wavenumbers. This upward peak shift does not agree with the lattice expansion obtained from the powder XRD patterns. However, the local Co environment in as-deposited thin-films is not necessarily related to the unit cell dimensions of the sintered powder. Note, that annealing treatment of the thin-films on stainless steel only broadens the Raman bands, indicating structural degradation of the film instead of improvement, possibly due to reaction with the substrate material.

IR-active modes are expected to complement the Raman-active modes. Hence, only distinct bands are expected for the Co-rich films. Low-intensity IR-bands have been observed for the LiCoO_2 films. The different vibration frequencies of the RF- and PLD-film suggest a correlation with the preferential orientation of the crystal lattice.

The substrate material has a large influence on the FTIR spectrum. For example, the stainless steel substrates show an increased absorbance at the Fe-O stretching frequency with annealing treatment. More measurements need to be performed on

thicker films in order to obtain a distinct spectrum of the film and a clear understanding of its lattice vibrations.

Cation oxidation state - The binding energy peaks of the Co and the Mn ions in the XPS spectra (Figure 7.12) of the (mixed) transition metal oxide films are well defined. The consistency in shape gives the impression that the oxidation state changes little with increasing Co substitution. According to Kajiyama *et al.* [11] the 780eV peak corresponds with Co^{3+} and its presence is expected in this fully intercalated state of the host material. The slight increase of the peak location with increasing y corresponds with the downward shift of the 529eV peak of the O-1s. This interaction could be the result of the stronger electronegative properties of the Co compared with Mn, which influences the electron distribution in the common M-O orbitals. Annealing treatment induces only a significant increase of the O-1s peak at 532eV, which coincides with the formation of either Co or Mn sub-oxides at the film surface. Detailed peak analysis has not been performed, due to the uncertain phase composition.

The bands of the Li-1s show a clear decrease at 61eV and an increase at 48eV, (just outside the graph), with decreasing value of y . The associated electrons appear to be two-fold in nature and could be related to the tetrahedral and octahedral site occupation of the Li ion in $\text{Li}_x\text{Mn}_2\text{O}_4$ and LiCoO_2 , respectively. The mixed transition metal oxides show intermediate distributions between both electron orbitals. However, taking into account the instability of the spinel structure, the 48eV band could also be associated with manganese sub-oxides or decomposition products. XPS analysis as a function of the lithium concentration is required to identify the Li electron bands and distinguish which transition metal ion is actually involved in the intercalation process. However, this could not be achieved in the specific time period.

7.5 Conclusions

The EDTA-synthesis is a suitable method to prepare mixed transition metal oxide powders. After calcination at 600°C, the pyrolysed product exhibits a crystal structure and some electrochemical features are observed (*e.g.* potential plateaus). However, the powder only obtains a fully ordered lattice and adequate intercalation capacity after calcination at 900°C.

An increasing degree of Co substitution in $\text{Li}_x\text{Co}_y\text{Mn}_{1-y}\text{O}_2$ powders leads to a decrease in the unit cell dimensions and improves the electrochemical performance of the composite electrodes. At $y > 0.5$ a structural transformation occurs from cubic to hexagonal crystal symmetry. An initial lithium deficiency is observed for all compounds, in spite of the 10% surplus lithium used in the preparation.

The PLD-films already are crystalline upon deposition at a substrate temperature of 300°C. Annealing treatment is observed to cause film degradation, possibly due to the reactivity of the metal substrate. LiCoO_2 shows very distinct lattice vibrations, while those of the manganese films appear vague and have low intensity. The $\text{Li}_x\text{Co}_y\text{Mn}_{1-y}\text{O}_2$ films of intermediate composition show a gradual transformation between the typical Co and Mn features. This suggests that the Co has a stronger interaction with the co-ordinating oxygen atoms than Mn. The structural integrity disappears with electrochemical cycling of the film.

The stoichiometry is critical for the Mn-based spinel hosts, as degradation during electrochemical cycling is accelerated by structural defects (*e.g.* cationic disorder, oxygen deficiency). Optimisation of the synthesis and sintering procedure is recommended.

7.6 References

1. M. Morcette, P. Barboux, J. Perriere, T. Brousse, A. Traverse, J.P. Boilot, *Solid State Ionics*, **138** 213 (2001).
2. C. Julien, E. Haro-Poniatowski, M.A. Camacho-Lopez, L. Escobar-Alarcon, J. Jimenez-Jarquin, *Mat. Science and Engineering*, **B72** 36 (2000).
3. H. Kawai, M. Nagata, H. Kageyama, H. Tukamoto, A.R. West, *Electrochimica Acta* **45** 315 (1999).
4. L.M. van der Haar, "Oxygen Permeation through Dense Perovskite Membranes", Thesis University of Twente, The Netherlands (2001).
5. E. Zhecheva, R. Stoyanova, M. Gorova, P. Lavela, J.L. Tirado, *Solid State Ionics*, **140** 19 (2001).
6. E. Zhecheva, R. Stoyanova, M. Gorova, R. Alcantara, J. Morales, J.L. Tirado, *Chem. Mater.*, **8** 1429 (1996).
7. R. Alcantara, P. Lavela, J.L. Tirado, R. Stoyanova, E. Zhecheva, *J. Solid State Chem.*, **134** 265 (1997).
8. K. Kanamura, S. Toriyama, S. Shiraishi, M. Ohashi, Z. Takehara, *J. Electroanalytical Chem.*, **419** 77 (1996).
9. M.R. Palacin, G. Rouse, M. Morcette, L. Dupont, C. Masquelier, Y. Chabre, M. Hervieu, J-M. Tarascon, *J. Power Sources*, **97-98** 398 (2001).
10. M. Inaba, Y. Iriyama, Z. Ogumi, Y. Todzuka, A. Tasaka, *J. Raman Spectroscopy*, **28** 613 (1997).
11. A. Kajiyama, K. Takada, T. Inada, M. Kouguchi, S. Kondo, M. Wanatabe, *J. Electrochem. Soc.*, **148** [9] A981 (2001).



Small Angle Neutron Scattering

Neutron reflectometry has been performed to investigate the evolution of the lithium concentration profile during the electrochemical intercalation process. For this purpose a 20nm LiCoO_2 film is RF-sputtered over a large area directly on a conducting silicon substrate. The galvanic cell is aligned in the neutron beam and operated in-situ using a three-electrode system and metallic lithium as counter and reference electrode. The initial measurements are conducted at specified cell potentials. No significant changes of the static lithium density in LiCoO_2 or film thickness variations have been observed under potentiostatic control between 3.60V, 3.90V and 4.20V against lithium. This is to be expected for this particular film exhibiting cationic disorder, as it showed virtually no intercalation activity.

8.1 Introduction

Neutrons can be a powerful probe for the study of the microscopic structure and dynamics of condensed matter, having significant advantages over other forms of radiation [1]. The main reason for the low popularity of Small Angle Neutron Scattering (SANS) as analysis tool is the limited availability of neutron sources and the applications being unfamiliar to investigators outside the field of particle physics. Here, we describe how this technique can assist in characterising the lithium intercalation process.

The pathway and the kinetic energy of a neutron (impulse vector) is altered through a direct collision with another species. Not the electrons, but the core of atoms has enough mass to disturb the path of a neutron beam. The scattered neutrons can be described with a wave function, which is influenced by the mass of the ions and their ordering in reciprocal space.

The basic principle of a reflection experiment is to bring a well-collimated neutron beam in at a glancing angle (θ) to the surface, and to measure the intensity of the reflected beam as a function of the momentum transfer (q) defined by:

$$q = \frac{4\pi \sin \theta}{\lambda} \quad (8.1)$$

The variation in the reflectivity with q depends on the scattering length density profile along the normal to the interface (z -direction). The scattering length density, $\rho(z)$, depends only on the number density of the different atomic species, $N_i(z)$, and their neutron scattering lengths, b_i :

$$\rho(z) = \sum_i N_i(z) b_i \quad (8.2)$$

This function is defined by the structure of the film and composition of the interface and can be deduced from the observed variation of neutron reflectivity with q . As the specular reflection technique averages over x and y , structural information can only be deduced in the z -direction.

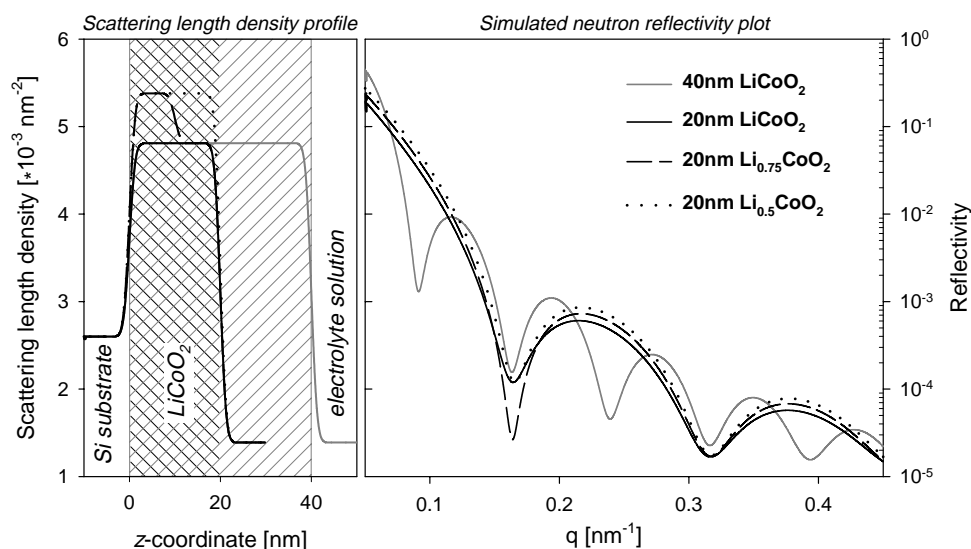


Figure 8.1: Reflectivity simulation plot of the 20nm and 40nm thick LiCoO_2 RF-film on silicon substrate calculated with the estimated scattering length profile shown on the left.

A typical plot of reflectivity vs. q shows a critical edge, below which the reflectivity is unity. Above the critical momentum transfer, the neutron reflection decays as the fourth power of q in accordance with the Fresnel law. The fringes in the signal, known as the film factor, are the result of interference between any discontinuities in the scattering density profile. The period of the ripple depends inversely on the distance between these discontinuities. The intensity of the oscillations in the film factor depend on the magnitude of the step between regions of differing scattering length density and are damped by the diffuseness of the interface [1].

Figure 8.1 shows a simulation of the reflectivity measurement of a LiCoO_2 film on the Si substrate surface of 20 and 40nm thickness. The influence of the film thickness (variation) is large. For the 20nm film three situations are considered: a fully intercalated film (discharged state), half de-lithiated film (charged) and an intermediate situation exhibiting a separation of the lithium-rich and lithium-poor phase. These situations correspond to the composition Li_xCoO_2 with x equals 1, 0.5 and 0.75 (on average). The estimated scattering length density profiles used as

input for the simulation of these three situations are shown in Figure 8.1, the absolute values are listed in Table 8.1.

With the information on the layer expansion and the lithium concentration profile obtained from the *in-situ* neutron reflection experiments, more details of the intercalation mechanism are resolved. The object of the measurements performed at one particular cell potential (static) is to study the lattice expansion of the preferential LiCoO₂ film for possible influence of substrate constraint. The measurements performed during galvanostatic cycling are directed to study the density profile of the (de-)intercalating lithium in the z-direction. These results is expected to show whether the intercalation proceeds uniformly (flat concentration profile) or with the progress of a phase transformation (stepwise concentration profile).

Table 8.1: Calculated neutron scattering length density listed for materials in the path of the neutron beam.

| Material | Scattering length density [nm ⁻²] |
|------------------------------------|--|
| Si | 2.6·10 ⁻³ |
| LiCoO ₂ | 4.81·10 ⁻³ |
| Li _{0.5} CoO ₂ | 5.38·10 ⁻³ |
| EC:DEC 1:1 1.0M LiClO ₄ | 1.67·10 ⁻³ |

8.2 Experimental

Two silicon monocrystalline bars (dimensions l/w/h:100/50/16mm) were cut from a silicon spindle with the (111) plane aligned parallel to the surface. These bars were then polished chemically and mechanically to a surface roughness of approximately 5Å and a surface flatness of 0.15µm. The silicon was made n-conducting by heating to 950°C in an atmosphere of 800ml O₂ and 8dm³ 1% PH₃ in argon, followed by etching to remove the deposited glassy layer.

The LiCoO₂ film was RF-sputtered on the silicon bar substrates using a 6” stoichiometric target and low RF-power (150W) to obtain the (110) preferential

orientation. Back-sputtering (power ratio 1:2) was applied to improve the film uniformity over the exposed substrate area. The samples were annealed *ex-situ* at 600°C for 30min ($4^{\circ}\text{C}\cdot\text{min}^{-1}$) in an oxygen/nitrogen gas flow ($27/3\text{ ml}\cdot\text{min}^{-1}$). The thickness of the film was determined with a Dectac 8 and observed to be approximately 20nm. The crystal structure was determined with XRD analysis using similar, thicker films deposited under identical conditions as the 20nm films.

The electrical connection of silicon substrate to the working electrode was made externally using silver paint. The LiCoO_2 film was cycled against two metallic lithium strips, which served as counter and reference electrode, respectively. The cell was constructed in a helium glove box. The liquid electrolyte, LiClO_4 1.0M EC:DEC, was injected into the teflon cell compartment and closed off before exposure to ambient. A stainless steel set-up was designed to align the entire electrochemical cell in the neutron beam of the ROG (abbreviation for the “Reflectometer voor Oppervlakte en Grenslaagonderzoek”). Figure 8.2 shows the LiCoO_2 film on the silicon bar substrate and the area exposed by the neutron beam entering under low angle.

The distance between the sample and the single, one-inch XERAM 30NH15 He^3 detector is one meter. The time-of-flight of the detected neutrons is calculated using a beam chopper operated at 25Hz. The experimental data was simulated using the program Star and a self-programmed user interface [3].

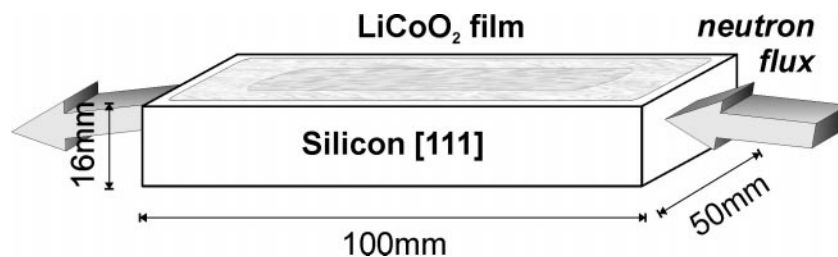


Figure 8.2: Schematic representation of the monocrystalline silicon substrate and the RF-sputtered LiCoO_2 film. The area exposed to the neutron flux is indicated.

8.3 Results and Discussion

The XRD texture analysis of the silicon bar has been performed on the (111) plane diffraction, as these planes are oriented parallel to the substrate surface. This peak is found at 28.42° , which is 0.02° off the expected location. The FWHM of this peak is 0.057° degrees and is typical for monocrystalline materials.

The surface of the polished substrate had been analyzed with the light interferometer scope prior to film deposition. No multiple light bands were observed, which suggests the flatness of the substrate is less than $0.16\mu\text{m}$. After film deposition the surface height profile is measured and plotted in Figure 8.3. The average surface roughness increases insignificantly

from 5.2\AA to 6.3\AA after RF-sputtering of the LiCoO_2 film.

The neutron reflectometry signal from the LiCoO_2 film is first tested without the electrochemical cell under ambient conditions. The results are plotted in the inset of Figure 8.4 and show an interference pattern, caused by the difference in density in the z -direction between the silicon substrate, the LiCoO_2 film and the air. This result indicates an adequate degree of flatness and surface roughness of the silicon substrate. The film thickness could be derived from the spacing of the minima.

For the actual neutron reflectometry experiment at specific electrode potential the electrochemical was prepared in an inert argon atmosphere and sealed before alignment in the neutron beam and connection to the potentiostat. The results are plotted in Figure 8.4 for the 3.60V, 3.90V and 4.20 electrode potential against a metallic lithium reference electrode.

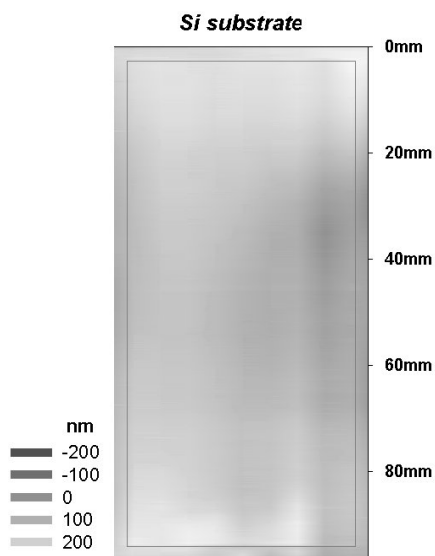


Figure 8.3: The height profile of substrate measured after deposition of the 20nm LiCoO_2 film.

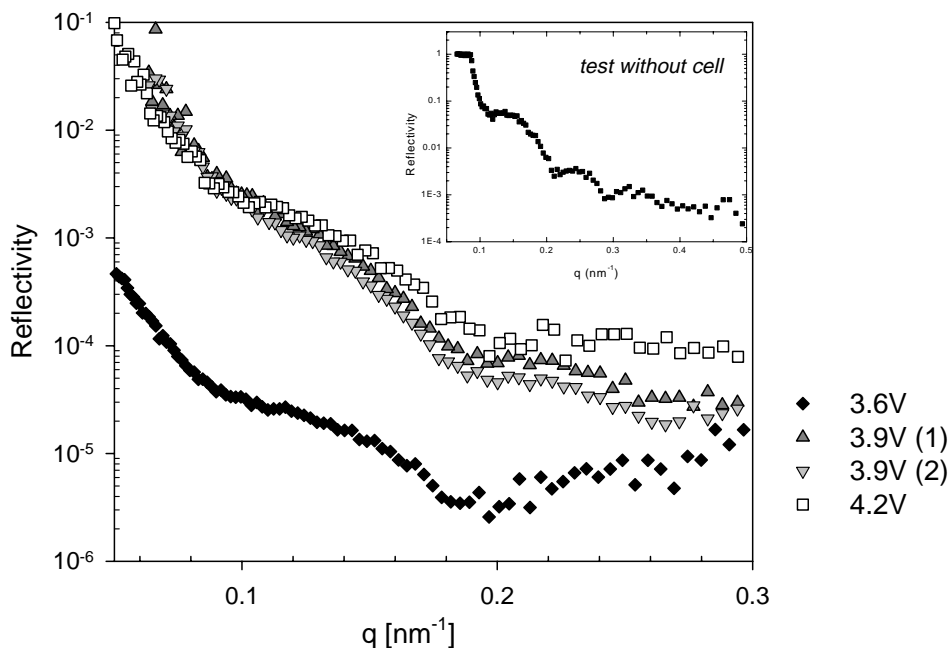


Figure 8.4: Neutron reflectivity of the LiCoO_2 film exhibiting cationic disorder, measured at the indicated potential against metallic lithium.

The interference pattern is not as intense as observed in case of the initial ‘dry-test’ experiment. The addition of the electrolyte solution has decreased the difference in neutron scattering density between the LiCoO_2 film and its background, as it is now in contact with an organic electrolyte instead of air.

The curve measured at the 3.60V is displaced below the other curves, as it has not been corrected for the zero-reflection intensity. The characteristics of all curves appear similar and the influence of the cell potential appears to be small. The slight changes between both 3.90V curves can be attributed to the Solid Electrolyte Interface, which is known to increase with the measurement time and more rapidly at high cell potentials. The damping effect on the interference pattern suggests the growth of an inorganic layer on the surface of the LiCoO_2 film. An increase of the surface roughness of the film itself could have a similar result, due to the increase of the film thickness distribution. The homogeneity of the SEI layer growth is to be investigated.

The volume of the unit cell of LiCoO_2 is expected to change as a function of the degree of lithium intercalation. The graph in Figure 8.5 shows that the film can be galvanostatically de-intercalated, but lithium re-intercalation upon discharge appears to be difficult. Merely 5% of the theoretical capacity is engaged and almost no reversible capacity is observed. This inactivity is the result of the cationic disorder in the LiCoO_2 , induced by the applied RF-sputtering conditions (*i.e.* back-sputtering), which benefits smooth film morphology, but proves to be detrimental for the intercalation performance as discussed in Chapter 6.

In the case of this particular neutron reflectometry experiment the increase of the cell potential did not alter the degree of intercalation. Pre-measurement charge-discharge cycles of the electrochemical cell have already removed the mobile lithium ions and a lithium-deficient, inactive intercalation host remained. This explains the absence of film thickness variations as function of cell potential.

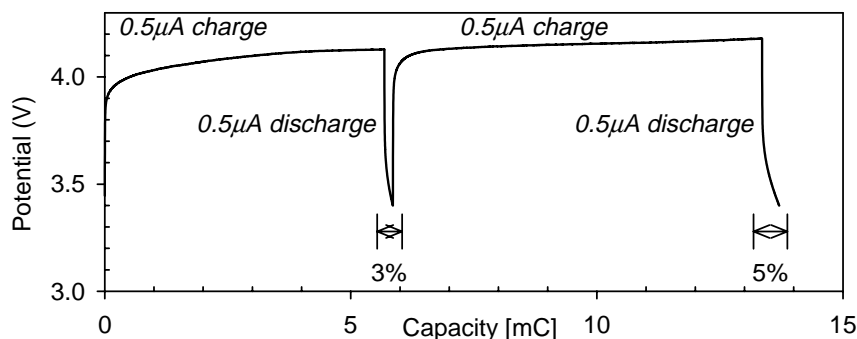


Figure 8.5: Galvanostatic cycling curve of the 20nm LiCoO_2 film on the silicon substrate. The reversible capacity is indicated as percentage of the intercalated charge.

Currently measurements are being conducted on RF-films exhibiting the ordered HT- LiCoO_2 lattice structure. If the static cell potential measurements prove successful, the dynamic voltage-sweep experiments will be initiated and hopefully information on the penetrating and receding concentration profile of Li can then be obtained. A conclusion is in this case inappropriate.

8.4 References

1. ISIS, Faculty annual report (2000-2001).
2. R.M. Richardson, M. J. Swann, A.R. Hillman, S.J. Roser, *Faraday Discuss.*, **94** 295 (1992).
3. M. Wagemaker, self-designed computer program (1999).

9

μ -Battery development

The preferentially oriented LiCoO_2 films, characterised in the previous Chapters, are used as basis for the construction of a complete solid-state microbattery: the liquid electrolyte is replaced by a solid-electrolyte film (LiPON) and the metallic lithium is evaporated directly onto the material stack and sealed with a Cu current collector.

It appears that the preferential orientation of the RF-sputtered LiCoO_2 films depends on the RF-power used for its deposition. High deposition rates result in a preferential $[00\ell]$ orientation, while an intermediate rate leads to $[104]$ orientation.

Preliminary electrochemical measurements have demonstrated the feasibility of this microbattery.

9.1 Introduction

There is a growing interest in the microelectronics industry for small-scale energy storage, due to a tendency towards complete integration of electronic circuitry, designed for one specific purpose. For example, a motor controller device has to contain everything from memory to the power regulation in one module called a Multi Chip Module (MCM). The functions can subsequently be implemented on separate silicon substrates and then interconnected and stacked in a single housing [1]. An additional secondary lithium microbattery provides backup power and allows the digital memory states to remain unaffected during power failure or storage. Several operational designs of the micro-battery have been reported. These consist of a wide variety of materials for electrodes and electrolyte [4,5].

The maximum capacity of the intercalation cell is largely determined by the amount of active electrode material, which translates here to the surface area and the film thickness (porosity ignored). Decreasing the film thickness implies a large electrode area or a limited capacity. A thin electrode film is expected to have a short diffusion distance L for the lithium ions and thus exhibit high intercalation rates. However, Wang *et al.* [6] reported that thick electrodes ($>1\mu\text{m}$) could deliver higher current pulses.

The solid-state electrolyte film must be able to withstand the electrical field between both electrodes. Usually the electrical potential jump is directly at the electrode interface and the dimensions of the electrolyte film are of no effect. However, the EMF of the cell relates to the chemical potential gradient of the electrons in the electrolyte phase, as derived in Section 5.2.3. Hence, a thin electrolyte film exhibits an increased gradient, which due to a finite mobility of 'electrons' in the electrolyte phase, also increases the self-discharge rate of the microbattery.

The sub-micron LiCoO_2 films RF-sputtered on silicon substrates form the basis of the processed micro-battery stack shown schematically in Figure 9.1. The composition and thickness of each layer is chosen according to its function, which is elucidated in the next section.

9.1.1 Material stack

Al back contact – This layer is used to make electrical contact with the n-doped silicon wafer. This construction is more practical than using lithographical techniques in attempts to contact the LiCoO₂ current collector directly. It thus circumvents the use of aggressive chemicals.

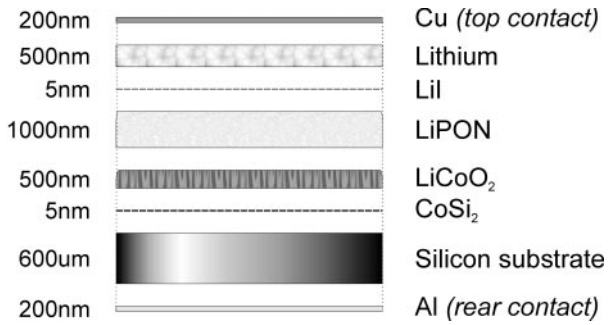


Figure 9.1: Schematic overview of the microbattery stack design.

Si substrate – Silicon is a practical choice, as there is a vast amount of experience and equipment available for the processing. Due to the large production quantities, the cost of such a high-quality substrate remains low.

CoSi₂ current collector - An intermediate Co film is deposited as adhesive layer and to establish ohmic contact between the LiCoO₂ and the doped Si substrate. At elevated temperature ($T > 250^{\circ}\text{C}$) conducting cobalt-silicide phases are formed at the interface, which exhibit good thermal stability, low resistivity ($14\text{-}20\mu\Omega\cdot\text{cm}$), easy formation ($\Delta G_{\text{F}}(\text{CoSi}_2) = -32.9\text{kJ}\cdot\text{mol}^{-1}$). There is only a small lattice mismatch with the Si substrate [8]. As an alternative to metals, the use of silicides to contact doped silicon reduces the voltage drop of the ohmic contact, due to an increase in effective contact area. For this solid state reaction to occur it is essential that the native silicon oxide is removed with HF-etch and reversed sputtering, as Co is stable in contact with SiO₂ up to temperatures of 700°C. For the reaction of 1nm Co film, 3.6nm of Si is consumed. The local increase in volume caused by the silicide formation on the interface, results in a

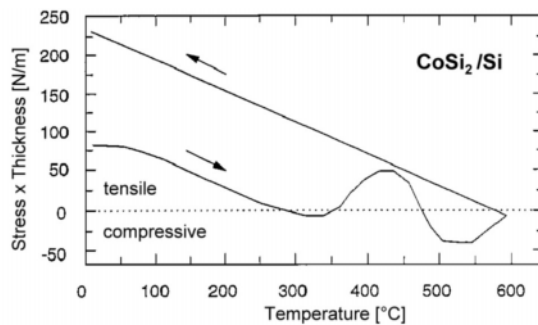


Figure 9.2: In-situ stress of a 65nm Co layer on Si substrate [9].

compressive stress (in the silicide), which can be relieved by rearrangement of atoms. Hence, there is a maximum in the compressive stress during silicide formation and a tensile stress after cooling as can be seen in Figure 9.2 [1].

LiCoO₂ – This layer has been well characterised in the previous Chapters. The LiCoO₂ is RF-sputtered to a thickness of 0.5µm at an intermediate deposition rate, in order to achieve a preferential [104] orientation. Partial back-sputtering is optional by applying a dc-bias voltage to the substrate. This technique could improve the step coverage of the film by enhancement of the atomic movement on the surface, through an increase in temperature caused by impulse energy dissipation and an increase in ion bombardment, or a decrease in species that retard the surface migration [1]. A low surface roughness is welcome here, as a small non-uniformity is enlarged in the course of the stack build-up.

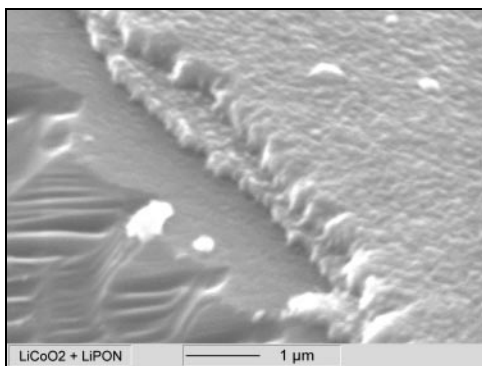


Figure 9.3: Cross-section of the silicon substrate with the Pulsed Laser Deposited LiCoO₂ and LiPON film.

LiPON – In Chapter 2 several solid-state electrolytes have been brought to attention. LiPON has first been reported by J.B. Bates *et al.* [2] and is renowned for its ease of application, stability in air and large stability window. This material can also be applied in addition to a liquid electrolyte to provide a well-defined electrode|electrolyte interface, which has been reported to decrease leakage currents [3]. Figure 9.3 shows a micrograph of a LiCoO₂

film on silicon substrate covered with a LiPON film. In this preliminary experiment the deposition was performed with PLD for practical reasons.

LiI – This intermediate layer is applied with thermal evaporation directly before lithium MBE to shield the strongly reducing metal from direct contact with the electrolyte. The lithium|electrolyte interface is prone to degradation upon cycling of the cell as the lithium deposited on charging of the cell is very reactive. The ionic conductivity is 10⁻⁷ S·cm⁻¹. LiI itself is not suitable as solid electrolyte, because it is known to form ‘colour centres’ that exhibit electron conductivity if the stoichiometry of the material is modified [10].

Lithium – This material serves as high-capacity negative electrode and also provides a stable reference potential. The application is difficult since the material is not stable in air. Loss of lithium through irreversible reaction is anticipated by an oversized thickness of lithium layer in comparison with the capacity of the positive electrode. Variation of the thickness is expected with cycling of the cell, due to subsequent dissolution and re-deposition of lithium. The resulting mechanical stress could inflict damage to the stack and cause a decrease of the cell performance. Capping of the stack with a rigid material has been reported to assist withstanding the stress and benefits the cell lifetime.

Cu – This layer serves as current collector of the negative electrode and functions as a coating to protect the lithium metal from exposure to air. It is evaporated directly following the lithium metal without breaking vacuum. Its shiny, red metallic appearance indicates a good integrity of the entire stack.

Capping layer – Generally this consists of a polymer coating (*e.g.* resist) to provide mechanical stability and prevent penetration of water vapour. The dimensions of this capping layer are not critical.

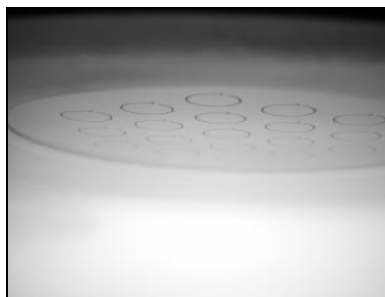
9.2 Experimental

Circular substrate discs (10mm \varnothing) were laser cut from an *n*-type silicon wafer (4" inch, one side polished), but remained attached at one edge. Separation of these discs and bonding into chip packages was done after complete processing of the wafer, which involved pre-treatment and full stack deposition).

First the wafers were etched in buffered HF to remove the native SiO₂. In the Balzers Bak600 the wafers were placed in vacuum ($<1 \cdot 10^{-6}$ mbar) and additionally subjected to Ar ion bombardment. The Co layer (25nm) was deposited with MBE. Next the 200nm aluminium film was deposited on the backside of the wafers using the same procedure. During annealing treatment at 600°C for 15min (ramp rate 5°C·min⁻¹) the CoSi₂ phase was formed and an ohmic connection between the Al and the Si was established.

The LiCoO₂ was RF-sputtered on the Nordico 2000 using a stoichiometric 6" target. The background pressure was 2.0 mbar, consisting of an Ar:O₂ mix ratio

4:1. Optionally, the power split was set at 2:1 to divide the RF-power in this ratio over the target and the substrate, respectively. No additional substrate heating was applied. The average growth rate normalised to RF-power and deposition time is $1 \cdot 10^{-13} \text{ m} \cdot \text{W}^{-1} \cdot \text{min}^{-1}$.



The LiPO_4N_y layer was subsequently applied in the same vacuum chamber by RF-sputtering LiPO_4 (6" target) in an N_2 atmosphere of 2.0 mbar. Deposition was performed at 300W RF-power (no back-sputtering applied) for 120min. A picture of the deposition process in operation is shown in Figure 9.4.

Figure 9.4: *Picture of the RF-sputtering of LiPO_4N_y on a 4" silicon substrate suspended upside down in a nitrogen plasma. The pre-cut Si samples are visible.*

The third deposition step was executed in the Balzers BAK 600 vacuum chamber, where the LiI was thermally evaporated, directly followed by lithium and copper E-beam deposition. A resonator crystal in line with the substrates monitored the thickness of the layers. Exposure to the atmosphere was minimized by quickly sealing the wafers in plastic together with metallic lithium as scavenger. Mounting and measuring of the separate disc samples was done in the helium glove box.

The composition of the LiCoO_2 films was analysed using chemical back-titration of the layers dissolved in acid. The crystal structure was studied with XRD. The film morphology was analysed with RBS and SEM.

Electrochemical measurements were performed on the Autolab PGstat20 potentiostat with integrated FRA20 impedance analyser using a two-electrode configuration.

9.3 Results

9.3.1 Structural analysis

The deposition rate of several LiCoO_2 films deposited on 4" silicon substrates are plotted as function of the RF-power in Figure 9.6, normalised to the deposition time. The dotted line indicates the film average growth rate in the case all RF-power directed to the target. The thickness of the films deposited using simultaneous back-sputtering are plotted with diamonds as function of the effective RF-power (forward power minus back-sputtering power).

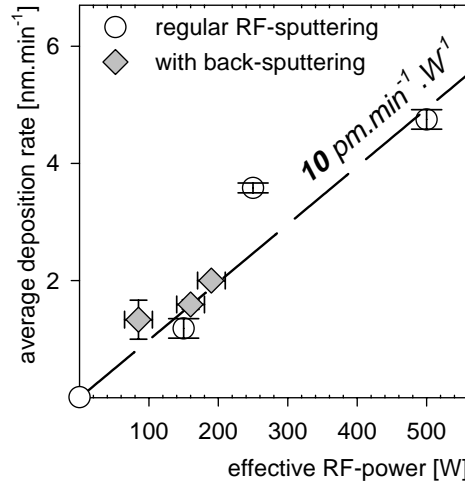


Figure 9.5: Average RF deposition rate of LiCoO_2 with and without simultaneous back-sputtering.

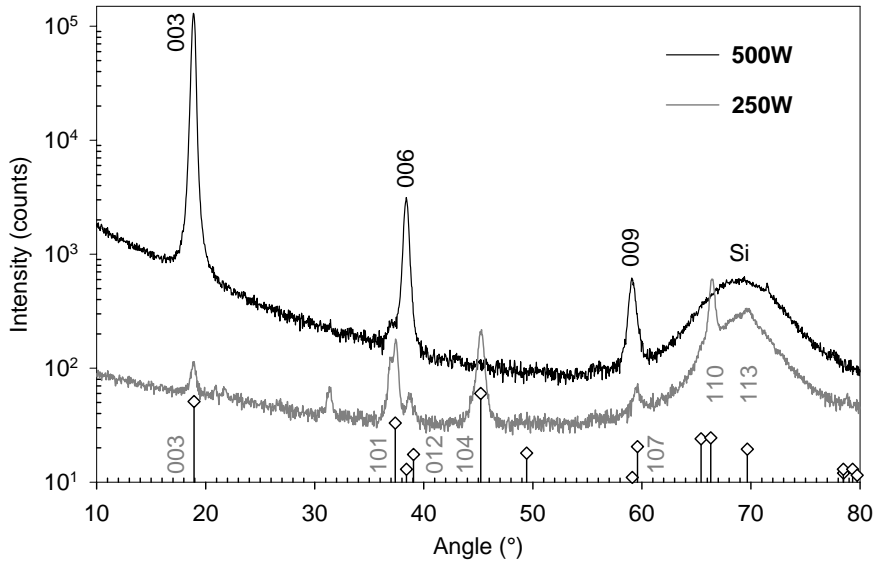


Figure 9.6: XRD pattern of LiCoO_2 films RF-sputtered on a 4" wafer with 500W for 60min and 250W for 120min, respectively. The substrate has been tilted 0.5° to decrease the Si (400) diffraction intensity at 69° .

LiCoO₂ film structure - The preferential orientation of the LiCoO₂ film is determined by the RF power applied for its deposition. Figure 9.6 shows the XRD pattern of a 250W and 500W film of 430nm and 285nm thickness, respectively, after annealing at 600°C for 30min. The lattice orientation of the polycrystalline structure shows a shift from a (00 l) alignment obtained with high power deposition, to a combined (110) and (104) alignment during deposition with intermediate power. LiCoO₂ films deposited with low power (<150W) showed a preferential orientation similar to the 250W film, but with an increased relative (110) diffraction intensity. However, the simultaneous increase of Co₃O₄ diffraction peaks suggested non-stoichiometric deposition.

The RF-deposition with simultaneous back-sputtering resulted in LiCoO₂ films with a true FCC NaCl-type structure. The XRD pattern of a 200nm film deposited with 310W forward power and 120W backward power is shown in Figure 9.7 (measured after annealing at 600°C for 30min). The unit cell dimension of the cubic lattice structure is $a = 4.05\text{\AA}$. This LiCoO₂ structure has also been observed with Pulsed Laser Deposition on a RF-seed layer (Figure 6.1).

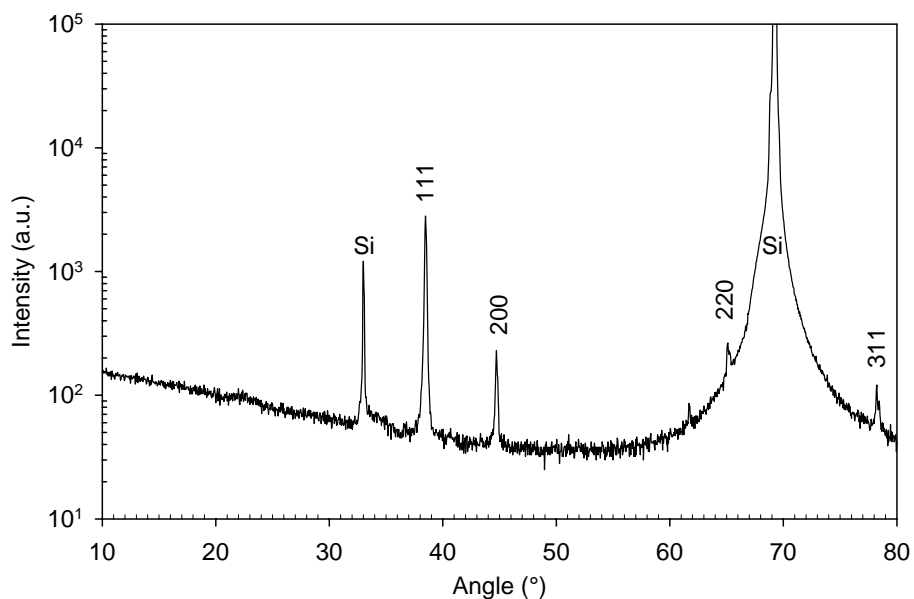


Figure 9.7: XRD pattern of LiCoO₂ films RF-sputtered (310W) on a 4" wafer with simultaneous back-sputtering (120W) exhibiting a cubic FCC structure.

The progression of the mechanical stress during the annealing treatment in air has been studied for a 140nm RF-deposited LiCoO₂ (100W, 120min) film on a 4" wafer substrate. The applied temperature profile consists of a 5°C·min⁻¹ ramp rate and a 15min hold at 700°C. Figure 9.8 shows the tensile stress as function of the temperature.

After an initial build-up of tensile stress due to a thermal expansion mismatch, the crystallisation process of the LiCoO₂ induces a compressive stress, which remains constant from 550°C to 650°C. The standard annealing procedure targets this temperature regime (600°C). At 700°C the stress becomes tensile again and remains so upon cooling up to 400°C. The onset of a linear increase of tensile stress is observed, as if the film structure hardens at this temperature. The incline suddenly becomes stronger at 200°C, indicating a (second) structural transformation, however, TGA-DSC measurements on film scrapings did not reveal any phase transformations on subsequent temperature cycles to 550°C.

Annealing treatment changes the film morphology. The appearance of the wafer changed from shiny black to a dull grey. The RBS spectrum suggests the formation of an 'open' LiCoO₂

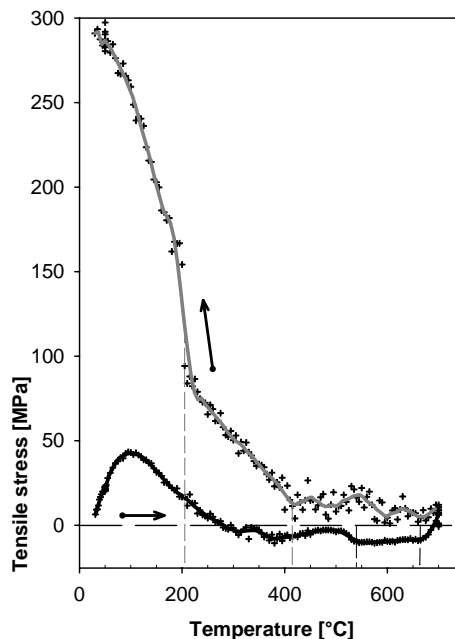


Figure 9.8: Wafer curvature interpreted as mechanical stress in the LiCoO₂ film induced during annealing treatment.

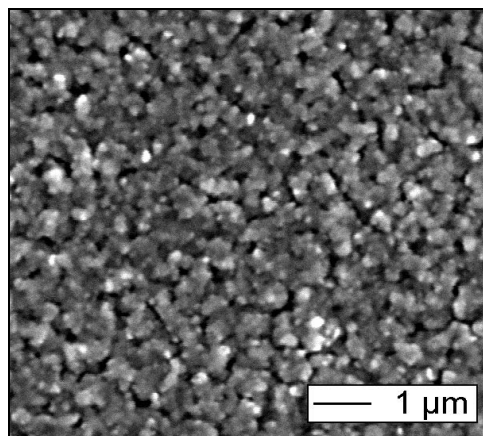


Figure 9.9: Surface morphology of LiCoO₂ film after annealing at 700°C.

structure, where the silicon substrate is exposed. The SEM micrograph in Figure 9.9 indeed shows a granular structure. The observed porosity could be related to the effect of tensile stress. In this case the chemical composition has changed as well: post-annealing XRD analysis revealed Co_3O_4 formation; the RBS measurement estimates the Co:O ratio at 2.2 ± 0.1 and chemical titration indicated a Li:Co ratio of 1.4 ± 0.15 . This deviant stoichiometry can be attributed to oxidation of the film and increased amount of Li_2O formation, due to the different heating process endured within the stress measurement equipment. The usual annealing procedure (600°C for 30min) does produce polycrystalline films with Li:Co ratio of approximately 0.97 ± 0.1 .

High-temperature XRD was performed to study the evolution of the crystal

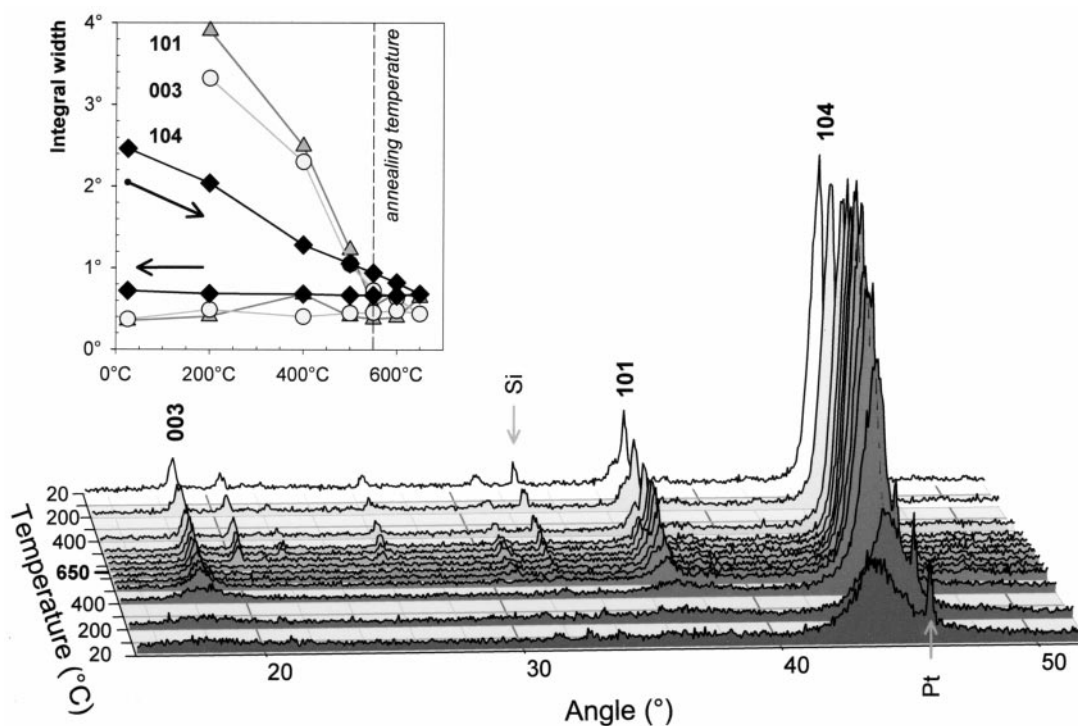


Figure 9.10: High-temperature XRD patterns of a 430nm LiCoO_2 film, RF-sputtered (250W) on silicon substrate, recorded during annealing treatment. In the inset the integral width of the major diffraction peaks is plotted as function of temperature.

structure during the annealing treatment up to 650°C. Figure 9.10 shows the sequential diffractograms and the inset reveals the calculated decrease of the integral width* of the major LiCoO₂ diffraction peaks with temperature increase. The minor diffraction peaks appearing in the range of 20-32° during the cooling period, cannot be attributed to a specific compound. The position of the Pt heating element diffraction peak (45°) confirms that the actual measurement temperature is within the accuracy of this experiment.

The XRD patterns plotted in Figure 9.10 has been used to calculate the thermal expansion from the shift of the lattice plane reflections of the preferential (104) LiCoO₂ film. The results are listed in Table 9.1 for the (003), (101) and 104 reflection together with the calculated thermal expansion of LiCoO₂ powder, based on the data plotted in Figure 7.2. The thermal expansion of the (104) RF-film is more isotropic than that of the powder. Especially the *c*-axis expansion appears constrained. Unfortunately, it is not feasible to detect the (003) reflection in case of (110) orientated films (and likewise, the (110) reflection in *c*-axis oriented films) so the thermal expansion of the fully constrained planes aligned normal to the substrate surface, cannot be measured with XRD.

Table 9.1: Thermal expansion of the indicated lattice planes of LiCoO₂ calculated from the XRD patterns of a (104) oriented RF-film and a powder as a function of temperature.

| LiCoO ₂ lattice plane | (104) RF-film [×10 ⁶] | powder [×10 ⁶] |
|-------------------------------------|--------------------------------------|-------------------------------|
| (104) | 16.8 ± 0.2 | 15 ± 0.9 |
| (101) | 15.9 ± 2.5 | 10.8 ± 0.6 |
| (003) | 18.1 ± 1.1 | 34.1 ± 2.1 |

Microbattery stack – Due to the unknown deposition rates of materials other than LiCoO₂, the preparation of a microbattery stack with the intended dimensions is difficult. Figure 9.11 shows an example of a stack cross-section of one of the first attempts. On this micrograph it is clearly visible that the solid electrolyte layer is too thin, but also not uniform. As the LiPON_y material is not

* The ‘integral peak width’ is the calculated width of a rectangle fitted to match the intensity and area under the measured diffraction peak.

stable in contact with water (vapour), degradation of this layer could have taken place during preparation for SEM analysis.

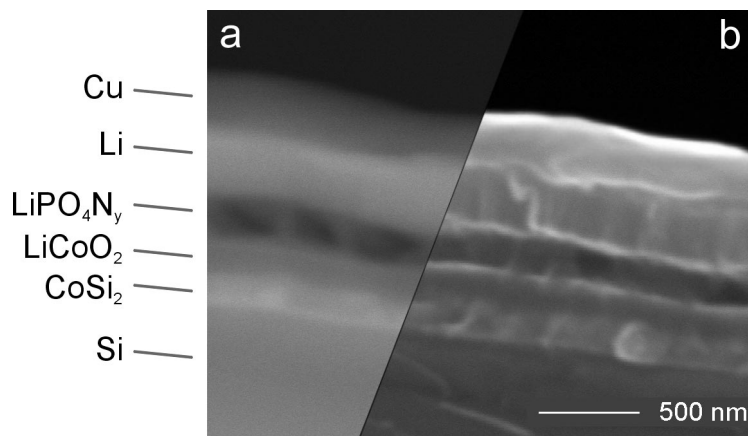


Figure 9.11: Micrograph of a micro-battery stack cross-section using two separate detectors to reveal the composition (a: BEI-detector) and the morphology (b: SEI-detector).

9.3.2 Electrochemical measurements

After deposition of the final Li and Cu layers the open the microbattery is active and exhibits an OCP of approximately 0.5 to 1.5V. This voltage is increased using the potentiostat to a stable voltage of approximately 2.7V. Note, that the LiCoO₂ layer of these initial microbatteries has not been annealed before the deposition of the solid electrolyte. Hence, the electrode material is amorphous and the intercalation potential profile appears sloping instead of showing the usual pronounced voltage plateau at 3.9V.

Cyclic voltammetry measurements on the microbattery revealed an anodic peak around 4.0V and a cathodic peak around 3.4V (see Figure 9.12). The peak location appeared fairly independent of the scan rate. However, the reversible capacity and the Faradaic yield of the scans increased with increasing scan rate. This contradiction can be attributed to a leakage current of approximately 1μA (measured at 3.60V). A fast potential sweep leaves less time for self-discharge and improves the efficiency of the cycle.

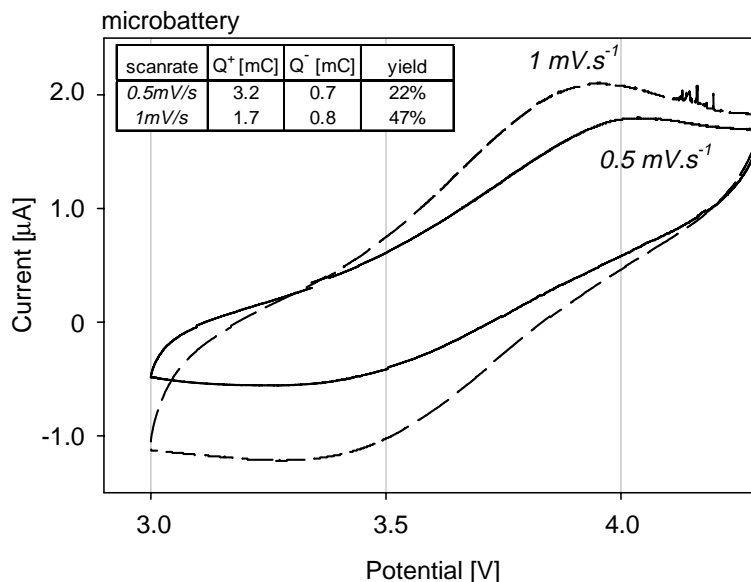


Figure 9.12: Cyclic voltammogram of a microbattery recorded at a scan rate of 0.5 and $1.0 \text{ mV}\cdot\text{s}^{-1}$. The inset table indicates the charge and discharge capacity and the Faradaic yield of both cycles.

The galvanostatic charge and discharge profiles are shown in Figure 9.13. There is a clear voltage plateau at 4V during charge, but the discharge profile appears sloping. Similar potential profiles have been reported by Wang *et al.* [6] for amorphous LiCoO_2 electrodes in lithium microbatteries. There is also a significant influence of the leakage current. The application of a $5 \mu\text{A}$ cycling current instead of $1 \mu\text{A}$ increases the Faradaic yield from 10% to 88%. However, in the latter case the observed capacity is approximately 15% of the theoretical capacity. This value is expected to improve significantly with the use of polycrystalline LiCoO_2 films. These samples are currently in preparation.

The impedance spectrum of the microbattery has been recorded in the frequency range $10 \text{ kHz} \dots 10 \text{ mHz}$ at 3.60 V OCP and is shown in Figure 9.14. The calculated R_0 indicates an electrolyte resistance of 45Ω . The sloping line observed at low frequencies suggests a large influence of diffusion. The spectrum could not be described with the models discussed in the previous Chapters 4 and 5. More microbatteries have to be subjected to an impedance measurement study before definite conclusions can be drawn.

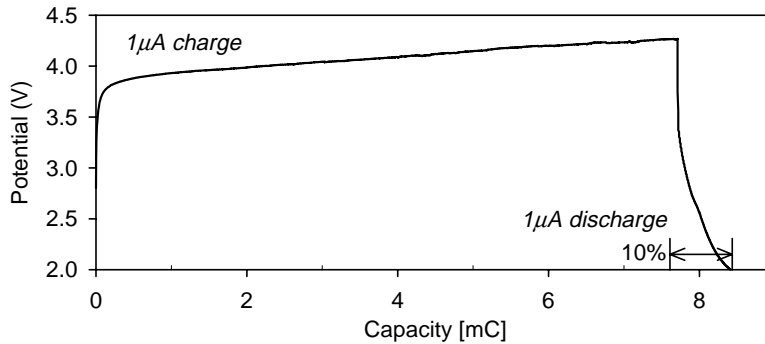


Figure 9.13: Galvanostatic cycling of the microbattery with $1.0\mu\text{A}$ between the cut-off limits of 2.0V and 4.3V .

9.4 Discussion

Intercalation electrode - The applied RF-power determines the deposition rate of the film and thus the preferential orientation of the crystal structure. This result coincides with our previous findings. However, the strong [110] preferential orientation observed in Chapter 3 could not be achieved with this large-scale deposition equipment. Low power deposition ($<100\text{W}$) produces non-stoichiometric LiCoO_2 films, which appear to have high lithium content, but also show a significant amount of Co_3O_4 .

Simultaneous back-sputtering during RF-deposition has a beneficial effect on the deposited film morphology, which remains optically smooth even after annealing treatment. No significant discrepancy in grain size distribution could be observed from the SEM micrographs, which could suggest a difference in growth conditions between regular RF-sputtering and simultaneous back-sputtering. Apparently, a more effective interaction of the LiCoO_2

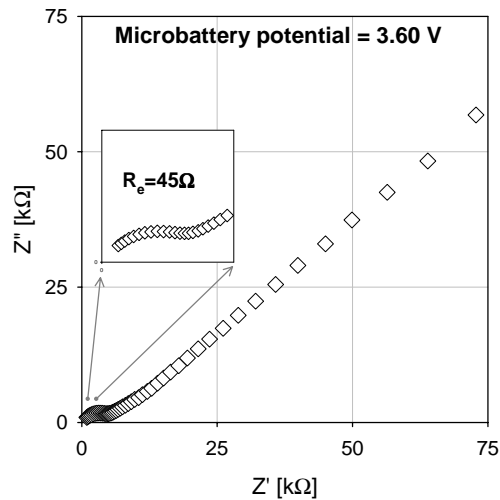


Figure 9.14: Impedance plot of microbattery recorded at an OCP of 3.60V .

film with the plasma is sufficient to enhance the mobility of the deposited species and produce *c*-axis oriented films exhibiting full cationic disorder.

Post-deposition annealing treatment is required to obtain a fully ordered LiCoO₂ crystal structure. It has been shown that a short exposure to a temperature of 550°C is sufficient to obtain a polycrystalline film with a sharp diffraction pattern. The loss of volatile Li₂O is reduced by regulating the annealing treatment to just the time and temperature required. Note, that the first batches of microbatteries, which have been subjected to electrochemical measurements, exhibit an amorphous intercalation electrode. These samples have not been removed from the vacuum chamber for the annealing of the LiCoO₂ films (substrate holder not equipped with heating element) to prevent surface contamination.

The annealing treatment induces a strongly tensile stress in the film, which accumulates upon cooling in two stages. This stress is not directly correlated to the thermal expansion, as the lattice plane expansion appears continuous. The micrographs of the LiCoO₂ films (Figure 9.9) taken after annealing show a granular morphology with voiding between the columnar grains. Without the presence of an adhesive layer such as CoSi₂, the LiCoO₂ film peels off the silicon substrate at a film thickness above 0.75μm. Such thick films, although a prerequisite for high capacity microbatteries, have not been prepared due to the long period of time required for their deposition.

Electrolyte phase - The LiPO₄N_y layer decomposes if the substrate temperature increases above approximately 100°C due to energy dissipation of the N₂ plasma. Even at intermediate RF-power (250W) the film shows peeling during the deposition process. This can be attributed to insufficient cooling of the substrate holder. Under these circumstances only a low RF-power could be applied which results in low deposition rates for the solid electrolyte film. Hence, the deposition of thick films becomes time consuming. More important is the possibility that low deposition rates could lead to non-stoichiometry of the deposited film, as observed for the LiCoO₂ film deposition. Insufficient thickness of the solid electrolyte or a slightly deviating of its composition could explain the observed leakage current. The substrate cooling capability needs to be improved.

Lithium electrode - The adhesion of the material stack is good. No peeling of individual layers is observed. The exact functionality of the LiI intermediate layer

is questionable here, considering the low number of cycles to which the microbattery is tested. The evaporation of the metallic lithium is most critical process. The presence of adsorbed water or impurities in the LiI intermediate layer could lead to reaction and subsequent contamination of the interface with the lithium electrode. Neudecker *et al.* [11] has reported that the lithium layer need not be deposited before the microbattery operation, but can be electroplated on the Cu current collector on first charge. However, significant capacity loss is observed after the first cycle of this microbattery. The method is particularly functional if the material stack has to survive solder reflow conditions ($T=250^{\circ}\text{C}$).

The performance of the current micro-battery prototype is not yet up to par for application, but it does provide the proof of principle. It is possible to confine the potential of the lithium cell to several micrometers. Regarding the high energy storage capability and the potential risk of hazards, it is important that all the separate layers of the material stack are well characterised, before potentially dangerous high capacity batteries are prepared. Unfortunately, there was insufficient time to complete this work before the publication of this thesis.

9.5 Conclusions

The oriented thin-film LiCoO_2 electrode forms a good basis for the construction of a complete microbattery. The RF-sputtering deposition rate determines the eventual LiCoO_2 lattice orientation and thus also controls the maximal rate of electrochemical lithium intercalation. A tailor-made, solid-state microbattery is a valuable instrument for fundamental research on the intercalation mechanism.

The present material stack configuration has shown promising results concerning interfacial adhesion and electrochemical performance. Proper annealing treatment of the intercalation electrode prior to assembly of the stack, should provide the LiCoO_2 -based microbattery with the expected charge and discharge characteristics and improve its reversible intercalation capacity.

9.6 References

1. D. Morrison, *Electronic Design*, **47(26)**, 63 (1999).
2. J.B. Bates, N.J. Dudney, G.R. Gruzalski, R.A. Zuhr, A. Choudhury, C.F. Luck, *J. Power Sources*, **43-44** 103 (1993).
3. J.B. Bates, N.J. Dudney, B. Neudecker, A. Ueda, C.D. Evans, *Solid State Ionics*, **135** 33 (2000).
4. Proceedings of "3rd Korea-Japan Joint Seminar on Advanced Batteries", 88 (1999).
5. C. Julien, "Lithium microbatteries", Kluwer Academic Publishers, Dordrecht, 381 (2000).
6. B. Wang, J.B. Bates, F.X. Hart, B.C. Sales, R.A. Zuhr, J.D. Robertson, *J. Electrochem Soc.*, **143** [10] (1996).
7. J.P. Gambino, E.G. Colgan, *Mat. Chem. and Physics*, **52** 99-146 (1998).
8. J. Liu, J. Feng, B. Li, J. Zhu, *J. Crystal Growth*, **209** 795-500 (2000).
9. L. van der Hove, *Advanced Materials for ULSI*, Vol. 88-19, Electrochemical Soc. Inc. Pennington, NY, p 165 (1988).
10. S.D. Jones, J.R. Akridge, *J. Power Sources*, **54** 63-67 (1995).
11. B.J. Neudecker, *J. Electrochem. Soc.*, **147** [2] 517 (2000).

10 Evaluation & Recommendations

In this final chapter results and major accomplishments are reviewed and some indications for further research are given.

The key feature in this thesis is the ability to grow LiCoO_2 films with a specific preferential orientation. The (110) oriented films have not been reported before. Their large and fast intercalation capacity facilitates the study of the electrochemical properties as a function of the degree of lithium intercalation. The developed solid-state microbattery is based on the thin-film LiCoO_2 electrode. This device allows the use of a large array of analysis techniques for in-situ study of the intercalation mechanism outside of the helium glove box.

10.1 Tailoring the LiCoO₂ film

The key feature of this thesis is the deposition of submicron LiCoO₂ films with a specific preferential orientation and the subsequent comparison of their structural and electrochemical properties. In this chapter the important results are highlighted and suggestions for further research are provided.

Preferential film orientation –It was shown that the as-deposited LiCoO₂ RF- and PLD-film already shows some degree of ordering. This ‘semi-amorphous’ film rapidly develops into a poly-crystalline structure during heat treatment above 400°C. The preferential orientation of the film is strongly correlated to the rate of LiCoO₂ deposition: high rates produce (00 ℓ) films, intermediate rates lead to (104) and (101) films, while the low deposition rates result in (110) films. The RF-sputtering conditions can be tuned to produce all mentioned film orientations, while PLD can only produce (00 ℓ) films due to its pulsed nature of the deposition method. To our knowledge the (110) preferential orientation has not been reported before.

Note that the *c*-axis oriented LiCoO₂ films exhibiting full cationic disorder, can be prepared with both deposition methods. In case of RF-sputtering this is achieved using simultaneous back-sputtering, which causes the partial removal of deposited material. The PLD-film deposited on an annealed (110) RF-film seed layer also exhibits full cationic disorder. The relationship between both cases is yet unclear.

Substrate materials - The substrate on which the LiCoO₂ film is deposited has a significant influence on the intercalation properties, as it serves three purposes:

- Mechanical support
- Film adhesion
- Current conductor

The first point specifies no particular requirement for the substrate material. A smooth surface is sufficient to obtain a uniform film. Silicon substrates appear most suitable for the purpose of fundamental research due to their high quality surface, availability (all dimensions), compatibility with standard wafer processing (doping, metal film deposition, etching, etc.) and their relative

inertness during heat treatment. The use of 'low-quality substrates' leads to a less uniform preferential orientation of the host lattice, which can prove beneficial in the case of the *c*-axis oriented films. Often the applied type of substrate can explain mutual discrepancies between the reported properties of LiCoO₂ films.

The second point indirectly determines the maximum film thickness and thus the total intercalation capacity of the electrode. Proper adhesion to the substrate prevents peeling of the film, which is induced by accumulating mechanical stress during annealing treatment (see Section 9.3.1). Pt current collectors proved unsuitable as substrate material because of poor adherence. The adhesion of the LiCoO₂ to the substrate is improved if an interfacial reaction occurs. This is observed in the case of the polished metallic substrates or (more controlled) with the application of thin Ti adhesion layers on the silicon substrates. Here, slight voiding at the grain boundaries is observed from the micrographs of the annealed LiCoO₂ film surface (see Figure 9.9), probably caused by relieve of tensile stress. The Co₂Si intermediate layers, which are applied in the microbattery (Chapter 9), appear promising, but require further characterisation.

According to the third point metallic substrates are preferred over doped semi-conducting silicon substrates. An (low-) ohmic electrical contact between the current lead and the actual intercalation material reduces the polarisation resistance under current drawing situations and subsequently the observed overpotential. A good indication of the 'ease of intercalation' is the potential separation between the anodic and the cathodic current peak during cyclic voltammetry. At comparable scan rates the RF-films and PLD-films on silicon substrates exhibit a larger current peak separation (see Figure 6.3 and Figure 10.1) than the PLD-films on stainless steel substrates (see Figure 6.9). The latter samples exhibit a value close to the theoretical minimum of 59mV, as predicted by the Nernst equation [1].

Another essential requirement is the chemical inertness of the current collector material in contact with the electrolyte phase. For example, we observed dissolution of the substrate into a LiPF₆-containing electrolyte, due to its finite HF concentration. This resulted in a significant leakage current. Side reactions commonly cause electrolyte decomposition, leakage currents and subsequent self-discharge of the cell [2]. In general, care should be taken to seal off the exposed areas of the substrate and current collector from the electrolyte solution. Likewise,

the presence of pinholes in the thin-film electrode can also decrease the cell performance.

10.2 Improving intercalation properties

The intercalation rate of the Li_xCoO_2 film is mainly determined by the *accessibility* of the lithium diffusion planes for lithium ions in the electrolyte solution. The intercalation rate also determines the available intercalation capacity, when the extent of the charge-discharge cycle is limited by a preset time period or cut-off voltage limits. The aspects that influence the electrode performance are discussed below.

Diffusion plane alignment – The observed difference between the RF- and PLD-films on silicon substrates could be attributed to the orientation of the host lattice towards the electrolyte solution, as discussed in Chapter 4. The apparent chemical diffusion coefficient, normalised to the film thickness, is determined to be around $10^{-5}\text{cm}^2\cdot\text{s}^{-1}$ for the (110) film and around $10^{-12}\text{cm}^2\cdot\text{s}^{-1}$ for the (00 ℓ) film (see Figure 4.13). This discrepancy reflects the difference in the lithium diffusion length and does not indicate a dissimilar atomic diffusion process. Hence, a diffusion plane orientation normal to the electrolyte solution benefits the diffusion rate. Note that the diffusion length of a (104) film is roughly 1.3 times that of a (110) film and this increase is not expected to affect the electrode properties significantly.

Structured pinholes - In the case of a *c*-axis oriented film the exposure of the unfavourably aligned diffusion planes can be improved with the introduction of an etch pattern, as described in Chapter 6. Effectively, this reduces the diffusion length and increases the surface area of the electrode|electrolyte interface. An increase of the intercalation rate of the PLD-film on silicon is observed. However, the effect of defect introduction could not be quantified, due to the fact that the mesh dimension of the lithographic pattern is relatively coarse compared with the film thickness and the applied etching processes have not yet been optimised.

PLD-films deposited on stainless-steel substrates show a significantly higher intercalation rate than PLD-film deposited on silicon substrates. This improvement is attributed to the coarser substrate surface, which results in an increased randomness in preferential orientation and substantially more ‘natural’ defects in the LiCoO_2 film structure.

Grain boundary conductivity - The possibility that grain boundary diffusion contributes significantly to the intercalation process has not yet been resolved. Films grown with increased substrate temperatures exhibit large grains and show increased intercalation resistance relative to films with a smaller average grain size. However, experimentally it is difficult to distinguish between the intra-granular and the (two-dimensional) inter-granular lithium diffusion.

Host volume constraint – The de-intercalation of lithium from the LiCoO_2 host structure induces anisotropic volume expansion, mainly along the c -axis. The substrate constrains the film expansion in directions parallel to its surface. Therefore, the (110) films, which have the c -axis parallel to the substrate surface, are expected to suffer most from the effects of volume constraint during de-intercalation. However, the influence is not measurable. STM or XRD measurements performed *in-situ* could provide details on the local lattice expansion. The *in-situ* neutron reflectivity method described in Chapter 8 is also suitable for accurate measurement of the average film expansion in the direction normal to the surface. Its further development is recommended.

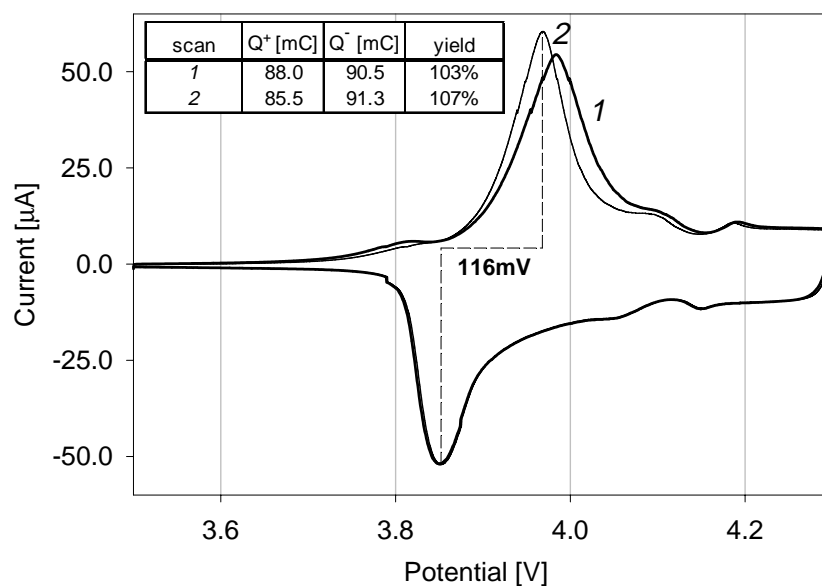


Figure 10.1: Cyclic voltammogram of a $0.5\mu\text{m}$ RF-film against metallic lithium. The a -axis oriented LiCoO_2 is deposited on silicon substrate with an intermediate 200nm Al current collector and an adhesive layer of 50nmTi. (scan rate: $0.1\text{mV}\cdot\text{s}^{-1}$).

Phase transformation - The electrochemically-induced phase-transformation in Li_xCoO_2 has a limiting effect on the lithium intercalation rate due to the drag effect of the phase boundary movement. This is best observed for the (110) films on silicon during potentiostatic titration (see Figure 4.7). Fortunately, the (110) films show fast adaptation of the host lattice in response to the varying lithium composition. The OCP plot shows a clear potential plateau as a function of the lithium content, which indicates a two-phase region in equilibrium. For the best samples the phase transformation that occurs at several intercalation stages, could be observed clearly in the voltammogram (Figure 10.1).

It is virtually impossible to obtain quasi-equilibrium intercalation results from the *c*-axis oriented films. Due to the slow stabilisation of the host structure and the resulting continuous potential decay (see Figure 4.3), the OCP measurements become inaccurate. Predictions of the 'initial OCP values' suggest that the expected phase transformations do occur, but are confined to the surface of the electrode film. The unstable OCP can be explained by the gradual equilibration of the internal lithium concentration gradient. It is unknown to what extent the limiting effect of the phase boundary movement delays the slow inward transport of lithium.

Ageing – All active LiCoO_2 thin-film electrodes in contact with liquid electrolyte solution show a decrease of the intercalation rate capability with ageing of the cell (for an example, see Figure 4.13). This observation is attributed to the growth of the Solid Electrolyte Interface (SEI) layer between the electrode and the liquid electrolyte phase, which poses another barrier for lithium intercalation. The exact composition and growth mechanism are unclear [3]. Due to the increase in the intercalation resistance, less lithium can be accommodated under specified experimental conditions and thus the reversible capacity is observed to decrease with subsequent, identical measurements.

The application of a (intermediate) solid electrolyte film directly on the thin-film electrode could stabilise the interface properties and prevent the deterioration of the intercalation rate. Solid electrolyte films, *e.g.* LiPON, have also been applied in the microbattery. Extensive characterisation of these devices is planned.

10.3 Proposed research directions

The physical growth process of the LiCoO_2 films remains interesting for fundamental research, as the influence of nucleation and the growth rate of the individual lattice planes on the eventual preferential orientation is still unclear. The effect of the annealing procedure shows that the temperature controls the crystallinity and the grain size distribution of LiCoO_2 films. However, it cannot be excluded that the choice of substrate material also affects the film structure. Epitaxial growth of intercalation films has not yet been reported.

Due to their high intercalation rate the LiCoO_2 RF-films with the 'accessible' (110) orientation, are very suitable as thin-film electrodes. These intercalation electrodes can be applied in devices like the microbattery or used for research experiments to further unravel the intercalation mechanism.

There are still some unanswered fundamental questions, for example:

- Does the lithium intercalation in Li_xCoO_2 proceed through sequential filling (alternate) lithium layers (staging mechanism), or gradually through the entire host? The intercalation mechanism also determines the form of the phase boundary.
- An electron enters the intercalation host simultaneously with the intercalation of a lithium ion, but does it reside on the transition metal ion ($\text{M}^{3+/4+}$) or does it occupy a hole in the oxygen p-band?

A large array of measurement techniques can be used to study these and other problems. For instance, HR-TEM could visualise the lithium diffusion planes; the STM adapted to monitor the intercalation of a single lithium ion; Li-NMR applied to determine the lithium component diffusion coefficient; the temperature dependent OCP measurement used to analyse the thermodynamic quantities; Hall-effect measurements employed to determine the charge carrier concentration as a function of lithium content; XANES used for determining the oxidation states in Li_xCoO_2 . The preparation of the proper samples for all these experiments should not be a problem, as the entire LiCoO_2 film synthesis procedure is compatible with standard wafer processing techniques.

With the realisation of the microbattery, the thin-film lithium intercalation has become available for application or measurements outside of the Helium glove box. Unfortunately, these microbatteries are expensive and their preparation time-consuming. Note, that comparable lithium ‘microbatteries’ can also be assembled in a simpler manner using powder materials and polymer electrolytes, and these would serve less fundamental research purposes perfectly. To my opinion, the submicron secondary lithium cell should be tailored to match the energy requirements of the integrated electrical circuit, in other words: development of ‘*smart power*’.

10.4 References

1. D.K. Gosser, “Cyclic Voltammetry – simulation and analysis of reaction mechanisms”, VCH Publishers Inc. New York, (1993).
2. D. Aurbach, “Nonaqueous Electrochemistry”, Marcel Dekker Inc., New York (1999)
3. D.D. MacNeil, J.R. Dahn, *J. ElectroChem. Soc.*, **148** [11] A1205 (2001).

Summary

The basic principle of rechargeable lithium batteries: the “lithium intercalation” of the positive electrode has been studied to determine the key aspects of this process.

The active material is a LiCoO_2 ceramic layer. Two different plasma deposition techniques have been applied to grow well-defined LiCoO_2 films on silicon and polished stainless steel substrates. These are: Pulsed Laser Deposition (PLD) and RF-sputtering. These films obtain a layered, polycrystalline structure (R-3m) after an annealing treatment (600°C for 30min). The orientation of the two-dimensional host lattice towards the substrate depends on the deposition rate. A (pulsed) high deposition rate leads to a so-called c -axis orientation, as observed here in the case of the PLD-film, while a continuous low deposition rate results in an a -axis oriented film, as observed here for the RF-films.

The lithium content is controlled by electrochemical (de-) intercalation of lithium ions from the electrolyte solution. As only one side of the film is exposed to the electrolyte, the orientation of the film has large consequences for the intercalation rate and capacity: the a -axis oriented films are able to sustain high currents for long periods of time due to the accessibility of the host structure. The c -axis oriented films appear inaccessible and thus exhibit inferior properties. Using polished stainless steel substrates or etching holes in the film after deposition, improves the intercalation properties of the c -axis oriented films.

Finally a ceramic micro-battery has been constructed on the bases of the a -axis oriented LiCoO_2 films on silicon substrates. This prototype shows the feasibility of on-chip power (backup) for integrated circuits.

Samenvatting

In dit proefschrift is het basisprincipe van de oplaadbare lithium batterij onderzocht, de zogenaamde: “lithium intercalatie”. Eén aspect daarvan is het achterhalen van o.a. de snelheidsbepalende stap voor de positieve elektrode.

Het actieve materiaal is een keramische laag van Li_xCoO_2 . Twee verschillende plasma depositie technieken zijn gebruikt om goedgedefinieerde Li_xCoO_2 films te groeien op silicium en roestvast staal (RVS) substraten. Deze zijn: Pulsed Laser Depositie (PLD) en RF-sputteren. Tijdens een warmtebehandeling (600°C gedurende 30 minuten) krijgt de film een gelaagde, poly-kristallijne structuur (R-3m). De oriëntatie van deze tweedimensionale structuur ten opzichte van het substraat blijkt afhankelijk te zijn van de depositie snelheid. Bij (kortstondig) hoge depositie snelheid, zoals in dit geval de PLD-films, treedt er een zogenaamde *c*-as oriëntatie op, terwijl een constante lage depositie snelheid leidt tot een *a*-as oriëntatie, zoals hier is geconstateerd bij de RF-films. De lithium concentratie wordt elektrochemisch geregeld door (de-) intercalatie van lithium ionen vanuit de elektrolyt fase. Doordat slechts één zijde van de film in contact staat met de elektrolyt, heeft de oriëntatie van het actieve materiaal grote gevolgen voor de intercalatie snelheid en capaciteit: de *a*-as georiënteerde films zijn in staat om hoge stromen te leveren doordat deze roosterstructuur toegankelijk is voor lithium, terwijl de *c*-as georiënteerde films juist ontoegankelijk zijn en zodoende slecht functioneren. Met het gebruik van RVS substraten of door na depositie defecten in de film te etsen wordt de toegankelijkheid en daarmee de prestatie van de *c*-as georiënteerde film verhoogd.

Uiteindelijk is er op basis van de *a*-as georiënteerde LiCoO_2 film een prototype van een keramische microbatterij gerealiseerd met voldoende capaciteit om geïntegreerde schakelingen van (back-up) stroom te kunnen voorzien.

A Ladder network impedance

Figure A.1 shows a schematic representation of a ladder network describing ambipolar diffusion. The opposite connections for the ionic and the electronic rail represent the electronic equilibrium with the current collector and the ionic equilibrium with the electrolyte solution, respectively

$$\begin{aligned}\nabla V_i(x, \omega) &= -Z_i(\omega) \cdot i_i(x, \omega) \\ \nabla V_e(x, \omega) &= -Z_e(\omega) \cdot i_e(x, \omega)\end{aligned}\quad (\text{A.1})$$

The drop in the current, due to the “leakage” from the ionic to the electronic rail is given by:

$$\nabla i_e(x, \omega) = -i_y(x, \omega) = -Y_y(\omega) \cdot [V_e(x, \omega) - V_i(x, \omega)] = -Y_y(\omega) \cdot \Delta V_{ei}(x, \omega) \quad (\text{A.2})$$

and *vice versa*:

$$\nabla i_i(x, \omega) = +i_y(x, \omega) = +Y_y(\omega) \cdot [V_e(x, \omega) - V_i(x, \omega)] = +Y_y(\omega) \cdot \Delta V_{ei}(x, \omega) \quad (\text{A.3})$$

Taking the second derivative of equations (A.2) and (A.3) and combining these leads to the expression:

$$\nabla^2 \Delta V_{ei}(x, \omega) = [Z_e(\omega) + Z_i(\omega)] \cdot Y_y(\omega) \cdot \Delta V_{ei}(x, \omega) \quad (\text{A.4})$$

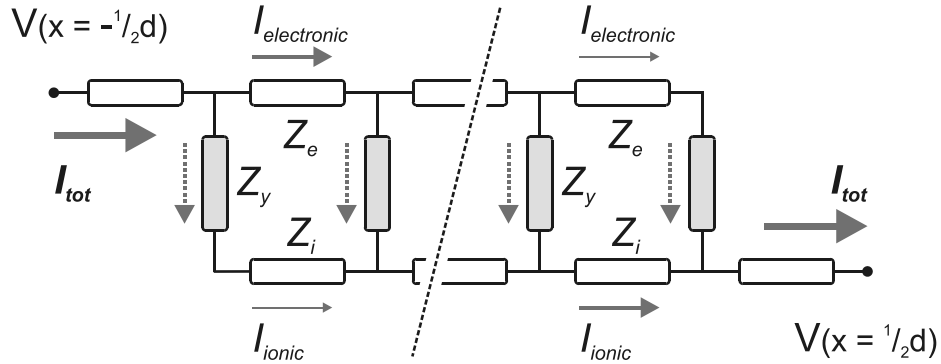


Figure A.1: The schematic representation of a ladder network consisting of an electronic (top) and an ionic (bottom) pathway and an interconnecting impedance denoted Z_y .

The general solution for this differential equation is:

$$\Delta V_{ei}(x, \omega) = A \cosh(xQ(\omega)) + B \sinh(xQ(\omega)) \quad (\text{A.5})$$

with: $Q(\omega) = \sqrt{[Z_e(\omega) + Z_i(\omega)] \cdot Y_y(\omega)}$

The boundary conditions are defined as follows:

$$\begin{aligned} I(\omega) &= i_i(x, \omega) + i_e(x, \omega) \\ \nabla V_i(x, \omega) \Big|_{x=-\frac{1}{2}L} &= 0 \\ \nabla V_e(x, \omega) \Big|_{x=-\frac{1}{2}L} &= -Z_e(x, \omega) \Big|_{x=-\frac{1}{2}L} = -Z_e(\omega) \cdot i_e(x, \omega) \Big|_{x=-\frac{1}{2}L} = -Z_e(\omega) \cdot I(\omega) \\ \nabla V_i(x, \omega) \Big|_{x=\frac{1}{2}L} &= -Z_i(x, \omega) \Big|_{x=\frac{1}{2}L} = -Z_i(\omega) \cdot i_i(x, \omega) \Big|_{x=\frac{1}{2}L} = -Z_i(\omega) \cdot I(\omega) \quad (\text{A.6}) \\ \nabla V_e(x, \omega) \Big|_{x=\frac{1}{2}L} &= 0 \\ \text{thus: } V_{\text{tot}} &= V_e \Big|_{x=-\frac{1}{2}L} - V_i \Big|_{x=\frac{1}{2}L} \end{aligned}$$

The solution of the differential equation considering these boundary conditions reads:

$$\begin{aligned} i_i &= I(\omega) \cdot \left[\left(\frac{Z_i}{Z_i + Z_e} \right) - \left(\frac{Z_i}{Z_i + Z_e} \right) \cdot \frac{\cosh(xQ(\omega))}{\cosh(\frac{1}{2}LQ(\omega))} + \frac{\sinh((x + \frac{1}{2}L)Q(\omega))}{\sinh(LQ(\omega))} \right] \\ i_e &= I(\omega) \cdot \left[\left(\frac{Z_i}{Z_i + Z_e} \right) + \left(\frac{Z_i}{Z_i + Z_e} \right) \cdot \frac{\cosh(xQ(\omega))}{\cosh(\frac{1}{2}LQ(\omega))} - \frac{\sinh((x + \frac{1}{2}L)Q(\omega))}{\sinh(LQ(\omega))} \right] \quad (\text{A.7}) \\ V_i &= I(\omega) \cdot \left[- \left(\frac{Z_i Z_e}{Z_i + Z_e} \right) \cdot x - \left(\frac{Z_i Z_e}{Z_i + Z_e} \right) \cdot \frac{1}{Q} \cdot \frac{\sinh(xQ(\omega))}{\cosh(\frac{1}{2}LQ(\omega))} - \frac{Z_i}{Q} \cdot \frac{\cosh((x + \frac{1}{2}L)Q(\omega))}{\sinh(LQ(\omega))} \right] + K \\ V_e &= I(\omega) \cdot \left[- \left(\frac{Z_i Z_e}{Z_i + Z_e} \right) \cdot x - \left(\frac{Z_e^2}{Z_i + Z_e} \right) \cdot \frac{1}{Q} \cdot \frac{\sinh(xQ(\omega))}{\cosh(\frac{1}{2}LQ(\omega))} + \frac{Z_i}{Q} \cdot \frac{\cosh((x + \frac{1}{2}L)Q(\omega))}{\sinh(LQ(\omega))} \right] + K \end{aligned}$$

where K is an arbitrary constant. On combination of (A.6) and (A.7) we obtain:

$$Z_{tot}(\omega) = Z_p(\omega)L + (Z_s(\omega) - 2Z_p(\omega)) \left(\frac{\coth(LQ(\omega))}{Q(\omega)} \right) + 2Z_p(\omega) \frac{1}{Q(\omega)\sinh(LQ(\omega))}$$

with :

$$Z_p(\omega) = \frac{Z_i(\omega)Z_e(\omega)}{Z_i(\omega) + Z_e(\omega)} \quad (\text{A.8})$$

$$Z_s(\omega) = Z_i(\omega) + Z_e(\omega)$$

The definition of Y_y depends on the process this element represents. In the case of the lithium intercalation electrode it symbolizes the admittance of the intercalation capacity

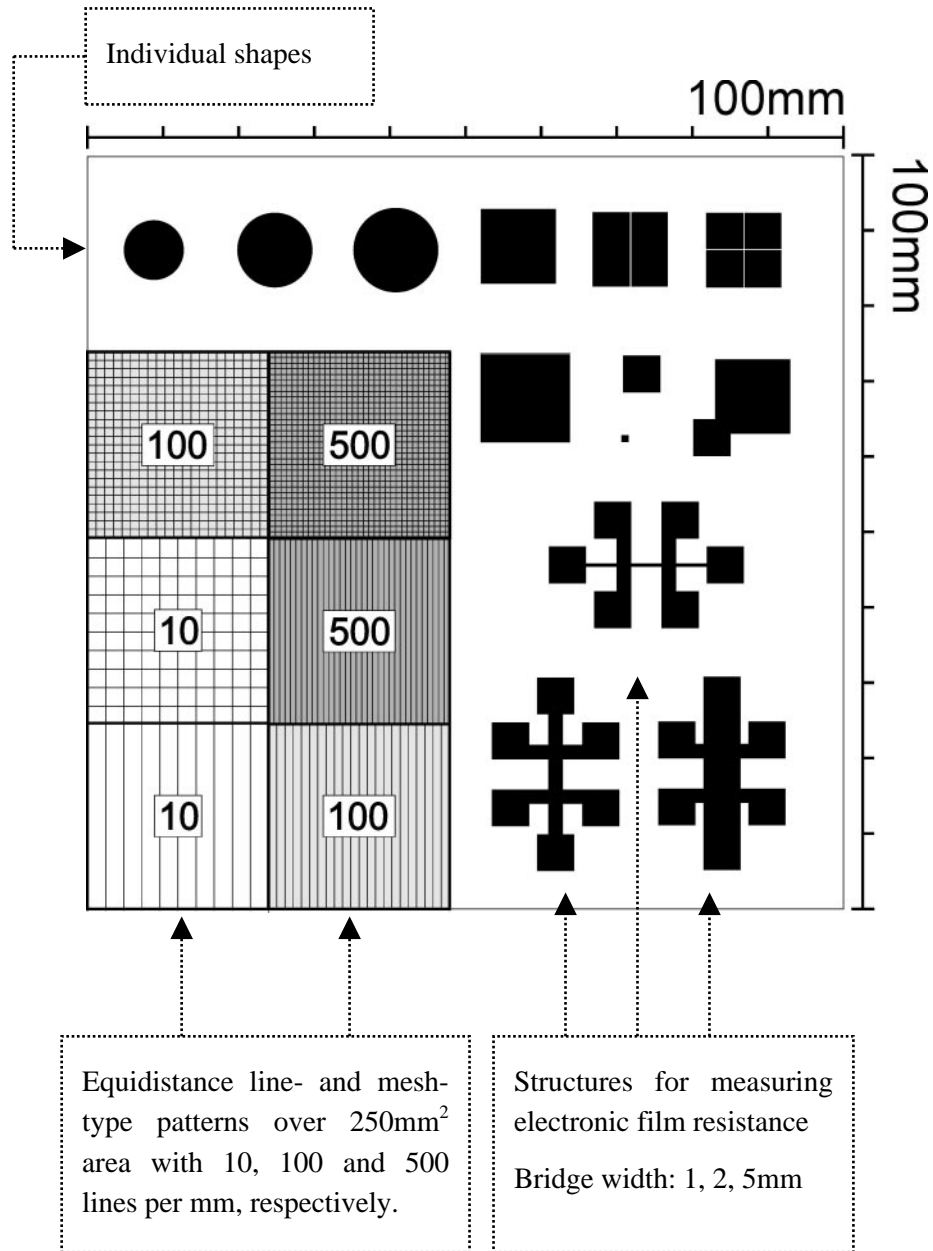
$$Y_y(\omega) = (Z_y(\omega))^{-1} \equiv (j\omega C_{int})^{-1} = \left(j\omega \cdot \left[\delta L \cdot A \cdot q_e^2 \frac{\partial \mu_{Li}}{\partial c_{Li}} \right] \right) \quad (\text{A.9})$$

where $\delta L \cdot A$ represents the intercalation volume element with thickness δL and cross section area A . If Boltzman statistics apply, the partial derivative $\left(\frac{\partial \mu_{Li}}{\partial c_{Li}} \right)$ in equation (A.9) can be evaluated, yielding:

$$C_{int} \propto c_{Li} \quad (\text{A.10})$$

As expected the intercalation capacity is proportional to the number of charge carriers within the volume element of the electrode.

B Lithographic mask design



C Temperature sensor circuitry

The AD590 is a two-terminal integrated circuit temperature transducer, which produces an output current proportional to absolute temperature. For supply voltages between +4V and +30V the device acts as a high impedance, constant current regulator passing $1\mu\text{A}\cdot\text{K}^{-1}$ (Figure A.2). Laser trimming of the chip's thin film resistors is used to calibrate the device to $298.2\mu\text{A}$ output at 298.2K (25°C).

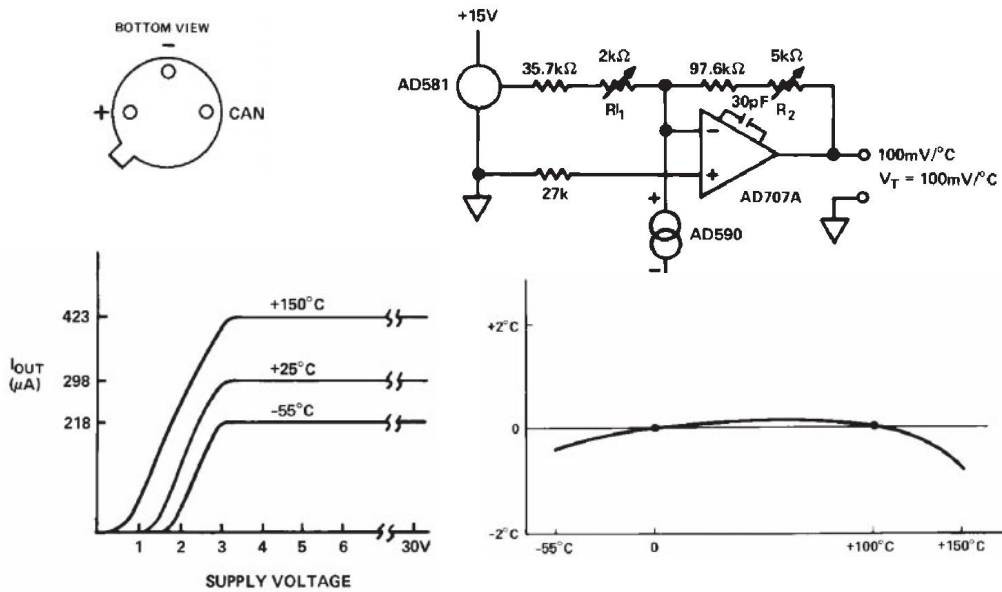


Figure A.2: Output current as a function of supply voltage for different temperatures.

Figure A.3: Plot showing the non-linearity of the current output adjusted using the 'two temperature trim' circuit displayed above.

The accuracy of the AD 590 is determined by the non-linearity of the output current. Figure A.3 shows the maximum deviation from the actual temperature when connected to the displayed 'two temperature trim' circuit and calibrated at 0°C and 100°C . The power supply is delivered by the Autolab potentiostat.

THANKS EVERYBODY!

The road that a fresh Ph-D student commences is initially wide, scenic, unknown, then winding, steep, adventurous and finally narrow, treacherous and endless. After four exciting years I managed to pass the final milestone and it becomes time to choose a new direction. First I would like to take the opportunity to thank the people who have shed light on my path and those who have encouraged me to enjoy the view.

The FOM foundation is thanked for the financial support and prof. H. Verweij for appointing this project to me. I also appreciate the willingness of prof. D.N. Reinhoudt to act as my promoter together with prof. P.H.L. Notten. Within the IMS group I could always rely on my guardian angel Bernard Boukamp and also Henny Bouwmeester for proper coaching through very specific fields of research. Peter Notten witnessed my progress from a somewhat longer distance, but his pinpoint observations are not less appreciated. I consider myself lucky with your supervision and I thank you all for your sharing of knowledge, your faith in me and the plain good company.

As common for OiO's, my working space became a second home. From the moment Fiona and Marco asked me to join their room I enjoyed the working atmosphere and all of its pleasant interruptions. A pity '*Kansas has gone bye-bye*'. Luckily, I bonded well with the population of the IMS and catalysis group and sincerely I hope the feeling is mutual. Although you're not all mentioned by name, you are remembered!

Pretty soon I had to apportion my presence between Enschede and Eindhoven. All but easy; I met a lot of people in Eindhoven who deserve my full attention. I will start with the 'electro&chemistry' group at Philips: Hans, Rene, Petra, Eric, Jan, Maxim, Fred and all others, I wish you all the best of luck! Thanks Martin, Robert, and Marie-Jeanne for sharing working hours as well as social time and keeping me posted. I'm also grateful towards Fab-WA and Eric van den Heuvel and Jan Verhoeven in particular, for you have greatly contributed to my sample collection. Thank you Harry Wondergem (and the rest of Philips CFT) for looking at my collection so often. Fortunately for them, I was also able to do something myself thanks to the equipment and

directions of Hans Cillessen, Harry van Hal and Wilco Keur. Hopefully, I have not worn out my welcome.

I owe my knowledge of lithium to several other battery sanctuaries as well: first of which is the group of prof. J. Schoonman in Delft. Thank you Michiel, Frans, Nitte, and Erik for showing me around. In the neighborhood is the IRI facility: remember Marnix, you still promised me to see the core! I am also grateful to prof. Josh Thomas for having me over at the Ångström Laboratory and thank you, Tom, Andrea, Amy and Linda for your the measurements and discussions. To me the visit was definitely fruitful.

My social life in Eindhoven was initiated thanks to Goovert, who introduced me to a great group of volleyball players. The adventures as a Super Schredderrr team member were absolutely unforgettable: Claudia, Gabi, Gerrit-Jan, Wilbert, Hendrik, Marion and everybody, once more: "Metertje plezier voor...?!"

It was inviting to see other wonderful people outside of volleyball and, Jennifer and Bianca, I hope to see much more of you! Ofcourse, I want to meet everybody from 'van Mol' again. Thank you Sandra and Rob for providing me with comfort and shelter during my unpredictable stay in your home.

In Enschede I was eager to realize newfound ideas and solutions and not without the help of Attila. You successfully taught me the house rules and tool shed rules as well as lab rules and allowed me some freedom to bend them (a little). Your friendship is a privilege. People who also put a lot of energy in fulfilling my desires are Herman, Leon, Gerrit, Henk, Joop, Natasha and Cindy; not to forget my lovely Italian cake-baking-expert Neva Cuneo! I could not have done it without you. The Mesaplast cleanroom of was another world of wonders to me, until Johnny, Hans, Peter, Huib and the others patiently showed me how to make useful things. Without their advice and assistance I would have been just another monkey in a suit.

In Enschede sports have also been an absolute must to let off steam. Wu-Shu is sacred to me: Sifu Maulany showed me how to stay focused and relaxed under pressure, which certainly did come in handy at times. It has been stimulating training with enthusiastic people like Oluf, Eric, Jaap, Bijou, Leon, Menno, Frank, Pieter, Astrid, Kim, Lidewij, Maurits but also Sebo, Ebor, Dennis and the rest. Fortunately, our quality time is not limited to training

hours. Through sports I came into contact with the AKI. This attractive alternative to the UT-atmosphere, just a corridor away, has been an appreciated experience indeed. Keep it up, guys!

If there ever was a society I belonged to, it would be the '*Jotter*'. Strictly limited to the members Jurgen, Patrick, HJ, Tom, Arjan, Leon and myself, this gang engages all leisure activities regarded interesting to 'man'-kind. Thanks for being patient with me, guys and I will *try* not miss out on anything anymore!

Now comes a round of applause for superb social support I enjoyed in Enschede: To all my roommates in "Temple MarMas": Sorry I had to spill my guts at times and please remember those GOOD times. Rianne, Nienke, Jeroen, Marieke, Jochem, Kirsten, Mascha and the generation Harco, Mark, Hanneke, Paula, Marit, Arian and all the other people I've had the pleasure to live with in the past years: You've been absolutely Fab! Occasionally good friends dragged me from the house for other social activities. Please do continue! Jan-Hindrik and Saskia, you used the excuse of swimming, but it was seldom the only event planned. Iwan, you always know just when to call. Marie, more email asap! For my lifelong friends in distant cities: Corrie, Saskia and Gea, time is always too short. As also goes for Bas and Dennis; I owe you special gratitude for backing me up for most of my life and on this occasion as 'paranimf'.

As paper is running out, I will directly apologize to the people I have forgotten and those who have heard the excuse of "the OiO-workload" once too often. This goes especially for my family, who haven't seen the best of me lately. I have missed you! I hope you can appreciate this final result and we'll catch up during the celebration. All that is left are a few words for the people closest to me: Karen, I know you can beat this (but don't) and to my parents Gert Wouter and Guda, thanks for all your love and support. This milestone is yours as well.

Thank you Anouk for making my life so satisfying.

Peter

Curriculum Vitae

Peter Jaime Bouwman was born in Cardenas, Mexico on July 22, 1974. In 1986 he finished his primary education at the Bogor Expatriate School (Indonesia). Secondary education (VWO) was at the Johannes Fontanus College in Barneveld (the Netherlands). In 1992 he started studying Chemical Technology at the University of Twente in Enschede (The Netherlands). During his studies he participated in a study tour to South Africa in 1996. He did his traineeship at IMEC in Leuven (Belgium), where he studied voiding of passivated aluminium interconnects on chips. In November 1997 he graduated on the topic of porous, doped silica gas-separation membranes in the group Inorganic Material Science of prof.dr.ir. H. Verweij.

Here, he continued to work as a Ph-D student and initiated the research on lithium intercalation at the University of Twente under the supervision of dr. B.A. Boukamp, dr. H.J.M. Bouwmeester and prof.dr. P.H.L. Notten. A large part of the work was executed at Philips Research Laboratories in Eindhoven (The Netherlands) due to project collaboration. During this period he also attended the 1999 NATO Lithium Battery summer school in Sozopol (Bulgaria) and visited the Structural Chemistry group of prof. J. Thomas at the Ångström Laboratory, Uppsala University (Sweden) in 2001. At the ECerS2001 conference in Brugge (Belgium) he won the European student speech competition with the presentation of his work, which is described in this thesis.
